Instituto de Óptica

CSIC
CONSEJO SUPERIOR DE INVESTIGACIONES CIENTÍFICAS

Doctoral thesis

Corneal Ablation and Contact Lens Fitting: Physical, Optical and Visual Implications

by Carlos Dorronsoro Díaz

To aspire to the degree of PhD in Visual Science at the

Universidad de Valladolid

ioba
Instituto Universitario de
Oftalmobiología Aplicada

Thesis supervisor: Prof. Susana Marcos Celestino

Madrid, October 1st, 2009

A Uca.

Contents

Corneal Ablation and Contact Lens Fitting: Physical, Optical and Visual Implications

Acknowledgements

Key words

Optics Physiological optics Eye Refraction Medical Optics Instrumentation
Cornea Visual optics Ophthalmic optics Presbyopia Myopia
Anterior Segment Tear Biomechanics Artificial corneas Optical
Quality Aberrometry Ocular aberrations Laser Ray Tracing
Videokeratoscopy Corneal topography Asphericity Spherical
Aberration Stroma Back cornea Corneal Aberrations Posterior cornea
Internal Aberrations Surface Measurements Surface fitting Profilometry
Surface comparison Refractive Error Laser surgery PMMA
Laser ablation Incubation Refractive Surgery Excimer laser Beer-
Lambert Law Ablation of tissue Depth per pulse Blow-off model
LASIK PRK Aberration correction Ablation profile Efficiency Effects
Reflection Losses Excimer Laser Munnerlyn Parabolic approximation
Filofocon A Laser materials processing Contact lens fitting Flexure
Semirigid lens Soft contact lenses Multifocality Rigid Gas Permeable
Tear Lens Visual Acuity Thru-focus Scheimpflug Imaging

Abbreviations

BOZR   Back Optic Zone Radius
BCVA   Best Corrected Visual Acuity
CCD   Charge Coupled Device
CL   Contact Lens
CS   Contrast Sensitivity
CSF   Constrast Sensitivity Function
D   Diopters
FDA   Federal Drug Administration
HOA   High Order Aberration
HS   Hartmann-Shack
IOL   Intraocular Lens
LASIK   Laser in situ Keratomileusis
LRT   Laser Ray Tracing
MTF   Modulation Transfer Function
nm   Nanometers
OCT   Optical Coherence Tomography
PMMA   Polymethyl-methacrilate
PRK   Photorefractive Keratectomy
PSF   Point Spread Function
RGP   Rigid Gas Permeable
RMS   Root Mean Square
SA   Spherical Aberration
VA   Visual acuity
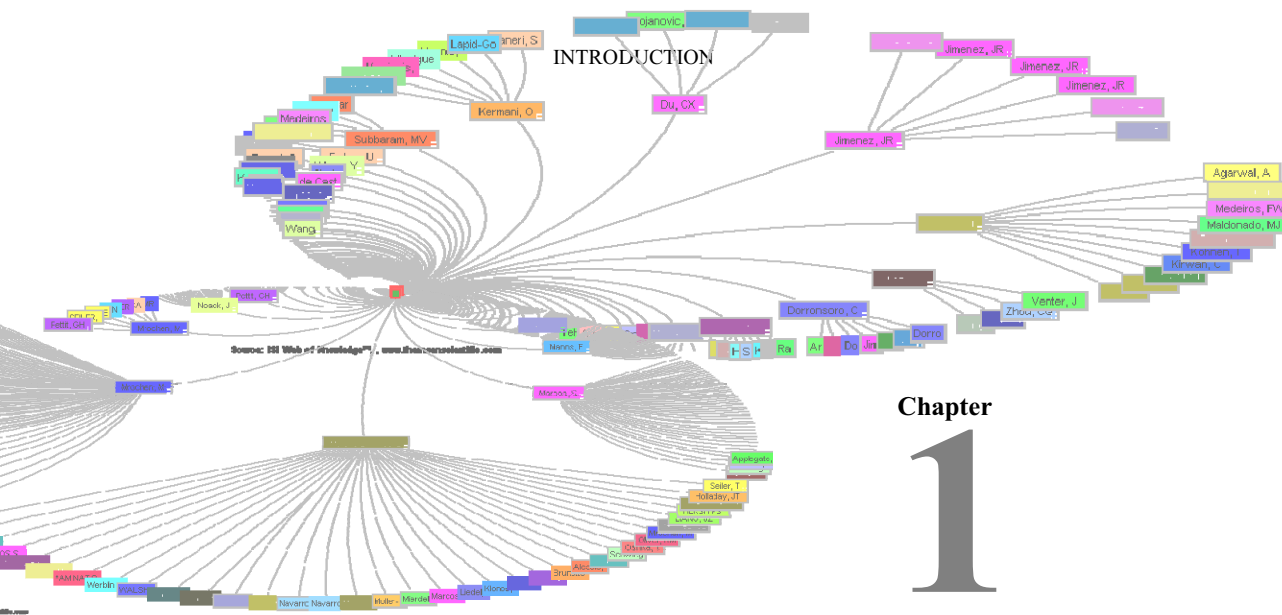
Chapter

1

Introduction

The goal of this doctoral thesis is to study the physical phenomena involved in corneal ablation for refractive surgery, and in the fitting of contact lenses on the cornea. In Chapter 2 we will describe the techniques and procedures developed in this thesis for the measurement of the geometry (and changes in geometry) of optical surfaces, the optical quality they provide, and their visual impact. Chapters 3, 4 and 5 present in vitro studies of physical factors involved in laser ablation. Chapters 6 and 7 are devoted to the measurement of the posterior surface of the cornea, and its longitudinal change after refractive surgery in patients. Chapters 8, 9 and 10 present studies of different aspects of the fitting of contact lenses (soft and rigid, monofocal and multifocal, positive and negative, in vitro and in vivo), and the visual outcomes that these lenses produce.

In this chapter we introduce the main background and key concepts regarding the approach followed in this thesis. We present a short review of aberrometry on the human eye, introducing basic concepts, history and its state-of-the art, along with the most relevant results to date using aberrometry. We present an overview of the other important techniques for this thesis. Finally, we will review Laser Refractive Surgery and Contact Lenses, in relationship with geometrical changes of the ocular surfaces and optical aberrations of the cornea. We will enumerate open questions in the field that we will address in the thesis.

1.1. MOTIVATION

The framework of this doctoral thesis is physiological optics and in particular the optics of the cornea. The research reported here is dedicated to the study of refractive corrections applied to the cornea, that aim at altering the shape of the first surface of the eye, the most accessible and the most important from an optical point of view. Specifically, this research work addresses refractive surgery and contact lenses. We will study the physical phenomena involved in corneal ablation and in fitting lenses on the cornea, and we will show results of the shape changes that they introduce, their optical consequences and their visual impact.

Corneal ablation in refractive surgery and fitting of contact lens are well established procedures for monofocal corrections. Multifocal corrections have also been introduced in the clinical practice, both in the form of contact lenses and refractive surgery. Customization and wavefront guided corrections, both for ablation algorithms and lens designs are also a hot topic, not only in research laboratories but also a major focus on ophthalmic industry and advanced clinical practice.

However, there are still many open questions and plenty of room for improvement, both in monofocal, multifocal, optimized and customized refractive corrections applied to the cornea. A better knowledge of the physical processes (ablation and fitting), isolated in controlled conditions, will provide the understanding and quantification needed to improve the corrections, and in particular the optical quality (and ultimately, vision) of the treated eye. This thesis is based on the use of physical models, artificial eyes, and measurements on patients, and advanced methods for surface characterization and optical quality assessment to study in detail corneal ablation and contact lens fitting. The results will be relevant for the improvement of the techniques, procedures and/or designs associated to refractive corneal ablation and contact lens fitting.

These two fields of study, refractive surgery and contact lenses, are interconnected, not only as many of the methods that can be used for research are similar, but also as mutual feedback can be gained from the results. Contact lenses are a good laboratory test for evaluating and improving multifocal patterns and designs, that are relevant in refractive surgery. Achieving a higher control on the ablation process on curved surfaces will make possible the precise manufacture of customized and/or wavefront optimized contact lenses by laser ablation. The fine control of the final surface geometry requires deeper understanding on laser efficiency effects that have affected refractive surgery outcomes in the past (and still does, although to a minor extent).

Corneal abation and contact lens fitting aim at altering the first surface of the eye to change its optical performance (in most cases to reduce ametropia or to induce multifocality). However, as will be shown in this thesis, the posterior surface of the cornea (or the contact lens) can also play a role. The posterior surface of the cornea, and the instruments used for its biometry, will also be studied in this thesis in the context of refractive surgery, through the use of another model cornea.

Physical and optical factors contribute to the quality of the retinal image, but they constitute only the initial steps of the vision process. Neural factors need also to be considered when determining visual quality following a refractive procedure or a contact lens fitting. In this thesis, we will approach the study of these visual implications with multifocal contact lenses by a through-focus visual acuity test. The study was performed with contact lenses of different designs (including monofocal

lenses) fitted to the same eye. In this case, we the optics is modified in each condition while the neural factors remain the same.

1.2. THE OPTICAL SYSTEM OF THE EYE

1.2.1. Cornea

The eye is, from an optical point of view, an image forming device than achieves its high optical power (60 diopters) with two refractive elements, the cornea and the cristalline lens (Atchison and Smith, 2000). The images of the outside world are projected onto the retina (the eye fundus) directly connected to the brain. Figure 1.1 shows the main optical elements, with dimensions and refractive indices.

The cornea is an inhomogeneus cellular and fibrilar structure, composed of different layers: Epithelium, Bowman's Membrane, Stroma, Decemet's membrane and Endothelium (Barbero, 2006). The cornea is alive, and protected from environmental elements by the tear film. The Stroma is the thickest layer (90% of the corneal thickness, around 500 μm).
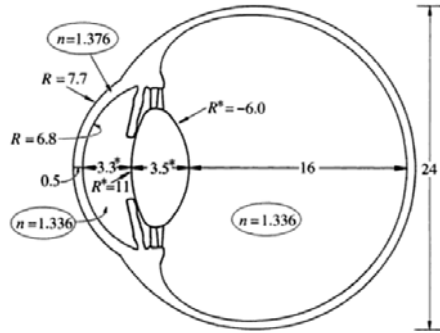
Fig. 1.1. The eye can be considered an optical system (Atchison and Smith, 2000). The dimensions and refractive indexes of the human eye are shown.

The anterior cornea is the front surface of the eye and has a regular and stable shape. The tear film has the important role of providing the anterior cornea with a smooth and polished optical surface. In optical terms, the anterior cornea is the most important optical surface, providing 48 diopter of optical power, and it is extremely transparent. The average cornea is not spherical. The radius of curvature increases from the apex or, in other words, the cornea flattens in the periphery. If we consider the equation of a conicoid:

$$(X^2 + Y^2)^2 + (1+Q)Z^2 - 2ZR = 0 \ , \tag{1.1}$$

(where Z is the coordinate along the optical axis, R the apical radius and Q the asphericity), and fit it to real corneas, the average R obtained will be around 7.7 mm and the average Q will be -0.25 (see table 2.3 in Ref. (Atchison and Smith, 2000)). This shape corresponds to an ellipsoid.

Some optical inhomogeneities inside the cornea contribute to the scattering of light, what allows the imaging of optical sections of the cornea with different instruments and techniques as slit lamp imaging, Scheimpflug imaging and Optical Coherence Tomography.

The posterior cornea has a smaller importance in optical terms (-6 D of optical power), due to the lower refractive index difference than the aqueous humour (the transparent liquid between the cornea and the lens). This small index difference and the strong influence of the anterior surface, makes the posterior cornea more difficult to measure.

1.2.2. Lens

Right after passing through the cornea and the iris (the variable optical pupil of the eye) the rays of light coming from the object find the crystalline lens. This biconvex lens has the ability, in the young human eye, to change its shape and refractive index distribution to increase its optical power. This ability, named accommodation, enables the young eye to adapt its power to different object distances, and focus the rays on the retina. The mechanism of accommodation is traditionally explained on the basis of Helmholtz's theory (Von Helmholtz, 1909). In the un-accommodated eye (with the focus at its far point) the ciliary muscle (around the lens) is relaxed, pulling on the lens and flattening it. When accommodating (bringing the focus to a closer position) the ciliary muscle contracts, reducing the tension on the lens. The axial thickness increases, and the anterior surface moves forward, increases its curvature and changes its shape (Atchison and Smith, 2000, Glasser and Campbell, 1999).

1.3. MYOPIA AND PRESBYOPIA

1.3.1. Myopia

Myopia is a refractive error that allows the eye focusing near objects, but not distant objects. The images of distant objects formed by a myopic eye on the retina are blurred. Parallel rays coming from infinite (distant objects) are focused in front of the retina, even when the accommodation is relaxed. The focal length of the eye is short, relative to the eye dimensions (Fig. 1.2). The opposite condition (light focused behind the retina) is called hyperopia.
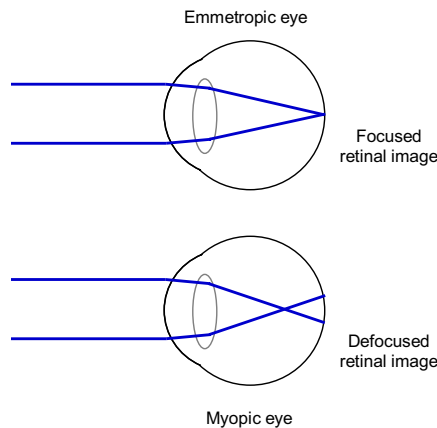
Fig. 1.2. In an emmetropic eye, parallel rays (coming from far objects) are focused on the retina. In myopic eyes the eye power and the axial length are not tuned, and rays coming from far objects are focused before reaching the retina. The retinal image for far objects is blurred.

Myopia is a very common condition in humans, typically associated to age, genetic factors, and visual habits. The prevalence rate in adults is more than 70% in some Asian populations, and around 25% in western countries. Emetropia (absence of refractive errors) demands a fine tuning between the power of all the ocular components of the eye and the axial length (distance between the cornea and the retina). The growing eye has an active control mechanism to tune the eye elongation to the optical power of the optical elements of the eye. This process is called emetropization, and when it is disrupted, leads to myopia in most cases.

1.3.2. Presbyopia

As age increases, the lens movement is reduced, and accommodation is gradually diminished. The first symptoms are usually noticed at around the age of 40, when visual tasks at near distances become more difficult. The ability to accommodate is completely lost at 55 (Weeber and van der Heijde, 2007). This condition is called presbyopia (Fig. 1.3).

Although several potential causes for presbyopia have been hypothesized, the best supported is the progressive loss of elasticity of the lens produced by the continuous growing of the nucleus (inner part of the lens), blocking the capacity of changing its shape and its refractive index distribution (Glasser and Campbell, 1998, Charman, 2008).
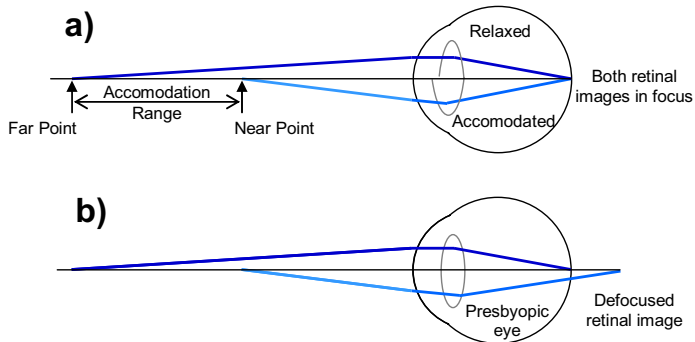
Fig. 1.3. Accomodation and presbyopia on a myopic eye (for an emmetropic eye the far point would be at infinity). a) In the non presbyopic eye the cristalline lens changes its power to keep objects at different distances in focus at the retina, a process called accommodation. b) In the presbyopic eye the ability to accommodate is partially or totally lost, the cristalline lens does not change its power and therefore different object distances correspond to different defocus states at the retina.

Even when the ability to accommodate is completely lost, the depth of focus of the eye provides certain capacity to observe objects at varying distances (i.e. there is a range for which the eye cannot appreciate the blur introduced by defocus). This depth of focus is highly dependent on the pupil size, on the amount of aberrations and on the criterion used to measure or estimate it, and is around ± 0.5 D for the human eye (Tucker and Charman, 1975, Atchison et al., 1997).

1.4. OPTICAL ABERRATIONS

1.4.1. Chromatic aberrations

Optical aberrations can be divided in chromatic and monochromatic (i.e. geometrical) aberrations. Chromatic aberrations are a consequence of the dispersion (variation of refractive index with wavelength) of the refractive media of an optical system. There are two types of chromatic aberrations. The longitudinal chromatic aberration is produced because the different wavelengths are focused at different image planes, and can be quantified as the variation in power with wavelength. The transverse chromatic aberration is produced when obliquely incident rays are focused at different transverse positions within the image plane (Charman and Jennings, 1976, Marcos et al., 1999).

1.4.2. Monochromatic aberrations

Monochromatic (or geometrical) aberrations are those present when only one wavelength is considered, and arise from geometry, irregularities, tilts and decentrations of the optical surfaces of the optical system (Liang et al., 1994, Atchison and Smith, 2000). The magnitude of the geometrical aberrations increases with the diameter of the exit pupil considered. In this thesis polychromatic aberrations are not considered, and therefore we will refer to monochromatic or geometrical aberrations simply as optical aberrations.

There are many representations to describe the geometrical aberrations. In this thesis we use the concepts by Seidel and the quantification by Zernike, both described hereinafter.

There are different methods to specify the image quality of the image formed by an optical system. An alternative that is usually applied to describe the optical performance of the eye, is in terms of the wave aberration (see Fig. 1.4). The wave aberration, *W (x,y)*, describes the distortions of the wavefront (represented by red curves in Fig. 1.4) as it goes through an optical system. The wavefront is the surface containing the points of a wave on the same phase, and are orthogonal to the corresponding ray pencils.

a) Non-aberrated eye   b) Aberrated eye
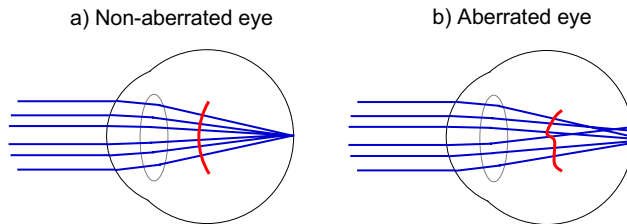
Fig. 1.4. a) Schematic representation of a non-aberrated eye. b) Aberrated eye

In aberrations-free optical systems (as the eye of Fig. 1.4 (a)) all the parallel rays entering the pupil will intersect the image plane (retina) at the same point, or equivalently, all the imaging wavefronts will be spherical, centred on the image point. Under this condition paraxial optics predict accurately the behavior of the optical system. However, when the optical system is aberrated (Fig. 1.4 (b)) there is no longer

a point focus: the different rays will intersect the image plane (retina) at different points, and the wavefronts will no longer be spherical.

Thus, the optical aberration can be described in terms of wave aberration maps: the distance that each point of the wavefront departs from the ideal sphere at the exit pupil (Charman, 1991). An example of wave aberration map is shown in Fig. 1.5, where the colour indicates the distance between the wavefront and the reference sphere. Besides in terms of wave aberrations, optical aberrations can also be represented as: transverse aberration (departure of a ray from its ideal position at the image surface), or longitudinal aberration (departure of intersection, where this occurs, of a ray with a reference axis, from its ideal intersection) (Atchison and Smith, 2000).
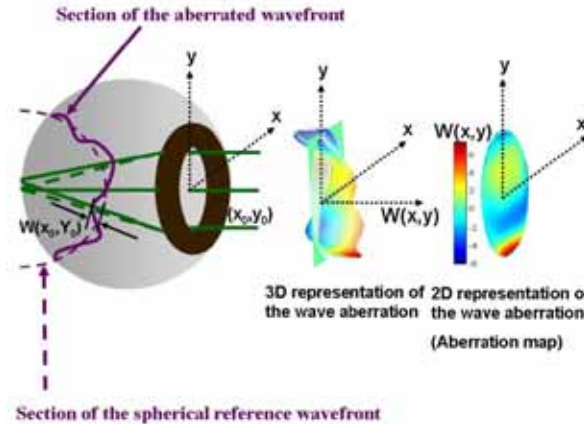
Fig. 1.5. Schematic representation of the wave aberration. Wave aberration values (distances between the distorted aberrated wanefront and the spherical reference) can be represented as z coordinate referred to the pupil plane (three-dimensional representation) or can be represented as a colour gradation (Aberration map).

From the wave aberration maps, two classic descriptors of the optical quality of an optical system can be directly derived, after simple mathematical operations: the Modulation Transfer Function (MTF) and the Point Spread Function (PSF). These two are alternative ways to describe the optical quality of a system. The MTF quantifies the loss in contrast associated to each spatial frequency. The higher the MTF, the better the image provided by the system. The PSF is the impulse response of the system: the degraded image of an ideal point, as imaged by the system. Finally, the retinal image associated with any observed image image can be simulated. A common procedure (Barbero S and Marcos, 2008) consist of convolving the ideal image with the PSF of the system.

Figure 1.6 shows two examples, corresponding to the same eye (right eye of the author of this thesis), under two different conditions: naked eye (top row) and correction of aberrations (botton row) with adaptive optics (explained in Section 1.5.3) (Marcos et al., 2008). When the eye is aberrated (normal condition, top row) the aberration map has considerable deviations from zero (the reference), the MTF drop is sharper (from the initial point: unity at the center), the PSF suffers a larger spread at the retina and the retinal images are blurred. When the aberrations of the eye are corrected (botton row), the residual wavefront map is closed to zero at all points, the MTF fall is gradual, the PSF is a point and the retinal image sharp.
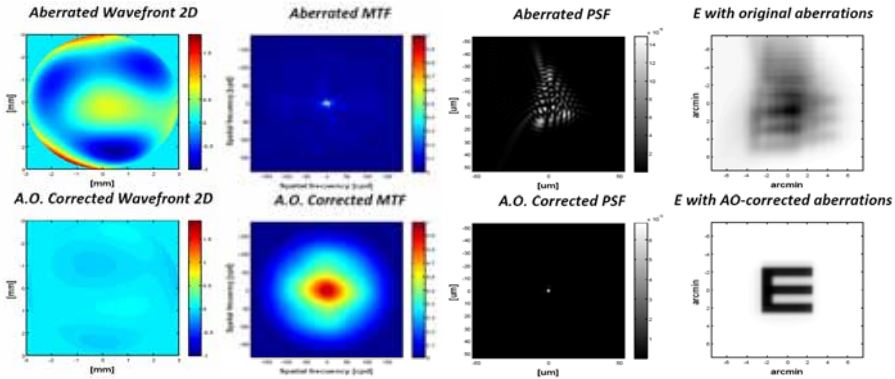
Fig. 1.6. Example of aberration maps and optical quality descriptors derived from them. Top row: right eye of the author of this thesis. From the aberrated wavefront we obtain the MTF (up to 200 cicles/mm) and PSF (100 microns side), and simulate retinal images (20/20 VA Snellen E). When the aberrations are corrected (with adaptive optics in this case) the MTF fall is gradual, the PSF concentrated and the retinal image sharp.

1.4.3. Seidel aberrations

Seidel named in 1865 the seven primary aberrations, which include, apart from the chromatic aberrations already mentioned, five monochromatic aberrations: Astigmatism, Spherical Aberration, Coma, Field Curvature and Distortion. In the presence of any of the first three aberrations, the optical system will not be able to image a point source as a point, and the resulting image will be blurred, degrading the retinal image in different ways (as shown in Fig. 1.7).

When astigmatism is present (Fig. 1.7 (a)), parallel rays along different directions are focused down to two mutually perpendicular focal lines at different positions. Astigmatism in the eye is usually due to lack of symmetry of at least one surface, usually the anterior cornea in the eye.

Positive (or negative) spherical aberration is present when parallel non-paraxial rays do not intersect at the paraxial focus, but in front of (or behind) it (Fig. 1.7 (b)). The further the ray from the optical axis, the greater the effect. Spherical aberration is rotationally symmetric, and depends on the radius of curvature (R) and on the aspherici̇y (Q) of the optical surfaces (decreases when R increases, increases with Q).

In a rotationally symmetric system, coma is an off-axis aberration, where rays departing from an off-axis point reach the image plane at different points (see Fig. 1.7 (c)). In the eye, coma-like aberrations present at the fovea are the result of the lack of symmetry of the optical elements around an optical axis.

Field curvature and distortion are also off-axis aberrations. In both cases a source point is imaged as a point, but the position will be different from that expected in absence of this aberrations: when field of curvature is present the point will be imaged in front of (for systems with components of positive power such as the eye) or behind the paraxial focal plane, and when distortion is present, the point is formed in the paraxial image plane but further away (positive distortion) or closer (negative distortion) to the optical axis than expected (Atchison and Smith, 2000). Piston, tilt and defocus are not considered Seidel aberrations but first order properties of the wavefront. Piston is the mean value of the wavefront across the pupil of an optical

system, and tilt represents the average slope of the wavefront in X and Y directions (Malacara, 1992). Defocus occurs when parallel rays (paraxial and not paraxial) converge in front of (positive defocus) or behind (negative defocus) the paraxial focus. Although not a Seidel aberration, defocus is considered a low order aberration when the wave aberration is described in terms of a polynomial series.
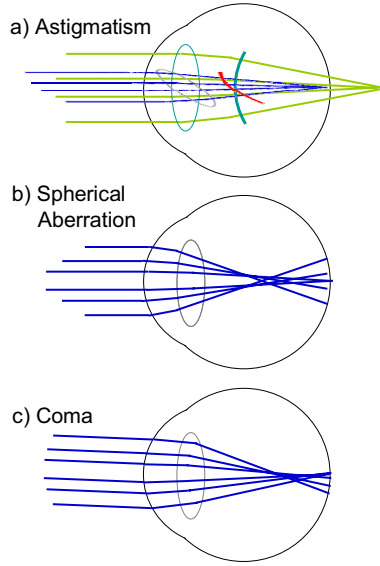
Fig. 1.7. Schematic representation of Seidel aberrations: (a) Astigmatism, (b) Spherical Aberration, (c) Coma.

1.4.4. Zernike representation of aberrations

The wave aberration of a general optical system can be described mathematically by a polynomial series. Zernike polynomial expansion has become the standard for representing ocular wave aberration data, since they present some advantages for this purpose: 1) they are orthogonal over the unit circle, and aberrations are usually referred to circular pupils; and 2) some terms can be identified with Seidel aberrations (Born and Wolf, 1993). Therefore, a wave aberration can be described as a summation of Zernike polynomial functions weighted by the so-called Zernike coefficients, which indicate the magnitude of each particular aberration present:

$$W(\rho,\theta) \approx \sum_{n=1}^{K} \sum_{m=-n}^{n} c_n^m Z_n^m(\rho,\theta)$$

(1.2)

where $W(\rho,\theta)$ is the wave aberration phase in microns as a function of polar coordinates, c_n^m and $Z_n^m(\rho,\theta)$ are the (n, m) Zernike coefficient (in microns) and Zernike polynomial (dimensionless) as a function of polar coordinates, respectively, and K is the maximum polynomial order in the expansion. The Optical Society of America established a set of recommendations regarding sign, normalisation and ordering that will be followed throughout this thesis (Thibos et al., 2000). In

particular, the double-script notation, which designates each basis function according to its order (subscript n) and frequency (superscript m) will be used.

The Root Mean Square (RMS) wavefront error, defined as the root square of the variance of the wave aberration, is typically used as a global metric for the optical quality. We compute the RMS directly from the Zernike coefficients, using the following approximation:

$$RMS = \sqrt{\sum_{i,j}\left(Z_i^{j}\right)^2} \tag{1.3}$$

where Z_i^{j} is the Zernike coefficient corresponding to the order i and frequency j.

Figure 1.8 (Maeda, 2003) shows the two-dimensional representation of the Zernike polynomials up to 6th order with the corresponding notation. Terms beyond 7th order can be considered negligible for human ocular aberrations (Porter et al., 2001, Castejon-Mochon et al., 2002) (Thibos et al., 2002).
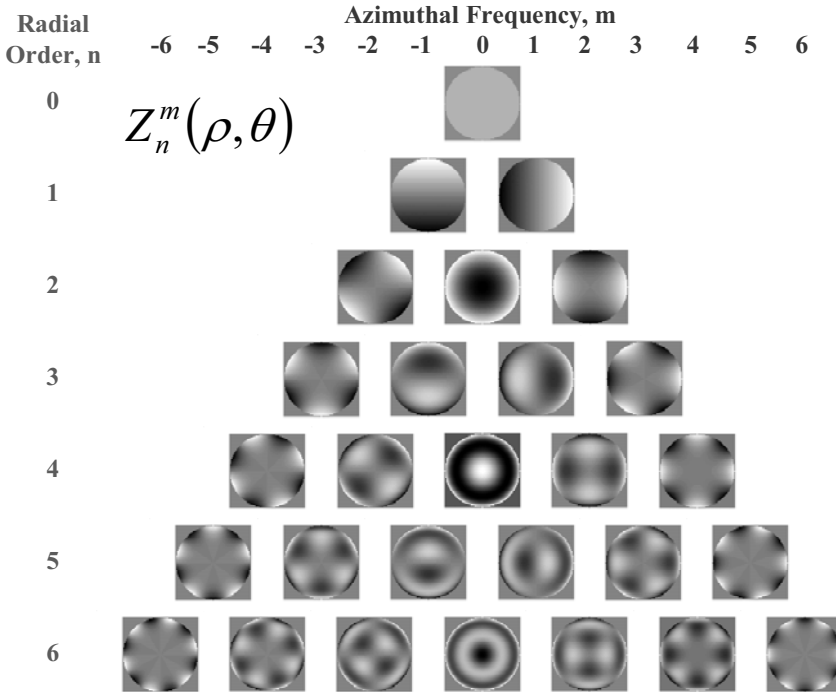
Figure 1.8. Zernike polynomials up to 6th order (Maeda, 2003).

Figure 1.9 (Maeda, 2003) shows the corresponding PSFs (in this case the image of a point in presence of aberrations and diffraction) for a 4 mm pupil diameter, and an RMS wavefront error of 0.53 λ. The images are saturated to emphasize the fine structure and tails in the PSFs.

Some of these aberrations are identified with specific names, or have a direct correspondence with Seidel notation. The Z_0^{0} term (Z_n^{m} where n=0, m=0) (vertex of the pyramid) is the constant term or piston. Z_1^{-1} and Z_1^{1} are tilt in the vertical and horizontal directions and can correspond to Seidel distortion if it changes with the field angle. Z_2^{-2} y Z_2^{2} correspond to astigmatism at ±45º and at ±90º, respectively. The

term Z_2^0 stands for defocus. The terms Z_3^1 and Z_3^{-1} are equivalent to Seidel coma, and Z_4^0 to spherical aberration.
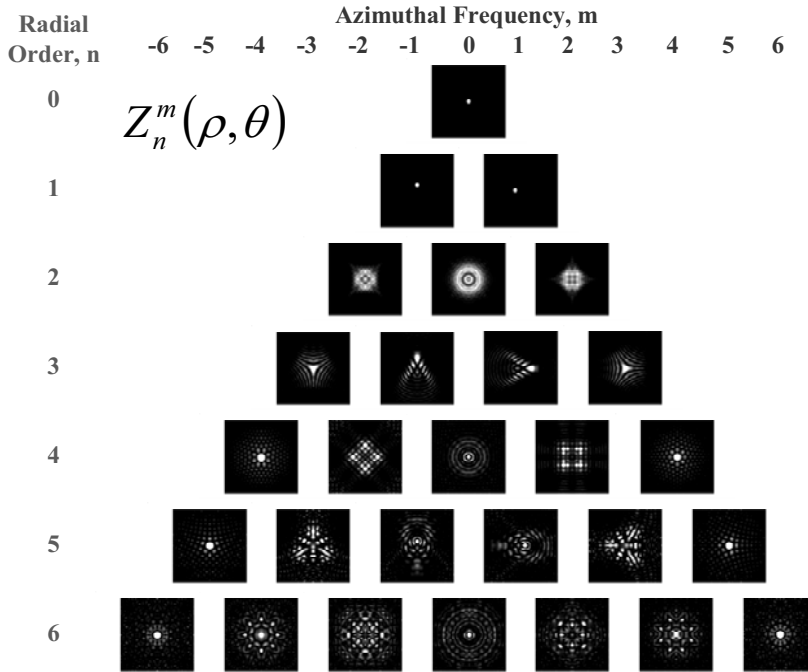
Figure 1.9. PSFs of Wave Aberrations Corresponding to Each Zernike Mode up to 6th Order, 4 mm Pupil Diameter, RMS Wavefront Error = 0.53 λ (Images are saturated to bring out fine structure in PSFs) (Maeda, 2003).

1.4.5. Measurement of Optical Aberrations

The measurement of the ocular optical aberrations has proved to be useful to understand the optical properties and image forming capabilities of the human eye (As we will describe in Section 1.4.6.1). In the last years, aberrometers have started reaching the clinical environment. These new tools have already proved to be very informative in studying changes of the optical quality after surgical procedures (such as corneal refractive surgery (Marcos et al., 2001a, Moreno-Barriuso et al., 2001b), keratoplasty (Munson et al., 2001), or intraocular lens implantation after cataract surgery (Barbero et al., 2002a, Artal et al., 1995)), physiological processes (such as aging (Mclellan et al., 2001, Artal et al., 2002) or accommodation (He et al., 2000)), or pathological conditions (i.e. keratoconus (Barbero et al., 2002b) or myopia (Collins et al., 1995, Marcos et al., 2000)). Wavefront sensors or aberrometers (Sections 1.4.5.3 and 1.4.5.4) measure the wave aberrations of the entire ocular system, typically in less than a few seconds (Moreno-Barriuso et al., 2001a, Moreno-Barriuso and Navarro, 2000). Current videokeratographers provide a rapid and accurate description of the corneal shape (Schultze, 1998). Several authors have used corneal elevation data from commercial corneal topography systems to estimate corneal wave aberrations (Schwiegerling and Greivenkamp, 1997, Applegate et al., 2000, Barbero et al., 2002c, Barbero et al., 2002b, Guirao and Artal, 2000), as will be described in Section 1.4.6.2.

The corneal wave aberration can then be subtracted from the whole eye wave aberration to obtain the aberrations of the internal optics (Section 1.4.6.3). Recently, several methods have been proposed to correct optical aberrations (Section 1.5.3), which open possibilities for imaging the retina with unprecedented resolution, and to study directly the impact of ocular aberrations on vision.

In this thesis, we present wave aberration measurements under different conditions. Total and first surface aberrations measurements are presented in Chapter 3 (in contact lenses fitted in an in vitro model) and Chapter 4 (subjects wearing RGP contact lenses). Total aberrations of eyes wearing (or not) different designs of soft contact lenses are presented in Chapter 5. The optical aberrations of the anterior cornea after refractive surgery are presented in Chapters 6 and 8, obtained from elevation measurements of ablated plastic surfaces. In Sections 1.7 and 1.10 of this Introduction we will provide an overview of the most relevant knowledge today of optical aberrations in relation with contact lenses and LASIK refractive surgery for myopia.

1.4.5.1. Basic concepts of ocular aberrations

Most methods of estimation of the wave aberration are based on local sampling of the pupil and measurement of the local wave aberration slope. The local slope (partial derivatives) of the wavefront is proportional to the ray aberration (Born and Wolf, 1993):

$$\Delta x' = \frac{1}{R_p}\frac{\partial W(\bar{\xi},\bar{\eta})}{\partial \bar{\xi}}; \quad \Delta y' = \frac{1}{R_p}\frac{\partial W(\bar{\xi},\bar{\eta})}{\partial \bar{\eta}} \qquad (1.4)$$

where $\bar{\xi} = \xi / R_p, \quad \bar{\eta} = \eta / R_p$ are dimensionless canonical pupil coordinates and R_P is the pupil radius (Moreno-Barriuso et al., 2001a). The wave aberration is reconstructed by integrating the slopes of an array of beams intersecting the eye's entrance (or exit in some cases) pupil (Howland, 2000). Usually, a least-square estimation is used for phase reconstruction. Some questions to consider when selecting the reconstruction model are the compatibility with the sampling geometry of the sensor and the optical surfaces to be measured, the reconstruction algorithm complexity (convergence problems, computation speed requirements), and the propagation error. In this Thesis we used modal reconstruction, the most widely used method in ocular aberrometry, that is based on the expansion of the derivatives of the wave aberration as a linear combination of a set of basic functions (most frequently the derivatives of Zernike polynomial expansion, already explained in Section 1.4.4), and a subsequent least-squares fit of the expansion coefficients to the measured gradients (Rios et al., 1997).

1.4.5.2. Early aberrometers

The history of aberrometry dates back to 1619 when Scheiner invented a disk with a central and a peripheral pinhole that was placed in front of the eye of a subject, so that an imperfect eye would form two retinal images when looking at a distant point light source. Helmholtz (1821-1894) foresaw that human ocular aberrations were significant enough to degrade the retinal image (Von Helmholtz, 1909). Around the same time, Tscherning (Tscherning, 1894) built what he called "an aberroscope" to measure human eye aberrations, consisting on a grid superimposed on a 5-diopter lens

which image was shadowed on the subject's retina when viewing a distant point light source through the "aberroscope". Aberrations were estimated from the distortions of the grid. In 1900 Hartmann used Scheiner's idea to measure aberrations in mirrors and lenses, using an opaque screen perforated with numerous holes, which is commonly referred to as wavefront sensor. Smirnov (Smirnov, 1961) modified the Scheiner's disk in order to sample the whole pupil, and Howland (Howland, 1968) modified the Tscherning's aberroscope with a crossed cylinders lens to study aberrations in camera lenses. It was not until eighteen years later that it was applied to measure aberrations of the human eye subjectively (Howland and Howland, 1976), with the subject drawing the perceived distorted grid. In 1984, Walsh et al. (Walsh et al., 1984) turned Howland's aberroscope into an objective method by photographing the image of the grid on the retina.

1.4.5.3. The Hartmann-Shack (HS) aberrometer

In 1971 Shack and Platt (Shack and Platt, 1971) improved Hartmann's screen by using an array of microlenses (or lenslets) instead of the perforations to analyse the wavefront coming out of the optical system to study. The array of microlenses is called a Hartmann-Shack (HS) wavefront sensor, and it is composed of a number of microlenses with the same focal length, arranged in a known geometry.
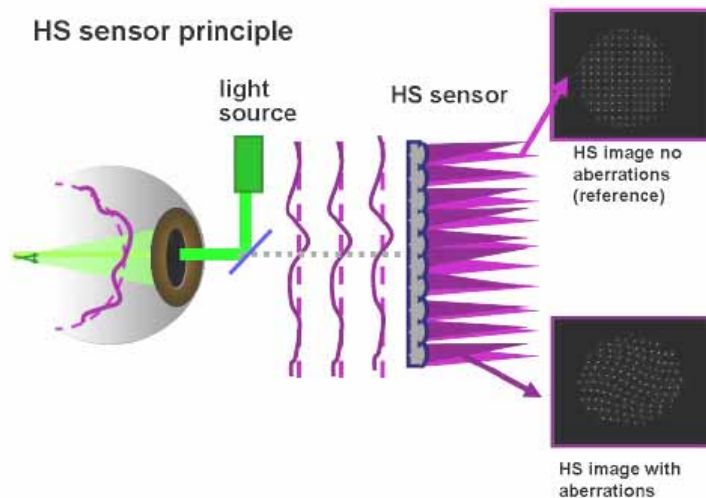
Figure 1.10. Schematic diagram of the working principle of Hartmann-Shack (SH) sensor. A point source emits from the retina, and the spherical wavefronts are distorted by the eye aberrations. Each lenslet will sample a portion of the wavefront on a different phase, and will form a point image away from its focal point (reference) a distance proportional to the phase distortion. Modified from original by S. Marcos.

A diagram of the working principle of a HS sensor for measuring the aberrations of the eye is shown in Fig. 1.10. In this technique (Liang et al., 1994), a point source is created on the retina by illuminating the eye with a narrow beam (generally from a superluminescence diode). In an aberration-free optical system the wavefront

emerging from the eye is plane, which is sampled by the HS microlens, and each lenslet focuses the sampled portion of the wavefront at the focal point (forming a regular array of spots). In the presence of aberrations, the wavefront exiting the eye is distorted, and the focused points get deviated. The shift of each spot with respect to the focal point is related to the slope of the wavefront at the corresponding lenslet position. The wave aberration is estimated from a least mean square fitting to its local derivatives (Eq. 1.4 in Section 1.4.5.1).

The HS sensor was first applied in astronomy. It was in 1994 when it was adapted by Liang et al (Liang et al., 1994) in Heidelberg for measuring aberrations of the eye, and a couple of years later it was developed in Rochester and integrated in an adaptive optics flood illumination fundus camera to image the human eye retina with unprecedented resolution by removing the eye aberrations using a deformable mirror (Miller et al., 1996).

1.4.5.4. The Laser Ray Tracing aberrometer (LRT)

Some years later, the Ray Tracing technique (LRT) (Navarro and Losada, 1997) was applied to measure ocular aberrations. This technique, which has been used throughout this thesis will be more extensively described in Chapter 2, Section 2.3.2. A diagram of the working principle of LRT is shown Fig. 1.11. Briefly, collimated laser pencils are sequentially delivered through different pupil positions, according to the sampling pattern desired. Each pencil will deviate an angle proportional to the local wave aberration, and will impact at a different foveal location. Transverse aberrations are obtained from the deviations of each ray with respect to the chief (central) ray. A spot diagram can be represented by plotting jointly the impacts sequentially collected for all the pupil locations. There is a psychophysical version of the ray tracing, the Spatially Resolved Refractometer (SRR), where the ray aberration at each pupil point is computed as the angle that the subject has to tilt the incoming beam in order to visualize the ray centred on the retina (Webb et al., 1992, He et al., 1998). In this thesis, we have used primarily the LRT technique to measure ocular aberrations. This technique has a large dynamic range and can measure largely degraded eyes given that, since images are captured sequentially, the entire CCD sensor is available for each aerial image. This makes LRT well-suited to study eyes with optical quality varying widely in magnitude (as is the case with multifocal contact lenses). The flexibility in its configuration has allowed us to carry out experiments that would have been more challenging with other techniques. Finally, this objective method allows shorter measuring times compared to its psychophysical counterpart (SRR).

1.4.6. Optical aberrations in the human eye

In this section we present a description of the characteristics of the aberrations pattern that are common in the normal population. We will describe the aberrations of the entire eye, the aberrations of the cornea and the interaction of corneal and internal aberrations.

1.4.6.1. Ocular Aberrations

There is a large variation of the magnitude and distribution of the aberrations across individuals. In addition, optical aberrations are known to change with age, refractive error and pupil size. However, some general conclusions across the population can be extracted.

The defocus Zernike term, followed by both astigmatic terms (second Zernike order), are the main contributors to the total RMS.
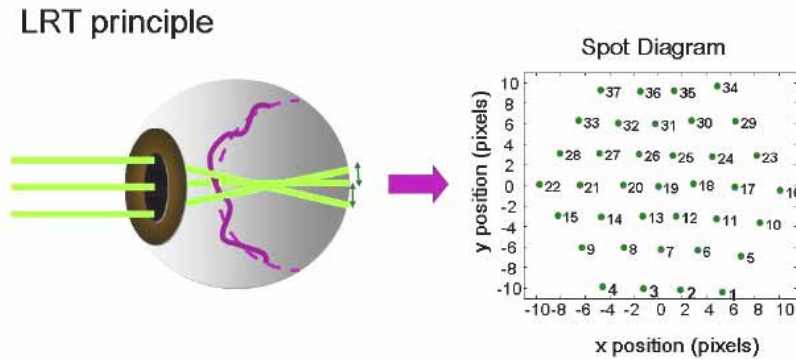
Fig. 1.11. Schematic diagram showing the working principle of Laser Ray Tracing (LRT): parallel rays sequentially delivered through different pupil positions deviate an angle proportional to the wave aberration will impact at a different foveal location. A spot diagram can be represented by plotting jointly the impacts sequentially collected for all the pupil locations. Modified from an original diagram by S. Marcos.

In general, for each subject, the magnitude of the aberrations decreases as the Zernike order increases (Porter et al., 2001, Thibos et al., 2002, Cheng et al., 2004), with terms beyond fourth Zernike order being practically zero (Cheng et al., 2004), except for 4th order spherical aberration Z_4^0, which has reported to be larger in magnitude than the previous third order terms (Porter et al., 2001, Castejon-Mochon et al., 2002, Thibos et al., 2002). However, third order aberrations (coma and trefoil) have been reported to dominate the 3rd and higher order aberrations pattern of normal eyes (Applegate et al., 2007).

The average value of each term across the population is zero, except for 4th order spherical aberration Z_4^0, which has been found to be significantly positive in most subjects, with average reported values ranging from 0.037 μm (6 mm pupil) (Plainis and Pallikaris, 2006), 0.065±0.083 μm (5 mm pupil) (Cheng et al., 2004), to 0.128±0.096 μm (6 mm pupil) (Salmon and de Pol, 2006) and 0.138 μm (5.7mm pupil) (Porter et al., 2001).

The aberrations of the eye seem to be related in such a way that the overall optical quality of the eye was optimised (McLellan et al., 2006).

Reported RMSs values for third and higher order aberrations are between 0.22 and μm (5 mm pupil) (Cheng et al., 2004), 0.26 μm (6 mm pupil) (Plainis and Pallikaris, 2006) and 0.33 μm (6 mm pupil) (Salmon and de Pol, 2006).

A bilateral symmetry in the aberration patterns corresponding to both eyes of the same subject has been reported (Castejon-Mochon et al., 2002, Marcos and Burns, 2000, Plainis and Pallikaris, 2006, Thibos et al., 2002, Porter et al., 2001, Kelly et al., 2004). Aberration patterns from both eyes present a mirror symmetry, which is confirmed by negative correlations found between left and right eyes for most of the Zernike coefficients corresponding to asymmetric Zernike functions (Porter et al., 2001). The highest correlation between Zernike terms was found for defocus, followed

by spherical aberration and astigmatic terms (Porter et al., 2001, Castejon-Mochon et al., 2002).

Ocular aberrations have been reported to increase with age (Applegate et al., 2007, Artal et al., 2002, Mclellan et al., 2001, Calver et al., 1999) for a fixed pupil diameter. The spherical aberration has shown to change with age towards positive values, attributed to a loss of the compensation between the cornea and the crystalline lens (Artal et al., 2001, Mclellan et al., 2001, Smith et al., 2001, El Hage and Berny, 1973, Radhakrishnan and Charman, 2007). Salmon et al. (Salmon and de Pol, 2006) found agradual increase of spherical aberration with age, although the wide variability indicated the influence of other factors than age. Recent studies in emmetropic eyes (Atchison et al., 2008, Plainis and Pallikaris, 2006) did not confirm this change, suggesting that interactions between age and refraction might have influenced the results of previous studies. Third order aberrations have also been reported to increase with age (Mclellan et al., 2001), particularly horizontal coma Z_3^1 (Atchison et al., 2008, Salmon and de Pol, 2006). Salmon et al. also found correlations for terms Z_3^{-1}, Z_4^2 and Z_4^4. McLellan et al. found a strong significant positive correlation between 5th and higher order aberrations RMS and age, and Salmon et al. found significant correlations for 3rd, 4th, 5th and 6th RMSs.

1.4.6.2. Corneal Aberrations

Given that the cornea contributes about two-thirds of the power of the relaxed eye (Atchison and Smith, 2000), it has a great influence in the ocular aberrations. The most extended way today to estimate anterior corneal aberrations is from the elevation maps obtained from a corneal topographer in combination with virtual ray tracing through the optical surface defined by these maps (Applegate et al., 1996, Barbero et al., 2002b, Guirao and Artal, 2000). Similarly to ocular aberrations, corneal aberrations have been reported to vary widely in the population (Guirao and Artal, 2000). Corneal aberrations also tend to present bilateral symmetry (Wang et al., 2003). The anterior cornea presents on-the-rule astigmatism (vertical meridian steeper), although this asymmetry generally reverses with age. The anterior cornea presents positive spherical aberration. Wang et al. reported average values of 0.280 ± 0.086 µm, 0.248 ± 0.135 µm and 0.479 ± 0.124 µm for spherical aberration, coma and HOA, respectively for a population ranging from 20 to 79 years old (mean age was 50 years). In terms of aging, anterior corneal aberrations have been reported to increase moderately with age (Oshika et al., 1999, Guirao and Artal, 2000, Atchison et al., 2008). Particularly, third order coma has been found to increase with age (Oshika et al., 1999, Guirao and Artal, 2000). However, Atchison et al. also found a significant increase in the 6th order terms. The posterior corneal surface has a smaller effect on high order aberrations of the eye (Dubbelman et al., 2007), due to the small index difference between the cornea and the aqueous humour (Atchison and Smith, 2000). Using a distortion corrected Scheimpflug camera Dubblemann et al. (Dubbelman et al., 2006) found a compensation of 31% of the anterior corneal astigmatism by the posterior cornea. Using the same technique, Sicam et al. (Sicam et al., 2006) found that spherical aberration of the posterior cornea is negative in young eyes and becomes positive with age, disrupting the compensation of the positive spherical aberration of the anterior cornea. Dubbelman et al. (Dubbelman et al., 2007) also found a coma compensation of 3.5% between both corneal surfaces, that disappeared with age.

1.4.6.3. Internal Aberrations: interaction between total and corneal aberrations

Internal aberrations can be estimated from the subtraction of anterior corneal aberrations from ocular (total) aberrations, and include the aberrations of the lens and the posterior cornea (as the humours are not believed to play a significant role in terms of aberrations). Knowledge of the relative contribution of the cornea and the lens to the ocular wave aberration is important for both, basic study of the human eye and clinical applications, as will be shown in Chapters 6 and 7, respectively.

The existing compensation of the positive corneal spherical aberration by the negative spherical aberration of the lens has been reported since the 70's (El Hage and Berny, 1973, Millodot and Sivak, 1979), and has been confirmed since, using different techniques (Tomlinson et al., 1993, Smith et al., 2001, Artal and Guirao, 1998, Artal et al., 2001, Barbero et al., 2002a, Kelly et al., 2004). This compensation had also been reported for astigmatism (Le Grand and El Hage, 1980, Artal et al., 2001, Kelly et al., 2004) and is quite well known in clinical practice. The development of techniques to measure the aberrations has allowed the initial studies on astigmatism and spherical aberration compensation to be expanded to other aberrations. Artal et al. (Artal et al., 2001) found compensation in both astigmatism Zernike terms, spherical aberration and coma. Kelly et al. (Kelly et al., 2004) confirmed Artal's findings for Horizontal/vertical astigmatism Z_2^2, horizontal coma Z_3^1 and spherical aberration Z_4^0.

The increase in optical aberrations (see section 1.4.6.1) with age has been attributed to the loss of this compensation with age, reported for spherical aberration. The changes in the crystalline lens must be responsible for this increase in optical aberrations with age (although the relative contribution of the surfaces and gradient index is yet to be determined), as the corneal aberrations have been found to remain fairly constant (Smith et al., 2001).

1.5. CURRENT METHODS OF CORRECTION

It is interesting to note that myopia and presbyopia are the results of failures in the two fine active mechanisms of tuning the power of the eye: Emmetropization in the case of myopia and accommodation in the case of presbyopia. Most people are affected by one or both conditions (myopia and presbyopia), which compromise their visual performance. Several ways to correct (or at least reduce) the effects of myopia and presbyopia have been developed over the years, which re-stablish (completelly or in part) the functionallity of the eye. This thesis aims at exploring further some of the pending issues related to methods of correction for myopia and presbyopia.

1.5.1. Myopia correction

Negative lenses, reducing the power of the eye, are needed to correct myopia. Spectacle lenses and contact lenses are the most common solutions worldwide, as they are external and removable lenses. There are many different designs and materials for spectacle and contact lenses.

Spectacle lenses are a non-invasive way of correcting myopia. The optical coupling between the eye and the spectacle lens is straightforward. However, aside from an important cosmetic impact, spectacle lenses have some optical disadvantages over contact lenses (magnification and prismatic effects, distortions), that will be explained in Section 1.8.2.

Some of the issues present in spectacle lens correction are reduced with the use of contact lenses. However, the back surface of the contact lens is in contact with the

anterior surface of the cornea (with a thin tear film in between), what causes many complex physical interactions and to some extent, a lack of predictability in the optical outcomes. Examples of these factors are optical interactions of the internal surfaces of the eye, including the back surface of the cornea, lens flexure and conformity to the cornea, optical influence of the tear film (acting as a lens). This factors can change across subjects, lens designs and materials, some of which will be studied in this thesis (Chapters 8, 9 and 10). There are two main types of contact lenses: rigid gas permeable (RGP), and soft (or hydrogel). RGP lenses generally provide better visual quality, although soft lenses are more comfortable. The material determines the relative contribution of the different physical effects involved in the fitting. For example, the lens flexure and conformity to the cornea.

Besides external solutions already mentioned, there are two widespread surgical procedures that correct myopia: corneal refractive surgery and intraocular lens (IOL) implantation, with the former of these techniques being addressed in this thesis. Refractive surgery by excimer laser ablation is a well established surgical procedure to eliminate refractive errors of the eye. In this technique, a laser sculpts the cornea by laser ablation to change its shape and to alter its refractive power (as will be explained in Section 1.6).

1.5.2. Presbyopia Compensation

There is extensive research aiming at providing the presbyopic eye with both near and far acceptable vision, but none of the different approaches has reported satisfactory results in humans yet. Some promising research lines are lens refilling (Parel et al., 1986, Nishi et al., 2009), and accommodating IOLs (Findl and Leydolt, 2007).

Although the full correction of presbyopia is beyond the scope of clinical practice today, some optical solutions for the compensation of presbyopia have been developed over the years, with general acceptance. This section will review the most common solutions, with special attention to the optical quality they provide, as these designs often entail a reduced optical quality to achieve an increased visual functionality.

1.5.2.1. Reading spectacles

The most immediate solution for presbyopia is using reading spectacles for near vision. This can be combined with far vision correction: by alternating with other spectacles or adding contact lenses correction. This presbyopia treatment, while the simplest, it is not always the most well accepted by the patient.

1.5.2.2. Monovision

Monovision, implemented with contact lenses, still remains the most successful alternative to reading spectacles. It is usual to correct the non-dominant eye for near and the dominant eye for distance. with Monovision contact lenses produces inherently much less aniseikonia than that with the same correction with spectacles, and patients can theoretically attain a well-focused image for any intermediate viewing distance when the reading addition is less than 2 D. This relatively simple approach is often successful, and meets most visual demands of the patient. The success of monovision is usually confirmed after an extended tolerance trial, preferably for a few days, although many patients are not willing to persevere long enough. Some patients complain of imbalance or disorientation.

1.5.2.3. Alternating vision spectacles

In alternating vision, the lens is divided in different regions each of which have a different power. For example, in bifocal lenses, there is a bifocal segment added to a base lens. The base lens provides the distance correction. The bifocal segment (usually in the lower part of the lens) provides correction for near vision. The bifocal segment location is carefully selected: the line of sight of the eye for distance vision must be separated from the bifocal segment, while near vision visual tasks must be performed through the bifocal segment.

Progressive spectacles are an evolution of the bifocal spectacles. They provide a "channel" of progressive addition. Different heights on the channel correspond to different observation distances. Therefore, the position and length of the channel must match the path followed by the gaze at the lens plane (including binocular convergence), when looking at near objects at different distances.

All alternating vision designs in spectacle lenses take advantage of the fact that there is some distance between the eye and the lens, and that it is certainly easy to orientate the line of sight through different zones of the lens. These possibilities are no longer available in contact lenses, where the lens is in contact with the eye, and moves as the eye moves.

1.5.2.4. Alternating vision contact lenses

Theoretically, translating or alternation vision contact lenses (usually bifocal designs) also provide alternating vision, in a spectacle lens way: the patient looking through a distance portion for distance vision, the lens moving upwards for close work through the near portion. A prism ballast is often incorporated to orient the lens correctly and in addition the lens is often truncated. The lens must move up easily when the eye looks down for close work, but the lens must not be so loose that the lens rides up when looking straight ahead causing the near portion to cover the pupil. As the pupil is usually overlapping the near and distance zones, the retinal image quality is affected by some out of focus light. Most alternating vision contact lenses are RGP lenses. Their use is decreasing in favor of soft multifocal contact lenses.

Achieving alternating vision is difficult in contact lenses, and impossible in other correction alternatives such as intraocular lenses or laser refractive surgery, where there is no possibility of relative movement between the line of sight and the refractive correction.

1.5.2.5. Simultaneous vision

Figure 1.12 illustrates the working principle of multifocal corrections by simultaneous vision. The lens has different focus positions, corresponding to different regions so it is able to provide focused images of objects at different distances, without an active focusing mechanism. The concept is explained with a contact lens, but simultaneous vision is often applied to intraocular lenses and even refractive surgery ablation pattern designs.

Light from objects at different distances are focused by the different zones of the lens on the retina, achieving the intended multifocality (Fig. 1.12 (a)). But on the other hand, when the eye looks at a certain object (Fig. 1.12 (b)), light coming from that distance passes through the different portions (distance and near) at the same time and is focused on different planes, in front of and behind the retina. The result (when the design, the fitting and the coupling with the optics of the eye are correct) is a sharp

retinal image (corresponding to the plane of focus) superimposed to a blurred background: several blurred images (coming from zones of the lens corresponding to different object distances). The subject needs an adaptation period to this new visual experience, that entails a decrease in contrast, although ideally no loss of resolution. Fitting of this type of contact lenses often fails and to date, the procedure is based on trial an error with different lenses, and therefore very inefficient. The situation is more dramatic when simultaneous vision is permanent, as with intraocular lenses or refractive corrections.
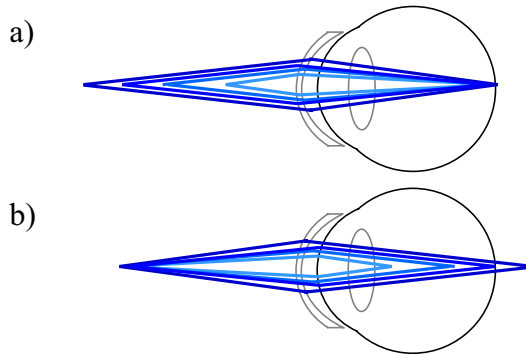
Fig. 1.12. Working principle of multifocal design contact lenses by simultaneous vision. a) Different zones have different powers, and therefore light from objects at different distances are focused, by the different zones, on the retina, achieving the intended multifocality. b) Conversely, light coming from an object at a certain distance passes through the different zones at the same time and is focused at different distances. The result on the retina is a sharp image (corresponding to the right zone) superimposed to several blurred images (coming from portions of the lens corresponding to a different object distance).

One advantage of multifocal corrections is that the patient does not have to hold the reading material in a particular position to read. The main disadvantage is that the vision is not as sharp as with single vision lenses due to side effects from the superimposed images (Pujol et al., 2003, Gispets et al., 2002). Failure of the adaptation is typically attributed to lack of neural adaptation but recent studies show that optical reasons are important (Section 1.10). Some manufacturers' claim that "the eye will automatically choose which image to concentrate on" is largely untrue (Phillips and Speedwell, 1997).

Diffractive lenses can be considered a form of simultaneous vision multifocal refractive lenses, previously explained. Diffractive lenses break up each ray of light into rays with different degrees of bending, each of them corresponding to a plane of focus. As in refractive solutions, light from both distance and near can be focused on the retina, but the balance between distance and near vision does not depend on the pupil size.

1.5.3. Correcting Optical Aberrations

Second-order aberrations such as myopia, hyperopia and astigmatism have been corrected for over 200 years. Today it is possible to measure higher order aberrations,

and further-more, at least in a laboratory setting, to correct most of the aberrations of the eye and provide the visual system with an almost perfect optics.

Custom phase plates (Navarro et al., 2000) have demonstrated to correct 80% of the wave-aberrations in the human eye, and to improve contrast of confocal retinal imaging (Burns et al., 2002). Phase plates have also been used to correct high order aberrations in keratoconic patients (Sabesan and Yoon, 2009). However, phase plates have to be optically coupled to the optics of the eye by other optical elements, what limits their practical usefulness.

Other static corrections, i.e. in form of customized ablations (MacRae et al., 2000, Mrochen et al., 2000) or custom contact lenses (Lopez-Gil et al., 2002) have more potential interest for widespread use. They will be discussed in Sections 1.10.4 and 1.7.5. Wavefront-corrected intraocular lenses will be straightforward, once the techniques for ablation in plastic curved surfaces will be well controlled, although centration remains a critical issue in all these correction strategies.

The great advantage of adaptive optics is the possibility to produce dynamic wavefront corrections. One can measure the optical aberrations of the eye and correct them on a closed loop with an active optical element, typically a deformable mirror. This technique is called adaptive optics (Fernandez et al., 2001, Hofer et al., 2001), and allows providing the eye with unprecedent resolution and contrast (Marcos et al., 2008) or to investigate the role of the ocular aberrations on the accommodative response (Gambra et al., 2009) or in the visual function (Sawides et al., 2009). While great advances have been done in the laboratory, the results obtained so far in the correction of the ocular aberrations of the eye clinically are promising, but still distant from being optimal. There are many open questions, and it is necessary to revisit the procedures, and push the involved techniques and methodologies further.

In any case, wavefront correction (specially static corrections) will never provide unlimited optical quality, as there there other limits for vision, apart from optical aberrations and diffraction: Neural limits, scattering, temporal changes of aberrations (Marcos, 2002) or chromatic aberrations.

1.6. LASER REFRACTIVE SURGERY

1.6.1. The origins of refractive surgery

Besides providing most of the power of the eye, the cornea has easy access. The idea of changing its power to correct ametropias is straightforward. The early attempts of incisional corneal refractive surgery were made more than 200 years ago (Sakimoto et al., 2006, Donders, 1864) (see page 95). The techniques have been evolving since then. Incisional refractive surgery (Fyodorov and Durnev, 1979) has been abandoned now. The first laser refractive surgery applied to the corneal epithelium of a patient eye to treat his myopia was reported by MacDonald et al. in 1989 (McDonald et al., 1989). Previously, Seiler (Seiler and Wollensak, 1986) had applied the same procedure (PRK) to a blind human eye. Munnerlyn et al. (Munnerlyn et al., 1988) calculated the thickness of tissue necessary to correct a given quantity of myopia or hyperopia. Pallikaris (Pallikaris et al., 1990) combined PRK with Keratomielousis (removing a thin layer of cornea to change its power, that had been introduced by Barraquer in the 1960's (Barraquer, 1967), creating the Laser Assisted Keratomileusis (LASIK), which is one the most popular surgical approach to correct myopia.

1.6.2. The LASIK technique

The LASIK procedure is illustrated in Fig. 1.13. A flap is created in the cornea by means of a microkeratome (Fig. 1.13 (a to f)), and folded back to leave the stroma exposed (Fig. 1.13 (g)). An excimer laser photosculpts the stroma by means of tissue ablation with a flying spot (Fig. 1.13 (h)). Finally, the flap is repositioned on its original place (Fig. 1.13 (i)). No suturing is needed.
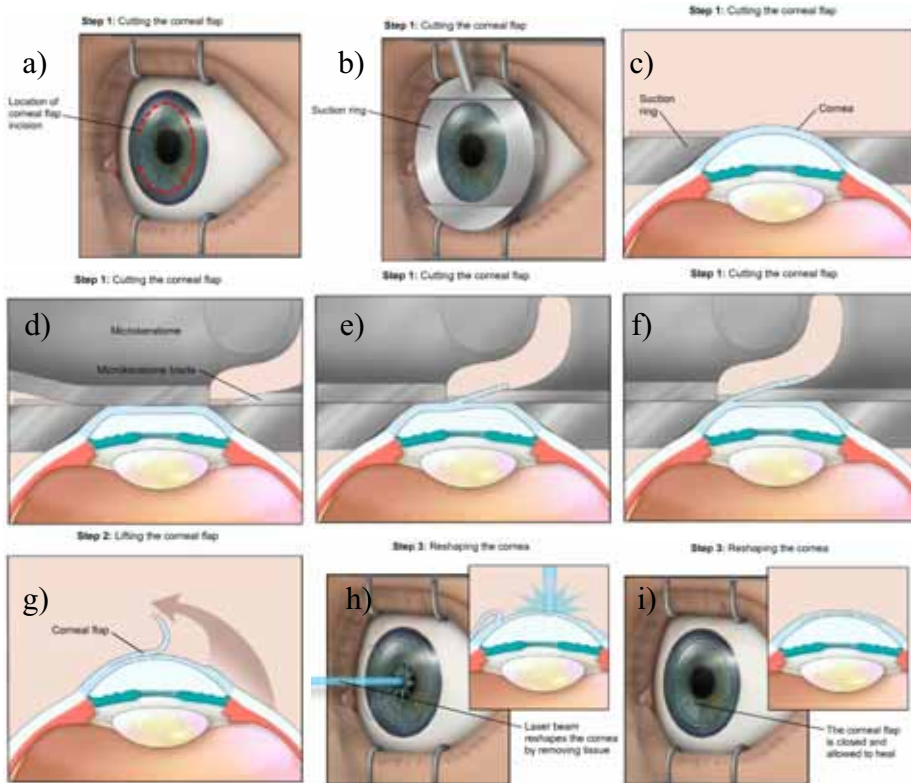
Fig. 1.13. The LASIK technique. Frame excerpts from the video animation "How LASIK Eye Surgery Works" (FDA). http://www.fda.gov/cdrh/lasik/

The density of spots at each location defines the ablation pattern, which changes depending on the ametropia to be corrected. In the case of myopic corrections, more tissue is removed at the center of the cornea, so that the cornea is flattened during the surgery. This reduces the optical power of the cornea, and corrects myopia. A smooth transition zone between the corrected optical zone and the non-treated zone is often introduced, to prevent abrupt changes and the peripheral edge (Dierick and Missotten, 1996).

Some commonly used modifications of the LASIK technique, which do not create a permanent flap in the deeper corneal layers, are LASIK, PRK, LASEK and Epi-LASIK. With PRK, the corneal epithelium is removed and discarded, allowing the cells to regenerate after the surgery. In LASEK and Epi-LASIK surgery, the patient's epithelium is not removed. The epithelium is lifted as a sheet and then after laser ablation, the epithelial sheet is re-placed to cover the treated area. In LASEK dilute

alcohol is used to loosen the epithelium. In Epi-LASIK, a purely mechanical means of epithelial dissection (using Epikeratome) allows the creation of the epithelial sheet.

1.6.3. Safety and efficacy of laser refractive surgery

An average of 700,000 patients in the U.S. have LASIK anually, with procedures growing worldwide from 3.6 million to 4.2 million (MarketScope, 2008). To date, more than 28.3 million LASIK procedures have been performed worldwide. Collectively, 7,830 patients (representing 16,502 eyes) participated in clinical trials from 1993 – 2005. In April 2008 the Food and Drug Administration reaffirmed the Safety and Efficacy of the LASIK procedure (Ellin, 2008). Although the number of patient complains has risen in the last few years, the post-operative visual outcomes have improved in the most recent studies. In FDA studies recruiting patients that had undergone surgery before 2000, 1.4% of patients lost 2 lines or more of BSCVA versus 0.6% in studies after 2000. Before 2000, 1.68% of patients with a preoperative BSCVA 20/20 or higher had a postoperative BSCVA 20/25 or higher, compared with 0.16% after 2000. The surveys determining patient satisfaction with LASIK have found most patients satisfied, with satisfaction range being 92–98 percent. A meta-analysis dated March 2008 performed by the American Society of Cataract and Refractive Surgery over 3,000 peer-reviewed articles published over the past 10 years in clinical journals from around the world, including 19 studies comprising 2,200 patients that looked directly at satisfaction, revealed a 95.4 percent patient satisfaction rate among LASIK patients worldwide (Ciccone, 2008, Solomon et al., 2009).

1.6.4. Laser ablation

All models of excimer laser corneal refractive surgery (experimental, analytical or numerical) rely on the validity of the assumption of energy deposition occurring in a well-defined layer which is then removed by ablation. For absorbing media, which is the case for cornea and most polymers at the processing wavelength (193nm), the intensity I of the electromagnetic wave propagating into the material (z-direction) decreases exponentially following the Beer-Lambert expression, according to

$$I(z) = I_0 \cdot e^{-\alpha \cdot z}, \tag{1.5}$$

with

$$\alpha = \frac{4\pi \cdot k}{\lambda}. \tag{1.6}$$

This physical model of ablation is called the *blow-off* model. The inverse of the absorption coefficient α is the optical penetration depth, i.e. the depth in which the major fraction of the energy is deposited (1/e of the total amount absorbed). k is the extinction coefficient. As a consequence of Eq. (1.5), the etch rate d (etch depth/pulse) is expected to relate linearly to the natural logarithm of the laser fluence F according to

$$d = \frac{1}{\alpha} \ln\left(\frac{F}{F_{th}}\right), \tag{1.7}$$

where F_{th} is the ablation threshold.

Figure 1.14 shows the relation between the laser-pulse fluence and the corneal-ablation depth (Fisher and Hahn, 2007). The points represent experimental values, while the curves illustrate the results of different models (Pettit and Ediger, 1996). The upper and lower lines correspond to a blow-off model (the one described here) with different parameters.
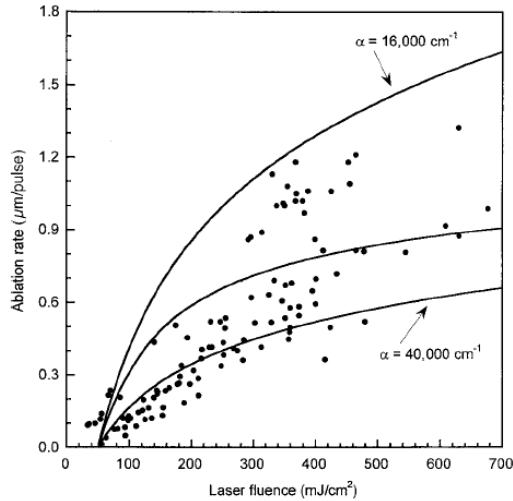
Fig. 1.14. Ablation rate as a function of laser fluence for ArF excimer laser ablation of corneal tissue, comparing reported experimental data with values predicted by different models of ablation, considering different ablation coefficients α (Fisher and Hahn, 2007).

1.6.5. Optical and ablation properties of the corneal tissue

The fact that the Beer-Lambert´s law appropriately describes photoablation of corneal tissue is fairly well established (Pettit and Ediger, 1996, Fisher and Hahn, 2004). While some authors consider the assumptions of Eq. (1.4) to be valid for corneal tissue ablation (Pettit and Ediger, 1996), recent studies also suggest a dynamic absorption coefficient in the cornea (Jimenez et al., 2006, Fisher and Hahn, 2007) changing under excimer laser ablative conditions.

Many studies use $Fth_{,cornea}$=40 mJ/cm^2 (Berns et al., 1999) as ablation threshold of the cornea, but some authors have recently reported (Pettit et al., 2005) 60 mJ/cm^2. Srinivasan reported $F_{th, PMMA}$= 80 mJ/cm^2 for PMMA.

Reports of the absorption coefficient of the cornea vary largely in the literature: from 2700 cm^{-1} to 39.000 cm^{-1} (Pettit and Ediger, 1996). Fisher and Hand (Fisher and Hahn, 2007), proposed a dynamic absorption coefficient between 16.000 and 22.000 cm^{-1}.

The upper and lower curves of Fig. 1.12 represent the theoretical fit to the data on the basis of the simple blow-off model of pulsed laser ablation (as described here), with α = 16.000 cm^{-1} and 40.000 cm^{-1} (Fisher and Hahn, 2007, Pettit and Ediger, 1996).

The ablation in cornea does not appear to change with the number of accumulated laser pulses (Fisher and Hahn, 2004), and incubation seems to be negligible in cornea (Pettit et al., 1991). However, varying tissue hydration during the ablation can cause

changes in reflectivity and absorption, among other effects (Manns et al., 2002b, Fisher and Hahn, 2007).

Pettit and Ediger reported a refractive index of the cornea, at 193 nm, of 1.52. For visible light, Barbero (Barbero, 2006) proposed a multilayer model of the human cornea (and tear) with refractive index between 1.40 and 1.33.

1.6.6. Theoretical ablation profiles

Standard algorithms for corneal refractive surgery are based on the Munnerlyn formula (Munnerlyn et al., 1988). The corneal tissue to be removed is a lenticule with an anterior radius of curvature equal to the pre-operative corneal radius and the posterior radius of curvature equal to the post-operative corneal radius (easily related to the attempted correction).

The Munnerlyn equation can be expressed as:

$$f_{\text{Mun}}(\rho) = (R_1{}^2 - \rho^2)^{1/2} - \left[\left(\frac{R_1(n-1)}{n-1+R_1S}\right)^2 - \rho^2\right]^{1/2}$$
$$- \left(R_1{}^2 - \frac{\Phi^2}{4}\right)^{1/2}$$
$$+ \left[\left(\frac{R_1(n-1)}{n-1+R_1S}\right)^2 - \frac{\Phi^2}{4}\right]^{1/2} + f_0^{\text{TZ}}.$$

(1.8)

Where R_1 is the initial radius of curvature, S is the optical power correction and $n= 1.377$ is the average index of refraction of the cornea (with visible light) (see (Cano et al., 2004) for details).

Sometimes the Munnerlyn equation is expressed by its parabolic approximation, which is obtained by truncating the Taylor expansion (Jiménez et al., 2003):

$$f_{\text{par}}(\rho) = \frac{4S\rho^2}{3} - \frac{S\Phi^2}{3} + f_0^{\text{TZ}}.$$

(1.9)

In this expression, the refractive index of the cornea has already been replaced by its numerical value, 1.377 (Schwiegerling et al., 2001, Munnerlyn et al., 1988). The parabolic approximation of the Munnerlyn formula (Eq. 1.9) states that the maximum depth of the ablation (in microns) per diopter of refractive change is equal to the square of the optical ablation zone (in millimeters), divided by three.

Figure 1.15 shows ablation profiles based on the Munnerlyn's equation (Eq. 1.8, black solid line) and its parabolic approximation (Eq. 1.9, red solid line of Fig. 1.15). Both profiles are similar in the central part of the profile, but different in the periphery. The optical effects of the different asphericity associated with both profiles will be described in Section 1.7.2.

1.7. CORNEAL ABLATION AND OPTICAL ABERRATIONS

1.7.1. Optical aberrations and visual performance after refractive surgery

Although the degree of accuracy in the refractive correction achieved with PRK and LASIK soon increased with the use of nomograms, some frequent complains include night vision problems: decreased vision, glare, halos or ghost images in mesopic and scotopic vision. The low contrast VA and the CS was found to decrease (Verdon et al.,

1996, Fan-Paul et al., 2002). Optical aberrations were identified as the cause for this CSF decrease (Seiler et al., 2000, Marcos, 2001).
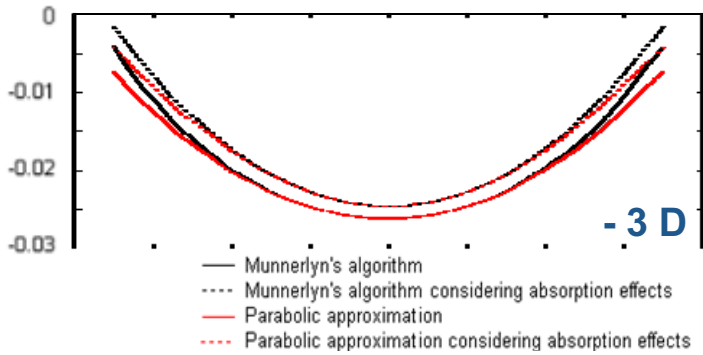
Fig. 1.15. Theoretical ablation profiles based on Munnerlyn's algorithm (black solid line) and its parabolic approximation (red solid line). Absorption effects (dashed curves) will be described in section 1.7.3. Data from (Dorronsoro et al., 2003b).

Increase of optical aberrations are still one of the most important side effects of refractive surgery. Early studies with aberrometry showed that post-operative wave aberration maps showed large amounts of spherical aberration compared with pre-operative maps. Seiler et al. measured for the first time the changes in the total aberration pattern induced by myopic PRK (15 eyes, mean pre-op spherical error = -4.8 D). Moreno-Barriuso et al. (Moreno-Barriuso et al., 2001b) first measured increased aberrations after standard myopic LASIK (22 eyes, mean pre-op spherical error = -6.5 D). Both studies found a significant increase in 3rd and higher order aberrations (by a factor of 4.2 and 1.9 in the RMS, respectively). The largest increase occurred for spherical and 3rd order aberrations.
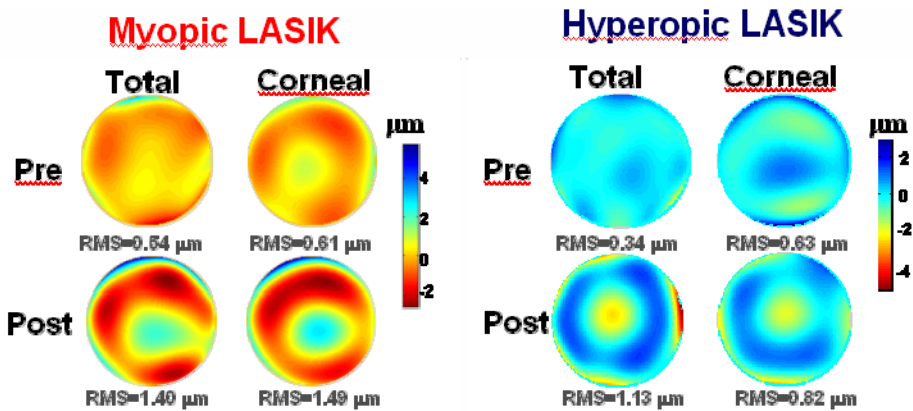
Fig. 1.16. Examples of corneal and total wave aberrations (third and higher order aberrations) before and after LASIK surgery for myopia (left panel) and hyperopia (right panel). The increase is aberrations is indicated by the increased RMS. After surgery the total aberration map is dominated by the corneal contribution, primarily by positive spherical aberration after myopic LASIK and by negative spherical aberration after hyperopic LASIK. Data from (Marcos et al., 2001a).

Marcos et al. (Marcos et al., 2001a) showed that the changes of total spherical aberrations are not fully accounted by changes in the anterior corneal surface. Total spherical aberration increased slightly less than corneal aberrations in all eyes, likely due to significant changes in the posterior corneal shape (shifting toward more negative values of spherical aberration). The increase in the total spherical aberration is highly correlated to the amount of spherical error corrected, and it is associated to an increase in corneal asphericity (see Eq. 1.1).

Changes of corneal and total aberrations with LASIK surgery for hyperopia are even higher than those for LASIK surgery for myopia. While spherical aberration becomes more positive after myopic LASIK, it shifts toward negative values after hyperopic LASIK. Figure 1.16 shows wave pre-and post-operative high order aberration patterns in patients that had undergone myopic LASIK and hyperopic LASIK. Figure 1.17 compares the induced aberration (total and corneal) after myopic and hyperopic LASIK respectively.
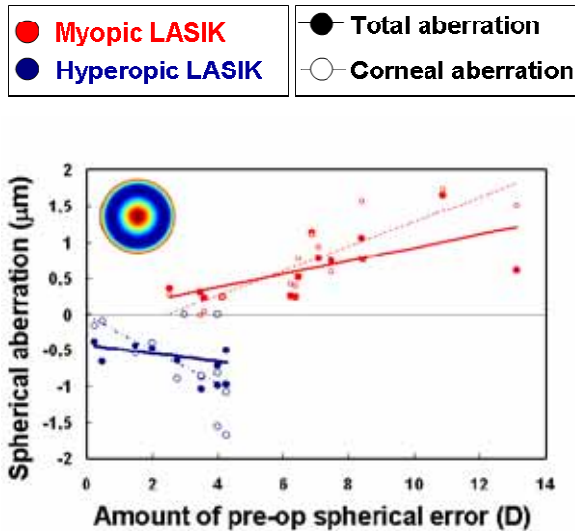
Fig. 1.17. Induced spherical aberration versus spherical correction (positive for hyperopia and negative for myopia). Corneal spherical aberration increases at a rate of 0.17 μm/D in myopic LASIK and –0.23 μm/D in hyperopic LASIK. Total spherical aberration increases at a rate of 0.09 μm/D in myopic LASIK and –0.06 μm/D in hyperopic LASIK. The inset depicts the 4th order spherical aberration Zernike term. Data from (Llorente et al., 2004a).

The decrease in the area under the CSF was shown to be well correlated with corneal aberrations (Applegate et al., 2000), and to match the decrease in the area under the MTF obtained from ocular aberrations. This fact indicates a prominent role of the aberrations in the degradation of visual performance (Marcos et al., 2001a).

There are three possible reasons for the consistent increase corneal asphericity (and the associated spherical aberration) after myopic refractive surgery, that will be addressed in subsequent sections: 1) the assumptions inherent to the theoretical ablation profile; 2) changes in laser efficiency from the apex to the periphery of the curved cornea; 3) the corneal biomechanical response and wound healing.

1.7.2. Influence of the ablation profile

Several studies have estimated the changes in corneal asphericity expected from the theoretical application of the standard ablation pattern, using both the formula reported by Munnerlyn et al. (Munnerlyn et al., 1988), which assumes that both pre- and post-operative corneal shapes are spherical, or a parabolic approximation of the Munnerlyn formula. In Fig. 1.15 (already explained in Section 1.6.6) the different asphericity of both profiles, for an ablation of the same power (-3 D), is apparent, as both profiles are similar in the center but different in the periphery. Numerical analysis performed by Gatinel et al. (Gatinel et al., 2001) demonstrates that the Munnerlyn pattern should not increase the asphericity of corneas with typical preoperative asphericities, in contrast to clinical findings. Jiménez et al. (Jiménez et al., 2003) carried out analytical calculations and found that the parabolic approximation of the Munnerlyn function should produce some increase in corneal asphericity after myopic corneal ablation.

In recent studies (Marcos et al., 2003, Cano et al., 2004), Marcos et colleagues simulated post-operative corneal surfaces by subtracting the standard Munnerlyn ablation pattern and a parabolic approximation of the Munnerlyn pattern from real pre-operative corneas, and compared the estimated post-operative asphericity (Q) and spherical aberration with the real post-operative values. They found that while the actual surgical procedure increased asphericity from -0.14±0.14 to 1.1±1.3 on average, for treatments ranging between -2.0 to -11.5 D, corneal asphericities expected from the computer simulations with the standard Munnerlyn pattern did not increase (mean post-operative asphericity = -0.21±0.19). Simulations with the parabolic approximation of the Munnerlyn formula only increased slightly the corneal asphericities (mean post-operative asphericity = 0.3±0.4). These results, shown in Fig. 1.18 indicate that the increase in corneal asphericity is not due to an inappropriate design of these ablation patterns, or the assumptions upon which these patterns are based.
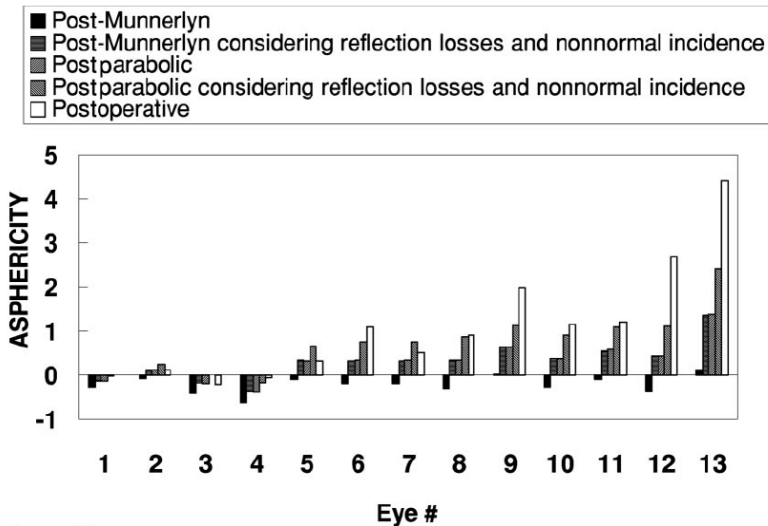
Fig 1.18. Post operative asphericity for postoperative real corneal topographies and for simulated post-operative corneas (with the Munnerlyn algorithm and with its parabolic approximation, and with and without efficiency effects (Section 1.7.3)). Patients are sorted by increasing correction. From Cano et al. (Cano et al., 2004).

1.7.3. Ablation efficiency

Mrochen and Seiler (Mrochen and Seiler, 2001) proposed that the increase of asphericity with the refractive surgery procedure is due to changes in the ablation efficiency as the laser spot moves from the center to the periphery of the cornea. As the angle of incidence α increases, both the reflected energy and the illuminated area increase and therefore, the ablation depth per pulse decreases (Fig 1.19).

$$F_\alpha = F_0 \cdot \cos \alpha \,(1- R)$$
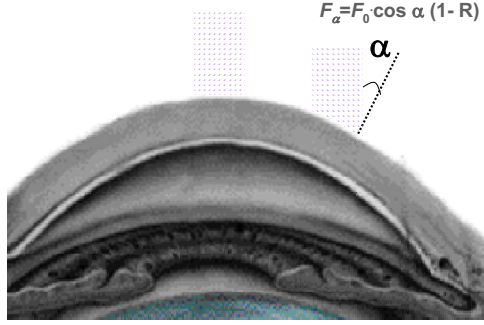
Fig 1.19. As the laser spot moves from the center to the periphery of the cornea the angle of incidence increases. The ablation depth per pulse decreases in the periphery because both the reflected energy and the illuminated area increase.

Ablation efficiency can be defined as the ratio of the amount of removed material when the angle of incidence is α (namely d_p^{corr}) to the amount of removed material when the illumination is perpendicular to the corneal surface (d_p). Jiménez et al. (Jimenez et al., 2002, Anera et al., 2003) estimated theoretically the corneal ablation efficiency ($K(\alpha)$ in this study) using Fresnel equations and taking corneal curvature into account. They provided an equation (Eq. 1.10) that relies on several assumptions regarding the laser properties and laser-tissue interactions. These assumptions include: 1) homogeneous laser beam intensity; 2) non-polarized light; and 3) Beer-Lambert's law, i.e. logarithmic dependence of the ablation depth on the absorbed energy density. In Jiménez's model, the resultant corneal shape after ablation depends not only on the laser fluence pattern but also on the corneal radius of curvature and on the tissue properties (ablation fluence threshold and refractive index) at 193nm.

$$\frac{d_p^{corr}}{d_p} = 1 + \frac{\ln[\cos \alpha (1 - \tilde{R})]}{\ln(F_0 / F_{\text{th}})} \tag{1.10}$$

where $\tilde{R}$ is the reflectivity that can be obtained from Fresnel equations:

$$\tilde{R} = \frac{1}{2}\left[\left(\frac{1.52 \cos \alpha - \cos \alpha'}{1.52 \cos \alpha + \cos \alpha'} \right)^2 + \left(\frac{\cos \alpha - 1.52 \cos \alpha'}{\cos \alpha + 1.52 \cos \alpha'} \right)^2 \right], \tag{1.11}$$

and cos α' can be obtained from the Snell law.

Figure 1.20 shows graphically the ablation efficiency effects obtained with Eq. 1.10, for three different materials used in this thesis: corneal tissue, PMMA and

Filofocon A (spherical surface of radius 8 mm, ablated at 193 nm). It changes with the refractive index of the material at the processing wavelength, the geometry of the surface and the ablation properties of the material (ablation threshold and effective absorption coefficient).
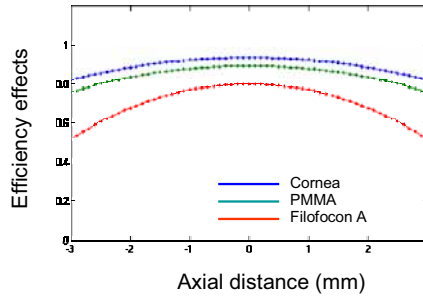
Fig. 1.20. Efficiency effects as a function of axial distance for three different materials: Cornea, PMMA and Filofocon A.

In a previous study in our laboratory (Cano et al., 2004), Jimenez´s expression for $K(\alpha)$ was incorporated into computer simulations of corneal refractive surgery on real pre-operative corneal topographies, in combination with both the exact Munnerlyn and the parabolic patterns. Changes in ablation efficiency as given by the theoretical expression of $K(\alpha)$ were found to contribute to increase the asphericity of the ablated corneas. An average corneal post-operative asphericity of 0.3±0.4 was found when incorporating efficiency changes into the exact Munnerlyn equation, and 0.7±0.4 when incorporating efficiency changes into the parabolic approximation. While those values are still lower than those found in the real corneas, these results suggested that a parabolic ablation profile and, more importantly, the fact that the effects of corneal curvature on laser ablation efficiency were not being taking into account, are a major cause of the increased asphericity after myopic refractive surgery.

1.7.4. Biological response of the cornea

Corneal biomechanical effects and wound healing are other potential causes for the inaccurate prediction of the corneal postoperative shape. Although the mechanism is not fully understood, it seems clear that the biomechanical properties of the cornea are affected by the flap creation and/or the laser ablation. Some authors have investigated the impact of biomechanical response on refractive surgery outcomes. Roberts & Dupps (Roberts and Dupps, 2001) suggested that the breakage of lamellar structures during ablation could produce a redistribution of both corneal strain and intrastromal fluid. These authors proposed a corneal biomechanical model to explain the unintended hyperopic shift found in treated eyes (Fig. 1.21).

Differential epithelial growth and excessive wound healing after ablation have also been proposed to have an effect on final corneal shape. In any case, although the biomechanical response of the cornea after the tissue removal and the wound healing may undermine the predictability and stability of refractive surgery, these are added effects to physical factors (Dupps and Wilson, 2006).

While the laser refractive surgery procedure does not affect directly the posterior surface of the cornea, and a large proportion of the optical changes can be explained at the anterior corneal surface level (Marcos et al., 2001a), a modification in the posterior

corneal surface may be expected, since the surgery weakens the cornea (see Fig. 1.21). As corneal biomechanical properties are largely unknown, it is not possible to predict theoretically the extent of this potential deformation (Dupps and Wilson, 2006).
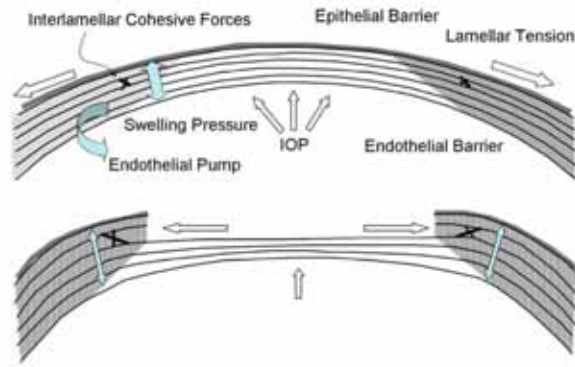
Fig. 1.21. From (Dupps and Wilson, 2006). Major biomechanical loading forces in the cornea and a model of biomechanical central flattening associated with disruption of central lamellar segments. According to Roberts (Roberts, 2000, Roberts, 2002), a reduction in lamellar tension in the peripheral stroma reduces resistance to swelling and an acute expansion of peripheral stromal volume results. Interlamellar cohesive forces (Smolek, 1993) and collagen interweaving, whose distribution is greater in the anterior and peripheral stroma and is indicated by grey shading, provide a means of transmitting centripetal forces to underlying lamellae. Because the central portions of these lamellae constitute the immediate postoperative surface, flattening of the optical surface occurs, resulting in hyperopic shift.

1.7.5. Current trends in refractive surgery

Refractive surgery has been improved over the past years, thanks to the refinement of the involved technologies and the improvement in the ablation pattern design. Presumably, the improvements of the ablation patterns with the estimated correction factors obtained theoretically are now included in the proprietary ablation algorithms of most laser platforms, which are now most likely compensated for efficiency effects. The final goal of refractive surgery is the possibility for correction of higher optical aberrations of the eye, and not only conventional refractive errors. Most laser manufacturers claim that current ablation algorithms are now wavefront-optimized or customized to the patients' optical aberrations (aspheric, wavefront-guided or topography-guided) (Kohnen, 2006, Kohnen, 2008), with the aim of avoiding the increase of spherical aberration that was a major issue with standard ablation profiles (Moreno-Barriuso et al., 2001b, Marcos et al., 2001a). Customized wavefront guided surgery is assisted by wavefront sensors and topographers (to measure optical aberrations) and precise lasers provided with precise control of the energy delivery at each point, thanks to flying spot technology, pupil tracking, and fast repetition rates. Femtosecond laser technology allows for flap creation that induces less change in high-order aberrations and corneal biomechanics (Kim and Chuck, 2008).

Recent studies (Arba-Mosquera and de Ortueta, 2008, Kwon et al., 2008) describe sophisticated numerical models that take into account most of the knowledge gathered in the last years on the physical effects affecting refractive surgery (in particular some of the results of this thesis), with less approximations, and considering the temporal

evolution of the process. These models pretend to obtain precise prediction of the outcomes of the surgery, by including a detailed description of the phenomena involved. Kwon and Bott have recently presented a model that takes into account the corneal remodelling that occurs through healing (Kwon and Bott, 2008). All these numerical models need experimental data for validation and parameter adjustment that are presumably difficult to obtain from measurements on real corneas.

1.7.6. Experimental models for refractive surgery

Ablation of plastic flat surfaces had been used before in the context of refractive surgery (Gottsch et al., 1996, Odonnell et al., 1996, Roszkowska et al., 2003), to assess post-operative roughness. Corneal laser ablation models have not only attracted the interest of the scientific community, but also of normalization agencies. For instance, the ANSI Z80.11-2007 norm requires the ablation of plastic plates for calibration (energy adjustment and laser profile testing) of corneal refractive surgery (2007). The standard also recommends the use of plastic corneal models for in vitro testing of the ablation characteristics of the laser systems and to validate experimentally mathematical models, simulations, and ablation algorithms. The Ophthalmic Devices Panel of the Food and Drug Administration (FDA) is currently evaluating the ANSI Z80.11 Standard for recognition (2008), and the FDA section on Medical Devices has pointed out the necessity to develop accurate calibration techniques to assure that the achieved corneal ablation depth map equals the one intended through plastic corneal models (Drum, 2007, Drum, 2003, Drum, 2005).

1.8. OPEN QUESTIONS IN CORNEAL REFRACTIVE SURGERY

Refractive outcomes are subject to some variability due to regression (Chayet et al., 1996), hydration (Feltham and Stapleton, 2002) or other factors that lead to empirical adjustments of the ablation nomogram (Mrochen et al., 2006, Ditzen et al., 1999). Concerning wavefront-guided refractive surgery, there is still an important lack of predictability (Kohnen et al., 2007). Despite some initial promising clinical results and some evidence that the increase of spherical aberration is attenuated (Mrochen et al., 2000) in many cases spherical aberration is still introduced. Although some studies show trends toward better visual and optical outcomes following wavefront-customized procedures (Kim and Chuck, 2008), the improvement is hardly significant when compared with the new generation of conventional procedures (Padmanabhan et al., 2008, Netto et al., 2006, Alio and Montes-Mico, 2006). Many causes have been pointed out for the relatively minor impact of aberration correction (Kohnen et al., 2007), such as fluctuations in the aberrations or errors in their measurement, centration, alignment or torsion errors (during the measurements or the ablation), and flap creation effects. Corneal biomechanics is another potential cause for the inaccurate prediction of the corneal postoperative shape. Therefore, the current objective of refractive surgery is still preventing the induction of spherical aberration and the changes in asphericity. This objective is required for successful wavefront-guided surgery. The controlled induction of shape changes required in customized ablation algorithms, entails 1) an adequate profile design (Manns et al., 2002a, Klein, 1998, Mrochen et al., 2004), 2) the correct transfer of the pattern to the cornea through deep knowledge of the ablation process, 3) validated numerical models based on experimental data, 4) the consideration of biological effects and 5) the back surface of the cornea, as described hereafter:

Algorithm design: The design of the ablation pattern is the key element for improving refractive surgery. The patterns, and the algorithms used to apply them to the cornea, are proprietary. Although much of research assumes certain shape (Munnerlyn or parabolic approximations) the programmed pattern could deviate from these equations. Furthermore, even calculations and simulations of the manufacturers based on their own nominal proprietary algorithms can be incorrect, as the effective ablation pattern can be substantially different of that pretended, due to optical, mechanical or electrical variability or miss-calibrations. Tools for precise assessment of the ablation pattern, both in flat and in curved surfaces, are an important requirement for the improvement of refractive surgery. These can allow the direct comparison across laser systems, and help explain clinical results.

Transfer of the ablation pattern to the cornea: Undoubtedly, not only the ablation pattern design itself, but also how accurately it is transferred to the cornea (i.e. physical aspects of the ablation process) determine the optical outcomes of the surgery. Experimental studies of the physics of the ablation in curved surfaces, isolated from biological processes, performed in controlled environments with low variability (from ocular parameters, centration or alignment), can help understand and improve the energy transfer to the cornea. Precise tools and procedures for measuring the outcomes of the ablation (from isolated pulses to complete patterns) are also essential.

Input data and experimental validation for numerical models: Computational models for the precise simulation of corneal ablation require several input numerical parameters (mainly physical properties of the material and physical parameters of the laser). Many of them need to be measured and checked experimentally. Moreover, the whole model needs validation, by testing it over different controlled conditions. Calibration procedures for the lasers, and measurements of their efficiency effects, are among the most needed results in this field.

The role of Biological effects: Most models of the effect of wound healing and biomechanical changes on refractive surgery are vague and mostly at a quantitative stage. Although these effects are likely to produce uncertainty and instability, the boundaries of biological effects are not yet defined, as they are entangled with purely physical effects. More studies on long term and short term shape surface shape changes after surgery are needed.

The role of the back surface of the cornea: The biological changes (wound healing or biomechanical effects) will likely affect the back surface of the cornea, which can compensate in part the aberrations of the anterior surface. Several studies have shown important changes in the posterior corneal surface suggesting an influence of corneal biomechanical effects in the optical outcomes, although these results are controversial.

1.9. CONTACT LENSES

Refractive surgery and contact lenses can be considered alternative approaches to achieve the same goal: the refractive correction of the eye by manipulating the corneal power. While the former achieves this goal by permanently removing tissue, the latter places a thin lens of transparent material on the cornea, which is removable. The tissue removed in refractive surgery is sometimes conceptually modelled as a contact lens removed from the cornea (Munnerlyn et al., 1988).

Understanding the optical coupling between the contact lens and the optics of the eye is not easy, as we will discuss in the following sections. The problem is more complicated that combining the intended design of the lens and the aberrations of the eye, as one needs to consider the fitting of the lens: tear film on the lens, tear lens between the contact lens and the cornea, lens position, lens material, hydration, conformity and flexure. All these factors, and many others, affect the final optical performance. At the initial stages of this thesis there were very few studies on contact lens fitting in terms of optical aberrations, but with suggestive results.

1.9.1. The origins of contact lenses

Leonardo da Vinci in 1508, René Descartes in 1636, and Thomas Young in 1801, anticipated the idea of contact lenses (Phillips and Speedwell, 1997), but the first one to suggest their use to correct the refractive errors of the eye was Sir John Herschel, in 1845 (Walls, 1950), who never tested these ideas. Interestingly, Herschel pointed out that the operation of "*applying in contact with the surface of the eye some transparent animal jelly contained in a spherical capsule of glass*" (fitting a contact lens) "*…would, of course, be delicate, but certainly less so than that of cutting open a living eye, and taking out its contents*". This sentence, that is recognized to constitute the beginning of modern thinking in contact lenses, also seems to anticipate the basic idea or refractive surgery as an alternative procedure for correcting the refractive errors of the eye, although (even more) invasive than contact lenses (See page 185 of this thesis for a detailed revisit of that moment (Walls, 1950)).

It was not until 1887 that a German glassblower, F.E. Muller, produced the first eye covering to be seen through and tolerated. In 1888, the German physiologist Adolf Eugen Fick constructed and fitted the first successful contact lens. He fabricated and fitted the glass lenses, initially on rabbits, then on himself, and lastly on a small group of volunteers (Phillips and Speedwell, 1997).

Plastic (PMMA) was not introduced until 1936 by Feinbloom. By the end of the 1970s, and through the 1980s and 1990s, a range of oxygen-permeable but rigid materials were developed. The first soft (hydrogel) lenses appeared in the late 1960s. These lenses were soon prescribed more often than rigid lenses, mainly due to their immediate comfort.

1.9.2. Optical differences between contact lenses and spectacles

Similarly to what happens in refractive surgery, correcting refractive errors with contact lenses is different in optical terms to correcting with spectacles.

The more apparent effect is cosmetic. The magnification of the eyes is eliminated (an observer sees the eyes looking their normal size), and reflections are also removed.

Unlike with spectacle lenses which limit the field of view both by the spectacle frame (and the area covered by the lens) and magnification and prismatic effects, with

contact lenses the field of view remains unchanged, as the lens moves with the eye.. As for binocular vision, prismatic and magnification effects can produce alterations in convergence with spectacle corrections, specially for anisometropic wearers, that are not present with contact lenses. Field distortions, curvatures and oblique aberrations associated to gaze through the periphery of spectacle lenses are not present in contact lenses neither.

On the other hand, halos and scattering (from lens deposits, interruptions to the tear of abrupt transitions between zones of the lens) are more common in contact lenses.

1.9.3. Rigid gas permeable (RGP) contact lenses

It is widely accepted in the clinical practice that RGP contact lenses (made of oxygen-permeable polymers) provide the best ophthalmic correction, at least from a purely optical viewpoint (Phillips and Speedwell, 1997). RGP contact lenses are expected to mask the anterior corneal surface with a perfectly regular surface, and fill in with tear all the corneal irregularities. The refractive index similarity between the tear film and the anterior corneal surface reduces the impact of corneal aberrations (Griffiths et al., 1998).

The better visual response of RGP contact lenses, compared to soft contact lenses (which would produce the same magnification) or spectacles, is well documented in the optometry literature (Griffiths et al., 1998, Phillips and Speedwell, 1997). Most of these studies are based on psychophysical measurements of visual performance and conclude that RGP contact lenses provide higher visual acuity and contrast sensitivity.

RGP lenses on-eye are affected by a number of forces. The correct fitting needs a balance among those forces: capillary attraction between the lens and the cornea, gravity, tear meniscus, lid forces, and frictions. The back optics zone radius (BOZR) is the main parameter to vary, when looking for an optimal fitting balance. A correctly fitted contact lens has certain movement during and after blinking, but rests in a stable position between blinks.

A particular type of RGP lenses are reversed-geometry contact lenses. These lenses have a secondary curve in the periphery that is steeper than the base curve. These lenses are used in two particular cases: 1) to fit the topographically altered post surgical corneas, and 2) Ortho-K procedures: flattening the cornea after extended wear, to correct refractive errors without surgery.

1.9.4. Soft contact lenses

While rigid lenses require a period of adaptation before full comfort is achieved, the main advantage of soft lenses is that they are immediately comfortable. They allow longer wearing times, and do not produce corneal oedema or corneal deformations, or at least to a less extent. Soft contact lenses remain typically more centered on the cornea, and the movements with blinking are small, if compared with RGP lenses. These lenses are almost unaffected by gravity.

However, optical quality (Torrents et al., 1997) and visual outcomes are more variable and often not as good as those obtained with rigid lenses. The tear film is not so stable, and the lens shape can fluctuate with blinking. The materials of the lenses are softer than the cornea, and so are more readily deformed by eyelid pressure. The refractive result is neither fixed not absolute. It can change from moment to moment, from day to day.

1.9.5. Multifocal contact lenses

Presbyopic contact lens correction is still a challenge for both patients and practitioners. Despite the number of potential patients as the population gets older, the use of multifocal contact lenses accounts for only a small proportion of contact lens wearers (Section 1.9.6). As a result, a number of different fitting strategies and designs continue to be developed for the presbyopic subject. Most of the more successful current types are concentric and based on the principle of simultaneous vision. Soft lenses are frequently the only choice, as the larger total diameter enables the practitioner to achieve better control of centration and lens movement. Figure 1.22 shows some examples of simultanoeus vision multifocal designs. In this thesis only lenses with progressive transitions are considered, to avoid problems in the topographic and aberration measurements.
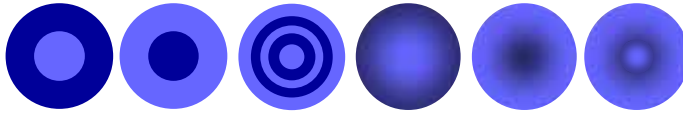
Fig. 1.22. Some examples of multifocal designs by simultaneous vision. The far and near zones (different tones of blue) are arranged at different radial distances.

As already mentioned in Section 1.5.2.5, the adaptation to the new visual experience these lenses provide is often difficult. Moreover, no adjustments are possible with hydrophilic lenses and the fitting procedure in quite inefficient, as it is based on trial and error with different lenses.

Depth of focus and tolerance to blur, pupil diameter and optical aberrations of the eye are additional issues in understanding the fitting of multifocal contact lenses, to be considered in combination with other fitting effects already mentioned affecting monofocal contact lenses.

1.9.6. Prescribing trends

Contact lenses are a popular way to correct refractive errors of eyes. Contact lens wearers are a significant proportion of the population in western countries, and their use is increasing: about 3 in 10 contact lens fits around the world are prescribed as "new fits" (Morgan et al., 2009). Soft lenses account for 90 percent of fits worldwide. The use of rigid lenses is declining (14 per cent of all fits in 2002 to 9 per cent in 2008), but the proportion of ortho-K lenses has risen from 0 to 11 per cent of rigid fittings. Multifocal and monovision lenses represent 5 per cent of the rigid fittings, and 7 per cent of the soft fittings (1% and 15 % respectively, in Spain).

1.10. FITTING CONTACT LENSES AND OPTICAL ABERRATIONS

Wavefront aberrometry offers exciting new opportunities to advance our understanding of the ways in which contact lenses interact with both the normal and abnormal eye, and will likely become a common tool in the contactology practice. This in turn should allow significant improvements in the optical design of lenses and in our ability to select lens designs which produce the optimal overall visual performance for the individual eye (Charman, 2005).

1.10.1. Tear studies

Already in the origins of wavefront theory of the human eye, Smirnov (Smirnov, 1961) made the important observation that the form of the tear layer might significantly influence the ocular aberration (Charman, 2005).

The first surface of the eye is not the corneal epithelium of the eye but the surface of the precorneal tear film. Changes in the tear volume and tear fluid dynamics can induce changes in the HOAs even if the corneal shape is completely ideal (Maeda, 2009). During the 10-second period after opening the eye, 25% of the normal eyes have a stable HOA pattern, 45% have small fluctuations, and 20% have a sawtooth behaviour (Maeda, 2009). Subjects with short tear-film break-up time have a sawtooth pattern with a marked upward curve that increase after blinking. From 5 to 9 s after blinking, the total HOAs are significantly higher than that inmediately after blinking, indicating that the optical quality might deteriorate in subjects with short tear-film break-up time by supressing the blinking. When measuring HOAs, specially with contact lenses (that can alter the tear dynamics), careful selection of the timing (blinking vs measuring) is needed to avoid artifactual data.

1.10.2. Monofocal contact lenses

When a lens is placed on the eye, its HOAs will tend to add to, or substract from, those of the eye, depending upon whether the signs of the wavefront errors are the same or opposite. In the past, however, it has been difficult to predict how the lens and the eye aberrations will combine. The aberrations of the lenses themselves have often been unknown. Even if the design aberrations have been specified, the on-eye performance may differ due to such effects as manufacturing errors, lens flexure, dehydration and decentration, and the presence of the tear film.

With the generalization of the use of RGP contact lenses, it was generally recognized that tear lens effects could result in the almost complete neutralisation of many irregular aberrations and modest amounts of astigmatism associated with the anterior corneal surface. However, in parallel with the early developments of this thesis, only Hong and colleagues (Hong et al., 2001) had measured aberrations in subjects wearing RGP contact lenses, finding that in 3 out of 4 subjects, RGP contact lens provided lower aberrations than soft contact lenses and spectacle lenses. However, a direct comparison of the optical changes produced by RGP contact lenses on the anterior surface of the cornea and total optical system had not previously been reported at the initial stages of this PhD project. Chapter 9 of this thesis will provide new evidence on this field.

Concerning soft lenses for myopia, many studies have proven that they tend to increase the HOAs (Roberts et al., 2006). The aberrations can be affected by the manufacturing method (Jiang et al., 2006) and the power (Awwad et al., 2008). Dietze and Cox (Dietze and Cox, 2004) showed that thin soft lenses with certain amount of spherical aberration in air contributed the same level of spherical aberration on eye.

It is well known that the tear film on the anterior surface of the contact lens is thinner and easier to break-up than the normal tear film on the anterior cornea, affecting the aberrations variability. Besides, lens flexure (Collins et al., 2001), movements, and decentrations will produce larger variability in the on-eye than off-eye measurements. Aberrometry provides a better understanding of the optical effects of the contact lenses ex vivo or in situ.

1.10.3. Multifocal contact lenses

There have been very few attempts to explore the on-eye behavior of contact lenses designed to aid the presbyopic patient. Wavefront aberration measurements should be useful for such studies in the cases of varifocal lenses with a smooth increase or decrease in power from the centre to the edge of the optical zone, i.e. lenses which effectively induce controlled amounts of spherical aberration. As in single vision lenses, wavefront aberrometry can reveal the way in which lens characteristics interact with the eye of the individual patient and can lead to a better choice of design for the particular patient (Charman, 2005).

There are some technical difficulties in the measurement of concentric multifocal designs in which zonal power alternates rapidly between a distance and a near correction: The resolution of the aberrometer an its dynamic range is limited, and the Zernike polynomials are poor descriptors of wavefront changing abruptly.

Martin and Roorda (Martin and Roorda, 2003) studied bifocal soft contact lenses by simply measuring the aberration of the eye alone and then calculating the theoretical performance of the eye combined with a particular contact lens design. They demonstrated that bifocal contact lenses do not always provide bifocal vision (even if the many fitting effects were not considered in this approach).

In this thesis, we will use a Laser Ray Tracing aberrometer, with high dynamic range and configurable sampling pattern for the in-vitro and in-vivo measurement of aberrations, to evaluate both optical coupling and fitting effects. Furthermore, only progressive designs with soft transitions between distance and near zones will be considered, to avoid the problems associated with Zernike description of surface discontinuities.

1.10.4. Correcting aberrations with contact lenses

Intriguingly, Smirnov (Smirnov, 1961) also suggested in 1961 that "in principle it is possible to manufacture a lens compensating the wave aberration of the eye" … and, noted that as spectacle lenses do not move with the eye as it rotates, …"the lenses must obviously be contact ones".

There is continued interest in extending the concept of a contact lens which corrects spherocylindrical errors and, perhaps, spherical aberration to one in which all the monochromatic wave aberration, in both lower and higher orders, is corrected. Correction of aberrations with adaptive optics have proved to increase optical (Hofer et al., 2001) and visual performance (Marcos et al., 2008).

Hong et al. (Hong et al., 2001) and Lu et al. (Lu et al., 2003) have demonstrated that rigid lenses can provide that sort of passive aberration compensation. The fitting of RGP contact lenses can reduce 66% of the severe HOAs found in postsurgical corneas (Gemoules and Morris, 2007). Other authors have explored the aberration correction with customized contact lenses. Full correction of aberrations with contact lenses is probably impossible, due to dynamic changes associated with tears, accomodation (Gambra et al., 2009), lens rotations and translations (Guirao et al., 2001) and other factors as chromatic blur. Nonetheless, the concept is attractive and can undoubtedly improve the optical performance of eyes with abnormally high aberrations, as those with keratoconic or post-surgical corneas.

Preliminary results with custom contact lenses for the correction of high order aberrations show a decrease in HOAs by a factor of 3 in normal and keratoconic eyes (Lopez-Gil et al., 2002, Sabesan et al., 2007). Although these results are suggestive,

there are still many unsolved issues (mainly related to fitting effects) that prevent the satisfactory clinical implementation of aberration corrective contact lenses.

1.10.5. Models, simulations and predictions

Several studies performed computer simulations to understand the optical performance of the contact lens (Atchison, 1995, Martin and Roorda, 2003, De Brabander et al., 2003). Using computer modeling, they evaluated the interaction of the lens with a model corneal surface and the optical contribution of the tear lens between the cornea and contact lens. Validating those simulations is difficult, as they tend to simplify the problem: Although some take into account contact lens decentration and corneal irregularities, they do not consider the flexing and the influence of the internal optics. Other studies (Collins et al., 2001) have measured the topography of the contact lens on the eye to study flexure on eye, but the analysis is based on corneal elevation data rather than on corneal wave aberrations.

1.11. OPEN QUESTIONS IN CONTACT LENS FITTING

Integrity of the contact lens design on-eye. It is well known that contact lenses (specially soft, but also rigid) are affected by flexure and shape deformations, when the lens is placed on the eye. An open question is, to which extent the design of the lens (starting with radius and asphericity) will be preserved after fitting and therefore the intended optical effect achieved. And in particular, with multifocal designs, how is the effective power distribution of the fitted lens?

Corneal biomechanics and corneal shape deformation: Long term or short term corneal shape changes due to the extended wear of contact lenses can determine the optical outcomes. To advance in this field, instrumental methods for the accurate measurement of not only the anterior but also the posterior cornea are needed.

Hydration and tear film: It is clear that the tear film has an optical effect in the normal eye. When fitting a contact lens, this tear film is modified, and the new tear film in the front surface of the contact lens has different optical consequences. The actual relevance of the optical effects induced by the tear film (introducing a refractive index difference with the cornea, and also shape variations), and changes in the tear film after fitting a contact lens need further exploration.

Optical interactions: What is the actual optical effect on the aberrations of the eye of fitting contact lens? How is the coupling between the aberrations of the contact lens and the aberrations of the cornea? What is the impact of the tear lens formed between the contact lens and the cornea? What is the optical relevance of this new source of internal aberrations? What is the impact of changing the balance with the aberrations of the cristalline lens?

Origin of inadaptation to multifocal contact lenses: Today, the fitting of multifocal contact lenses very often fails to satify the patient, and a trial and error procedure is often followed. New methods for the detailed study of successful and unsuccessful adaptations are needed, in order to gain knowledge about the origin of the failures, to anticipate or fix the problems, or to select good candidates for this kind of correction. For example, some unsolved question are: What is the baseline of neural effects in the failures to adapt simultaneous vision multifocal contact lenses? And what is the achieved multifocality, the actual depth of focus gain introduced by multifocal lenses?

How does it change with the lens parameters (thickness, correction)? How is the structure of the retinal images through a simultaneous vision lens fitted on an eye?

Predictions from optical estimates: The initial fitting of contact lenses (selection of the optimal design and parameters) is in many cases, a costly process in terms of wasted contact lenses and time for the patient and the contact lens practitioner. Precise methods to simulate contact lens fitting from objective measurements, considering the combined effect of shape deformations, tear, and optical interactions, and knowledge of the correct simulation parameters to use, are now of key importance to predict the optimal parameters, and to improve the efficiency of the fitting process.

1.12. HYPOTHESIS AND GOALS OF THIS THESIS

The main goal of this thesis is the detailed optical study of contact lens fitting and laser refractive surgery. Both are complex processes where the optical effects are entangled with biological effects, and subject to high variability. In this thesis we will test the following hypothesis: (1) that the development of novel rigorous experimental models based on artificial eyes will allow a better understanding of the physical basis, and therefore the subsequent improvement of the optical and visual outcomes, of corneal ablation for the correction of refractive errors and contact lenses for the correction of refractive errors and presbyopia; (2) that the optical, structural and visual quality measurements on patients will allow a deeper understanding of the mechanisms involved in refractive surgery and contact lens fitting.

The present thesis aims at isolating and quantifying

physical and **optical** effects such as:
- laser ablation on materials
- laser efficiency losses from the center to the periphery
- the design the ablation patterns
- influence of the posterior corneal surface
- optical coupling of the eye optics and the optics of the contact lens
- contact lens shape conformity to the cornea
- the design of contact lenses

from **biological** effects such as:
- biomechanics and wound healing
- corneal swelling and bulging after surgery
- tear variability
- movement of the contact lens
- neural effects of vision.

1.13. SPECIFIC QUESTIONS

The specific questions that we want to solve in this thesis are:

1. Reasons for the increase of spherical aberration in conventional refractive surgery.
2. Isolate physical from biomechanical contributions in refractive surgery.
3. Accurate measurement of the shape of corneal ablation patterns.
4. Assess and compare the optical outputs of different laser platforms.
5. Anterior and posterior corneal elevation changes in refractive surgery patients.

6. Evaluation and understanding of optical performance of eyes with RGP contact lenses.
7. Reasons for the improved optics with RGP contact lenses.
8. Evaluation of optical performance with monofocal and multifocal soft contact lenses in physical and real eyes.
9. Understanding of the failure/success of multifocal contact lenses in producing effective multifocality, on an individual basis.
10. Correlations of visual and optical quality in patient eyes.

1.14. THESIS SYNOPSIS

In this thesis we studied the physical implications of corneal ablation and the effect of contact lens fitting. Both are complex phenomena, entangled with biological effects, and with many mixed (and often yet unbounded) physical causes. Our approach was to study the problem starting with a high degree of control, and lowered complexity. In following steps, the degree of complexity is progressively increased.

Three experimental models have been developed during this thesis, with the aim of isolating the physical process of interest from the inherent variability of human eyes and gaining control (avoiding biomechanics, theoretical assumptions, cross-interactions, tear effects, etc): 1) a model for the study of the laser ablation of the anterior cornea, 2) a model for the study of the posterior surface of the cornea which was applied to the study of posterior cornea stability after refractive surgery, and 3) an in-vitro model of contact lens fitting, oriented to multifocal lenses. These three models were used to study, with high precision, the optical changes produced by the manipulation of the refractive properties of the cornea.

To support those experimental studies, we developed new measurement methods and procedures. In particular, a new generation of LRT aberrometer was implemented for this Thesis, and methodologies for the measurement of changes in optical surfaces. These were applied to the experimental models. Besides, during this thesis different clinical studies were performed on patients, of the specific questions studied in vitro: the posterior surface of the cornea, and contact lens fitting (from monofocal RGP – semirigid- contact lenses to soft multifocal contact lenses).

The body of this thesis is structured as follows:

Chapter 2 describes the common methods used throughout this thesis: instruments for the precise measurement of optical surfaces (and real and artificial corneas in particular), a versatile system (Laser Ray Tracing) for the measurement of optical quality of the eye, methods for the measurement of optical performance, and different techniques for computer simulation of different phenomena.

Chapter 3 introduces *in vitro* plastic artificial eye model for the study of the physical factors involved in refractive surgery. Efficiency effects were measured by ablating flat and spherical artificial corneas of PMMA, with a conventional refractive surgery system, provided with non-optimized algorithms.

In **Chapter 4** a study of the ablation process vs material, number of pulses and fluence is presented, aiming at a better understanding the use of plastic models in refractive surgery, and providing valuable information of the optical and ablation properties of the materials and for the improvement ot the model. A new material, Filofocon A, is introduced, with ablation properties that make it more suitable for refractive surgery models.

Chapter 5 presents the results of applying the improved refractive surgery plastic model of Filofocon A, to the study and comparison of state-of-the-art laser platforms, provided with optimized algorithms. Differences in the physical effects of the ablation, as well as optical outcomes are reported.

Chapter 6 describes a hybrid porcine/plastic model for the validation of topographic instruments measuring the backsurface of the cornea. The model was used to validate a Pentacam Scheimpflug Imaging topographer.

In **Chapter 7** the Pentacam topographer was used to study changes in the anterior and posterior corneal elevation maps with refractive surgery, by measuring several patients before and after (at several timepoints) refractive surgery.

In **Chapter 8**, a new in vitro physical artificial eye model, for the study of contact lens fitting is described and validated. Positive and negative monofocal and multifocal soft contact lenses were studied in controlled conditions, in terms of shape conformity and optical changes. The combination of total and first surface aberration measurements allows a detailed analysis of the fitting, and new understanding of its optical implications.

Chapter 9 addresses the study of the interactions between the optics of real eyes and RGP contact lenses. The changes in optical quality in presence of moderate flexure and conformity of the lens were analyzed, to better understand the process of contact lens fitting.

Chapter 10 presents measurements on patients aiming at understanding the physical factors involved in contact lens fitting (and multifocal lenses in particular) on real eyes. It presents studies of the optical and visual quality of soft contact lenses fitted on real eyes. Monofocal and multifocal contact lenses, of both positive and negative power were compared on the same subjects.

In **Annex A** the analysis of conic surfaces, used to describe the corneal shape during this Thesis is presented, in paticular the observed correlation between radius and asphericities. The problem is relevant in the analysis of changes of optical surfaces (for example after a refractive surgery procedure or when fitting contact lenses). A statistical analysis to increase the sensitivity of detection of changes is proposed.

Finally, the major findings of this work, and their implications, are summarized in the **Conclusions**.

<div align="right">

Chapter

2

Methods

</div>

This chapter is devoted to describe the experimental techniques used in this thesis. Specifically, the different instruments used to measure optical surfaces, the Laser Ray Tracing (LRT) technique used to measure ocular aberrations, and the psychophysical set-up used to measure visual performance will be described.

The author of this thesis has been the main contributor in testing the different working modes of the instruments used for measuring the topography of optical surfaces, modifying those instruments and developing the measurement procedures. He also led, in collaboration with Lourdes Llorente and Susana Marcos, the development of a new-generation LRT system that was built in the initial stages of this thesis. The specific contribution of the author of this thesis was the installation and programming of cameras, electronic hardware and computer boards, the development of control software and synchronization of the different elements, and of data management. He also developed the psychophysical experiments used to measure visual performance.

The work related with the new LRT device, was presented (Dorronsoro et al., 2003c), at the Spanish Optical Society (SEDOPTICA) Annual Meeting, where C. Dorronsoro won a Young Investigator Award as the first author of this work. It was also presented as an oral presentation at the Real Sociedad Española de Física (Royal Spanish Physics Society) at its Second Centenary Meeting. Summarized descriptions
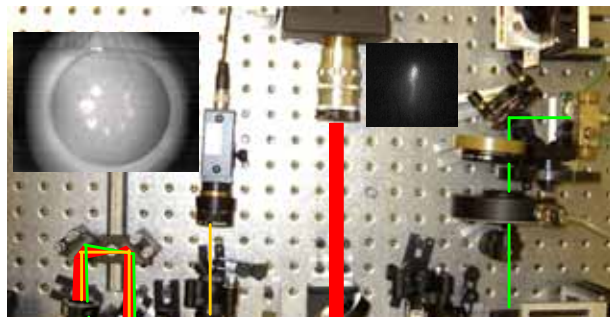
of the instrument can also be found in (Dorronsoro et al., 2003a, Llorente et al., 2004b, Llorente et al., 2007).

The authors of this work were: Carlos Dorronsoro, Lourdes Llorente, Daniel Cano, Sergio Barbero, Benjamín Alonso-Fernández, Laura Remón and Susana Marcos.

2.1. MEASUREMENT OF OPTICAL SURFACES GEOMETRY

Different instruments have been used in this thesis for the experimental assessment of optical surfaces. Fig. 2. 1 shows examples of raw data obtained with the different instruments used to measure optical surfaces all throughout this thesis. Non-contact optical profilometry was used for in vitro measurements: on spherical surfaces on Chapters 3, 5 and 6, and on flat surfaces on Chapters 4 and 5. Placido disk videokeratoscopy was used in-vivo in Chapters 3 and 9 and in-vitro in Chapter 8. Scheimpflug Imaging was used for in vitro measurements in Chapter 6 of this thesis, and for in-vivo measurements in Chapter 7.

Fig. 2. 1. Examples of raw data obtained with the different instruments used to measure optical surfaces in this thesis. (a) Non-contact optical profilometry on spherical surfaces. (b) Non-contact optical profilometry on flat surfaces. (c) Atlas Videokeratoscopy. (d) Pentacam Scheimpflug Imaging. Both the anterior and posterior surfaces of the cornea are measured.

2.1.1. Surface profilometry

In recent years, there has been considerable progress in surface geometry measurement. Contact and non-contact profilometry systems, with different measurement principles, are both capable of accurately and reliably measuring surface topographies on the scale of millimeters to nanometers. However, the optical surfaces used in this thesis are very demanding for profilometric instruments, specially curved surfaces used in the artificial eyes. For that reason, different systems were used depending on the requirements. In all of them, software modifications or measurement procedure adjustments were needed to reach the combination of precision and measurement range demanded by these particular samples. In Chapter 3 three different profilometry systems were evaluated: one contact profilometer for spherical surfaces, another contact profilometer for flat surfaces, and also a new generation system for non-contact profilometry. This last system was used in the rest of the thesis, both for flat and spherical surfaces.

The samples used in this thesis are mainly flat and curved artificial corneas. The measurements on the artificial corneas are very demanding for the instruments, due to their low radius of curvature (8 mm). The maximum difference between the surfaces to be compared (for example before and after surgery) is very small, of the order of 40 microns, while the range to be measured is of the order of millimeters (from the apex to the periphery of the cornea). Furthermore, the quality of the surface (of critical importance in the precision of the measurement) changes from optical smoothness before surgery to significant roughness after it.

As a consequence, several instruments were tested during this thesis. They had to be modified to some extent, and enhanced measurement procedures (with improved accuracy) had to be developed.

2.1.1.1. Contact profilometry

A Detek 3000 contact profilometry system, based in CIDA, Madrid, Spain, that provides the profile of a sample along a given direction, was used to measure flat surfaces in Chapter 3. This apparatus uses a small probe tip that is placed on the sample and moves across in continuous contact with the surface. The tip movement, that outlines the surface profile, is recorded in a computer as two vectors that represent the Cartesian coordinates of the profile. The operating range of this system is 0.2 mm (height) x 15 mm (across). Fig. 2. 2 shows an example of a raw measurement on a flat profile.
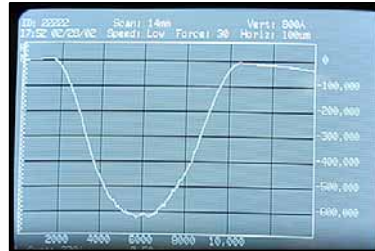
Fig. 2. 2. Example of a raw measurement on a flat ablated surface with the Detek 3000 contact profilometer. Custom algorithms were developed to extract the information to a digital format.

The vertical range of that system was too low to measure the elevation differences found in the spherical surfaces (radii 8 ~ mm). For that reason, we used a Talysurf contact profilometry system (Taylor-Hobson, Leicester, England), based at Indra Sistemas, Aranjuez, Madrid, Spain, for the measurement of spherical surfaces. This system has sufficient working range to measure the profile along the 12-mm diameter of the artificial cornea, and its resolution is higher than the roughness of the ablated surface (typically less than 1 μm). Fig. 2. 3 shows an example of raw measurement, in which the best fitting sphere has been subtracted by the instrument's software. This instrument was used to test the spherical surfaces presented in Chapter 3.
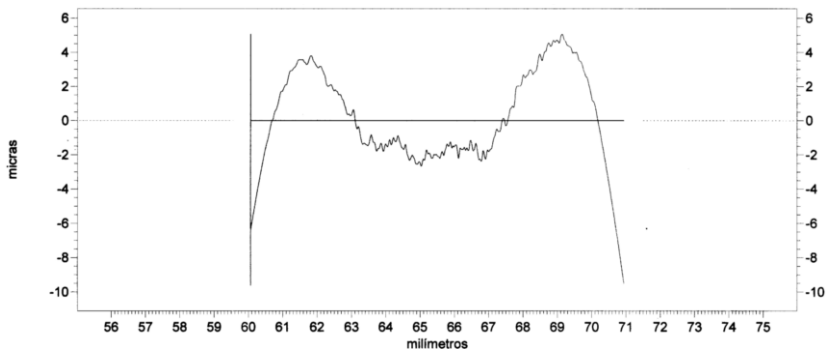
Fig. 2. 3. Example of a raw measurement on a spherical ablated surface with the Talysurf contact profilometer. The best fitting sphere has been substracted by the instrument. Custom algorithms were developed to extract the information to a digital format.

In both profilometers, custom algorithms were developed to extract the information (shown in a monitor and printed in paper) to a digital format, to be processed with our custom analysis algorithms (Section 2.2).

2.1.1.2. Non-contact profilometry

Most of the measurements of the shape of the surfaces used in this thesis (flat or spherical, ablated or not, Chapters 4 and 5) were obtained using a non-contact microscope profilometer (Plµ, Sensofar, Terrassa, Barcelona, Spain), based at the Visual Optics and Biophotonics Lab of the Institute of Optica, shown in Fig. 2. 4. The confocal mode, that reconstructs the surface map from a set of images at different planes of focus -as explained bellow-, was primarily used. The interferometric mode of the instrument was used under certain conditions. The different measurement modes, in combination with the corresponding microscope objectives provide different balances between measurement precision (axial and lateral resolution) and measurement speed. The interferometric mode was used to study ablation craters (Chapter 4) and to locate the apex in curved surfaces (Chapter 5). White field imaging was often used to study the sample appearance (Chapter 5).

Fig. 2. 4. Non-contact confocal microscope used for profilometry measurements (Plµ, Sensofar, Terrassa, Barcelona, Spain)

The basic setup of the illumination hardware is shown in Fig. 2. 5. The light source is a high power LED, emitting at a peak wavelength of 480 nm with a lambertian emission pattern. The light beam reaches a polarizing beam splitter cube (PBS), and the resulting polarized beam strikes a microdisplay, the key active device of the sensor head. The information transferred to the microdisplay will be imaged on the surface of the sample by a microscope objective. In this arrangement the surface of the illuminated sample will be also imaged on the CCD array. In order to obtain confocal images a binary pattern is displayed in the minidisplay and imaged onto the surface of the sample. The optical setup provides the required matching between pixels of the microdisplay and pixels of the CCD array, which in turn behave as confocal apertures (Artigas et al., 2004).

In our measurements, a pattern of parallel lines is projected with an infinity-corrected microscope objective (ELWD 100X) onto each point of the surface while a CCD camera images the reflected lines, through the same optics. The instrument scans

the sample in the Z direction, changing the focus position of the lines relative to the surface being measured. Image processing algorithms retrieve the Z point at which the reflected image of the parallel lines is sharpest, which is considered the height of the surface at that point.
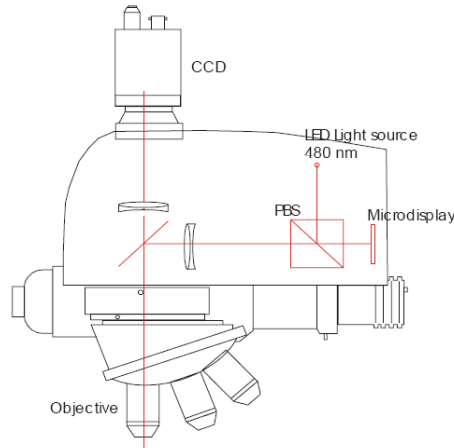
Fig. 2. 5. Optical set-up of the non-contact profilometer used in this thesis (Artigas et al., 2004).

For comparison purposes, in Chapter 5 we used the same instrument (and the same software and measurement procedures) for all the samples: flat and curved surfaces, ablated (rough) or not (polished). As with other instruments measurements on spherical corneas were more demanding than on flat corneas, due to the steep slope at the periphery causing two undesired effects: on the one hand, fewer projected lines are in focus on the sample at the same time, and on the other hand the intensity of the back-reflected light is relatively low. A new measurement procedure (and the corresponding control program) was developed for the measurement of the artificial eyes. This development was performed in collaboration with Benjamín Alonso-Fernández (University of Salamanca) and Cristina Cadevall (CD6 - Universidad Politécnica de Cataluña). Custom algorithms were developed as part of the measurement procedure definition, including the calculation of a confidence index for each point measured to help identify anomalous measurements in the analysis stage. Additional tests were performed to estimate the optimal measurement parameters and the significance thresholds (used to discard invalid points).

To obtain the shape of the artificial corneas, 1148 points of a rectangular grid covering the central 11 millimeters of the surface were measured. To achieve the maximum precision the system was mounted on an active vibration-isolated table. The interferometric mode of the microscope was used to identify the apex before the automatic measurement, in which the measurement grid was centered. We used predictive calculation and concave interpolation to predict the shape of the surface from previous measurements and the approximate z-location of the next point to measure. Consecutive confocal measurements of increasing resolution (and decreasing measurement range) were performed at each point taking the predicted point as starting point.

The measurement method that was followed for most measurements (confocal imaging) is slower than standard or interference imaging because a sequence of CCD frames must be acquired to build each single confocal image. The measurement was fully automatized, and it took more than 4 hours to measure all the points for each surface. As dilation of the sample during the measurement is a potential cause of error (see Fig. 2. 6), the laboratory temperature was monitored and controlled, and the samples were stored near the measurement instrument.
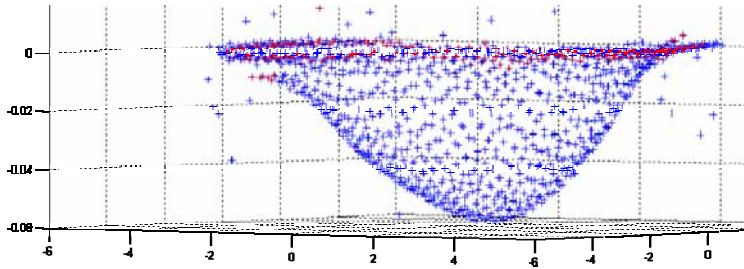
Fig. 2. 6. Dilation problems in a profilometry measurement. The points marked in red correspond to a non-ablated flat region and therefore all of them should be on the same plane. However, some of these points in the left side of the ablation profile are 10 microns bellow their expected position, due temperature changes (and dilation) occurred during the measurement. The whole ablated pattern is therefore affected by dilation.

In some of the measurements, we observed important deviations from rotational symmetry. The asymmetries appeared both on flat and spherical equivalent surfaces with some of the lasers and the location of the irregularity changed across repeated ablations. To discard dilation and other effects during the measurement, validation tests (involving repeated profilometric measurements of the same samples at different orientations) proved that the irregularities were a consequence of the ablation process and not of the measurement. Fig. 2. 7 shows an example, in which measurements of the same sample (an ablation profile) upside down provided similar results. Changing the orientation also entails changing the measurement axis. This experiment therefore also represents a cross-validation for the surface analysis algorithms (Section 2.2).
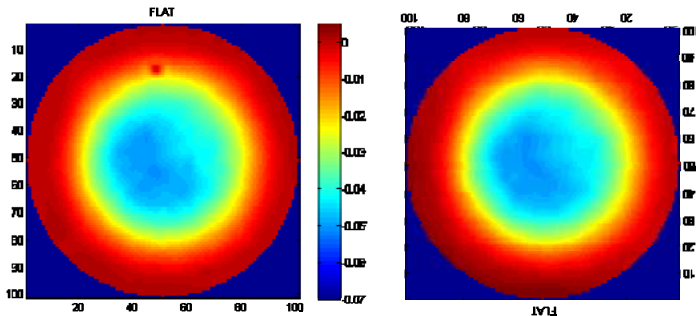
Fig. 2. 7. Two different measurements of the same sample (an ablation profile), at different orientations, provided similar results demonstrating that the irregularities were a consequence of the ablation process and not of the measurement.

2.1.2. Corneal topography with Placido disks (Videokeratoscopy)

Placido disk videokeratoscopes analyze specular reflection off of the cornea of a set of concentric illuminated rings (Placido disk) recorded by a video camera (Fig. 2. 8). The system has a central clear zone through which the subject views a fixation target. From the image of the reflected rings an algorithm reconstructs the shape of the anterior corneal surface.

Fig. 2. 8. The Placido disks in a videokeratoscope (right side picture of Placido disks reflected on the anterior surface of a contact lens, from Kopf et al. (Kopf et al., 2008))

In this thesis we used the Humphrey-Zeiss MasterVue Atlas Placido disk videokeratoscope. The reconstruction algorithm for the Humphrey-Zeiss topographer is referred to as 'arc step algorithm', and has been described in detail by Campbell (Campbell, 1997). This algorithm reduces the reconstruction to analyze the corneal surface in a set of meridian planes, "reconstruction planes", containing the videokeratoscope axis (VK axis). The VK axis is defined as the axis that intersects the image plane at the mean center of the inner rings reflections and passes through the center of the entrance pupil of the videokeratoscope (Campbell, 1997). The algorithm extracts corneal shape data in the reconstruction planes separately. This algorithm assumes that reflection rays in a meridional plane stay on the same plane. Rays not obeying this condition are named skew rays, and the error associated with this approximation is called skew error.

For each reconstruction plane, a meridional curve of the corneal surface is evaluated. These curves are fitted by small sections of circular arcs by an iterative algorithm obtaining the axial and radial positions and slope of the curve at different points. The Placido disk is formed by 24 rings. There are 180 reconstruction planes with 2 degrees of angular distances among planes. Therefore for each reconstruction plane there are 48 evaluated points, and the total number of points in the global reconstruction is 48*180. However, some of these data are lost because of tear film break up effects or eyelid oclusions. Fig. 2. 9 shows the set of points where the corneal surface is evaluated for a real cornea. Fig. 2. 1 (b) showed an example of raw data of corneal elevation obtained with this system.
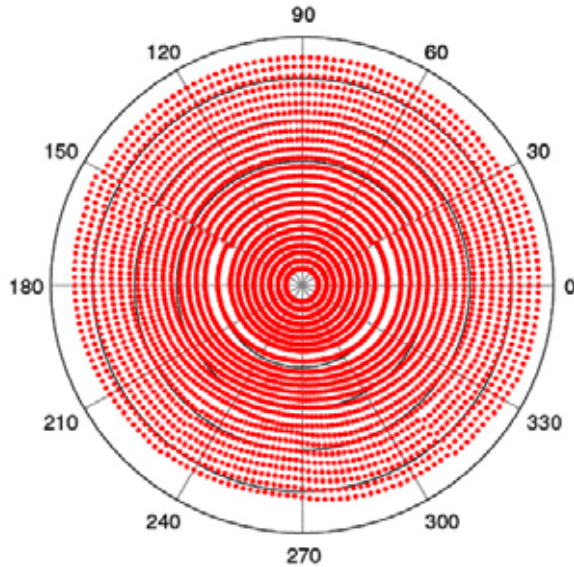
Fig. 2. 9. Set of points in corneal polar coordinates where elevation data are given by the videokeratoscope.

Corneal videokeratoscopy was compared with Talysurf contact profilometry on ablated spherical surfaces of PMMA. Fig. 2. 10 shows data of the laser ablation on a 8-mm sphere (with the laser system described in Chapter 3), for a -3D ablation. The base sphere has been substracted to the measurements. Confocal microscopy with Plµ was also performed, although only in the central 4 mm. The three techniques provided estimates of the apical radius of curvature (in the post-ablated surface) within 0.01 mm, and estimates of the asphericity within 0.02. The ablation depth estimated from the difference pre/post ablation topographies varies less than 2 microns across the three methods.
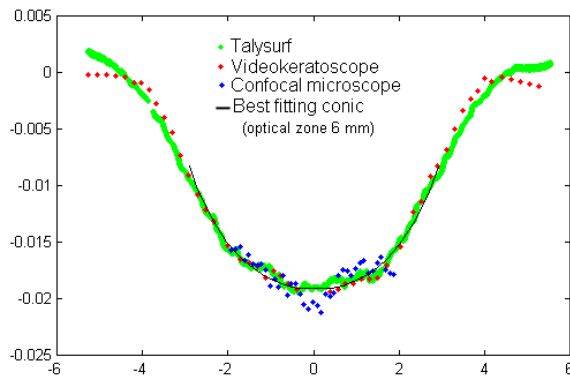
Fig. 2. 10. Comparison between videokeratoscopy (red) and contact profilometry (green) for an ablation of -3 D in a PMMA spherical surface. Confocal microscopy with Plµ is also shown (blue points). The discrepancy in apical radius and asphericity is below 0.01 mm and 0.02. The difference in ablation depth is less than 2 microns. The base spphere has been substracted from the measured elevation maps.

A complete description of the accuracy and sources of error of the technique can be found in Sergio Barbero's thesis (Barbero, 2004). Many software tools have been developed in the Visual Optics and Biophotonics lab during the last years for data export, and analysis using custom algorithms. One of the most important applications developed in previous works (Barbero et al., 2002b, Barbero et al., 2002c) is the estimation of corneal aberrations from the Atlas Placido disk videokeratoscopy (briefly described in Section 2.3.1).

2.1.3. Corneal topography with Scheimpflug Imaging

2.1.3.1. The Scheimpflug principle

Fig. 2. 11 (a) shows a conventional optical system. The object plane, the lens, and the image plane are parallel. In imaging systems following the Scheimpflug principle (Fig. 2. 11 (b)), the object plane, the lens plane and the image plane are no longer parallel, and they cross a line called the Scheimpflug intersection. The major advantage of the Scheimpflug geometry is that a wide depth of focus is achieved.
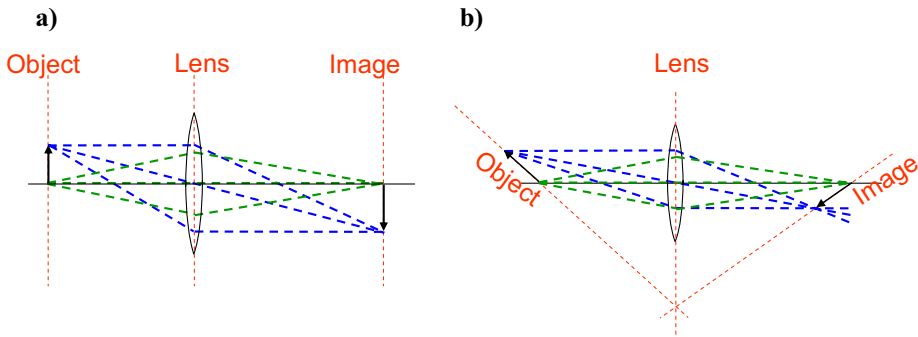
Fig. 2. 11. The Scheimpflug principle.

2.1.3.2. The Scheimpflug camera

In Fig. 2. 12 the basic principle of slit lamp photography and of Scheimpflug imaging is illustrated. Slit lamp photography (Fig. 2. 12 (a)) has not been used in this thesis, but it is a well established technique in clinical practice and the concept behind it serves as an introduction to Scheimpflug imaging. A narrow slit beam of very bright light produced by a lamp is focused on the eye which is projected with a 10x to 50x magnification microscope on a imaging sensor (a CCD chip in this example). The width, length and orientation of the slit is generally variable. A scheme of the Scheimpflug camera, for use in opthalmology is illustrated in Fig. 2. 12 (b). The Scheimpflug camera improves slit lamp imaging by using the Scheimpflug principle. The image plane (the CCD) and the lens plane intersects in a line. Therefore, the images correspond to sections of the eye, in which all the points are in focus. Sections of the entire anterior segment of the eye can be obtained.
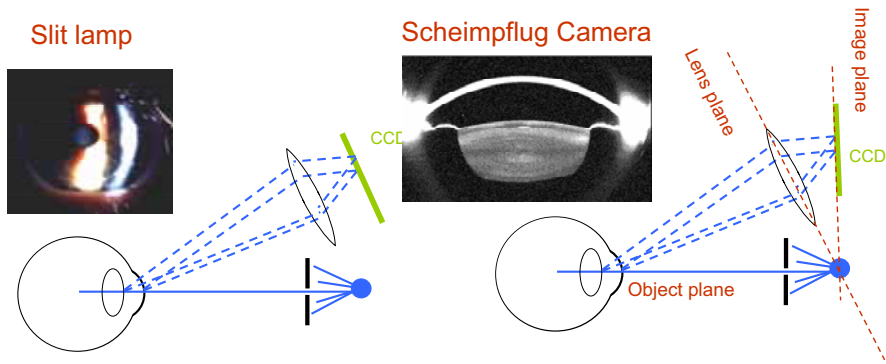
Fig. 2. 12 The Scheimpflug camera.

However, the Scheimpflug camera introduces a geometrical distortion (Fig. 2. 13, top row), because the magnification is not constant over the image. Additionally, because of the refraction from the different ocular surfaces, the Scheimpflug camera also introduces an optical distortion (Fig. 2. 13, bottom row), due to the fact that each of the ocular surfaces is seen through the previous one (i.e., the anterior lens is seen through the posterior and anterior cornea).
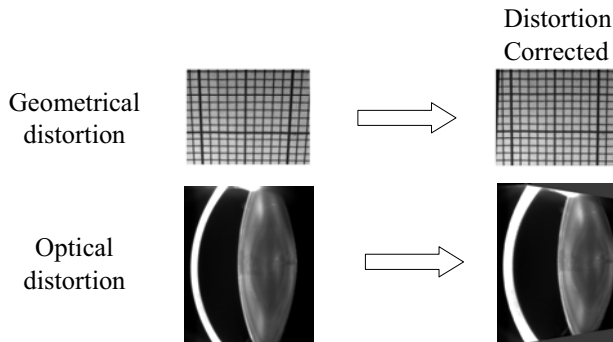
Fig. 2. 13. Image distortion in Scheimpflug imaging.

A validation of the correction of the images is needed before it can be reliably used to obtain posterior cornea surface shapes (Dubbelman et al., 2002, Rosales and Marcos, 2009).

2.1.3.3. The Pentacam Scheimpflug imaging system

We used a Pentacam (Oculus GmbH, Wetzlar, Germany) anterior segment imaging system based on the Scheimpflug principle (Fig. 2. 14). The slit rotates around the optical axis of the instrument, allowing the capture of 25 anterior segment diametral sections at different angles, and therefore 3-D elevation maps of the anterior and posterior corneal surfaces are obtained. According to the manufacturer, this device provides quantitative information of the posterior cornea, as it automatically corrects for geometrical and optical distortions. The commercial software also provides

measurements of anterior and posterior radius of curvature using either fitting the best sphere, or horizontal and vertical apical radii, asphericity and astigmatism fitting a biconic surface (see Section 2.2.1). Raw elevation maps are also provided, which can be used for further quantitative analysis in Matlab, Mathworks (see Data analysis section). The technique had been used in previous studies (Rosales et al., 2006, de Castro et al., 2007, Rosales and Marcos, 2009) in the Visual Optics and Biophotonics Laboratory, and therefore many software routines were available to retrieve and process the data obtained with this instrument. One of the major contributions of previous work is the development of optical and geometrical distortion correction algorithms for this system. A detailed description of the technique, calibrations and corrections can be found in Patricia Rosales's thesis (Rosales, 2008), and in (Rosales and Marcos, 2009).

In Chapter 6 of this thesis the accuracy of the measurements of the back surface of the cornea, including the geometrical and optical distortion corrections, will be tested, by using a model cornea of known posterior surface. In Chapter 7 we applied this instrument (validated in Chapter 6) for the study of changes in the posterior cornea after refractive surgery.
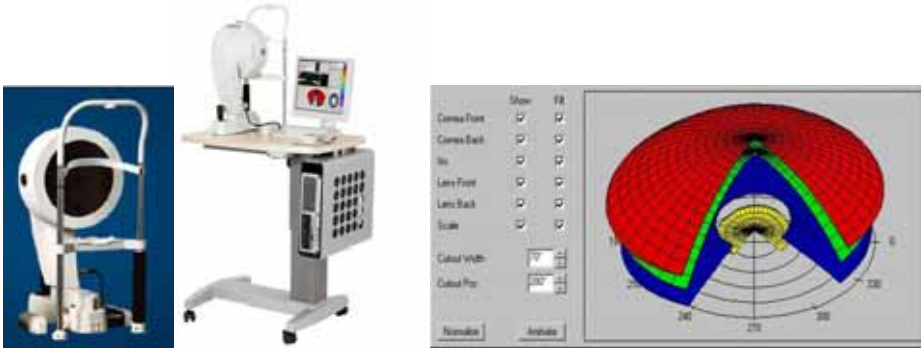
Fig. 2. 14. Pentacam Scheimpflug imaging system.

2.2. SURFACE ELEVATION ANALYSIS TOOLS

During this thesis, different tools for the analysis of the measured optical surfaces have been developed. In the following sections the different tools will be described, and their use illustrated with examples. The specific use of each tool will be described in the results chapters (Chapters 3 to 10).

2.2.1. Fitting surfaces

The optical surfaces of the eye (anterior and posterior surfaces of the cornea and the lens) are often described by surfaces whose profiles are conic sections.

The general equation of a conic curve is

$$x^2 = 2Ry - (1+Q)y^2 \tag{2.1}$$

where R and Q are the apical radius and asphericity, respectively. Any conic is described in terms of these two parameters, the radius R representing the radius of the circumference that best fits a small region around the apex, and the asphericity Q

representing the deviation of the conic with respect to a circumference. Conic curves are classified in circumferences ($Q=0$), hyperbolas ($Q<-1$), parabolas ($Q=-1$) and ellipses ($Q>-1$). Figure Fig. 2. 15 graphically describes the effect of asphericity on conic sections, as all the curves shown have the same apical radius. Therefore, the surfaces of the ocular components (cornea and crystalline lens) can also be described in terms of their radius and asphericity.
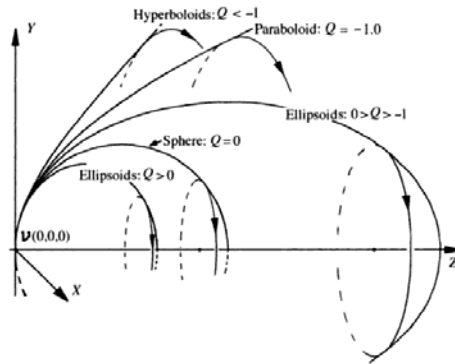
Fig. 2. 15. The effect of asphericity on the shape of a conicoid. All the curves have the same apical radius of curvature (Atchison and Smith, 2000).

The three-dimensional extension of this description based on conic sections can be made in terms of quadrics (rigorous extension of conic sections to three dimensions), conicoids (surfaces with revolution symmetry in which all the longitudinal sections are conic sections, as in Section 1.2.1 and Equation 1.1) and biconics (asymmetric surfaces with two preferential axes, which are conics). Consequently the surfaces of the eye are usually be described in terms of conics. A single apical radius of curvature and one single asphericity for conics, and two radii and two asphericities for biconics.

The representation of ocular surfaces in terms of conic-based surfaces, although very useful in many cases, constitutes only a coarse approximation of the real cornea. A point by point numerical description of the surface is often impractical. In these cases, fittings to a base of Zernike polinomials (Section 1.4.4) can be a good compromise (Schwiegerling et al., 1995).

In all cases, but specially with conic-based surfaces, it is important to choose the correct number of free parameters in the fitting to achieve the maximum accuracy. If the surface is (or could be) tilted or decentered, it is desirable to include two tilting and two centering parameters. In the studies presented in this thesis, many of the surfaces show a prioritary center (abation patters or multifocal designs). We found optimal results when the fitting was accomplished in two phases: one to locate the center and tilt of the surface (for example, after fitting an sphere) and another one (after removing tilt and decentration) to retrieve the radius and asphericity. As the optimal approach depends on the specific application and the characteristics of the surface, the procedures will be described in detail in the corresponding Chapter.

Annex A will analyse the existing correlation between radius and asphericity appearing when fitting different corneal surfaces to conics.

2.2.2. Comparing surfaces

In many of the studies of this thesis, the outcome results from the comparison of two or more surfaces. For example, the ablation pattern appears after comparing the

surface before and after the ablation. Furthermore, the measurement of the ablation efficiency effects is obtained after comparing the ablation pattern on flat surfaces from the ablation pattern on spheres (Chapters 3 and 5). The simulation of the three-dimensional shape of a contact lens fitted on the eye results from the comparison of the anterior cornea and the anterior surface of the contact lens fitted. These two surfaces are also compared to obtain the conformity or flexure of the lens to the underlying cornea. All these applications are described hereinafter.

2.2.2.1. Ablation patterns from flat surfaces

In flat samples ablated with a laser, the measurement of the surface elevation pattern (or profile) should directly provide a measurement of the ablation pattern. However, in most cases the raw measurements of flat surfaces are affected by tilt. This happens when the support of the samples in the profilometry system is not perfectly parallel to the translation of the probe tip in contact profilometers (as that used in Chapter 3), or if the support of the samples is not perfectly perpendicular to the optical axis of the instrument in non-contact profilometers (Chapters 4 and 5). Tilt also appears if the sample is not perfectly plano-parallel.

To remove this tilt, the non-ablated zone is fitted by a plane surface (a line in the case of a profile). That plane (or line) is subtracted from the measured surface. The location of the non-ablated zone is an input parameter, indicated as the ring between two given radii. The corrected measurement is more symmetrical than the original measurement (see Fig. 2. 16). Section 2.1.1.2 describes a cross-validation procedure of the measurement and the processing algorithms based on measuring the sample with different tilts and orientations (Fig. 2. 7). This cross-validation demonstrates (with the same sample) that the residual asymmetry obtained is in fact in the original sample, and is not an artifact introduced by the measurement procedure or the algorithms.
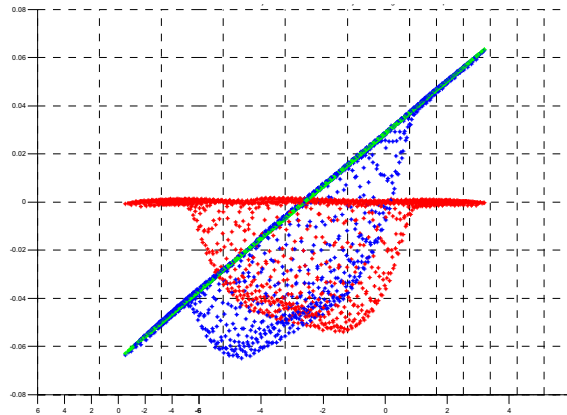
Fig. 2. 16. Removing tilt from topographies measured on flat ablated surfaces. The non-ablated zone (green points) of the measured elevation map (blue points) is fitted to a plane surface. This plane surface is subtracted from the measured surface to give the corrected measurement (red), which is more symmetrical than the original measurement (blue). The residual asymmetry is in the original sample, and is not introduced as an artifact of the measurement procedure, as can be demonstrated by measuring the sample with different tilts and orientations (Fig. 2. 7 and Section 2.1.1.2)

2.2.2.2. Ablation pattern from spherical surfaces

Retrieving the ablation pattern from an ablated spherical surface is more complicated, as it requires a precise comparison between two almost-spherical surfaces. Figure Fig. 2. 17 shows an example of ablation pattern estimation. The raw measurement looks spherical in Fig. 2. 17 (a), and the ablation performed on the surface is not noticeable. After subtracting the best fitting sphere from the non-ablated areas, the non-ablated zones appear flat and the ablation pattern is well described. Note that the Z-axis scale of Fig. 2. 17 (a) is more than 10 times larger than that of Fig. 2. 17 (b).
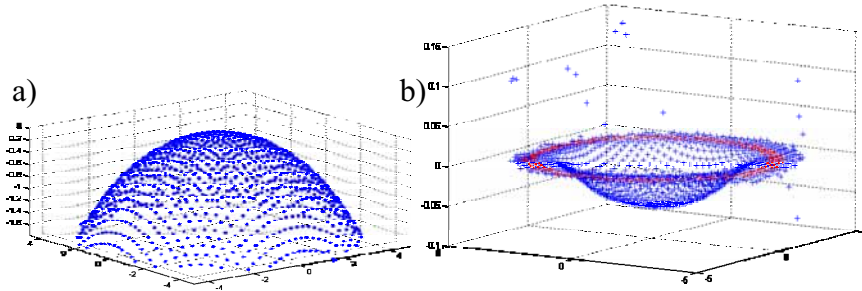
Fig. 2. 17. Retrieving an ablation pattern from an ablated spherical surface. a) Raw measurement. b) After subtracting an ideal sphere with the correct radius of curvature, the non-ablated zones appear flat. The red points indicate the points of the raw measurement that were used to center the best fitting surface. Note that the Z-axis scale of Fig. 2. 17 (a) is more than 10 times larger than that of Fig. 2. 17 (b).

Direct subtraction of the pre-operative and post-operative surfaces was not best to retrieve the ablation pattern from spherical surfaces. All the artificial cornea samples manufactured in this thesis (Chapters 3 and 5) were spheres (independently checked in the optical workshop using an optical gauge based on Newton rings before the ablations, and also measured –in Chapter 5- with the non-contact optical profilometer described in Section 2.1.1.2). Therefore an ideal sphere instead of the noisy point by point description of the surface was subtracted from the postoperative surface. The radius of the base sphere is a critical parameter, as it determines the ablation depth and the pattern shape. In Chapter 3 it was calculated from the pre-ablation curvature. In Chapter 5 the procedure was further sophisticated, to achieve higher accuracy taken advantage from the fact that the measurements on flat and on spherical surfaces were performed with the same instrument. The radius was that fulfilling the contour condition that the central ablation depth in spheres matches the central ablation depth in flat surfaces.

2.2.2.3. The shape of a fitted soft contact lens

The shape of a fitted soft contact lens on eye was simulated in this thesis, and visualized as three dimensional volumes. In soft contact lenses, the back surface of the lens is expected to conform the anterior surface of the cornea (as will be discussed in Chapter 10), with no tear lens in between. Therefore, the contact lens can be simulated by plotting together the elevation map of the anterior surface of the lens and the elevation map of the anterior surface of the cornea, separated by the nominal thickness of the lens. Some examples will be shown in Chapter 8. As in previous section, the surfaces of the contact lens are dominated by their spherical component. Substracting the best fitting sphere give insights into the details. If we want to study the real

thickness map, the same base sphere (typically the one corresponding to the anterior cornea) has to be substracted from both surfaces. The shape of the lens appears more clearly, as a positive or negative meniscus, depending on the lens power. To study the lens flexure or conformity to the underlying cornea, each of base spheres has to be substracted to each from the corresponding surfaces.

2.2.2.4. Representing surfaces

Throughout this thesis we have used different graphical representations for analysing the optical surfaces measured. Three dimensional scattered points plots (as those shown in Figs. 2.16 and 2.17) are often used to represent raw measurement (or deviations from a plane or a sphere). Figure 2.18 shows three other representations used. The same example surface, corresponfing to a highly assymetrical ablation pattern, is shown in a 2-D color-coded map of elevations (a), a 3-D topography (b) and a radial profile where only the radial coordinate of the points is plotted vs their heigh (c). To obtain the representations of Figs. 2.18 (a) and (b) an interpolation of the measured points to a regular grid is needed. Depending on the application and variability of the data Zernike polinominal expansions, splines or exact interpolation was used. As opposed to raw sets of data (scattered points), these interpolated data sets can be directly compared, point by point. To obtain representations as the one shown in Fig. 2.18 (c), the data sets have to be previously transformed to cilindrical coordinates. The position of the origin is critical. In the representation of corneal ablations a biconic fitting was performed to obtain the center of the ablation, which was used as origin of the cylindrical coordinates. The representation of Fig. 2.18 (c) can be used with or without previous interpolation of the poins. In rotationally symetrical ablations this representation provides a thin curve. In assymetrical surfaces, as the one shown in Fig. 2.18 (c), a wide region of scattered poins appears.
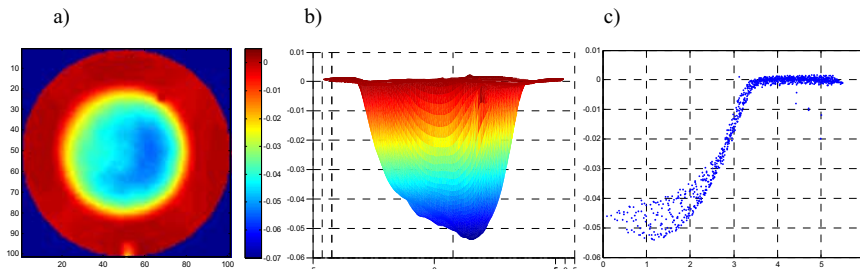
Fig. 2. 18. Different representations of the surfaces used in this thesis. a) Colormap of elevations. b) Three-dimensional map. C) Radial profile.

2.2.2.5. Operating with surfaces

Calculations are performed on the measured surfaces in different chapters of this thesis, to estimate physical effects or to obtain different predictions. For example, in Chapters 3 and 5 efficiency effects are calculated by comparing ablation maps. Also, theoretical calculations of efficiency effects are applied to ablation patterns in flat surfaces to predict the ablation shape in curved surfaces, or measurements in plastic are used to predict the outcomes in corneal tissue. In Chapter 8 the thickness map of contact lenses is calculated by substracting their base surface, alond the redial

direction. These calculations, performed on interpolated ablation maps, will be described in the corresponding chapters.

2.3. MEASUREMENT OF OPTICAL QUALITY

Estimates of optical quality in this thesis are based on measurements of corneal aberration, obtained after processing corneal elevation maps (Section 2.1), and total eye aberrations measured with a Laser Ray Tracing device (Section 2.3.2). This Section will describe the numerical procedures to calculate corneal aberrations (Section 2.3.1), and the experimental and numerical procedures to obtain ocular aberrations (Section 2.3.2). The calculation of the Strehl ratio (a metric of optical quality used in this thesis) and the simulation of retinal images and is also described (2.3.3).

2.3.1. Corneal aberrations

There are three steps in evaluating corneal aberrations of the anterior corneal surface: 1) obtaining experimental corneal elevation; 2) representing the corneal surface from these data; 3) evaluating corneal aberrations from the corneal model surface. The corneal aberrations were obtained from videokeratoscopy and profilometry measurements in this thesis.

2.3.1.1. Representing the corneal surface

Corneal surface representation is limited by the distribution of videokeratoscopic data. As this distribution is not uniformly spatially sampled in XY coordinates, with no data between rings, and especially within the central clear zone (around 0.4 mm radius), strategies based on local interpolations do not work properly. In general, a smooth global interpolation by polynomial expansion offers better results. Considering the circular symmetry of the data, the Zernike polynomial expansion appears to be a good choice (Schwiegerling et al., 1995). We fitted corneal surfaces with a Zernike polynomial expansion using 37 terms, and a standard least squares optimization by means of the inverse matrix built-in function given in Matlab. Once the surface is modelled by Zernike polynomial expansion, discrete points are evaluated in a XY equi-space grid to be introduced in an optical design program, Zemax V.9 (Focus Software, Tucson, AZ) for the corneal ray tracing evaluation.

2.3.1.2. From corneal surface to corneal wave aberration

The technique used in this thesis for the estimation of the corneal wave aberration is based on the work by Barbero and colleagues (Barbero et al., 2002b, Barbero et al., 2002c). It is based on calculations of the exact difference of the ray path between two points in the real and ideal wavefront for each pupil coordinate. The surface in a XY equi-space grid is introduced in Zemax, using a finite difference method to evaluate the normals to the surface –necessary to apply Snell's law-. The exact virtual ray tracing through the corneal surface is performed setting the index of refraction to that of the aqueous humor (1.3315). The wavelength was usually set to that used in the LRT measurement. Mean corneal Zernike coefficient variability of naked human eyes in vivo measured with Placido disk videokeratoscopy is 0.015 μm (averaged across terms). The technique has been validated and extensively used in previous work in the Visual Optics and Biophotonics laboratory (Barbero et al., 2002b, Barbero et al., 2002c, Marcos et al., 2007), as described in Sergio Barbero's Thesis (Barbero, 2004).

Several routines for processing corneal surfaces, available in the laboratory from those works, was used during this thesis.

For the purposes of this thesis, we will refer to "first surface aberrations" and "corneal aberrations" synonymously. This term will refer to the anterior corneal aberrations for naked eyes, aberrations of the artificial cornea in artificial eye measurements or the aberrations of the anterior surface of the contact lens in eyes with fitted contact lenses. We therefore intentionally exclude from the "corneal aberrations" the effect of the posterior surface of the cornea, the effect of the anterior cornea of the eye behind a contact lens or the effect of a tear lens between a contact lens and the cornea (that will be considered part of the "internal aberrations" of the eye).

2.3.2. Ocular aberrations: Laser Ray Tracing

The experimental measurements of ocular aberrations in this thesis were performed using Laser Ray Tracing (LRT) technique. This technique is well suited for the measurement of eyes post-ablation (due to its high dynamic range that allows successful measurements of highly aberrated eyes) and eyes with contact lenses (especially for soft multifocal contact lenses as, besides the extended dynamic range, it has flexibility in the configuration of the sampling pattern).

In brief, a set of parallel laser pencils samples the eye's pupil, by means of a scanning system (using different sampling patterns). Aerial images of the retinal spots corresponding to different entry pupils are collected sequentially onto a cooled CCD camera. The centroids of the set of aerial images are computed. The deviations of the centroids from the principal ray are proportional to the derivatives of the wave aberrations. The wave aberration is obtained by fitting the derivatives to a Zernike polynomial expansion (up to the 7th order) using a least-mean-squares procedure. All measurements were made foveally (the subject was asked to fixate a stimulus). A CCD camera centered at the optical axis of the instrument was used to monitor and center the pupil and also to monitor possible shifts of the contact lens, were present. Subjects were stabilized by means of headrest and dental impression attached to a three-dimensional positioning system. A near infrared laser diode (786 nm) was normally used as a light source. Light exposure was at least two orders of magnitude below safety limits.

2.3.2.1. LRT basic concepts

The LRT technique was first proposed in 1993 (Penney et al., 1993) and it was applied to measure ocular aberrations in human eyes in 1997 (Navarro and Losada, 1997, Molebny et al., 1997). A deeper description of the method can be found at Moreno-Barriuso's thesis (Moreno-Barriuso, 2000).

This is a double pass technique, since light is delivered into the eye and the reflection from the retina is captured on a CCD camera (Fig. 2. 19). In the first pass the pupil of the eye is sequentially sampled with laser pencils parallel to the optical axis. Each ray is deflected by a specific angle α depending on the slope of the wavefront at that particular point on the pupil plane (defined by the optical characteristics of the surfaces it goes through), and therefore will impact the retina at a specific point. In an aberration-free system, all rays superimpose on the same retinal location. However, when optical aberrations are present the rays hit the retina at different positions. In the second pass the light is reflected off the retina, exiting the

eye through the whole pupil, and forming an aerial image of the double-pass (or one-and-a-half-pass) point spread function (PSF) on a plane conjugated with the retina, but tilted an angle α from the chief ray (entering the eye through the pupil center). This angle α is proportional to the slope of the wavefront at the point where the incoming beam entered the eye. This image is collected by a high resolution cooled CCD camera. Although in this second pass the aberrations of the eye affect the PSF, its position relative to the reference is not affected (as long as the PSF is contained within the isoplanatic area of the retina). Therefore, the angles are preserved, and the ray (transverse) aberration can be computed from the distance between the position (centroid) of the aerial image corresponding to each pupil location, and that corresponding to the aerial image for the reference ray (chief ray). The sampled pupil size is defined by the diameter of the sampling pattern projected on the pupil, and therefore, can be controlled by software (as long as the eye pupil is at least of the same diameter to be programmed).

The reconstruction of the wavefront from the slopes of the wavefront measured at each point is performed as explained in Section 1.4.5.1. of the Introduction.
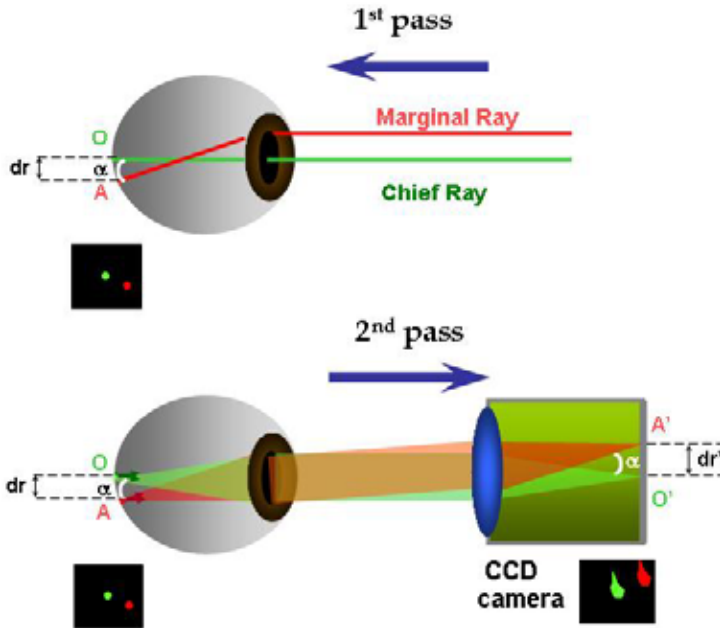
Fig. 2. 19. Laser Ray Tracing Technique. Modified from an original diagram by S. Marcos and E. Moreno-Barriuso. In the 1st pass (left) rays are deviated due to the aberrations, in the 2nd pass (right) light reflected off the retina exits the eye through the whole pupil and is recorded by a CCD camera. O and A indicate the position where the chief and marginal rays strike the retina, respectively, separated an angle α. O' and A' indicate the position (centroids) of the aerial images corresponding to the chief and marginal rays, respectively, collected by the CCD camera. These are separated an angle α in the CCD.

2.3.2.2. LRT evolution

Two different LRT devices, both built at the Instituto de Óptica, Madrid (Spain), were used to measure ocular aberrations in this thesis. The first device (LRT1) was built by Esther Moreno during her thesis (Moreno-Barriuso and Navarro, 2000, Moreno-Barriuso et al., 2001a, Moreno-Barriuso et al., 2001b, Navarro et al., 1998), with help from the author of this thesis, especially in the data processing and calibrations. Extensive validation of this instrument has been presented including comparison with other aberration measurement techniques, such as Hartmann-Shack and the Spatially Resolved Refractometer (Moreno-Barriuso and Navarro, 2000, Moreno-Barriuso et al., 2001a, Llorente et al., 2003, Marcos et al., 2002). This device was used in the work presented in Chapter 9. The second device (LRT2), which will be described briefly in the next section, was developed at the first stages of this thesis, with a high number of improvements over LRT1, and used in the work presented in Chapters 8 and 10. LRT2 incorporates some additional features specially advantageous for measurements in ametropic eyes (Dorronsoro et al., 2003a, Llorente et al., 2004b). The most important advantages of LRT2 over LRT1 are: 1) the use of infrared light in addition to visible green light; 2) increase of the speed to less than 1.5 seconds for an entire typical run; 3) continuous display of pupil images during the measurement and simultaneous recording of pupillary and retinal aerial images; 3) easy selection of the pupil sampling density and pattern by software; 4) fully automated control software; 5) compact and lighter instrument; 6) the possibility to correct large amounts of spherical defocus continuously by means of a Badal system (see Section 2.3.2.3 of this chapter); 7) the presence of a plane conjugate to the pupil plane, where trial lenses can be placed, without altering pupil and retinal magnification; 8) a channel for dynamic projection of visual stimuli; 9) the recording on pupilary images during the measurement (and synchronized with the retinal images) allows for passive eye-tracking correction of head and eye movements.

2.3.2.3. LRT Experimental setup

A schematic diagram of the LRT2 set-up is shown in Fig. 2. 20, a photograph from above in Fig. 2. 21, and an overview (with patient) in Fig. 2. 22. The system consists of 4 channels; 1) Illumination channel, with two possible light sources (green 532-nm or infrared 785nm laser diodes), focused on x-y scanner, and then collimated by the lens L3 in order to compose the desired sampling pattern on the pupil plane. 2) Retinal imaging channel, where the light reflected back from the retina is captured by the retinal CCD. 3) Pupil monitoring channel, where the pupil CCD captures the corresponding image of the eye's pupil, simultaneously with the retinal spots on the retinal CCD; 4) Fixation channel, where a target is displayed on a CRT monitor during the measurement. All channels share a Badal system, for compensation of defocus, formed by lenses L1 and L2 and mirrors M1, M2 and M3. P marks the position of a pupil conjugate planes, and R marks the position of retinal conjugate planes.

The light source can be selected between two diode lasers emitting in green (532 nm; Brimrose, Baltimore, USA) and IR wavelengths (785 nm; Schäfter + Kirchhoff, Hamburg, Germany). Prior to the systematic use of infrared wavelength in the measurements, we confirmed the equivalence of infrared and green light in the measurement of ocular aberrations (Llorente et al., 2001). Both lasers are attenuated below safety limits using neutral density filters: the maximum permitted exposure

(1993) power thresholds for 532 nm and 785 nm were 6.9 µw and 7.6 µm respectively. We used at least three ND4 neutral density filters to attenuate the power down to 4.1 µw and 6.8 µw, and more filters were added when possible/necessary. Exposure times (about 1.5 seconds for a typical run with 37 samples) are controlled by an electronic shutter (Vincent Associates, Rochester NY, USA).
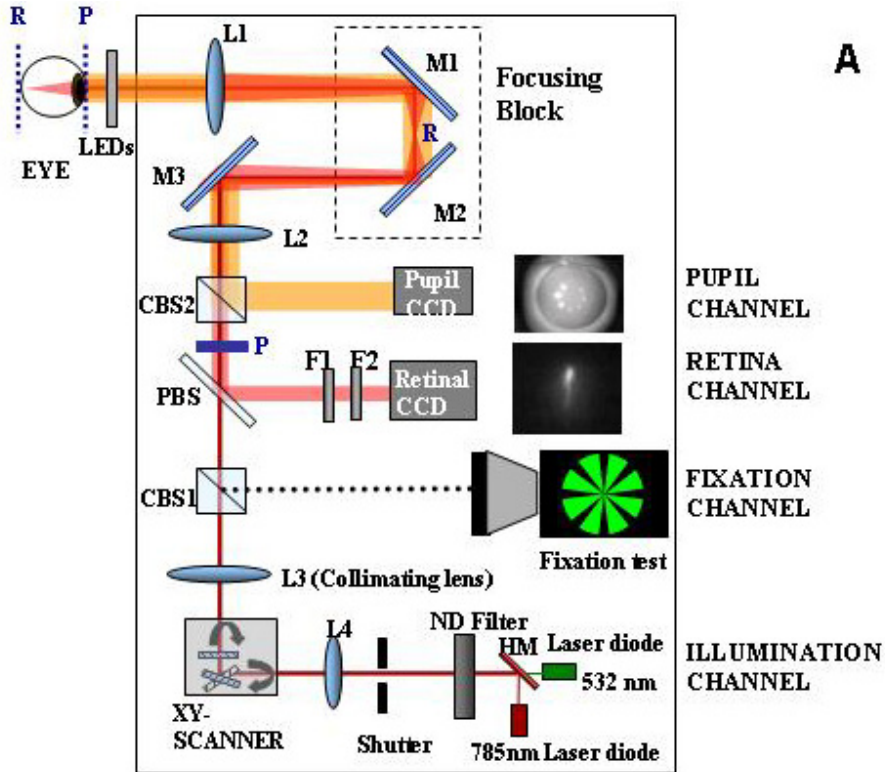
Fig. 2. 20. Schematic diagram of the LRT2 setup described in the text. L1 and L2 are 100-mm focal length lenses, and L3 and L4 are 50.8-mm focal length lenses, M1, M2, and M3 are plane mirrors, HM is a hot mirror, CBS1 and CBS2 are cube beam splitters, PBS is a pellicle beam splitter, F1 and F2 are interferometric filters for 785 and 532 nm, respectively, and P and R are planes conjugate to the pupil and the retina, respectively.

The XY scanner (mod.6210, Cambridge technologies, Lexington, USA), consists of two rotating mirrors that deflect the incoming unexpanded laser pencil in such a way that in combination with collimating lens L3 (f'=50.8 mm) compose the sequential sampling pattern. Due to the distance between the two mirrors (~5 mm), some astigmatism is induced in the system (Navarro and Moreno-Barriuso, 1999), and therefore a trial lens attached to the collimating lens (+2.50 at 0º) is used to correct this astigmatism (see Section 2.3.2.7). Lens L4 (f'=50.8 mm) forms the image of the laser waist on the scanner in order to obtain the smallest sampling aperture on the pupil plane (~400 µm). The flexibility provided by the scanner to configure sampling patterns with different distributions and densities of the samples was essential for the

study on contact lenses. The sampling patterns used in Chapters 8 and 10 were adapted to the geometry of the multifocal designs of the contact lenses.
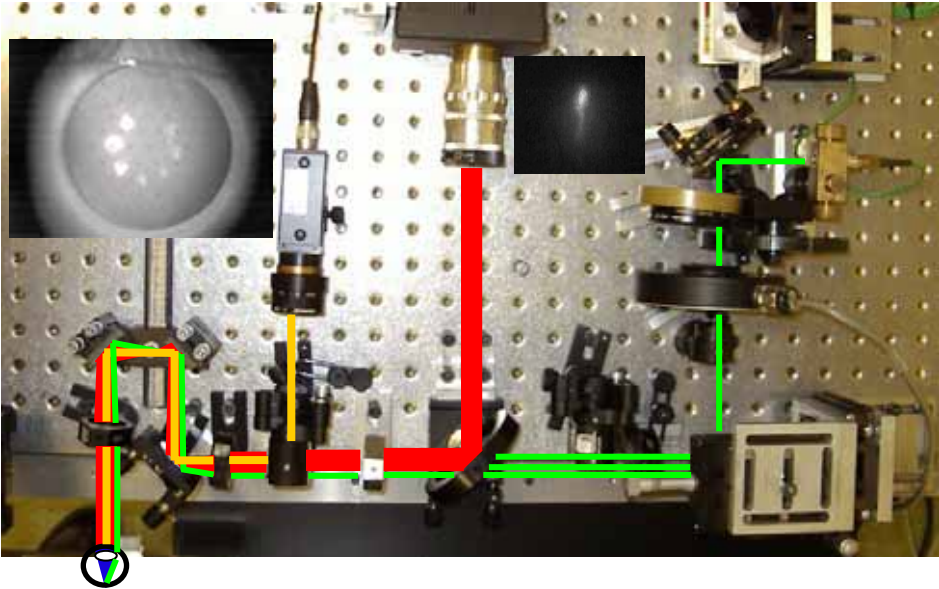
Fig. 2. 21. Photograph of the LRT2 setup from above. The input channel is shown in green, the pupil channel in orange, and the retinal channel in red. The laser scanner is not visible from above. Examples of pupil images, in which the software superimposes the sampling pattern, and retinal images, are also shown.

The light reflected off the retina is collected by a cooled highly sensitive CCD camera (12 bits, 30 frames per second with 2x2 binning, 1024x1024 pixels, pixel size: 14 μmx14 μm, nominal maximum quantum efficiency: 20% (700 nm); model 1M15 by Dalsa, Waterloo, Canada), conjugate to the eye retinal plane (retinal channel). In addition to record aerial images, this camera can display them in real time. This allows to find objectively the best focus position while assessing the aerial image for a centred ray. During the measurement, the retinal camera is synchronised with the scanner and the pupil camera.

In the pupil channel a CCD (8 bits, 60Hz (video), 646 (horizontal) x 485(vertical) pxls, pixel size: 7.4μm x 7.4μm; model XC-55 by Sony Corp., Tokyo, Japan) continually monitors the pupil and records pupil images during the measurement. Pupil monitoring prior to the measurement helps to verify that everything is ready for the measurement, assisted by marks superimposed on the pupil image in the control program (see Fig. 2. 23): pupil located on the corresponding plane (pupil edges focused), alignment of the center of the pupil and the optical system (centration cross), suitability of the sampling pattern to the pupil diameter (small circumferences for samples entry locations and circumferences of different diameters to estimate pupil size).

Pupil monitoring during the measurement allows to verify that no anomalies, such as blinking, contact lens movements on the eye, large eye movements, tear problems, etc, occurred and to ensure the eye's stability. Five IR LEDs (peak wavelength 880±80 nm) arranged in a circular frame in front of the eye illuminate the pupil during the

alignment (frontal-illumination), and provided enough contrast to appreciate the contact lens position on the eye. In addition, back-illumination is also possible when only the measurement light is used, and has proved to be very useful to visualize some features, such as tear film break up. Recorded images can also be used for passive eye-tracking (see Section 2.3.2.6), i.e. post-measurement correction on the pupil sampling coordinates when the eye moved during the measurement.
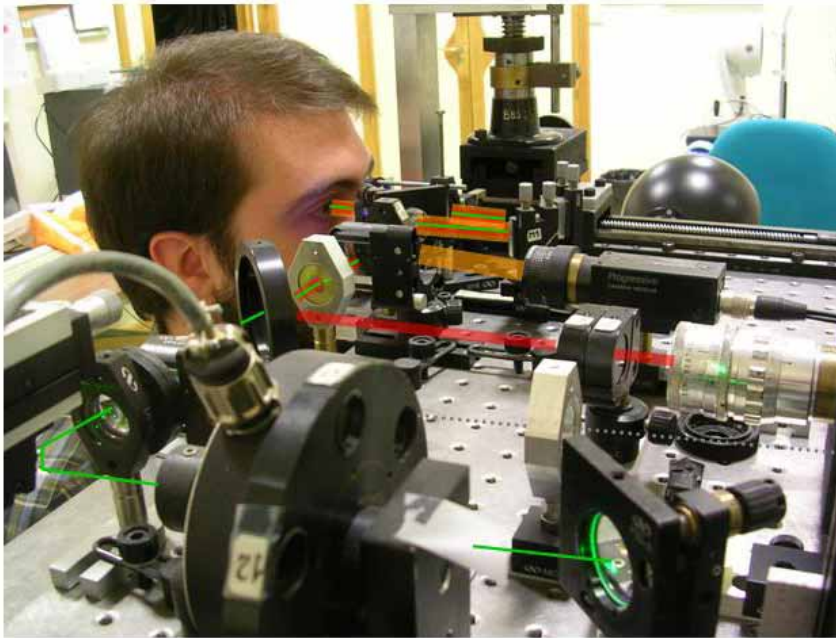
Fig. 2. 22. Detail of the actual system during a measurement on a subject (Llorente, 2009).

Recordings of a typical run can be seen at (Llorente et al., 2004b) http://www.journalofvision.org/4/4/5/article.aspx#Movie1, where the left side shows a video of the pupil (front-illuminated) as the entry beam scans discrete locations of the pupil, with the entry point of the ray marked with a circle, and the right side shows the set of corresponding retinal aerial images as the beam moves across the pupil. Fig. 2. 24 shows a frame of the movie.

The subjects were stabilized by means of a dental impression and a forehead rest. A 15" CRT monitor (Sony Corp., Tokyo, Japan) is used to project stimuli to help the subject keep his/her eye fixed along the optical axis of the system, and under relaxed accommodation during the measurement. The fixation test, consisting of a green circle with black radial lines thickening towards the periphery (see fixation test in Fig. 2. 20), can be used to assess subjectively the refractive state of the subject's eye to be measured.

Finally, defocus correction in the system is carried out by a Badal system (Smith and Atchison, 1997), which allows to change the vergence of the rays (and hence defocus) without changing magnification, and therefore ensuring that the pupil magnification or the sampling density will not be affected by defocus correction. Our

Badal system shares path with the different channels of the setup (See Fig. 2. 20 and Fig. 2. 21), so that defocus is corrected in the illumination, imaging and fixation channels as well as the pupil monitoring channel. It is composed by two achromatic doublets (L1 & L2) of equal focal lengths (100 mm), that form an afocal system of magnification X1, and three flat mirrors: M3, which bends the optical path to obtain a more compact device, and M1 and M2, which can be moved as a block (Focusing Block) to change the optical path between the lenses, and consequently the dioptric correction. Moving the mirrors instead of the lenses has the advantage of not displacing the optical planes of the system. Spherical error corrections ranging from -5.50 D to +13 D can be induced with this system. Furthermore, easy access to pupil conjugate plane (P) allows positioning trial lenses when a higher dioptric correction is needed.
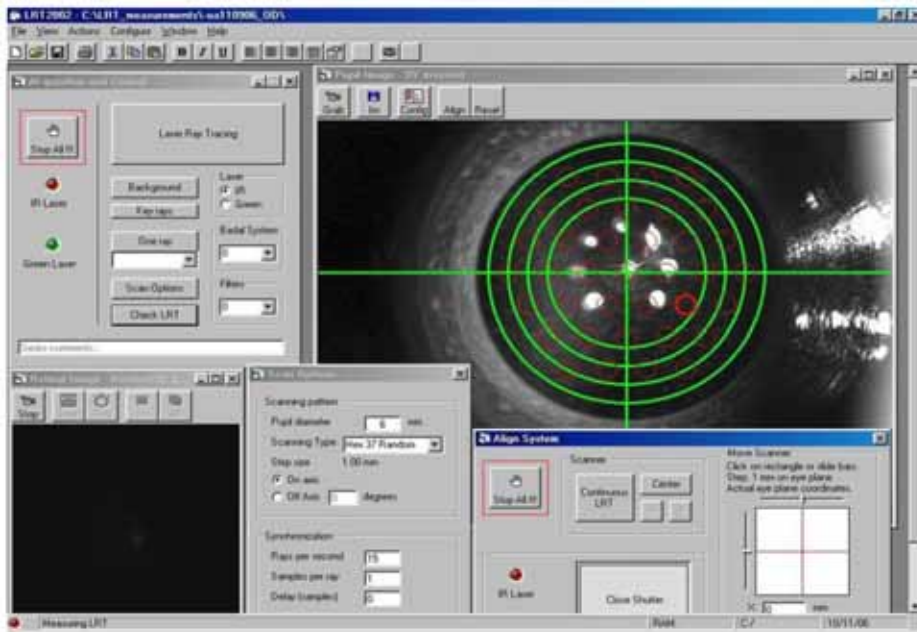
Fig. 2. 23. Snapshot of the control program developed in this thesis for LRT2, where the pupil (top right) and retin (botton left) images can be seen.

2.3.2.4. LRT control software

The software development was aimed at an intuitive and user-friendly, control program. The interface was written in Visual Basic (Microsoft Corp., USA), combined with Matlab (Matlab; Mathworks, Natik, MA) scripts. The data structure was organized so that data interchange between programs, such as control and processing software, was efficient, and tracking error sources was straightforward. The next subsections describe the control software, and processing software for retinal and pupil images software. The software was developed by the author of this thesis with the help of Lourdes Llorente (contributing suggestions and recommendations, testing and debugging).
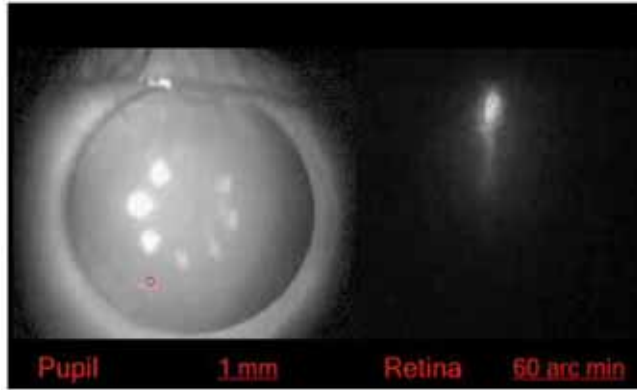
Fig. 2. 24. Example frame from pupil and retinal cameras. The left image shows a frame of the (front-illuminated) pupil, with the entry point of the ray marked with a circle, and the right image shows the corresponding retinal aerial image. Both images (Llorente et al., 2004b) belong to a frame of the movie that can be found at http://www.journalofvision.org/4/4/5/article.aspx#Movie1, showing recordings of a typical run with LRT2.

A completely new control software was created for the new LRT2 set-up, with some improvements that made the measurements faster (about 1.5 seconds versus 4 seconds for the former LRT1, for 37 samples), and therefore more comfortable for the patient. Real time pupil monitoring allowed discarding measurements on-line, and immediately running a new series.

Fig. 2. 25. Snapshot of the measurement reports automatically generated by the software, that serve as laboratory notebook.

The system control software operates and synchronizes the different elements (scanner, shutter and cameras) for the measurement, assisting in some other operations such as aligning the pupil and the optical system, with a user's friendly interface. All the useful data such as measurement (dates and times, sampling pattern, pupil size, etc) calibration parameters, or measurement condition (with or without contact lens, for example) are saved in a structured way using excel files that can be used as reports for the measurements (See Fig. 2. 25). All the actions performed (by the operator or by the different components of the software), and the result (successful or not, files involved) are recorded in a log file. This log file can be used as a backup laboratory book to retrospectively track all the measurement session, to improve the data analysis.

Fig. 2. 23 shows a snapshot of the control program. The form "Acquisition and Control" allows to set the measurement parameters as well as to start the measurement itself. The sampling pattern (scanned pupil diameter, sampling arrangement and density) can be easily changed. This feature has been very useful for measuring contact lenses, with annular designs. The forms "Pupil Image" and "Retinal Image" allow the visualization of the images corresponding to each camera in real time. This feature is not only useful for the measurements themselves, but also for calibration and alignment purposes.

The software also includes a routine, "Test LRT" that allows to verify the correct alignment of the laser beam as well as the correct delivery of the programmed pattern on the pupil. When "Test LRT" is clicked, a series of circumferences indicating the nominal position of the samples and a centration cross appear superimposed to the pupil image (see Image pupil frame in Fig. 2. 23. Simultaneously the shutter opens and the scanner starts to scan the programmed sampling pattern. If we place a screen on the pupil plane, the scanning spot will be visible with the circles superimposed. A thicker circumference indicates the nominal position for the corresponding sample, so that for a correct sampling, the laser spot should lay in the centre of that circle. If we stop the scanner and select the central position for the beam, we can verify that the spot is overlapped with the centration cross.

2.3.2.5. Processing Software for retinal images (ocular aberrations)

The software to estimate the ocular aberrations from the set of aerial images was profoundly improved from its original LRT1 version in order to make the computation of aberrations easier, quicker, more robust and efficient, with better quality and traceability of errors or detection of problems, and adapted to the new set-up parameters and possibilities. The contribution of the author of this thesis in this software, in collaboration with Lourdes Llorente, includes: the design of the new data structure; support in the writing of the new Matlab code; support in testing and debugging of the software; Visual Basic interface. Some specific improvements in the software include:

1) Calculation of the processing parameters based on the conditions of the experiment and included in the corresponding calibration data file;

2) Adaptation to the new data structure defined by the control software: input data were read from the files created during the measurements, and structured result files were created for the output data;

3) Organization of the program as a modular structure to allow for a Visual Basic interface, more efficient for the processing and more user-friendly;

4) New image processing tools: possibility of choosing different processing parameters (thresholds, Zernike order to fit), as well as using default values; manual selection of the Region of Interest or of the images to exclude from the processing when necessary; possibility of undoing the last change; on-line visualization of parameters significant for the processing such as maximum intensity of the images or spot diagram (joint plot of the centroids of the images already processed).

5) A graphic as well as numeric presentation of the results that allows easy detection of series that do not follow the common trend or do not have the same measurement conditions as the rest of the series of the same session. The results file also includes a worksheet were corneal aberrations are saved when available, in order to summarize all the related results in one file.
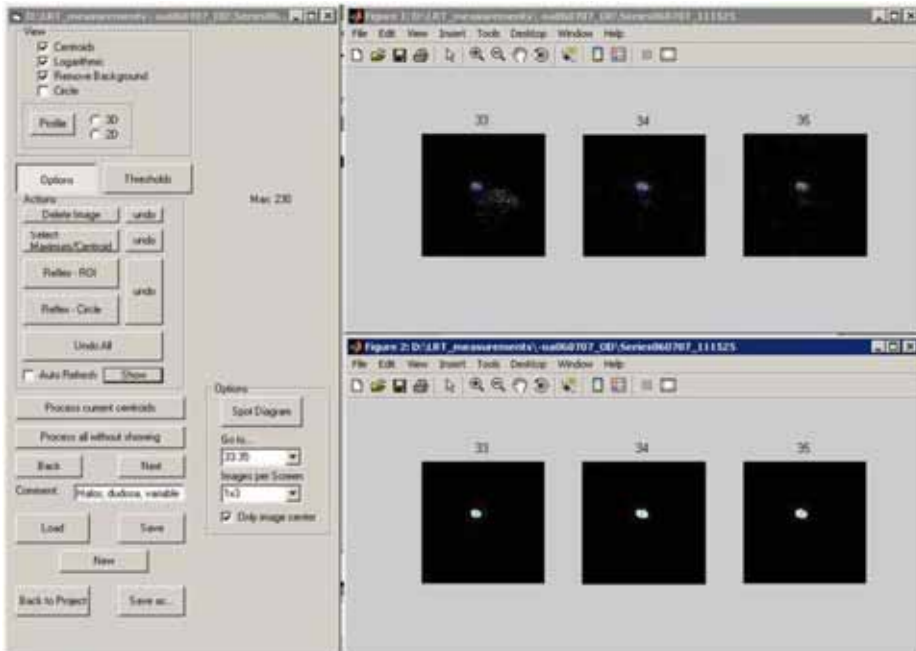
Fig. 2. 26. Snapshot of the processing software interface showing some images before (top row) and after (botton row) processing.

A snapshot of the processing software interface is shown in Fig. 2. 26. Basically, raw images are processed (background subtraction, filters and masks application, thresholds setting, etc) in order to isolate each aerial image and locate the corresponding centroid (Fig. 2. 27). Then, the relative distance of each centroid to that of the central ray is calculated (transverse aberration), and the wave aberration is then estimated by fitting the transverse aberration corresponding to each sampled point to the derivatives of the Zernike polynomials, using a least squares method (Cubalchini, 1979). The interface (Fig. 2. 26) allows the user to visualize the raw images, select the next processing to apply to the image and check the image appearance after processing has been applied, with the corresponding centroid position superimposed on the image. As previously mentioned, a joint plot with all the centroids positions (spot diagram) is also available. The program extracts the input data necessary for the wave

aberration estimation from the corresponding excel file stored during the measurement, and saves the results in a new excel file in the corresponding project folder.
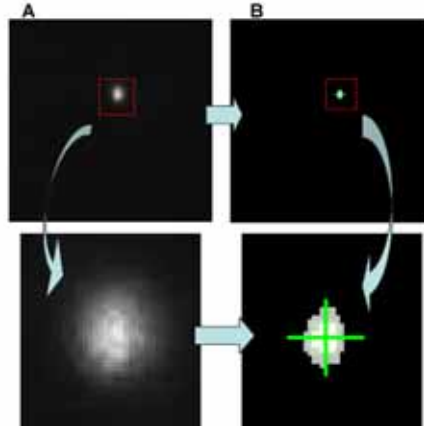
Fig. 2. 27. Detail of the centroid processing. (a) Raw Image corresponding to a recorded aerial image. (b) Processed image: background subtraction, filtering and thresholding. Botton row: zoomed images. The centroids are computed as an intensity mass center (green cross). (From Sergio Barbero's Thesis (Barbero, 2004)).

2.3.2.6. Pupil images (passive eye- and lens-tracking)

The system, saving pupil images during the measurement and synchronized with the retinal images allows for a new functionality in LRT measurements: passive eye-tracking. The edges of the pupil can be detected to estimate the exact pupil position at each frame. Then, the corrected entrance position of the ray can be considered in the wave aberration retrieval algorithms to retrieve a more accurate wave aberration measurement.

Fig. 2. 28 shows two examples of corrected entrance positions of a patient with important eye movements (a) and a patient with normal eye movements (b). The hardware needed was set-up and the acquisition software developed during this thesis. First, a preliminary version was tested in LRT1 and then a fully functional and synchonized version was incorporated in LRT2. Pupil images served to reject retinal images (subject to eye motion artefacts or occlusion). Further developments of the pupil image analysis in the LRT2 system by Lourdes Llorente, have allowed automatic detection of the pupil edge, and therefore to compensate for potential eye movements in the measurements (Llorente, 2009, Llorente et al., 2007).

The stored pupillary images also helped in the analysis of LRT measurements with contact lenses, as they allowed to estimate the lens position, relative to the pupil position, at each frame, as will be described in Chapter 9.

2.3.2.7. System Calibration

In this section the calibration procedure of the different elements of the system, and the validation of the measurements provided will be described. Additional descriptions can be found in Lourdes Llorente's thesis (Llorente, 2009).
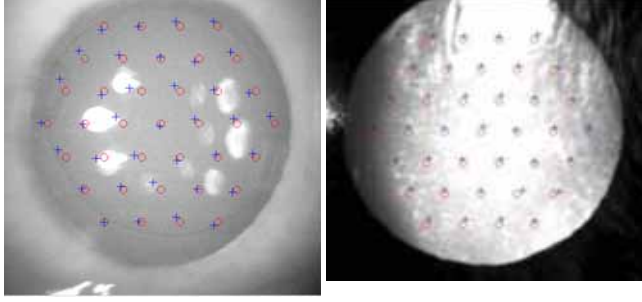
Fig. 2. 28. Corrected entrance positions in LRT measurements (passive eye-tracker based on recorded pupil images). (a) Patient with important eye movements. Pupil illuminated by LEDs. (b) Patient with normal eye movements. Pupil retroilluminated.

Two parameters (offset and slope) driving each scanner response to digital signals were set up, in order to use image plane coordinates instead of electrical voltages. The offset was chosen to obtain a laser beam aligned with the optical axis of the setup when coordinates (0, 0) were selected. Regarding the slope, or ratio scanner voltage/laser displacement, it was selected to obtain the displacement of the laser spot necessary to obtain the desired pattern. For this purpose, a screen with a square grid pattern (1 mm squares) was placed at the pupil plane with the shutter open to see both the spot and the grid. The ratio scanner voltage/laser displacement was calculated as one tenth of the voltage needed to move 10 mm the laser spot impacting on the screen (as observed by the camera) and taking the grid as a reference.

The equivalence between pixels and deviation angles in the retinal camera images was determined by imaging a metal calliper in a plane conjugate to the sensor, i.e. at the focal point of lens L2 (Fig. 2. 20). We obtained that each pixel in the image subtends 0.37 mrad. This value is used in the processing program to compute transverse ray aberration from the deviations of the spots in the CCD.

The pupil camera is used to ensure alignment of the eye pupil with the optical axis of the system, to visualize the sampling pattern superimposed to the pupil, and to assess distances, such as the pupil diameter or pupil misalignment. We ensured that the centration reference (green cross in Fig. 2. 20) is superimposed with the optical axis, by placing a screen at the pupil position and imaging a laser beam with the scanner is in its centered position. The position of the spot in the image is calibrated as the instrument axis. We calibrated the scale (equivalence between pixels and millimetres at the pupil plane of the camera) by imaging a graph paper screen. We obtained a correspondence of 43 pixels/mm.

As previously mentioned, some astigmatism is induced by the scanner due to the distance between its two rotating mirrors. The theoretical astigmatism induced due to the distance between the mirrors of the scanner, d=4.9 mm, depends also on the focal length of the collimating lens used, f'=50.8 mm, and in this case is:

$$Ast\ scanner = \frac{d}{(f'+d/2)(f'-d/2)} = 1.88D \qquad (2.2)$$

Some astigmatism can also be introduced by other elements of the set-up, such as lenses not completely perpendicular to the optical axis. A cylindrical trial lens of

+2.50 D, placed right after the collimation lens of the scanner, with its axis perpendicular to the line joining the mirrors of the scanner (axis at 0º), minimized the astigmatism. We then estimated the residual astigmatism by measuring the aberrations of an unaberrated artificial eye. We computed the value of the astigmatism from the coefficients Z_2^{-2} and Z_2^2 (oblique and perpendicular astigmatism, respectively) using the equation:

$$Astigmatism(D) = \frac{4\sqrt{\left(Z_2^{-2}\sqrt{6}\right)^2 + \left(Z_2^2\sqrt{6}\right)^2}}{R_{pupil}} \tag{2.3}$$

where R_{pupil} is the radius of the measured pupil. We obtained a value of 0.18±0.03 D (mean and std across 5 measurements). This value (through the corresponding Zernike coefficients) was subtracted from the astigmatism obtained in the measurements.

We verified that the sampling pattern selected using the control software was precisely delivered, by projecting the beams on a screen at the pupilary plane and analyzing the images captured by the pupul camera. The mean deviation from the expected position (±standard deviation) across all 37 spot positions was 0.05 (±0.04) mm; 0.08 (±0.05) mm and 0.03 (±0.02) mm for X and Y coordinates, respectively. These differences are smaller than those typically resulting in real eye measurements due to eye movements, and below the variability of the measurement. We checked that these differences do not affect significantly the estimation of aberrations in real eyes (Llorente et al., 2007).
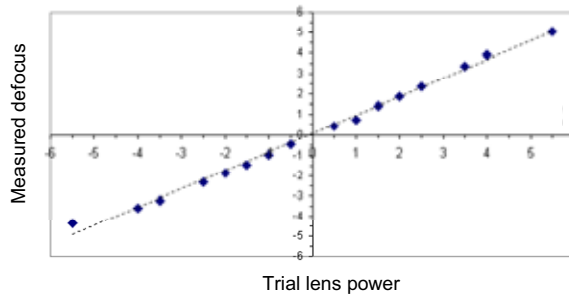
Fig. 2. 29. Validation of the defocus compensation.

The correct delivery of the samples on the pupil plane is crucial to obtain a reliable measurement. For this reason, a routine to perform quick real time verification of the pattern sampling the pupil plane ("test LRT") was included in the control software (see Section 2.3.2.4). This routine involves a real-time test of the position of the actual laser spot locations, which must fall within the red circles plotted in the pupillary images (see Fig 2.23), corresponding to the exact sampling locations.

Finally, to make sure that the processing program was correct, we confirmed that when computing transverse ray aberrations from the wave aberration (obtained after processing the experimental data), the corresponding spot diagram positions computed matched the spot diagram obtained experimentally.

The Badal system included in the set up to compensate for the subject's ametropic error was also calibrated. Moving the translational stage with two mirrors (Focusing Block) introduces a change in vergence that, for a focal length of 100 mm for each

Badal lens, corresponds to 0.2 D/mm (one dioptre each 5 millimeters). The 0 D position in the focusing block scale was determined using a non aberrated emetropic artificial eye. Trial lenses in front of the artificial eye were used to check the compensation of defocus by the focusing block (Fig. 2. 29). First, we checked by direct observation the change in the spot diagram dispersion when the focusing block was displaced. The final check was performed with the defocus term of the aberration pattern measured.

2.3.2.8. Optical aberrations introduced by the system

In order to discard that geometrical aberrations were being introduced by the system, we measured the aberrations of the nominally aberration-free artificial eye. For 3rd and higher order aberrations we obtained that the RMS departure of the wavefront from the reference sphere was much less than $\lambda/14$ (Marèchal's criterion (Born and Wolf, 1993)). For 2nd order aberrations (defocus and astigmatism), the residual values will be subtracted to the measured values. Therefore, we can consider the system is sufficiently corrected for the purposes of measuring human eyes.

Absence of chromatic aberration in LRT1 had been verified by measuring the aberrations of a phase plate (Navarro et al., 2000) in front of an artificial eye, using 543 nm and 783 nm as test wavelengths. The difference in defocus obtained with both wavelengths was 0.04D. Similarly, for LRT2 optical aberrations of an artificial eye were measured using infrared wavelength (785nm), under the same conditions (defocus correction, artificial eye position) we used for a wavelength of 532 nm. The difference between the values of defocus for both wavelengths was 0.12 D.

2.3.2.9. Validation of the aberration measurements

Measurements of wave aberrations from the systems LRT2 were validated by: 1) measuring cylindrical lenses of known power; 2) measuring phase plates of known aberrations; 3) measurements in plastic artificial eyes of known aberrations (Campbell, 2005), 4) comparing measurements on real eyes also measured with Hartmann-Shack aberrometers. More information can be found in Lourdes Llorente's (Llorente, 2009) and Elena G. de la Cera's Thesis (García de la Cera, 2008).

2.3.3. Simulations of retinal images

Retinal images were simulated from the results of optical quality (objective) measurements. Simulated retinal visual acuity charts were normally compared to the (subjective) measurements of visual perfomance, described in Section 2.4.

Point Spread Functions (PSFs) were obtained from the Zernike polinomial expansions. We performed the 2-dimensional Fourier Transform of the circular pupil function containing the wave aberration function (Atchison and Smith, 2000). In through focus simulations the Zernike defocus coefficient was changed accordingly. The Stiles Crawford function was not considered. From the PSFs we also calculated the Strehl ratio. The retinal images of visual acuity charts were simulated by two-dimensional image convolution.

2.4. MEASUREMENT OF VISUAL PERFORMANCE

The optical bench described in (Rosales and Marcos, 2006) was used and adapted to perform psychophysical measurements of visual acuity (Fig. 2. 30). The stimuli were presented on high resolution and high brightness minidisplay (LiteEye) through a

Badal system (that changes vergence at the pupil, i.e. thru-focus position, without affecting the magnification). This system, developed for Purkinje-image based phakometric/lens tilt and decentration measurements, was used, instead of the LRT2 psychophysical channel to achieve higher target luminances (as the target is subject to less losses by reflection and transmission through optical elements) and the availability of dynamic target which allowed full control of the psychophysical experiment.
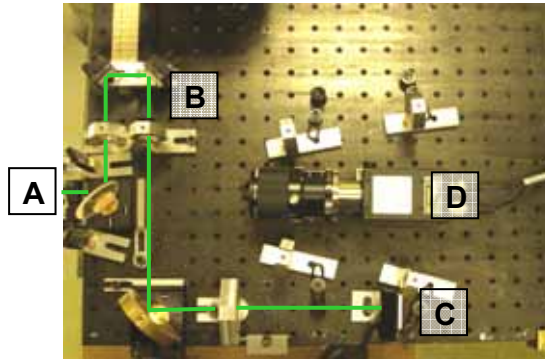
Fig. 2. 30. Optical bench used for the VA measurements, adapted from (Rosales and Marcos, 2006). A) Eye. B) Badal System. C) SVGA Minidisplay. D) Camera for pupil monitorizacion

We used a four alternative forced choice psychophysical paradigm to measure visual acuity with high-contrast tumbling Snellen E letters. The thickness of the lines and gaps of the E letter were one-fifth of their total size. The subject was asked to identify the orientation of the letter that was displayed on the minidisplay (one out of the four possible orientations), pressing right, left, up, or down on the keyboard. A QUEST algorithm, implemented with Psychtoolbox (Brainard, 1997, Pelli, 1997) and Matlab, based on previous responses of the subject at each trial, was used for letter-size threshold estimation at each trial, and for suggesting the letter size for next trial. Each letter was presented for 0.5 seconds. A point fixation stimulus was shown between letters.
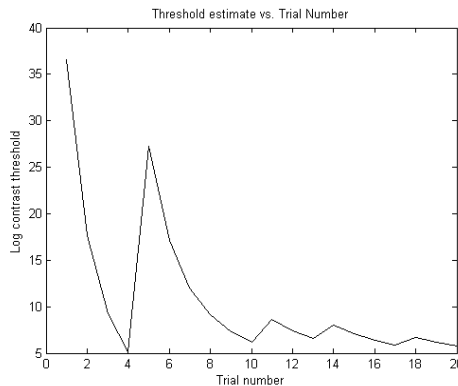
Fig. 2. 31. Detail of the typical evolution of the estimated threshold vs trial number. The final threshold is represented by a red line. In our experiments we used 30 trials.

Each VA measurement consisted of 30 trials (letters), with no feedback to the subject. The measurement was considered correct if there was a soft oscilating approah to the final threshold (Fig. 2. 31), and if the oscilation of the last 10 estimated thresholds was well below the oscilation of the size of the stimulus presented. Incorrect measurements, as assymptotic approaches to the final threshold or large oscilations, were repeated.

2.6. PROTOCOLS IN MEASUREMENTS ON SUBJECTS

The procedures involving subjects were reviewed and approved by Institutional Bio-ethical Committees of the Consejo Superior de Investigaciones Científicas, and Instituto de Oftalmobiología Aplicada (Universidad de Valladolid) and met the tenets of the Declaration of Helsinki.

All patients were fully informed and understood and signed an informed consent before enrolment in the study.

Measurements of the anterior and posterior corneal surface using the Scheimpflug Pentacam system were performed at the Instituto de Optica (CSIC) or IOBA (Valladolid) using the same instrument. Most of the aberration measurements presented in this thesis were performed under pupil dilation (with 1 drop tropicamide 1%). A complete measurement of the total wave aberration, including informed consent explanation, pupil dilation and dental impression fabrication took less than 45 minutes. In addition to total aberration and videokeratoscope other measurements were typically conducted on patients: Axial length and anterior chamber depth with an optical biometer based on Optical Coherence Tomography (IOL Master, Carl Zeiss, Germany), autorrefraction (Automatic Refractor Model 597, Humphrey-Zeiss), and slit lamp examination.

All subjects in the present thesis are selected patients from the Instituto de Oftalmobiología de Valladolid (IOBA) or normal volunteers. All participating subjects had a previous eye examination in a clinic.

§ 32. HYGIENE.—TREATMENT.—SPECTACLES.—ILLUSTRATIVE CASES.—HISTORY OF MYOPIA.

The cure of myopia belongs to the *pia vota*. The more our knowledge of the basis of this anomaly has been established, the more certainly does any expectation in that direction appear to be destroyed, even with respect to the future. So long as it was thought that the cause of myopia might be found in increased convexity of the cornea, the endeavour to restore the latter, by pressure, to its normal curvature (Purkinje* and Ruete) appeared perhaps not altogether to be rejected; but the idea, that the extended, attenuated, atrophic membranes in myopia, might be brought back to their natural condition is simply absurd. We should not even be able to approve of the practice of those, who, in order to compensate for the excessive length of the visual axis, endeavoured to bring the arching of the cornea below the normal. Systematic pressure is an excellent auxiliary in preventing a staphylomatous prominence of the cornea in morbid softening during the process of recovery; but, leaving out of the question, whether a healthy cornea would be affected by it, we should remember, that no more is to be expected from a compensating flattening than from a negative glass: the peculiar morbid process, on which the myopia depends, and which in high degrees threatens the destruction of the eye, would remain unchanged. Treatment is, alas, partly a matter of fashion. Thus discharging the aqueous humour from the anterior chamber of the eye, is now the order of the day. Some have even spoken of applying this method in myopia. If it be intended thereby to make the cornea flatter, the object will not be attained in this way, which is the less to be regretted, because, as I have already remarked, the myope would not be benefited by it: besides the paracentesis referred to is not always myotomists. Rendered rash by ignorance, some have actually employed their operation for the relief of myopia, and have even persuaded themselves that they had thus accomplished a cure. The truth is, that they in general subjected not myopic, but rather hypermetropic, eyes, which they mistook for myopic, to the operation, and that even in these the latter was ineffective.

F. C. DONDERS.

UTRECHT, *27th February*, 1864.

Chapter

3

Experimental prediction of post-refractive surgery corneal elevation using a PMMA corneal model

This chapter is based on the patent by Marcos et al. (Marcos et al., 2005) and in the article by Dorronsoro, C., et al. "Experiments on PMMA models to predict the impact of corneal refractive surgery on corneal shape", published in Optics Express, Vol. 14, Issue 13, pp. 6142-6156 (Dorronsoro et al., 2006a). The study was partially presented at ARVO in 2003 (Dorronsoro et al., 2003b) and 2006 (Dorronsoro et al., 2006c).

The contribution of Carlos Dorronsoro to the study, in collaboration with other coauthors, was the literature search, the design of the experiments, participating in the measurements, the development of the data analysis routines and the analysis itself.

Coauthors of the study are Daniel Cano, Jesús Merayo-Lloves and Susana Marcos.

3.1. ABSTRACT

Purpose: To measure the contribution of laser ablation efficiency changes across the cornea on post-operative corneal asphericity, using an experimental model cornea on PMMA (polymethyl-methacrilate).

Methods: Flat and spherical (8-mm radius of curvature) PMMA surfaces were ablated with a standard refractive surgery laser system for corneal myopic corrections of 3, 6, 9 and 12 D. Ablated surfaces were measured by profilometry (planes) and corneal topography (spheres). The ablation profile programmed on the laser system was obtained from the ablated flat surfaces, multiplied by a PMMA-corneal ablation rate factor. The ratio of profiles on flat to spherical PMMA surfaces was used to estimate experimentally the ablation efficiency factor, due to changes in laser efficiency from the center to the periphery of the spherical surface. The ablation efficiency factor for the PMMA was used to obtain experimental estimates of the ablation efficiency factor for the cornea, applying the Beer-Lambert's law and known ablation thresholds for PMMA and corneal tissue.

Results: Nominal ablation depth in cornea was 2.35 times the ablation depth in PMMA. Ablated PMMA spherical surfaces show a significant increase of asphericity (0.89 ± 0.73). The change in corneal asphericity after refractive surgery in real patients was compared to predictions from experimental estimates of the ablation pattern, with and without taking into account the experimental ablation efficiency factor (and the theoretical efficiency factor). We found that the actual corneal ablation patterns (as measured on flat surfaces) did not produce a significant change in asphericity (0.03 ± 0.49) while changes in ablation efficiency accounted for a significant part (1.39 ± 0.92) of the asphericity increase found clinically (1.97 ± 2.00), using the same laser system. Contribution of biomechanics to the increase of corneal asphericity in myopic refractive surgery can be estimated by comparisons with the predictions obtained from measurements on PMMA and the clinical outcomes.

Conclusions: We have obtained an experimental ablation efficiency factor, based on a PMMA corneal model, which allows to explain the contribution of laser efficiency changes across the cornea to the increase of corneal asphericity after ablation. This protocol is useful to obtain a correction factor for any ablation algorithm and laser system, and to estimate the contribution of biomechanics to the increase of corneal asphericity in myopic refractive surgery.

3.2. INTRODUCTION

Refractive surgery has become a popular alternative for the correction of refractive errors. However, as described in Section 1.7.1 of the Introduction of this thesis, one of the major issues of myopic refractive surgery is the increase of corneal asphericity with the procedure (Marcos et al., 2001a), which causes an important increase of spherical aberration (Moreno-Barriuso et al., 2001b) with significant visual consequences (Applegate et al., 2000). Specific details on the magnitudes of these changes and an extensive literature review can be found in the Introduction (Section 1.7.1). Some theoretical studies (Mrochen and Seiler, 2001) pointed at laser efficiency effects as the origin of the problem (see Section 1.7.3 of the introduction). The effective laser energy delivered onto the cornea changes as the laser beam moves from the center to the periphery. As a result the effective ablation pattern applied on the cornea varies with respect to the theoretical ablation pattern and the actual post-operative corneal shape differs from the expected one. Understanding the physical factors affecting the effective transfer of the energy to the cornea is essential.

The aim of the study presented in this chapter was to investigate the causes for the change in corneal asphericity (and spherical aberration) produced by refractive surgery. For this task we developed an experimental model of ablation on PMMA, which we compared with computer predictions and experimental data in patients obtained in previous studies in our laboratory.

In this study we used plastic corneal models to assess the laser ablation profiles programmed in standard LASIK surgery and estimate the geometrically-related laser efficiency effects.

Plastic models have been used in refractive surgery research and calibration for a long time, especially for the assessment of roughness and calibration of fluence (Gottsch et al., 1996, Odonnell et al., 1996, Roszkowska et al., 2003). However, it has not been until recently that plastic models have been used to study in detail the shape changes induced by refractive surgery on flat and spherical surfaces (Marcos et al., 2005b). Plastic models are also interesting for quality assessment and market approval of new laser platforms (2007, Drum, 2003, Drum, 2005), to check experimentally the calibration state of individual laser units, and the diagnosis of appropiate alignment. They will also help to validate theoretical models of refractive surgery (Arba-Mosquera and de Ortueta, 2008, Kwon et al., 2008).

In this study the model corneas were made out of PMMA, a widespread material for ophthalmic applications. The next chapters will present further elaborations of the model using a novel material, Filofocon A, which proved even better ablation properties. Spherical PMMA surfaces were made with similar radii of curvature than that of human corneas. Profilometric measurements of PMMA flat surfaces after ablation will test the actual ablation profile programmed into the laser system, and whether this is close to the theoretical Munnerlyn pattern. A comparison between the ablated spherical PMMA surfaces and identical ablations on flat surfaces will show the effects of laser efficiency changes across a curved PMMA surface. Once the difference in ablation rates between PMMA and corneal tissue are considered, as well as the differences in ablation threshold in PMMA and cornea, it is possible to estimate the effect of laser efficiency on post-operative corneal shapes. A direct comparison of real and model post-operative corneal shapes will give insight into the possible contribution of biomechanical and wound healing effects to the increase of corneal asphericity in myopic refractive surgery. The conclusions will be relevant both in the

optimization of refractive surgery algorithms, and in the manufacture of phase plates and contact lenses by laser ablation.

3.3. METHODS

3.3.1. Laser equipment

Laser ablation of polymethyl-methacrylate (PMMA) surfaces was carried out with a conventional flying-spot laser system used for corneal refractive surgery (Chiron Technolas 217-C equipped with the PlanoScan program; Bausch & Lomb Surgical). This system has an Argon Fluoride (ArF) excimer laser delivering laser pulses at 50Hz. The laser beam diameter is between 1 and 2 mm. The emission wavelength is 193nm and the radiance exposure is 120mJ/cm^2. The laser system is programmed to produce standard ablation patterns for correction of myopia, hyperopia and astigmatism. An identical equipment (operated by the same surgeon) had been used in the patients from previous studies (Moreno-Barriuso et al., 2001b, Marcos et al., 2001a, Marcos, 2001) in our laboratory, used in this study as a reference.

3.3.2. PMMA model

Laser ablation was performed onto flat and spherical PMMA surfaces. PMMA was supplied by Horniplas (Vitoria-Gasteiz, Spain) in form of flat-faced pieces. To manufacture the spherical surfaces, the flat-pieces were firstly machined into 12-mm cylindrical rods. The spherical surface was grinded on one tip of the cylinder following standard procedures in a manual lathe. Polishing was performed with a polishing cloth damped with Orma Polish (Gerard Kluyskens Company, NYC, NY) with precise polishing tools on the same lathe. The intended radius of curvature was 8.00 mm, similar to that in human corneas. Surface curvature was initially checked in the workshop with an optical gauge and Newton rings.

Two types of PMMA were used for laser ablation: extruded and cast PMMA. Preliminary tests were performed on cast PMMA, although final experiments were done using extruded PMMA. We observed that ablation profiles on cast PMMA were less repetitive, with some of the samples showing central islands after ablation.

3.3.3. Laser ablation of flat and spherical PMMA surfaces

Ten refractive surgery ablations were performed on flat surfaces and seven on spherical surfaces. Tables 1 and 2 list the ablation parameters used for each procedure. Both flat and spherical surfaces were ablated with myopic corrections of 3, 6, 9 and 12 D (for the cornea) and with optical zone diameters from 5 to 7 mm. Transition zone was 2 mm in all cases. The laser system computer showed the ablation depth that the applied radiation produces on corneal tissue. The surgeon operating the laser system centered the ablation at the surface apex, taking the corneal reflex as a reference.

Table 3.1. Description of the ten refractive surgery ablations performed onto flat PMMA surfaces

Myopic correction (D)	3	6	9	12
Optical zone diameter (mm)	7	7	6,5	5
Central ablation depth (μm)	72	142	180	142
Number of ablations performed	3	3	2	2

Table 3.2. Description of the seven refractive surgery ablations performed onto spherical PMMA surfaces[a]

Myopic correction (D)	3	3	6	6	9	12	12
Optical zone diameter (mm)	6	7	6	7	7	6	7
Central ablation depth (μm)	52	72	103	142	208	202	273

[a]The mean radius of curvature of the PMMA spheres before ablation was 7.97 ± 0.03 mm.

3.3.4. Profilometry and topography measurements

3.3.4.1. Flat surfaces

The shapes of the ablated flat surfaces were measured with a contact profilometry system (Detek 3000), described in Section 2.1.1.1. For each ablated flat surface, the ablation profile was measured along two perpendicular directions passing through the center of the ablation.

3.3.4.2. Spherical surfaces

The shapes of the spherical surfaces were measured by corneal topography before and after ablation, and by contact profilometry and confocal microscopy after ablation. The vertical range of the contact profilometry system used for the flat surfaces was not sufficient to measure the elevation differences in the spherical surfaces. Instead, a Talysurf contact profilometry system was used (Section 2.1.1.1).

Additionally, the shape of ablated spherical surfaces was obtained using a non-contact confocal profilometer (Plμ). Although the measurement range is much wider, only the central 4-mm region of the ablated model corneas could be tested with the maximum resolution for this study.

Profilometry and microscopy measurements on ablated spherical surfaces were compared to corneal topography measurements (Section 2.1.2) on the same surfaces. The aim of this comparison was to assess the accuracy of corneal topography on ablated surfaces, using contact profilometry as a 'gold standard' and to assess the possibility of using conventional corneal topography in this study, which would allow more direct comparisons to clinical data on patients' corneas. Corneal topography measurements of pre-ablated spherical surfaces verified radii of curvatures of 7.97±0.03 mm. Corneal topography measurements on spherical surfaces immediately following ablation were not possible, since the scattering produced by the increased surface roughness prevented appropriate reflection of the Placido rings. With the aim of increasing the surface reflectance, ablated surfaces were cleaned with a paper tissue soaked by a slight-scratch-remover liquid before topographic measurements. This slight polishing process removes the small ablation debris fixed to the surface and also smoothes the roughness generated by the ablation. An additional purpose of the comparison of the profiles obtained from the videokeratography, and contact and confocal microscopy was to assess whether the polishing process altered the global shape of the surface. The average difference, given by the root mean square error (RMSE), between the elevations provided by Talysurf and videokeratographer was 0.724 μm over the central 8 mm (see Section 2.1.2 and Fig. 2.10). The confocal microscope, although provides accurate measurements of the central surface, was rejected for this study, because at the moment of the study the available hardware did not meet the requirements of the measurement in the peripheral area.

These data demonstrate that videokeratoscopy produces reliable data on post-ablated surfaces, at least within the ablation zone. For this reason, all data on pre- and post-ablated spherical surfaces presented in this study are based on videokeratoscopy.

3.3.5. Assessment of the ablation pattern generated by the laser system

3.3.5.1. Flat surfaces

The surface profiles on ablated flat surfaces should represent the actual ablation profiles produced by the laser. The support of the samples in the profilometry system was not necessarily perfectly parallel to the translation of the probe tip, causing some tilt in the measured profiles. The measured profiles were corrected numerically for this tilt, until the untreated areas appeared flat (Section 2.2.2.1).

3.3.5.2. Spherical surfaces

The ablation patterns for spherical surfaces were obtained by subtracting the surface heights measured by videokeratography after ablation from the sphere with the pre-ablation curvature (as measured from videokeratography) (Section 2.2.2.2). As the reference axis for the videokeratographer (the line passing though the surface apex) may not coincide with the laser beam direction during ablation, the surface apex during topography measurements may not correspond with the ablation center. This may happen even if both ablation and measurement were well centered with respect to the surface circular limits. We wrote routines in Matlab (Mathworks, Nantick, MA) to rotate the measured corneal elevation profiles to bring the center (maximum depth) of the measured ablation to the apex, before subtraction. This results in a more precise (and symmetric) ablation pattern. In most cases, post-operative corneal elevation maps were repeated, tilting the cornea by the angle obtained from the programs, to align the ablation and measurement axes. This was achieved placing the base of the ablated model cornea on a tip-tilt table, and performing an iterative process until the estimated tilt and subsequent decentration were less than 0.2 deg and 0.05 mm respectively.

3.3.6. Ablation efficiency estimates

Ablation patterns on spherical surfaces are altered by variations in ablation efficiency due to changes in the angle of incidence of the laser beam as a function of surface location. In contrast, ablation efficiency is constant on flat surfaces, where laser incidence is always perpendicular. The ablation efficiency factor $K(\alpha)$ takes values between 0 and 1. From our measurements on PMMA, we will estimate $K(\alpha)$ by dividing the ablation profile measured on spherical surfaces by the ablation profile measured on flat surfaces, for the same conditions. This function describes the laser efficiency effects reducing the ablation depth at the periphery, and therefore the adjustment factor by which the laser ablation profile is multiplied to give the final ablation produced on curved surfaces. From a design point of view, $K(\alpha)$ represents the adjustment factor by which the intended profile should be divided to compensate for the changes in ablation efficiency on curved surfaces.

It should be noted that $K(\alpha)$ depends on the refractive index for the laser wavelength and the ablation threshold, and therefore if will be different for a material with different n and F_{th}. Following application of the Beer-Lambert law (Jimenez et al., 2002):

$$K = 1 + a \cdot f(R) \qquad (3.1)$$

where $a=1/ln(F_0/F_{th})$, with F_0 the laser fluence and F_{th} the ablation threshold, and $f(R)$ is a reflectivity function, depending on the surface location and material index of refraction, given by Fresnel equations. While the refractive index at 193 nm is similar in cornea and in PMMA (n_{cornea} = 1.52 (Pettit and Ediger, 1996); n_{PMMA}=1.49), and therefore we will assume $f(R)$ to be the same for both materials, the ablation threshold differs ($F_{th, cornea}$= 40 mJ/cm^2 (Berns et al., 1999) or $F_{th, cornea}$= 60 mJ/cm^2 (Pettit et al., 2005) ; $F_{th, PMMA}$= 80mJ/cm^2 (Srinivasan, 1986)).

The ablation efficiency factor for the cornea K_{cornea} will be estimated from the experimental estimates of K_{PMMA} using the following expression:

$$K_{cornea}(\alpha) = 1 + (a_{cornea}/a_{PMMA}) \cdot (K_{PMMA}(\alpha) - 1) \tag{3.2}$$

3.3.7. Post-operative asphericities

In order to estimate the asphericities produced by the actual ablation patterns when the effects of reflection losses and non-normal incidence are not present, we computed the post-operative asphericities produced on an spherical PMMA surface (radius = 8 mm) by the laser ablation profiles measured on flat surfaces. We used fitting routines written in Matlab, as described in a previous publication (Cano et al., 2004). To consider efficiency changes, these surfaces were multiplied by the measured K_{PMMA} before calculating their asphericity. Central radii of curvature and asphericities were also directly computed from the surface elevation maps measured on PMMA ablated spheres.

Corneal ablation patterns were calculated by converting PMMA ablation depths into corneal ablation depths by using a PMMA-cornea ablation factor to account for the different ablation rates (material removed per pulse) in PMMA and in cornea. The simulated postoperative corneas were calculated by: 1) applying an overall depth offset to the ablation profile, to account for a different transition zone; 2) multiplying by the estimated K_{cornea}, to account for the effects of ablation efficiency changes; 3) subtracting the resulting corneal ablation patterns from the simulated preoperative corneas. In all cases, the preoperative cornea was simulated as a conic surface with a typical human corneal shape (Radius of curvature = 7.8 mm; asphericity = -0.2). Corneal asphericity was computed as described above.

3.4. RESULTS

3.4.1. PMMA-cornea correction factor

The ablation rate is different on corneal tissue than extruded PMMA. A conversion factor was estimated, to account for the difference in the ablation depth per laser pulse between PMMA and cornea.

Figure 3.1A shows central ablation depths (for different refractive corrections) in both flat and spherical PMMA samples versus the nominal ablation depth displayed on the laser system. There is a good correlation between nominal central ablation depths in the cornea and those measured on PMMA, with a slope of 1.8 µm on cornea /1 µm on PMMA. Despite the good correlation, which was expected since the amount of material removed by each laser pulse must be the same in all samples, we considered that the ablation PMMA-cornea correction computed from the regression line may not sufficiently accurate for several reasons: 1) there appears to be an offset in the

regression line, since it does not cross the origin; 2) we ignore the reliability of the information on nominal corneal ablation depth provided by the laser system; 3) the factor only relies on ablation depth on a single central location (which in the case of elevation maps of spherical surfaces from videokeratoscopy is obtained by interpolation).

(A)   (B)
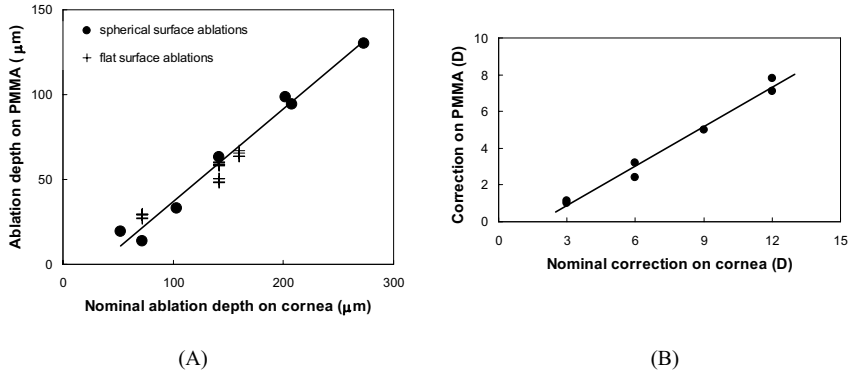
Fig. 3.1. (A) Central ablation depths in flat –for two perpendicular meridians- (crosses) and spherical surfaces (solid circles). PMMA ablation depth was obtained from contact profilometry on flat surfaces, and videokeratography on spherical surfaces. Corneal ablation depth as provided by the laser system, for a given refraction correction and optical zone. The solid line represents the best-fitting line (slope = 0.55). (B) Refractive correction achieved on the spherical PMMA surfaces versus the intended correction on the cornea, as provided by the laser system. The solid line represents the best-fitting line (slope = 0.71).

Alternatively, we obtained the ablation rate factor between corneal tissue and PMMA as that producing the attempted corneal correction in simulated postoperative corneas. This was obtained after an iterative process in which, at each iteration of the factor, all ablations in flat PMMA were transformed into corneal ablations and their central radii compared with the intended value. With this approach we obtained a PMMA-cornea correction factor of 2.65. Ablation depths in PMMA have to be multiplied by this value to obtain corneal ablation depths.

Figure 3.1B shows a linear correlation between the nominal spherical correction on cornea and on PMMA. It should be noted that in Fig. 1B the refractive index of PMMA in the visible (n=1.49), rather than the corneal refractive index (n=1.377) was used to calculate the actual power change of PMMA ablated spheres.
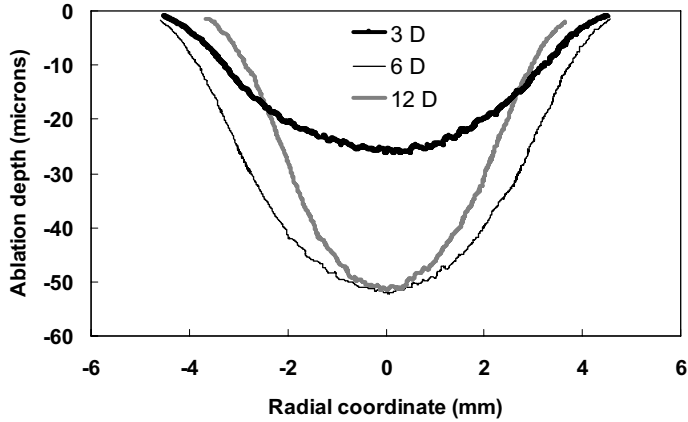
Fig. 3.2. Ablation profiles of three PMMA ablated flat surfaces for three nominal refractive myopic corrections (3, 6 and 12 D). Optical zone diameters were 7 mm for the 3-D and 6-D corrections and 5 mm for 12 D. These patterns were obtained by profilometry on ablated flat surfaces. These ablation patterns are not affected by ablation efficiency changes and represent the actual patterns for the cornea programmed into the laser system.

3.4.2. Ablation patterns from flat surfaces and from spherical surfaces

Figure 3.2 shows the profiles of three ablated PMMA flat surfaces, for three different corrections and optical zones. These ablation patterns are not affected by ablation efficiency changes and represent the actual patterns programmed into the laser system. It should be noted that the ablation depth depends both on the attempted correction and optical zone, and therefore two different corrections (i.e. 6 and 12 D) may result in similar central ablation depths.
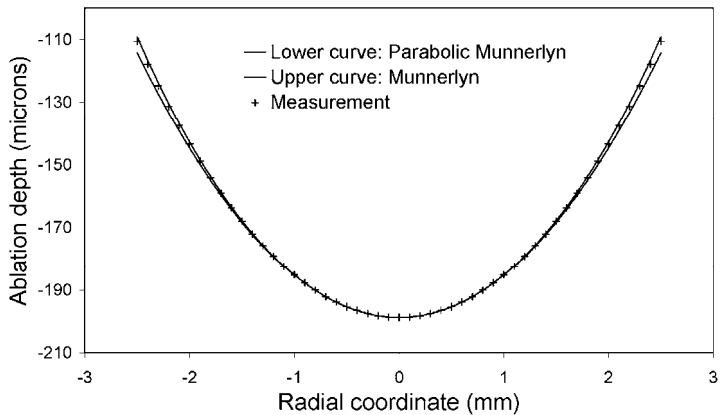
Fig. 3.3. Best fitting conic of the actual corneal ablation pattern -crosses- corresponding to the 12-D PMMA ablation pattern of Fig. 3.2, compared with the theoretical Munnerlyn and parabolic patterns -solid line- for the same correction and depth. The Munnerlyn pattern is calculated with the parameters of a typical preoperative cornea (radius 7.8 mm and asphericity -0.2).

Figure 3.3 shows one of the ablation profiles (12 D) of Fig. 3.2, after fitting to a polynomial curve, simulation of a different central ablation depth and multiplication by the PMMA-cornea correction factor, therefore representing ablation depths in cornea. For comparison, Fig. 3.3 also shows the theoretical Munnerlyn and the parabolic approximation of the Munnerlyn pattern, for the same correction. For this example, as in the majority of cases, the actual pattern programmed into the laser system is closer to the Munnerlyn pattern than to its parabolic approximation.

Figure 3.4 shows the shapes of two ablations measured on ablated PMMA spherical surfaces. This ablation patterns are affected by ablation efficiency changes across the curved surface.
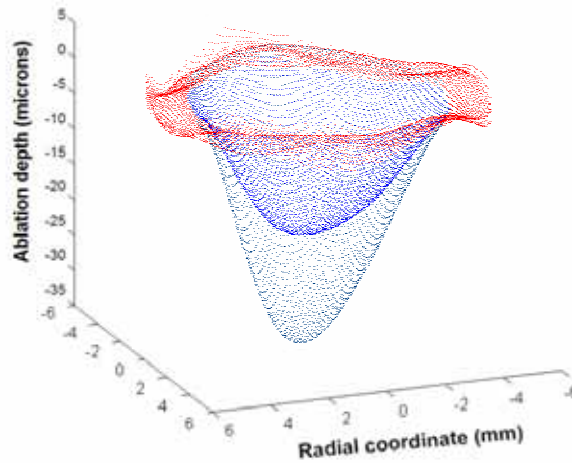
Fig. 3.4. Ablation profiles of two ablated PMMA spherical surfaces (3-D: dark blue, and 6-D: light blue; the non-ablated zone is marked with red), obtained by subtracting post-ablation elevation maps from the elevation maps of the spheres. This ablation patterns are affected by ablation efficiency changes across the curved surface. Outside the ablation the topographer has systematic errors, which are partially compensated after processing.

3.4.3. Experimental estimates of ablation efficiency

Figure 3.5 shows two ablation profiles on PMMA, one from a spherical surface (sections of all meridians superimposed), and another from a flat surface. Since both ablations have the same nominal correction (12 D), the energy profile delivered by the laser system is expected to be the same in both cases inside the central 5 mm (the smaller of the optical zones, indicated with vertical dashed lines in the plot). Therefore, the difference between both ablations (less penetration in the periphery of the ablated sphere) can only be attributed to laser efficiency losses.
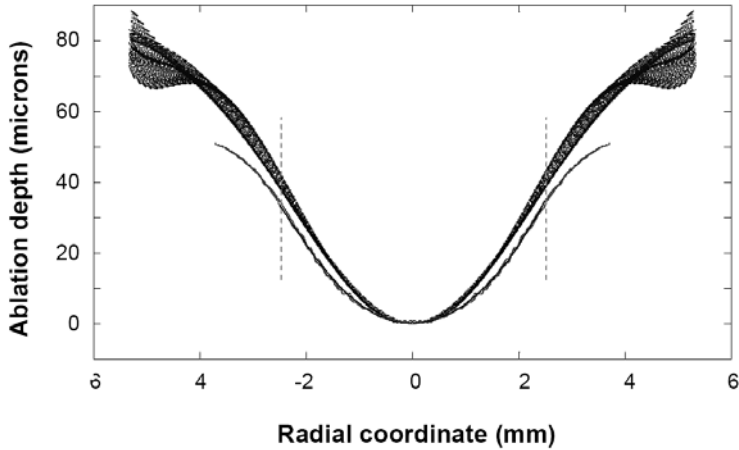
Fig. 3.5. Measurements of the ablation profile on PMMA from a spherical surface - upper curve- and a flat surface -lower curve- after myopic refractive surgery of 12 D. Although the optical zones are different, inside the central 5mm -vertical lines- the only expected difference among both measurements is due to laser efficiency losses. This produces a shallower ablation in the periphery of ablated spherical surfaces.

The profiles shown in Fig. 3.5 are highly symmetric, indicative of an accurate centration and alignment of the laser ablation, followed by an accurate measurement and processing. In many cases, the ablation profiles show slight defects or asymmetries, and for this reason the pair of ablation profiles shown in Fig. 3.5 were those used to estimate the ablation efficiency factor K. Figure 3.5 also shows the best fitting conics of these profiles, almost completely superimposed to the raw data. The ratio of these fitted curves were used directly to calculate the experimental ablation efficiency factor for PMMA (K_{PMMA}) shown in Fig. 3.6. The ablation efficiency factor for the cornea (K_{cornea}) is obtained from the experimental estimates of K_{PMMA} using equation (2). For comparison, Fig. 3.6 also shows theoretical estimates of K_{PMMA} and K_{cornea} using Jiménez et al's equations (that rely on the physical phenomena and the assumptions described in the introduction). Both the experimental and theoretical curves show a stronger ablation efficiency factor on PMMA than on the cornea. For both the cornea and PMMA, the theoretical factor seems to slightly underestimate the effect as compared to the experimental measurements. For example, at 2-mm from the corneal apex, laser efficiency decreases by 0.89 for PMMA from experimental measurements (0.92 theoretically) and 0.96 for the cornea (0.97 theoretically). The ablation rate of the material (or the PMMA-cornea correction factor) modulates the impact of the ablation efficiency factor $K(\alpha)$ on the final shape. For this reason, although K_{PMMA} is stronger than K_{cornea}, efficiency effects turn out to be more important in cornea that in PMMA.
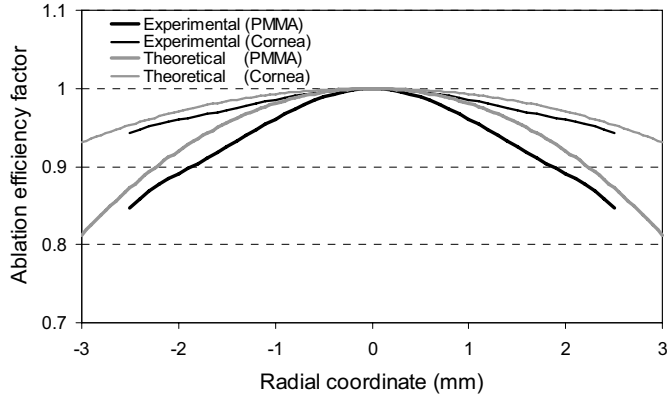
Fig. 3.6. Ablation efficiency factors obtained experimentally (black) for PMMA and cornea, compared with theoretical predictions using Jiménez et al's equations (Jimenez et al., 2002) for PMMA and cornea respectively. Data for PMMA are represented in thick lines and for the cornea in thin lines.

3.4.4. Post - operative asphericities on PMMA

Figure 3.7 shows postoperative asphericities estimated directly from the elevation maps of PMMA spherical surfaces (red circles), for different spherical corrections (the values indicate nominal corrections on the cornea, see Fig. 3.1 (b) for the equivalent corrections on PMMA). We found a systematic increase of asphericity in all the surfaces tested, the larger the correction the larger the increase. The graph also plots the predicted asphericities using the experimental ablation efficiency factor found in this study (orange diamonds) and the theoretical efficiency factor (blue triangles) proposed by Jimenez et al. (Jimenez et al., 2002), calculated with the values corresponding to PMMA material. The predicted ablation pattern is the result of direct subtraction of the experimental ablation pattern measured on flat surfaces multiplied by the efficiency factor considered from a spherical surface of 8 mm-radius. The asphericities without considering efficiency effects (ablations on flat surfaces computationally applied to the spherical surfaces) are also shown (green diamonds). Without efficiency effects, the measured ablations have asphericities close to zero (-0.03±0.1, mean and standard deviation), and no change with correction. We found experimentally a significant increase of asphericity that can be entirely attributed to reflection losses and non-normal incidence. The mean asphericity of ablated PMMA spheres was 0.89 ±0.76.

The asphericity predictions using the ablation profile from flat surfaces and the experimental efficiency factor agree well (0.93±0.37) with those obtained directly from experimental elevation maps on ablated PMMA spheres. For the 12-D sphere used in the calculation of the experimental efficiency factor, the coincidence is perfect, as expected. The theoretical efficiency factor predicts a mean increase in asphericity of 0.33±0.18, that is, 37% of the increase found experimentally.
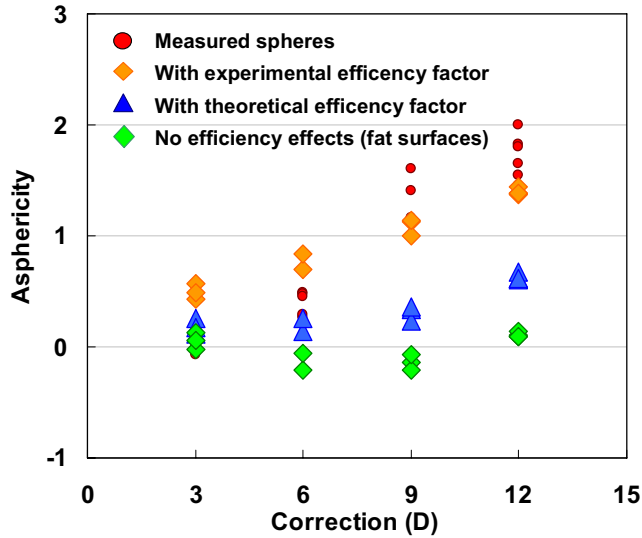
Fig. 3.7. Postoperative corneal asphericities of ablated PMMA surfaces as a function of nominal (on cornea) refractive correction, as measured directly on ablated spherical surfaces -red circles-. The figure also shows the predicted asphericity after direct subtraction of the experimental pattern measured on flat surfaces (non affected by efficiency factor) -green diamonds- as well as subtraction of this pattern multiplied by the experimental -orange diamonds- and theoretical -blue triangles- efficiency factors for PMMA. Pre-operative spherical surfaces had radii of curvature of 8-mm.

3.4.5. Post - operative asphericities on cornea

Our predictions of corneal asphericity using the experimental ablation pattern (actual profile programmed in the laser system) and our experimental estimates of K_{cornea} can be compared directly to data on real patients.

Figure 3.8 shows postoperative clinical asphericities compared with predicted corneal asphericities as a function of spherical correction. Clinical asphericities (open triangles) were measured in patients treated with standard refractive surgery from a previous study in our laboratory (Marcos et al., 2001a), with an identical laser operated by the same surgeon. Predicted asphericities were calculated from experimental data, for a typical preoperative cornea of radius 7.8 and asphericity -0.2. To simulate the postoperative cornea, the ablation measured in flat surfaces is multiplied by the PMMA-cornea correction factor and by the ablation efficiency factor K_{cornea}, and then directly subtracted from the preoperative cornea. Predictions without considering efficiency effects (green diamonds) show practically no change of corneal asphericity with ablation (-0.43±0.40). Predictions using Jimenez's theoretical K_{cornea} – thick gray line in Fig. 3.6– (blue triangles) show a slight increase of asphericity with attempted correction (0.03±0.49). Predictions using the experimental K_{cornea} from the current study –thick black line in Fig. 3– (not shown) estimate significantly higher corneal asphericities (0.78±0.70). It should be noted that throughout the study we have used a rather conservative value for corneal ablation threshold (Fth=40 mJ/cm^2). Figure 8 shows predictions with K_{cornea} estimated with a recently reported (Pettit et al., 2005) higher value –Fth=60 mJ/cm^2– (orange diamonds) which approaches even more (1.39±0.92) the asphericity values found clinically (red diamonds) (1.97±2.00

111

considering the same set of corrections). This change in the corneal ablation threshold affects only slightly the predictions of the theoretical factor (0.29±0.53) (not shown).
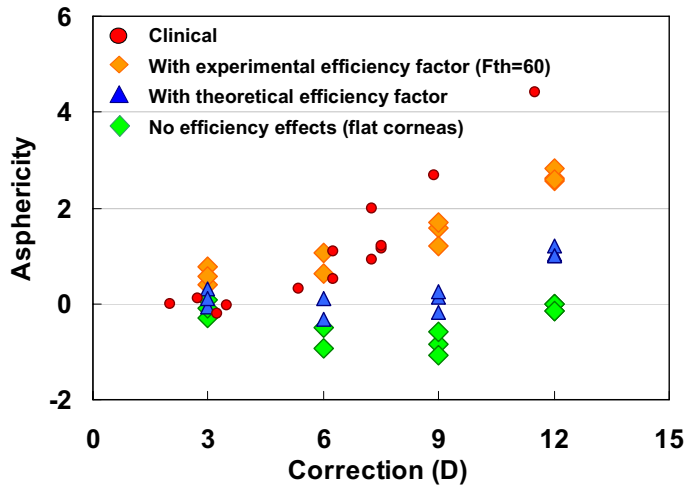
Fig. 3.8. Asphericities of simulated postoperative corneas (central radii 7.8 mm, asphericity -0.2) as a function of nominal correction, in comparison with clinical data (red diamonds) on real patients operated with the same laser system. Predictions include asphericities obtained from post-operative corneas after subtracting the corneal ablation pattern obtained from flat PMMA, i.e. with no efficiency effects (green diamonds), as well as this pattern multiplied by the experimental (orange diamonds) and the theoretical efficiency factor (blue triangles).

In summary, the predicted corneal asphericities from the experimental efficiency factor are higher than those obtained with the theoretical factor, although for the highest corrections they are still lower than the clinical data on patients.

3.5. DISCUSSION

3.5.1. Ablation pattern programmed into the laser

The comparison of the theoretical ablation patterns with the experimental ablation pattern (all shown in Fig. 3.3) suggests that the actual pattern programmed into the laser is close to the theoretical equations (Munnerlyn and parabolic). In addition, corneal asphericities induced purely by the experimental ablation pattern (see open diamonds in Fig. 3.8), without taking into account ablation efficiency changes and corneal biomechanics are close to those induced by the Munnerlyn pattern and show almost no change with correction, as reported before from analytical (Anera et al., 2003, Gatinel et al., 2001) and computational simulations (Marcos et al., 2003, Cano et al., 2004) of the Munnerlyn algorithm. Those asphericity predictions are far from the post-operative asphericities in real patients, indicating that the ablation profile *per se* is not the cause for the increased asphericity found clinically.

3.5.2. Experimental estimates of the ablation efficiency correction factor

As opposed to ablation patterns obtained from ablated flat PMMA surfaces, ablation patterns calculated from ablated spherical PMMA surfaces are affected by changes in

ablation efficiency, i.e. the ablation depth per laser pulse decreases as the spot moves from the apex to the periphery, due to variations in the angle of incidence of the laser radiation. Measurements on both flat and spherical PMMA surfaces have allowed us to obtain a direct estimate of the ablation efficiency factor on PMMA, and a prediction of the ablation efficiency factor for the cornea based on those measurements.

Previous estimates of the ablation efficiency factor had been obtained mathematically (Anera et al., 2003, Jimenez et al., 2002), using approximations as a truncated polynomial series expansion, and assuming only reflection losses using Fresnel equations and non-polarized light, along with nominal values for laser fluence and corneal refractive index and ablation thresholds. However, there are other effects that potentially affect the changes in laser efficiency. These include spot shape, beam divergence changes from the center to the periphery, beam scanning effects, polarization, defocus, etc.

Unlike the theoretical factor, the experimental ablation efficiency factor K_{PMMA} –and K_{cornea} estimated from K_{PMMA}– include these effects. While K_{PMMA} is a direct measurement of the ablation efficiency changes on PMMA and does not rely on any assumption, the estimates of the experimental K_{cornea} from the experimental K_{PMMA} rely on three assumptions: 1) that the Beer-Lambert's law applies to the cornea as well as on PMMA. 2) that the reflectivity factor $f(R)$ is similar in PMMA and corneal tissue, which is true provided that the index of refraction at the laser wavelength is the same on cornea and PMMA and 3) that the laser fluence and the ablation thresholds for PMMA and corneal tissue are known.

The fact that the Beer-Lambert's law appropriately describes photoablation of corneal tissue is fairly well established (Pettit and Ediger, 1996, Fisher and Hahn, 2004). We have also tested assumption 2 by computing the difference in the reflectivity factor when changing the index of refraction by 1.52 instead of 1.49 and found no appreciable change. For PMMA, an ablation threshold of 80 mJ/cm^2 seems to be an accepted value. For the cornea however, while many studies use 40 mJ/cm^2 (Berns et al., 1999), some authors have recently reported (Pettit et al., 2005) 60 mJ/cm^2 . The ablation efficiency factor that we present represents therefore a conservative estimate. We repeated the computations using a corneal ablation threshold of 60 instead of 40 mJ/cm^2 and found predicted corneal asphericities closer to the clinical estimates, as shown in Fig. 3.8 (gray solid diamonds). Tissue hydration, that causes changes in reflectivity and absorption, among other effects, during corneal ablation (Manns et al., 2002b), could also modify the laser ablation rate in corneas, and the cornea/PMMA factor.

Our experimental ablation efficiency factor K_{cornea}, although slightly stronger, agrees well with the theoretical K_{cornea} from Jimenez et al.'s (Fig. 3.6). However, the impact of this slight difference is important, and the predicted corneal asphericities using the experimental K_{cornea} are much closer to the clinical findings (Fig. 3.8). A similar effect was found on PMMA (Fig. 3.7).

The calibration protocols that we describe here can be generalized to any laser system and any material (with a refractive index similar to the cornea at the ablation wavelength), even if the numerous assumptions and simplifications of the theoretical model do not hold. This systematic calibration (Marcos et al., 2005b) will potentially be more effective than ablation efficiency factors empirically obtained by adjusting recursively the algorithm, which require prior treatments on real patients at different stages of the ablation algorithm refinement.

3.5.3 Impact of correction factors on post-operative corneal shape and aberrations

The experiments described here aim at explaining the increased asphericity found in eyes after standard LASIK for myopia, and at obtaining experimentally an ablation efficiency correction factor which corrects for the effect of laser efficiency changes across the cornea. As we tested experimentally, the laser system was programmed using a pattern close to the standard Munnerlyn algorithm with no further correction factor. Current generations of laser systems incorporate more sophisticated algorithms, aiming at canceling not only pre-operative sphere and cylinder but also high order aberrations.

The application of ablation efficiency correction factors, as derived here, is essential to avoid induction of spherical aberration by surgery (associated to the increased asphericity described here) which would override the benefits of the individual high order aberration correction. In fact, reports on the outcomes of wavefront guided refractive surgery still show an increase of spherical aberration (Aizawa et al., 2003, Caster et al., 2004). As an example, Fig. 3.9 shows wave aberration maps (for 3rd and higher order aberrations) for a patient before surgery (-5 D pre-operative spherical error), and the wave aberration after simulation of wavefront guided refractive surgery, not including the ablation efficiency correction factor, and including it (not considering biomechanical factors). Correction of ablation efficiency avoids induction of spherical aberration.

A   B   C
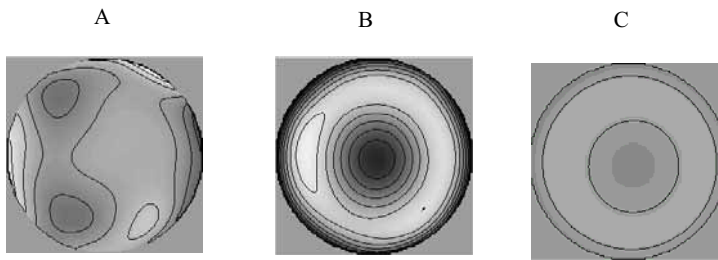
Fig. 3.9. Wave aberration maps (for 3rd and higher order aberrations) for a patient before LASIK (-5 D pre-operative spherical error, contour lines stand for 1 micron aberration steps) (A), and the wave aberration after simulation of wavefront guided refractive surgery, not including the ablation efficiency correction factor (B), and including it (C). Biomechanical factors are not considered. Correction of ablation efficiency avoids induction of spherical aberration.

3.5.4. The role of corneal biomechanics

The fact that the actual ablation patterns, when not affected by changes in ablation efficiency, do not produce major changes in corneal asphericity (and therefore do not induce the dramatic increase in spherical aberration found clinically) indicates that improvement in refractive surgery outcomes should rely not so much on a refinement of the theoretical design of the ablation patterns but their correction for both changes in ablation efficiency and biomechanical effects. Those effects need to be also taken into account when designing customized ablation algorithms.

Our experiments on PMMA spherical surfaces show that a non-biological material shows an important increase of asphericity after ablation, highly correlated with the amount of correction, indicating that a purely physical effects may have been previously underestimated (Roberts, 2000). We have demonstrated experimentally that changes in ablation efficiency across the cornea account for most of the asphericity

increase found clinically. Models in PMMA are therefore useful to obtain the correction factor to be applied in the algorithm to compensate for changes in ablation efficiency across the cornea, and to validate the assumptions implicit in theoretically derived correction factors. However, the increase of corneal asphericity found clinically is not fully explained by results obtained in a PMMA corneal model, particularly for high corrections, leaving some room to biomechanical and wound healing factors.

3.6. CONCLUSIONS

In this Chapter we were able to obtain experimentally a factor accounting for laser ablation efficiency changes from the center to periphery of the cornea, For the laser of the study, the efficiency loss was 6% at 2.5 mm from the corneal apex. The method involved ablating flat and spherical plastic surfaces with a surgical excimer laser.

We found that the increase in corneal asphericity with standard myopic LASIK is primarily caused by laser efficiency changes and not by the ablation algorithm. Efficiency losses explain therefore most of the increase in asphericity found clinically (in patients operated with an identical laser system).

This factor can be used by the laser manufacturers to compensate any laser ablation algorithm from induction of spherical aberration.

3.7. OUTLOOK

In this study we have used PMMA as material for the experimental ablation model. We have learned that the optical and ablation properties of the material determine the sensitivity of the experimental model and the precision of the predictions in cornea. In next chapter, a new material (Filofocon A) will be explored, and compared with PMMA.

This chapter was limited to a laser system (and ablation algorithm) that had demonstrated in clinical practice (see Section 3.3.1) to increase asphericity and spherical aberration. However, both the laser platforms and the algorithms that they incorporate have evolved over the last years. An elaboration of the methods presented in this chapter will be applied in Chapter 5 to evaluate state-of-the-art laser systems and algorithms.

Corneal topography and contact profilometry were used in this study to measure shapes before and after surgery. Corneal topography is limited in resolution, and fine polishing was required to increase reflectivity of ablated sufaces. Contact profilometry has a limited range of application, and in most cases provides only 2-D profiles. In next chapters we will use advanced profilometry methods of higher precision, and able to measure the shape pattern (and not only profiles) both in flat and curved surfaces, allowing a full 3-D comparison of surfaces (pre/post operative; flat/spherical ablated surface measured with the same technique).

Chapter

4

Evaluation of the ablation properties of a new material (Filofocon A) for a corneal model

This chapter is based on the article by Dorronsoro et al. "Suitability of Filofocon A and PMMA for experimental models in excimer laser ablation refractive surgery", published in Optics Express Optics Express, Vol. 16, Issue 25, pp. 20955-20967 (Dorronsoro et al., 2008b). The study was partially presented at ARVO 2008 (Dorronsoro et al., 2008a).

The contribution of Carlos Dorronsoro to the study, in collaboration with other coauthors, was the literature search, the design of the experiments, the experimental work (ablations and measurements), the development of the data analysis routines and the analysis itself.

Coauthors of the study are Jan Siegel, Laura Remón, and Susana Marcos.
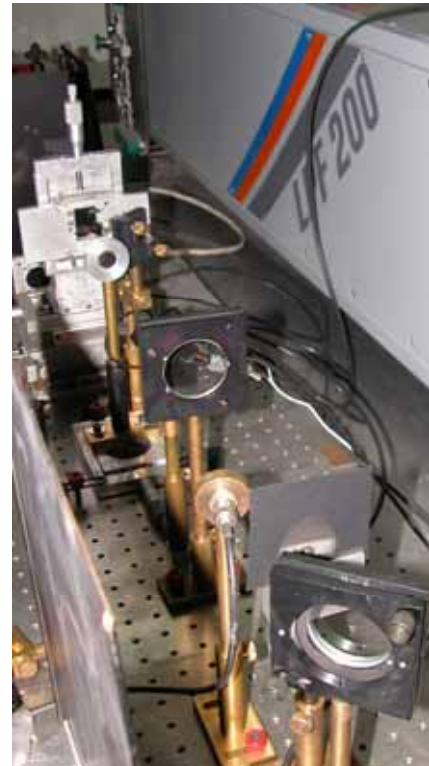
4.1 ABSTRACT

Purpose: Experimental corneal models in plastic (in PMMA, and more recently in Filofocon A, a contact lens material) have been proposed recently to overcome some of the limitations of the theoretical approaches aiming at improving the predictability of corneal reshaping by laser ablation. These models have also been proposed for accurate assessment of corneal laser ablation patterns. The goal of this chapter is to study optical and ablation properties of Filofocon A and PMMA using an experimental excimer laser set-up.

Methods: The relationship between number of pulses and ablation depth was measured, for Filofocon A and PMMA, for a range of fluences typical of refractive surgery laser platforms. Incubation effects, ablation threshold and absorption coefficients were obtained.

Results: Both materials follow a Beer-Lambert law in the range of fluences used in refractive surgery, and the number of incubation pulses is less than 4 (PMMA) and 2 (Filofocon A) above 140 mJ/cm^2. We found that above 40 pulses for Filofocon A and 70 pulses for PMMA, ablation threshold and effective absorption coefficients can be considered constant ($F_{th} = 90$ mJ/cm^2 and $\alpha_{eff} = 36000$ cm^{-1}, for Filofocon A, and $F_{th} = 67$ mJ/cm^2 and $\alpha_{eff} = 52000$ cm^{-1} for PMMA, respectively).

Conclusions: The absence of ablation artifacts (central islands), a lower number of incubation pulses, a lower pulse-number dependence of the ablation threshold, and a good correspondence between α_{eff} and the absorption coefficient α estimated from spectroscopic measurements make Filofocon A a more appropriate material than PMMA for experimental models in refractive surgery and for calibration of clinical lasers.

4.2 INTRODUCTION

The previous Chapter introduced the use of plastic models (Marcos et al., 2005b, Dorronsoro et al., 2006a) for the detailed study of the ablation process in curved surfaces, and the assessment of optical outcomes of post-operative surfaces. The presented experimental approach overcomes some of the limitations of theoretical approaches, as it does not rely on important assumptions and approximations present in the analytical method.

However, the study of the previous chapter that revealed that the ablation properties of specific plastic material used in the model and an accurate knowledge of those properties is critical in the success of the model as well as in the extrapolation of the results in plastic to cornea. The ideal material should have a predictable and stable response to laser ablation. The optical and ablation properties should be well known, to ensure a sensitive response to laser ablation (in the range of refractive surgery) and to provide accurate predictions for corneal tissue. On the other hand, it should be a stable solid material to assure shape stability, as measurements before and after the ablation are to be compared.

Laser refractive companies have identified Filofocon A, a material used in the contact lens industry, as a material potentially suitable for refractive surgery models, and this material holds promise in the community to establish itself as standard for calibrations of laser ablation profiles (Campbell, 2007). PMMA has already been used to test laser ablation properties of refractive surgery laser platforms (Chernyak and Campbell, 2003). PMMA was the material used in the corneal model of Chapter 3 (Dorronsoro et al., 2006a). Filofocon A is a recent material used in artificial eyes and its laser ablation properties have never been described.

In PMMA, the Beer-Lambert behavior (Section 1.6.4) is found only to hold under two restrictions (Srinivasan et al., 1986, Costela et al., 1995). First, it is only valid for a certain range of fluence and, second, the absorption coefficient α estimated from low intensity spectroscopic measurements has to be replaced by an effective absorption coefficient α_{eff} estimated from the slope of the representation of Eq. (1.7), in terms of d vs. $ln(F)$. Evidence has been found that this change in absorption coefficient in the high intensity regime occurs within a single pulse for PMMA (Srinivasan et al., 1986, Kuper and Stuke, 1987). While some authors consider the assumptions of Eq. (1.7) (Beer-Lambert law) to be valid for corneal tissue ablation (Pettit and Ediger, 1996), recent studies also suggest a dynamic absorption coefficient in the cornea (Jimenez et al., 2006, Fisher and Hahn, 2007), changing under excimer laser ablative conditions. These restrictions have recently been proposed as a possible limitation to the suitability of PMMA for experimental models (Jimenez et al., 2007, Dorronsoro and Marcos, 2007). In comparison, no information is available about the ablation properties of Filofocon A.

In this study we will investigate the suitability of this new material (Filofocon A) for experimental laser ablation refractive surgery models, and measure its excimer laser ablation properties. In particular, we will study the relationship between number of pulses and ablation depth (for a range of fluences typical of refractive surgery laser platforms), incubation effects, ablation threshold and absorption coefficient of Filofocon A, in comparison to PMMA. Knowledge of these properties is essential to characterize the ablation patterns on plastic plates, to calibrate the lasers, to measure laser efficiency correction factors, and to extrapolate those results to the cornea.

4.3. METHODS

Samples of Filofocon A were ablated using an excimer laser set-up. Ablation depths were measured using microscope interferometry to assess ablation rates as a function of number of pulses and fluence, the effective absorption coefficients and the ablation thresholds. Ellipsometry was used to measure the refractive index, *n*, and the extinction coefficient, *k*. The procedure was also followed for PMMA, a material previously used in refractive surgery ablation models.

4.3.1 Samples

Filofocon A (hydro-2) is a poly-fluoro-silicone-acrylate material (Innovision, Inc., Omaha, NE), used to manufacture rigid gas permeable contact lenses. This copolimer has a soft hydrophilic outer skin when inmersed in water or tear film.

PMMA (acrylic glass) is a widely used thermoplastic material. Pure PMMA is usually modified with varying amounts additives, to improve its specific properties for certain applications. Transparent extruded PMMA was used in these experiments (Horniplas, Vitoria-Gasteiz, Spain)

The samples for ablation were prepared as optically flat rectangular surfaces (10x20 mm), polished in a precision optics lathe. Two samples of each material (Filofocon A and PMMA), with 2 mm thickness, were used in the ablation experiments. For the measurement of optical properties, flat polished surfaces of 12-mm diameter, and 4-mm thickness (to avoid contributions from the back surface) were used.

4.3.2 Estimation of optical properties

Refractive index and extinction coefficients of Filofocon A and PMMA were obtained from spectrometric ellipsometry (WVASE J.A. Woollam, Lincoln, NE) under incident angles of 60, 65 and 70 degrees. Measurements were obtained with a xenon lamp in a wide wavelength range from 1000 to 270 nm, under ambient conditions. Measurements below 270 nm were noisy, due to the air absorption and reduced reflectivity of the material in UV, and therefore a Cauchy model extrapolation was used to retrieve *n* and *k* at 193 nm.

4.3.3 Laser ablation set-up

We used a laboratory Argon Fluoride (ArF) excimer laser (LPF200, Lambda Physik, Göttingen, Germany) delivering laser pulses (wavelength 193 nm, pulse duration 20 ns) to perform local ablation in Filofocon A and PMMA. The laser fluence was continuously adjusted by rotating a coated fused silica window inserted into the beam path, whose transmission depended strongly on the angle of incidence. The laser was operated at a repetition rate of 1 Hz in order to avoid remains of the expanding ablation plume to shield the sample from the next incident pulse.

The beam profile incident on the sample was designed to be top-hat to a very high purity by using an imaging setup. The latter consisted of a fused silica biconvex lens (focal length= 90 mm at 193 nm) that imaged a 4.5-mm diameter circular aperture, inserted into the beam path 2 meters after the laser output, precisely onto the sample surface. The exact z-position of the sample (image plane of the circular aperture plane) was adjusted until no diffraction rings surrounding ablation spot borders could be observed. Absolute energy measurements were performed using a calibrated energy detector (Gentec ED 100A).

The linearity of the ablation depth versus number of pulses was assessed by performing series of irradiations at constant fluence, varying the number of pulses (1 to 600 pulses). The measurements were repeated for different fluences (70 mJ/cm^2, 140 mJ/cm^2, 240 mJ/cm^2 and 400 mJ/cm^2). The agreement with a Lambert-Beer law was assessed by performing series of irradiations with varying fluences (from 30 to 400 mJ/cm^2) for three different number of pulses (1, 3 and 10).

4.3.4. Crater depth measurement by non-contact profilometry

The PLµ optical profilometric microscope described in Section 2.1.1.2 was used to measure the ablated samples. The interferometric mode of the microscope, with 20x and 50x interferometric objectives, was used to measure the ablation depth of each spot. A three dimensional topographic map of the spot was obtained. The instrument software for measurement analysis was used to remove tilt and to obtain the ablation depth from diametral profiles of the crater.

4.3.5 Data analysis

For each fluence series, ablation depths were plotted against the number of pulses. The regression coefficients of the linear fits to the data provided a numerical quantification of the linearity. The number of incubation pulses was also obtained from these fits as the number of pulses where the linear range reaches zero ablation depth.

For each series with equal number of pulses, the ablation rate (ablation depth per pulse) was plotted versus the natural logarithm of the fluence (see Eq. (4.3)) to obtain an experimental assessment of the Beer Lambert behavior of the material. The ablation threshold (F_{th}) is the fluence value separating two different regimes. Below F_{th}, the ablation rate is extremely low and flat. Above F_{th}, the ablation rate changes linearly with fluence. A linear fit to this second regime provided estimates of F_{th} (fluence value in which the ablation rate intersects zero) and of the effective absorption coefficient α_{eff} (inverse of the slope of the fit).

4.3.6 Microscopic structure of the ablation

The bright field imaging mode of the profilometric microscope described in Section 2.1.1.2 was used to obtain optical micrographs (100x) of the ablated samples. High-resolution measurements of the surface topography in the crater centre were performed with the SmartSPM 1000 fast Atomic Force Microscope (AFM) developed by AIST-NT Co (Moscow, Russia).

4.4. RESULTS

4.4.1. Optical properties

Table 4.1 shows the results of the refractive index (n) and extinction coefficient (k) measurements (and the corresponding absorption coefficient α, obtained from Eq. (4.2)) for both PMMA and Filofocon A, at the ablation wavelength (193 nm) and in the visible (540 nm).

Previous works on PMMA optical properties reported a similar refractive index in the visible but a lower one (1.49) at 193 nm (Wochnowski et al., 2000, Pfleging et al., 2003). The discrepancy is probably due to different additives or dopants in the material. The refractive index of Filofocon A measured in the visible matches the nominal data (1.46). To the authors' knowledge, the optical properties of Filofocon A

had never been reported at 193 nm, showing an extinction coefficient that is a factor of ten higher than that of PMMA.

Table 4.1. Refractive index (n) and extinction coefficient (κ) measurements for both PMMA and Filofocon A. The corresponding absorption coefficient (α) is also shown.

	n (193)	k (193)	α (193)	n (540)	k (540)	α (540)
PMMA	1.635	0.00585	3809 cm^{-1}	1.495	0.00013	30.3 cm^{-1}
Filofocon A	1.623	0.05483	35700 cm^{-1}	1.456	0.00122	289.0 cm^{-1}

4.4.2. Ablation profiles

Figure 4.1 shows typical profiles of the ablation craters found in PMMA and Filofocon A. PMMA ablation craters show central islands. The figure shows a typical example, although not all the central islands are so symmetric. These ablation artifacts are not present in Filofocon A.

The diameter of the spots is constant across materials and conditions (except for very high number of pulses at high fluence, in which thermal effects degrade the ablation walls). This diameter (422 microns) was used to calculate the irradiated area, and to set a multiplicative factor between the energy measurement of the detector and the fluence units (mJ/cm^2). The flatness of the crater floor combined with the steep crater walls justifies this procedure to calculate the fluence values.
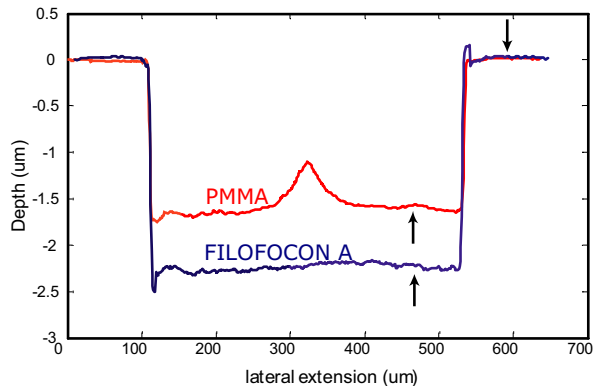
Fig. 4.1. Typical ablation profiles for PMMA and Filofocon A. These profiles are obtained as diametral cross-sections of the measured interferometric topography. The crater diameter is 422 microns. Crater depth was obtained comparing the depths measured in the proximity of the vertical arrows (see text). The profiles shown in the figure were obtained for 10 pulses at 240 mJ/cm^2.

Ablation depths were obtained for each ablated sample as in the example shown in Fig. 4.1. In order to avoid measurement artifacts near abrupt edges (oscilations in the interferogram) and central islands, depth measurements were performed in the proximity of the arrows of Fig. 4.1. For each crater topography, 2 to 10 depth measurements were obtained (depending on the roughness of the profile and the variability of the different diametral profiles) and the results averaged.

4.4.3. Linearity of ablation depth with pulse number

Figure 4.2(a) shows the ablation depth as a function of the number of pulses, for fixed fluences. For the sake of clarity ablations with very high number of pulses (>600) are not shown. The error bars are also not shown, as they are negligible in this scale (smaller than the symbol size). All points of each fluence series of ablation depth vs. number of pulses were fitted to a linear equation. There is a high linear relationship, both for PMMA and for Filofocon A. The regression coefficient (R^2) was higher than 0.999 in all cases.

   Figure 4.2(b) shows a closer view near the origin of the data shown in Fig. 4.2(a) (i.e. for few pulses and low ablation depths).

   For the higher fluences (400 and 240 mJ/cm^2) the ablation depth is larger (deeper penetration) for Filofocon A than for PMMA, for the same number of pulses. For the lower fluences (140 and 70 mJ/cm^2) this depends on the number of pulses.
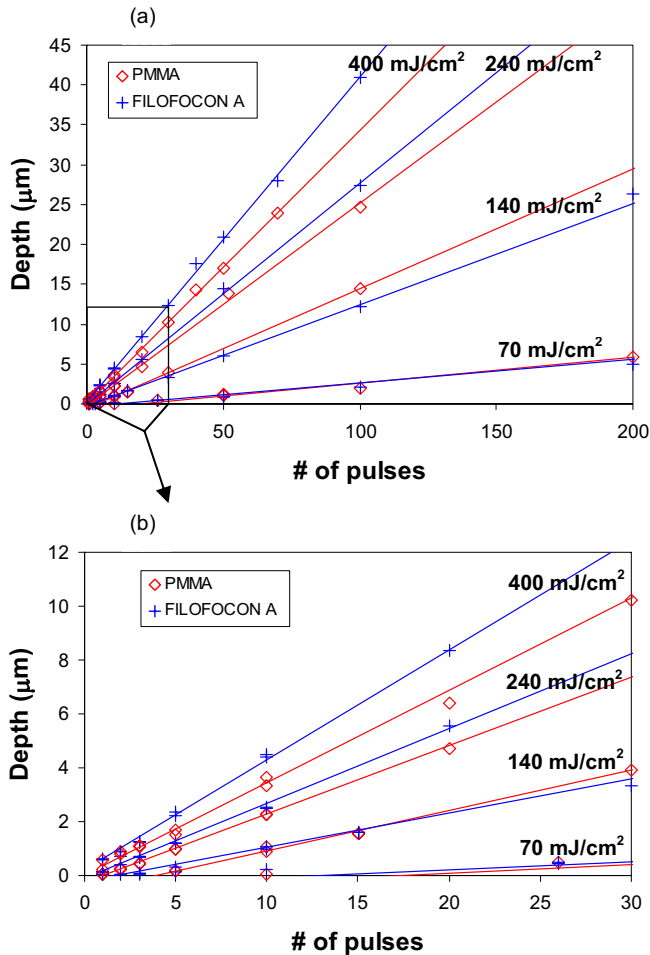
Fig. 4.2. Ablation depth as a function of the number of pulses, for selected fluences. a) 0 to 200 pulses. b) 0 to 30 pulses (zoomed view).

Although the data are well fitted by linear regressions, the fitted lines only cross the origin at 400 mJ/cm^2. This is a result of incubation, which is quantified as the number of the first pulses that do not contribute to ablation depth. Figure 4.3 shows the number of incubation pulses at all laser fluences, for the two materials. Filofocon A requires less incubation pulses than PMMA for a given fluence. The number of incubation pulses for Filofocon A is less than 2 above 140 mJ/cm^2 (4 pulses for PMMA). At 400 mJ/cm^2 the incubation is negligible (<0.01 pulses) for both materials.
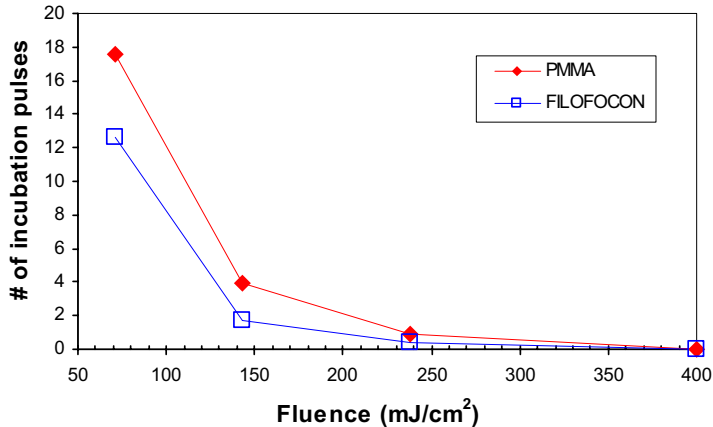
Fig. 4.3. Number of incubation pulses as a function of laser fluence.

4.4.4 Beer Lambert law: ablation threshold and absorption coefficient

The measured ablation depth was plotted against the natural logarithm of fluence (Beer Lambert law, Eq. (1.7)) for constant number of pulses. Figure 4.4 shows four representative examples of the experimental Beer Lambert plots for 10 and 1 pulses, for Filofocon A (Fig. 4.4(a)) and PMMA (Fig. 4.4(b)).

The bends of the 1-pulse curves near the ablation threshold -green small symbols in Fig. 4.4(a) (Filofocon A) and orange small symbols in Fig. 4.4(b) (PMMA)- could be indicative of a low energy ablation regime occurring below 0.08 μm/pulse. For these points (with fluence lower than 200 mJ/cm^2 for Filofocon A and 275 mJ/cm^2 for PMMA) the incubation is close or above one pulse (see Fig. 4.3). For higher number of pulses, there is an abrupt change between the two regimes. The zero intercept of the linear fits provide the estimated ablation thresholds (F_{th}), and the slopes represent the effective absorption coefficient α_{eff} . As the number of pulses increases, both the ablation threshold and the slope decrease.

Figure 4.5 shows estimations of the ablation threshold (a) and the effective absorption coefficient (b). The large open symbols and solid line represent the values for 1, 3 and 10 pulses estimated directly from the depth/pulse vs ln(Fluence) functions, as in the examples shown in Fig. 4.4. The small solid symbols and dashed lines represent estimates for higher number pulses (as typically required in refractive laser ablations). These values were estimated from the linear fits in Fig. 4.2 to obtain interpolated depth/pulse data for an arbitrary number of pulses. This approach is valid given the linear behavior of the ablation depth as a function of the number of pulses

(Fig. 4.2), and the Beer Lambert behavior of the ablation depth/pulse (Fig. 4.4). For all estimates, we checked that the number of pulses was above incubation and the fluence above the ablation threshold.
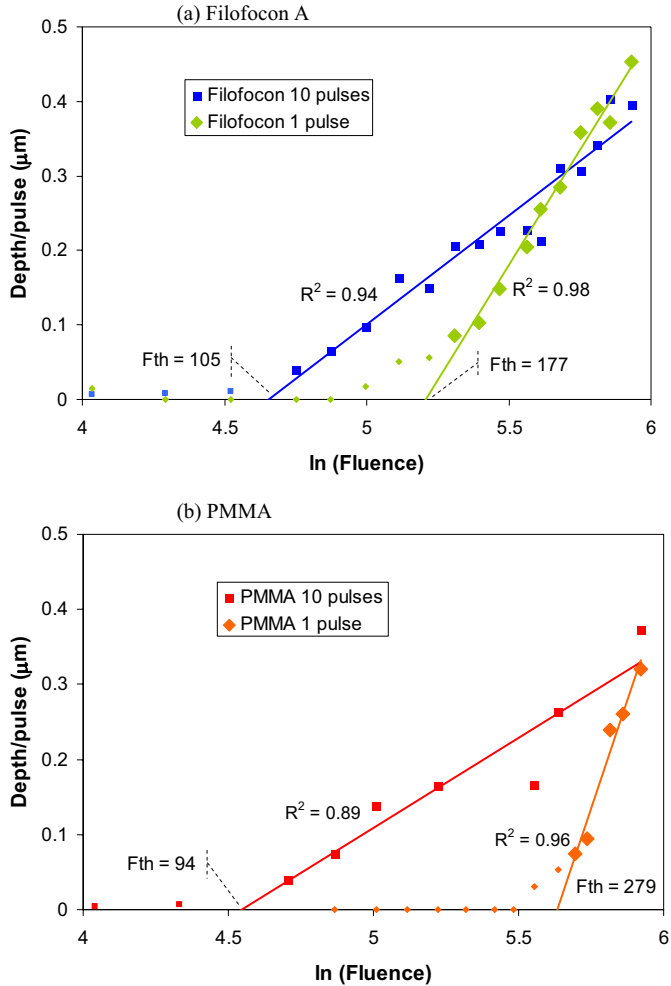
Fig. 4.4. Beer Lambert behavior for Filofocon A (a) and PMMA (b) for 10 and 1 pulses. The linear fits provide the estimated ablation thresholds (zero intercepts of the line), and the effective absorption coefficient (slopes). The regression coefficient, R^2, and the ablation threshold, F_{th}, are shown for each linear fit.

For more than 10 pulses, the ablation threshold is lower in PMMA than in Filofocon A, while the effective absorption coefficient is higher for PMMA (Fig. 4.5). The ablation threshold decreases and the effective absorption coefficient increases with the number of pulses in both materials. Filofocon A ablation parameters approach asymptotic values faster (with lower number of pulses) than PMMA. With 40-pulse ablations, the values of ablation threshold and absorption coefficient for Filofocon A are less than 2% higher those at 100 pulses (F_{th} = 90 mJ/cm^2 and α_{eff} = 36000 cm^{-1}).

For PMMA, more than 70 pulses are required to reach 2% of the corresponding values at 100 pulses (F_{th} = 66.79 mJ/cm^2 and α_{eff} = 52000 cm^{-1}).

(a) Ablation Threshold

(b) Effective absorption coefficient
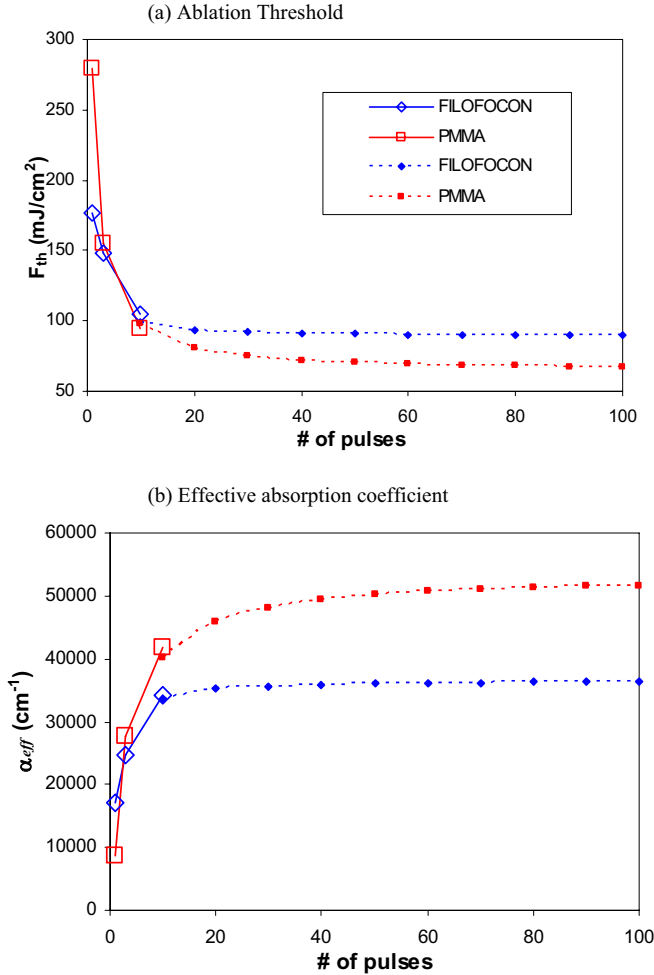
Fig. 4.5. Ablation properties vs number of pulses for Filofocon A and PMMA: a) Ablation threshold and b) Effective absorption coefficient. Large open symbols -solid line- come from the data of Fig. 4.4. Small solid symbols (dashed line) derived from a second analysis of Fig. 4.2(a). See text for details.

4.4.5 Microscopic structure of the ablation craters

Visual inspection of the ablated samples shows that they are transparent up to 240 mJ/cm^2. At this and higher fluences a progressive darkening with the number of pulses appears in Filofocon A, but not in PMMA. High magnification (100x) reflection images confirms this darkening inside the ablation, revealing different structures in the ablated areas for Filofocon A and PMMA. These images also show a border around the ablated areas which is darker and broader in PMMA. Figure 4.6 shows high

magnification optical images of unablated (left side of the image) and ablated (right) areas in Filofocon A (Fig. 4.6(a)) and PMMA (Fig. 4.6(b)), for 30 pulses and a fluence of 400 mJ/cm^2. The different structures inside the ablated area (right part of each image) are also present even with very low number of pulses.
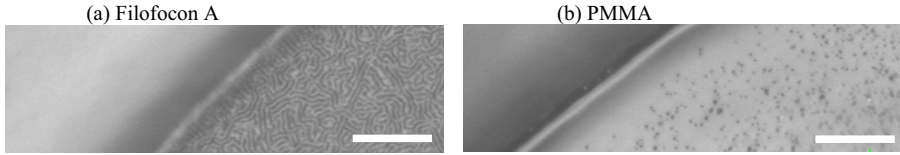
(a) Filofocon A   (b) PMMA

Fig. 4.6. High magnification (100x) optical micrographs of Filofocon A (a) and PMMA (b). In both pictures, the ablated zone (400 mJ/cm^2, 30 pulses) is on the right. The scale bar is 10 μm.

AFM images (shown in Fig. 4.7) confirm that these structures, close to the resolution limit of the camera of the optical microscope, are real physical structures and not optical effects such as aliasing.
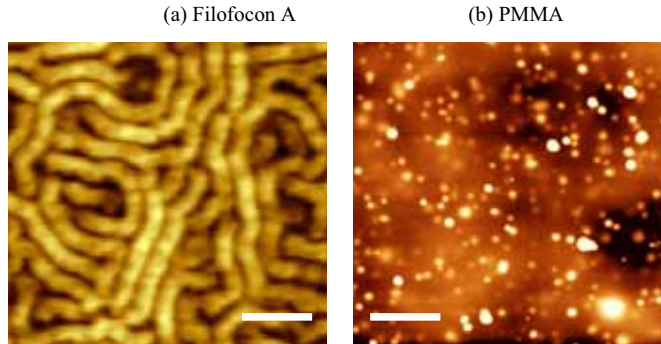
(a) Filofocon A   (b) PMMA

Fig. 4.7. AFM images of the ablated zone (400mJ/cm^2, 30 pulses) in Filofocon A (a) and PMMA (b). The scalebar is 2 μm. The peak to peak depth (color scale range) is 300 nm.

4.5. DISCUSSION

We have studied the excimer laser ablation of Filofocon A and PMMA materials, in the operational range of refractive surgery. These materials have been used in previous studies in experimental models of corneal refractive surgery (Dorronsoro et al., 2006a, Chernyak and Campbell, 2003, Dorronsoro et al., 2008a), although their ablation properties were not well established.

Both materials show a large range of linear dependence between ablation depth and number of pulses, for different fluences (see Fig. 4.2) as well as between ablation rate (depth/pulse) and the logarithm of the fluence (Beer Lambert law, see Fig. 4.4). We have measured optical and ablation properties of these materials at 193 nm (including index of refraction and extinction coefficient, ablation threshold and effective absorption coefficient) and investigated the structural changes in the material following ablation. We have shown that incubation is not negligible for low fluences, and that the ablation parameters change with the number of pulses, more so in PMMA

than in Filofocon A. All these findings are very relevant for the development of plastic models to assess refractive surgery ablation profiles and correction factors for ablation algorithms.

The results for PMMA can be compared with those in the literature in terms of ablation rate (obtained from the Beer Lambert parameters). At 500 mJ/cm^2, our estimates of ablation rate range between 0.39 and 0.42 microns/pulse (depending on the number of pulses) while Fisher and Hanh (Fisher and Hahn, 2004) reported 0.47 microns/pulse. Calculations from the data of Costela et al. yield an ablation rate of 0.45 (Costela et al., 1995), from Braren et al. (Braren and Seeger, 1986) 0.47, and from Srinivasan (Srinivasan and Braren, 1984) 0.43. Regarding incubation, Fisher and Hahn (Fisher and Hahn, 2004) reported the absence of appreciable incubation at 500 mJ/cm^2, and Pettit et al. (Pettit et al., 1991) reported 18 pulses at 115 mJ/cm^2 and 2 pulses at 265. All these results are in good agreement with those reported in this study, specially given the diversity of experimental methods and ablation conditions of the different studies (i.e. fluence range), and the possible discrepancies due to different amounts and types of impurities of the polymer.

4.5.1. Measuring a laser ablation pattern: energy to depth relationship

Plastic plates (generally of PMMA) are typically used in clinics to calibrate the fluence of the refractive surgery excimer laser. Depth measurements are usually performed (using a gauge) in the center of the ablation only, and related to laser fluence. But new standards (2007) recommend a profilometric evaluation of the entire ablated shape. Knowledge of the ablation rates of the plastic calibrating material is needed. Also, incubation and varying ablation properties with the number of pulses can affect the proportionality between the laser energy pattern and the measured ablation depth.

Clinical lasers differ in the energy profile of the laser spot. For flying spot laser systems, it is assumed that the achieved ablation depth at each point is proportional to the number of pulses. While this is only true for uniform spots (top-hat) profile, it is a good approximation also for other profiles (Gaussian or truncated Gaussian) provided that the density of pulses is high (with uniform overlapping) (Huang and Arif, 2002). The fluence of operation also differs across lasers (typically between 120 mJ/cm^2 and 400 mJ/cm^2), and consequently the number of pulses to achieve a given correction in cornea is different (with higher fluence lasers using a lower number of pulses and lower fluence lasers using a higher number of pulses). Our results demonstrate that for plastic models (as others have also suggested in corneal tissue (Fisher and Hahn, 2007, Jimenez et al., 2006)), the energy to depth relationship is potentially affected by incubation, proximity to the ablation threshold and variable ablation parameters, especially for low fluence lasers.

To explore these limitations in practice, it is necessary to refer the measured ablation properties to the characteristics of the refractive surgery lasers and of the clinical ablations (typical fluences and number of pulses). Previous profilometric measurements (Dorronsoro et al., 2008a) of the ablation profiles (for -9 D) on Filofocon A plates performed with different clinical lasers allow us to estimate the number of laser pulses applied to each given location, using the Beer Lambert parameters obtained in the present study and the nominal peak fluences of the lasers. The refractive surgery lasers under consideration were Technolas 217 Z100, Bausch&Lomb, with a peak fluence of 120 mJ/cm^2 and Ladar Vision, Alcon, with a peak fluence of 400 mJ/cm^2. It was estimated that the laser produced 124 pulses at the

edge of the 6.5-mm optical zone for the Technolas system (which is consistent with the total number of pulses of the ablation pattern, 4233, provided by the laser manufacturer) and 12 pulses for the Ladar Vision. These numbers of pulses are well above the number of incubation pulses for both materials determined in the present study (Fig. 4.3), for the corresponding laser fluences. These fluences are above the ablation thresholds for Filofocon A and PMMA (Fig. 4.5), indicating that the ablations are performed in the Beer Lambert linear region. Also, the effect of the variation in the ablation properties (the difference between considering the asymptotic or the real values for the ablation threshold and the effective absorption coefficient) is below 1 pulse for both materials and both lasers. One-pulse error (a fraction of a micron) is considered negligible in the design and characterization of ablation algorithms (2007). Therefore, in these two lasers and these two materials the energy pattern is expected to be correctly transferred to depths of ablation or, alternatively, the measured depth pattern reflects correctly the laser energy pattern. But, as PMMA has a higher number of incubation pulses and a higher variability in its ablation parameters, it is more subject to low-pulse number related artifacts than Filofocon A. In identical conditions, the error in depth can be up to three times larger in PMMA than Filofocon A.

Although it is not the case for the two lasers studied in Ref. (Dorronsoro et al., 2008a), under certain circumstances regions may be approached where the Beer Lambert law fails (number of pulses close to incubation, fluences near the ablation threshold and altered ablation properties). These circumstances include lower effective fluences (due to reduced laser fluence or radial efficiency losses), ablation patterns with shallow regions (as hyperopic patters), edges of the optical zone for low corrections, or transition zones. As a rule of thumb to avoid these effects, at a fluence of 120 mJ/cm^2, ablated zones deeper than 5 μm in Filofocon A and 7 μm in PMMA can be considered correctly ablated (with alterations in the depth pattern less than 1 pulse or 0.15 μm). At a fluence of 400 mJ/cm^2, all ablations are correctly transferred to depths. Since both materials show high linearity with the number of pulses, a valid strategy to avoid those effects is to multiply the number of pulses at each point, applying repeated ablations to the material.

4.5.2. Measuring ablation efficiency

An additional application of plastic corneal models for refractive surgery is the measurement of radial laser efficiency changes and calculation of correction factors. This is a more sophisticated application and involves the ablation of curved surfaces, with a geometry similar to that of the cornea (Dorronsoro et al., 2006a). The measured depth pattern in curved surfaces is compared with that obtained from flat surfaces in identical conditions. In this case, the pulse distribution pattern is exactly the same in both conditions, and the difference in depth is only due to geometry-associated variations in ablation efficiency.

The fact that the energy pattern can be correctly measured in flat surfaces of Filofocon A, and the linearity of the Beer Lambert in the ranges of operation, indicates that local energy differences associated to efficiency changes will be transferred to depth changes. The experimental complexity of measuring efficiency effects seems then to be associated to achieving precise alignment and accurate measurement techniques for the curved surfaces, and not to the ablation properties of the material. The same can be applied to the measurement of the induced asphericity (by refractive surgery) in curved surfaces.

4.5.3. Central islands in PMMA

Central islands are systematically observed in the ablation spot profiles in PMMA (Fig. 4.1), but not in Filofocon A. Our results reveal that it is a multipulse effect, not appearing with single pulses. This suggests that defect accumulation during the first pulses can play a role in the island formation.

AFM images (Fig. 4.7) also suggest different ablation mechanisms in Filofocon A and PMMA. The droplets observed in PMMA may be indicative a more explosive mechanism than in Filofocon A, where a dense worm-like structure appears after the ablation. These are also found to be multipulse effects. As the number of pulses increase, the droplet density increase in PMMA, while the worm thickness decreases in Filofocon A.

Central islands have been extensively reported in corneal tissue as isolated areas within the optical zone where the laser ablated tissue less efficiently. Central islands have been associated to shockwaves in water, shielding effects due to the plume and particle redeposition (Noack et al., 1997, Munnerlyn et al., 2006). Central islands have been also been observed in PMMA (Noack et al., 1997, Munnerlyn et al., 2006). It is remarkable that it is not observed in Filofocon A, indicating that the effect is not inherent to the laser energy distribution. In any case, as was previously reported in corneas (Munnerlyn et al., 2006), the use of flying spot lasers in refractive surgery, and the associated averaging effect, reduces the impact of inhomogeneities in the laser spot.

4.5.4. Absorption coefficient

It is enlightening to compare the absorption coefficient α determined from low intensity ellipsometric measurements (Table 4.1) to the effective absorption coefficient α_{eff} estimated from the slope of the Beer-Lambert representation and plotted in Fig. 4.5. The corresponding values differ strongly for PMMA, with α_{eff} always being much higher than α even for a low number of pulses. This is consistent to what is reported in the literature for PMMA (Srinivasan et al., 1986, Kuper and Stuke, 1987). In contrast, we observe a perfect agreement for Filofocon A in the stationary saturation regime at high pulse numbers (≥ 10 pulses). This agreement points to a fundamentally different absorption mechanism in Filofocon A, truly following a Beer-Lambert law in the multipulse regime as opposed to PMMA. As a consequence, the ablation behavior is expected to be also influenced, as evidenced by the different surface morphology/topography shown in Figs. 4.6 and 4.7.

4.6. CONCLUSIONS

We have presented the ablation properties of Filofocon A and PMMA in the operational range of refractive surgery excimer lasers.

PMMA is often used as an ablation material in the calibration of clinical lasers, and in model eyes (as that presented in Chapter 3). Filofocon A has been identified as appropriate material for refractive surgery research, and we will present an experimental model based on Filofocon A in the next chapter. We have learned that the ablation properties of Filofocon A make it a better material than PMMA for laser ablation refractive surgery research and for the development of calibration protocols. Filofocon A provides a more accurate energy-to-depth conversion (with no central islands and other ablation artifacts), has a predictive absorption coefficient, and shows

lower number of incubation pulses and ablation parameters less dependent on the number of pulses.

These findings are useful to design calibration and validation procedures for the refractive surgery excimer lasers, and to improve the outcomes and predictability of new ablation profile designs.

4.7. OUTLOOK

The optical and ablation properties of a new material, Filofocon A, have been measured for the first time. Knowledge of these properties is essential to establish accurate plastic models for refractive surgery. In the next chapter, we will use Filofocon A into a new refractive surgery model to predict experimentally the optical outcomes of state-of-the art laser refractive surgery laser platforms

Chapter

5

Evaluation of ablation profiles, post-operative outcomes and ablation efficiency factors of different optimized laser platforms

This chapter is based on the article by Dorronsoro et al. "Experimental evaluation of optimized ablation patterns for laser refractive surgery", published in Optics Express Optics Express, Vol. 17, Issue 17, pp. 15292-15307 (2009). This study was partially presented at ARVO 2008 (Dorronsoro et al., 2008a).

The contribution of Carlos Dorronsoro to the study, in collaboration with other coauthors, was the literature search, the design of the experiments, the ablations in clinical sites, the development of the measurement procedures, the measurement of the ablated surfaces, the development of the data analysis routines and the analysis itself.

Coauthors of the study are Laura Remon, Jesús Merayo-Lloves, Benjamín Alonso-Fernandez and Susana Marcos.

5.1 ABSTRACT

Purpose: Previous analytical, computational and experimental studies suggest that the increased asphericity found after myopic refractive surgery (and as a consequence, the induced spherical aberration) is largely due to laser efficiency losses from the corneal apex to the periphery. These effects can be measured experimentally to calculate a correction factor for each laser. This chapter further investigates the geometrically-related laser efficiency losses for three state of the art laser platforms, provided with optimized algorithms and their effect on plastic corneal models.

Methods: A new experimental model based on plastic (Filofocon A) artificial eyes was used to study the ablation profiles and the outcomes of three current clinical refractive surgery excimer lasers provided with narrow-beam flying spot and optimized algorithms (Ladarvision 4000, Alcon; Technolas 217 Z100, Bausch&Lomb; Allegretto wave Eye-Q, Wavelight). The line of sight of the artificial eye was aligned with the laser fixation reference, using an artificial retina (CMOS chip) and a tip & tilt platform. In-eye artificial pupils allowed centration as in patients' eyes. The 3-D ablation patterns produced by myopic laser corrections (-9, -6 and -3 D) on flat and spherical surfaces of Filofocon A were measured using high resolution optical profilometry.

Results: We found significant differences across lasers in the shape and depth of the ablation patterns. A comparison of the ablation patterns on flat and on spherical surfaces provided a measurement of the laser efficiency losses from the center to the periphery at each point of the spherical plastic corneas. This effect also varied across lasers, depending on their fluence (120-400 mJ/cm^2). Estimates of the post-operative corneal shapes were obtained from the measurement on Filofocon A and plastic-corneal tissue correction factors. The predicted post-operative corneal ablation shape, ablated volume, asphericity and spherical aberration varied across lasers, as well as the relative contribution of ablation pattern designs and efficiency losses to the increased asphericity.

Conclusions: Although the results show that the algorithms have been optimized to reduce the induction of spherical aberration, they would still benefit from the application of correction factors for efficiency effects derived from a systematic approach using experimental plastic models. These models have proved useful (1) to assess the outcomes of different lasers or ablation algorithms, (2) for precise calibration and testing of the lasers, and (3) to calculate experimental correction factors for efficiency effects.

5.2 INTRODUCTION

Chapter 3 introduced an experimental model for refractive surgery, based on the ablation of flat and spherical plastic surfaces. Chapter 4 presented a new material, Filofocon A, with interesting properties for refractive surgery research, along with improved methodology. The know-how from these two previous studies will be combined to produce an improved experimental model, using Filofocon A as base material for the artificial eyes, presented in this chapter. Apart from the new material, the improved surface measurement methods presented in Chapter 4 will be used, and the optical set-up of the model will be improved to overcome some of the limitations (alignment and centration) of the model presented in Chapter 3. Finally, the model will be applied to the study of three optimized clinical lasers, with new-generation algorithms.

Filofocon A has been identified as an appropriate material for plastic models since, as shown in Chapter 4, it produces a linear response to the laser pulses at all points. As we have obtained precise measurements of the ablation properties of Filofocon A (Dorronsoro et al., 2008b) (see Chapter 4), it will be possible to extrapolate the results to corneal tissue. The use of Filofocon A in combination with clinical lasers has not been reported before.

In this chapter we describe a new design for Filofocon A model eyes, including a new eye support that improves alignment. Flat and spherical artificial eyes were ablated with three different clinical lasers, provided with different optimized algorithms. The shape of the surfaces was measured with high resolution optical profilometry. Evaluation of the ablation profiles on flat surfaces allowed us to test the actual ablation pattern programmed into the laser system, differences across lasers, and possible miscalibrations of the laser units. Ablations on spherical surfaces allowed measuring changes in asphericity after refractive surgery. A comparison of the ablation profiles on spherical surfaces and identical ablations on flat surfaces allows quantifying geometry-related ablation efficiency losses. Once the differences in ablation and optical properties between plastic and corneal tissue are considered, it is possible to estimate the correction factor for efficiency effects for corneal tissue, and the relative contribution of physical factors affecting the post-operative corneal shape. Although efficiency losses are more important in PTK or hyperopic profiles, myopic procedures are much more common, and larger clinical databases are available for myopic than for hyperopic LASIK. Consequently, we chose myopic algorithms because the study of these patterns across lasers would have a larger impact in the clinical practice.

Although the results are obtained for particular laser systems, the understanding of the physics of the ablation in curved surfaces, and the methodology described can be generalized to design better ablation algorithms, not only for refractive surgery, but also for related areas, as customized contact lens manufacture.

5.2. METHODS

5.2.1. Lasers

Table 5.1 shows the three laser platforms used in this study, provided with state-of-the-art optimized algorithms. All lasers used flying-spot technology, and were Argon Fluoride (ArF) excimer lasers (193 nm emission wavelength) delivering nanosecond-

pulses. Fluence, repetition rate, and spot shapes and diameters varied across lasers. The optical zone was set to 6.5 mm in all cases.

5.2.2. Artificial eyes

The artificial eyes consisted on plastic cylinders of Filofocon A (Dorronsoro et al., 2008b), with a diameter of 12.7 mm, finished either on a polished flat or spherical (7.8-mm nominal radii of curvature) surface. All eyes had an artificial iris (6.5 mm aperture) located 3.5 mm behind the artificial cornea. The artificial iris is formed by a groove painted on its anterior surface. The nominal eye length was 24.65 mm in all eyes, so that the back focal plane of the spherical surfaces is near the back surface - also polished- of the cylinder. The artificial eyes were manufactured by MedLens, INC, Front Royal, VA, USA. The first surface was re-polished in a precision optics lathe to ensure high surface precision (individually assessed on a profilometer, section 2.4) before the ablations. To define the orientation of the artificial corneas, they were marked at the edge with a 1-mm length meridional line. Figure 5.1(a) shows a photograph of two of the artificial eyes of the study. A total of 40 Filofocon eyes (20 flat and 20 spherical) were ablated under different conditions during the study.

The artificial eyes were placed in a support (see Fig. 5.1(b)) that consists of a CMOS chip (from a webcam) acting as an artificial retina, a tip and tilt platform (for both the eye and the CMOS chip), and a tunable filter. The pixel position of the CMOS chip corresponding to the center of the cylinder was previously calibrated and considered as the artificial fovea. The artificial fovea and the artificial pupil define the line of sight of the artificial eye, which can be oriented using the tip and tilt platform.

Table 5.1. Laser platforms used in this study. (Nominal data from www.fda.gov)

	Alcon LADAR Vision	Bausch & Lomb Technolas 217Z100	Wavelight Allegretto EyeQ
Algorithm	Standard	Zyoptix Tissue Saving	F-CAT
Peak Fluence (mJ/cm^2) Average Fluence	400 210	120	400 200
Repetition Rate	100 Hz	100 Hz	400 Hz
Spot Shape Spot Diameter (mm)	Gaussian 0.95	Truncated G. 1 and 2	Gaussian 0.95
Optical Zone	6.5 mm		
Ablation Zone	8 mm	9.6 mm	8 mm
Eye tracker	Disabled		
Wavelength	193 nm		

5.2.3. Ablation protocol with clinical lasers

The artificial eyes were ablated in the different operating rooms where the clinical lasers were located, and the full experimental procedure supervised by the investigators. The lasers were fine-adjusted and calibrated by each company's technical support experts before each session. During the ablations, the lasers were operated by the surgeon or the operating room assistants in charge at each clinic. All standard procedures were followed except for the eye tracker that was disabled (and thus the pupil centered manually). The optical zone was set to 6.5 mm. The ablation

patterns selected were: Zyoptix Tissue Saving for the Technolas 217 Z100, Standard algorithm for the LADAR-vision and F-CAT for the Allegretto Eye-Q.

An additional procedure was needed to align the artificial eye to the laser. Each clinical laser has a different fixation stimulus, typically a collimated laser beam (red line in Fig. 5.1 (b)). The alignment requires the superposition of that stimulus beam with the eye's line of sight (green line in Fig. 5.1 (b)). In practice, this involves bringing the stimulus (imaged on the CMOS sensor through the artificial eye) to the fovea (reference pixel), by adjusting the tip and tilt platform. To avoid image saturation of the fixation spot, the intensity of the fixation stimuli was adjusted with a tunable filter. The filter was moved aside during ablation. After fixation adjustment, pupil centration was achieved as in patients. The presence of multiple colinear reflexes confirmed the correct centration and alignment of the eye.

Pairs of flat and spherical artificial eyes were always ablated consecutively (see Fig. 5.2), under identical conditions (correction, algorithm, calibration state, centration and alignment). Right before each pair (flat/sphere) of myopic corrections, the laser fluence was checked (and calibrated if needed), and the alignment adjusted.

Five pairs of clinical ablations (on flat and spherical surfaces) were performed for each laser. Three pairs of refractive surgery procedures were performed with -9 D corrections, one pair with -6 D and one pair with -3 D. As the F-CAT algorithm (Wavelight) has adjustable target asphericity, with this laser we ablated two sets of artificial corneas with two different values of the parameter Q: Q=0 and 0.25.

We checked (using a thermosensitive sheet) that the differences in laser vergence from the center to the periphery were negligible. Therefore the ablations on flat surfaces should not be affected by non-normal incidence.
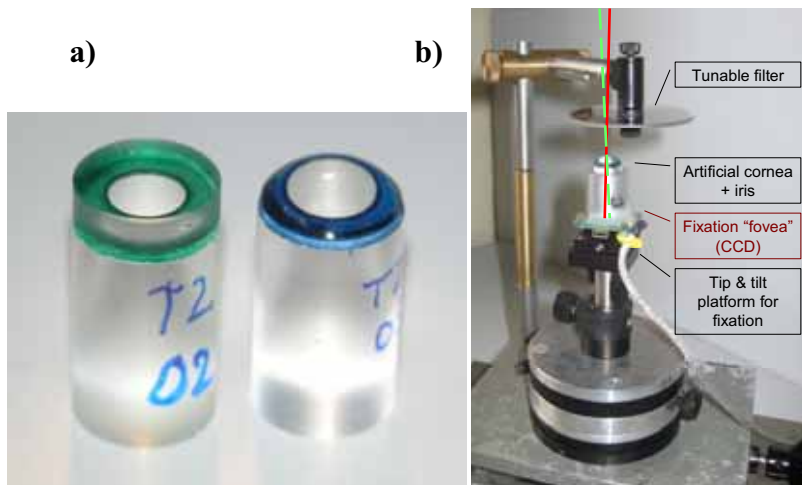
Fig. 5.1. a) Artificial eyes of Filofocon A (flat and spherical). b) Artificial eye support. The red line represents the fixation stimulus of the laser, while the green line represents the line of sight of the eye. Aligning means to make both axes coincident.

5.2.4. Pre- and Post- operative measurements

The PLμ optical profilometric microscope described in Section 2.1.1.2 was used to measure the shape of the first surface of the artificial eyes both before and after the

ablations. The slit-confocal configuration of the instrument was used to measure the surface height at each point, in an "extended shape" custom measurement mode.

Prior to the measurement, the artificial corneas were rotated until the reference mark was oriented along the y-axis of the microscope. The corneal apex, found using the 20x interferometric objective on the same instrument, was used as the origin for the measurements in the curved surfaces. In the case of flat surfaces, the apex was taken as the center of the cylinder (pre-operative) or the center of the ablation (postoperative).

All the spherical artificial corneas were measured before and after the ablation. All flat corneas were measured after the ablation. Only a few pre-operative flat corneas were measured, as the deviation from flatness was as low as the precision of the instrument (1 μm peak to peak for the whole surface).
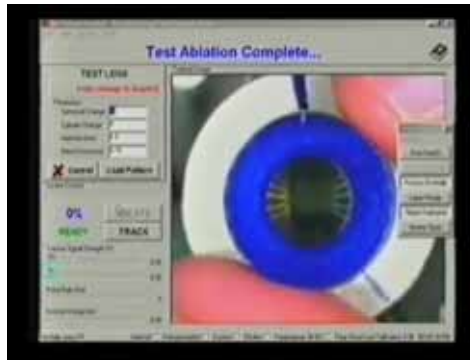
Fig. 5.2. Single-frame excerpt from video recordings of a refractive surgery procedure in a flat plastic artificial cornea of Filofocon A.

5.2.5. Data analysis

5.2.5.1. Extracting the ablation patterns

We wrote routines in Matlab (Mathworks, Nantick, MA, USA) to extract the laser ablation patterns from the shape measurements in flat and spherical surfaces.

The topographies measured on ablated flat surfaces should represent the actual spot density profile delivered by the laser. The measurements were only corrected numerically for the tilt found on the non-ablated area. This tilt appears in the measurement because the line of sight of the eye is not necessarily aligned with the microscope optical axis. We found tilts typically lower than 2 degrees. These tilts come from the topography measurement and not from the ablation, where the alignment and centration of the artificial eye were well controlled. We tested the procedure by measuring the same sample at different slight tilting angles, and checking that tilt was correctly compensated by the software.

The ablation pattern was also obtained from the ablated spherical corneas by subtracting a base sphere (corresponding to the pre-operative spherical surface) from the measured elevation. We found that subtracting the analytical surface produced a better estimation (less noise) than a point-by-point subtraction of elevation maps.

5.2.5.2. Computing the laser efficiency effects

The efficiency effects are described by the ablation efficiency factor K, depending on the incidence angle. For a particular geometry and material (plastic or cornea), the ablation efficiency factor is defined as the ratio of the ablation depth pattern on a spherical surface to the ablation depth pattern on a flat surface:

$$K = \frac{d_{SPH}}{d_{FLAT}}, \qquad (5.1)$$

where d is the ablation depth at each point. The effective ablation depth at each point of a curved surface can be predicted as $d_{eff} = d_{FLAT} \cdot K$. From a design point of view, $1/K$ represents the correction factor (one at the center and higher than one at the periphery) by which the intended profile should be multiplied to compensate for the changes in ablation efficiency on curved surfaces. The control algorithm should program d/K, in the laser, in order to obtain the desired pattern d ablated in the material.

For accurate estimations, it is essential that both ablations are registered, on the same coordinate center, which was estimated by fitting biconic surfaces to both ablation patterns. The selected radius of the base sphere subtracted from the ablated spherical surface elevation map was also critical in the assessment of the laser efficiency factor, as small discrepancies in the base sphere radius may result in slightly different ablation depths at the apex. As the ablation depth should be identical on flat and spherical surfaces in the center of the ablation, the base sphere radius was slightly refined (in steps of 0.05 mm) until that condition is reached. This refinement only affects the ablation patterns (estimated from spheres) in a few microns, but has a major impact on the fulfillment of the contour conditions (the efficiency factor is one in the center while the non-ablated zones are similar). The refinement needed in the base sphere is compatible with the small changes in the laser intensity observed between ablations and with the expected dilation effects on polymers (Goods et al., 2003) during the measurement.

5.2.5.3. Impact on cornea

The nominal ablation depth at the apex -provided by the system's software- is used to obtain a conversion factor between the ablation depth per pulse on plastic (Filofocon A) and corneal tissue. This factor changes with the laser, as it depends on fluence. The ideal ablation pattern in cornea (not affected by efficiency effects) can then be predicted by directly multiplying the ablation pattern on Filofocon by the plastic/cornea conversion factor.

To predict the actual shape of postoperative corneas, it is necessary to consider the geometry-related ablation efficiency factor for corneal tissue, which can be obtained from the ablation efficiency factor measured for plastic. According to the Beer-Lambert law, the etch rate (ablation depth per pulse) at each point of a flat surface should be given by $d_{FLAT}=(1/\alpha) \cdot ln\,(F_0 / Fth)$ where F_0 is the fluence of the laser and α and Fth are the absorption coefficient and the ablation threshold of the material respectively. The reflection loss is already implicit in the experimental estimates of ablation properties (α and Fth) as they were obtained from regressions of the ablated depth at different laser fluences on flat surfaces (Dorronsoro et al., 2008b). However, a reflection coefficient R, needs to be considered on non-flat surfaces

(Anera et al., 2003): $d_{SPH}=(1/\alpha) \cdot ln (F_0 R / Fth)$. That reflection coefficient depends on the surface geometry, incidence angle and refractive index. Then,

$$K = 1 + \frac{1}{\ln \dfrac{F_0}{Fth}} \ln R \tag{5.2}$$

The reflection coefficient R in this expression was obtained from the theoretical prediction of Jimenez et al. (ρ in Jimenez et al., 2002), but normalized to one, and therefore not including the reflection at the apex. The experimental (Eq. (5.1)) and theoretical (Eq. (5.2)) efficiency factors are normalized making both expressions for K equivalent. Operating with Eq. (5.2) for cornea K_C and Plastic, K_P we obtain:

$$K_C = 1 + \left(\frac{\ln R_C}{\ln R_P} \right)\left(K_P - 1 \right)\left(\frac{a_c}{a_P} \right) \tag{5.3}$$

Where $a_c = 1/ln(F_0 / Fth_C)$ and $a_P = 1/ln(F_0 / Fth_P)$, and the subscripts C and P stand for cornea and plastic respectively. The ablation thresholds Fth_C and Fth_P, and the refractive indices and surface geometry (through the reflection coefficients R_C and R_P) play a role in the conversion from the correction factor in plastic to the cornea. To calculate the correction factor for efficiency effects in cornea ($1/K_C$), we applied Eq. 5.3 point by point to the measured ablation efficiency factor in plastic. To estimate the postoperative corneal shape we multiplied the ideal ablation pattern in cornea obtained from the ablated flat plastic surfaces by the 2-D ablation efficiency factor in cornea. In this study we used the optical and ablation properties of Filofocon A reported in Ref. (Dorronsoro et al., 2008b): Fth_P=90 mJ/cm^2 and n=1.62. We used Fth_C=60 mJ/cm^2 and n=1.52 for the cornea.

5.2.5.4. Asphericities and spherical aberration

To assess the effect of the ablation pattern on the shape of the surfaces, we fitted the post-operative ablated spherical surfaces to conics and evaluated the change in asphericity (Cano et al., 2004). To study the clinical relevance of this shape change, we simulated postoperative corneas applying the corneal ablation pattern calculated in the previous section to spherical corneas of 7.8 mm. We calculated the corneal asphericity and the corneal spherical aberration of these simulated postoperative corneas (Barbero et al., 2002b).

5.3. RESULTS

5.3.1. Pre-operative shape measurements

The measured elevations of the pre-operative surfaces (plane or spherical) differed typically less than 1 micron (peak to peak) from their nominal shapes. The radius of curvature of the fitted spheres was also consistent with the nominal value (7.77±0.03 mm, on a 6.5-mm diameter). For diameters larger than 6.5-mm, a higher dispersion (up to 10 microns) was observed, more likely associated to the measurement technique than to the manufacture.

5.3.2. Ablation patterns on plastic

Figure 5.3 shows pairs (top row for flat surfaces, and bottom row for spherical surfaces) of representative ablation patterns for all lasers of the study. In all cases, a correction of –9 D was programmed in the laser. The ablation patterns differed notably across lasers. While the   Alcon and the Bausch & Lomb lasers provided highly symmetric patterns on both flat and spherical surfaces, the pattern delivered by the Wavelight laser showed asymmetries which were highly consistent across measurements.
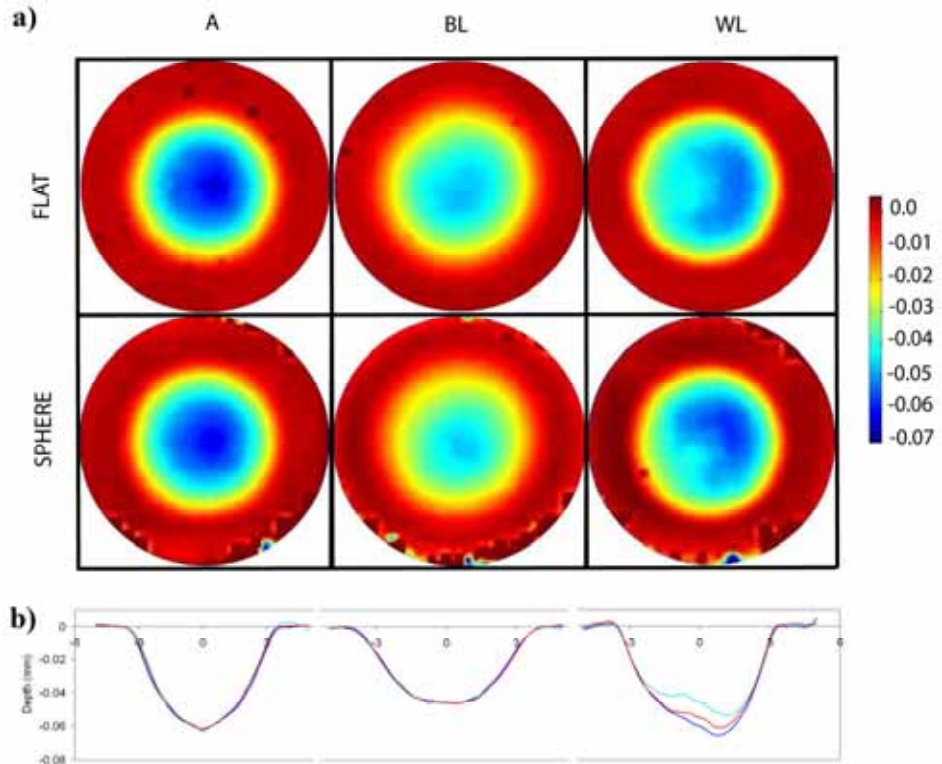
Fig. 5.3. a) Examples of ablation patterns obtained from ablated flat and spherical surfaces for the three different lasers, and a correction of -9 diopters. b) Horizontal sections of the ablation patterns on the flat surfaces (red lines), and other patterns obtained from different flat samples ablated on identical conditions (blue lines).

Efficiency effects were responsible for a lower ablation depth in peripheral areas on spherical than on flat surfaces. This effect is notably larger in low fluence lasers (i.e. Bausch & Lomb laser) than higher fluence lasers (i.e. Alcon).

Figure 5.3 (b) shows horizontal profiles of the ablation patterns on flat surfaces. The red lines correspond to the examples shown 2-dimensionally, while the blue lines correspond to different repetitions corresponding to different samples. The high similarity of the laser profiles estimated from different ablated samples (with the same laser and similar conditions) illustrates the high repeatability, particularly of the Alcon and Bausch & Lomb lasers. When asymmetries were present, as found with the Wavelight laser, the differences across repeated measurements also increased. The

asymmetries also appeared on different experimental sessions. Remarkably, the shape of the ablation profile and maximum ablation depth (on Filofocon A) differ substantially across laser platforms, for the same programmed refraction correction and optical zone.

5.3.3. Ablation efficiency factors on plastic

Figure 5.4 compares the ablation patterns for two of the lasers: Alcon (left side) and Bausch & Lomb (right side). Unlike Fig. 5.3 (b) where profile cross-sections of ablations on flat surfaces were plotted, Fig. 5.4 shows all the measured points in a radial plot, both for flat and spherical ablated surfaces (for -9 D corrections on Filofocon A). The figure illustrates the large differences in ablation patterns between the two laser platforms. Both the ablation depth and the radial extension of the ablated zone are different. These two lasers are also different in terms of efficiency losses. The high fluence laser (Alcon, left side of Fig. 5.4) is practically free from efficiency losses. The ablation pattern from flat and spherical surfaces are almost identical for this laser, as the measured point to point difference in depth between ablation in flat and spherical surfaces (less than 2 microns) is of the order of the measurement accuracy. Theoretical calculations using the formulation of Anera et al. (Anera et al., 2003) for the particular geometry of the artifical eyes and the ablation properties of this material (Dorronsoro et al., 2008b), predict a maximum difference of 1.1 microns.
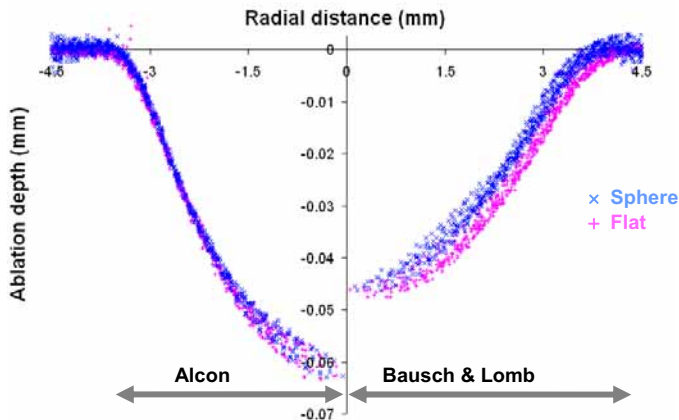
Fig. 5.4. Ablation patterns for two of the lasers: Alcon (left side) and Bausch & Lomb (right side). All the measured points are shown in radial plots, both for flat and spherical ablated surfaces (for -9D corrections on Filofocon A).

On the other hand, efficiency effects are clearly noticeable in the low fluence laser (Bausch & Lomb, right side of Fig. 5.4), as the ablation depth is lower on spherical than on flat surfaces. The difference between the ablation pattern on flat and on spherical surfaces is zero at the apex and also outside the ablation zone. There are systematic point to point differences, as high as 6.8 microns in the intermediate points (the theoretical prediction was 6.3 microns).

Figure 5.5 shows the measured ablation efficiency factor on Filofocon A (K, calculated from Eq. 5.1) as 2-D maps and radial plots, for the Alcon (Fig. 5.5 (a and b)) and Bausch & Lomb (Fig. 5.5 (c and d)) lasers. The square pattern observed in Figure 5.5 (a) is a trace of the profilometer trajectory. The red line in the 1-D plots

(Fig. 5.5 (b and c)) represents the theoretical ablation efficiency factor (K, from Eq. 5.2) for the corresponding laser fluences (400 mJ/cm^2 and 120 mJ/cm^2 for the Alcon and Bausch and Lomb lasers, respectively), and using the ablation properties for Filofocon A that we have reported in a recent study (Dorronsoro et al., 2008b). The experimental ablation efficiency factor at each radial distance from the apex (black squares) is obtained as an angular average of all the measured points (in gray). While the efficiency factor is practically 1 at all points for the high fluence laser (Alcon), it decreases significantly from the center to the periphery in the low fluence laser (Bausch & Lomb). For this laser (and Filofocon A) the effectiveness of ablation in the periphery of the optical zone is only 60%. The theoretical model captures the main experimental trends. The reported ablation efficiency factors were obtained from –9 D ablation patterns. We performed the same analysis on flat/spherical ablated surfaces with –3 D and –6 D corrections, and obtained similar results, although noise had a higher impact on the measured ablation depths.
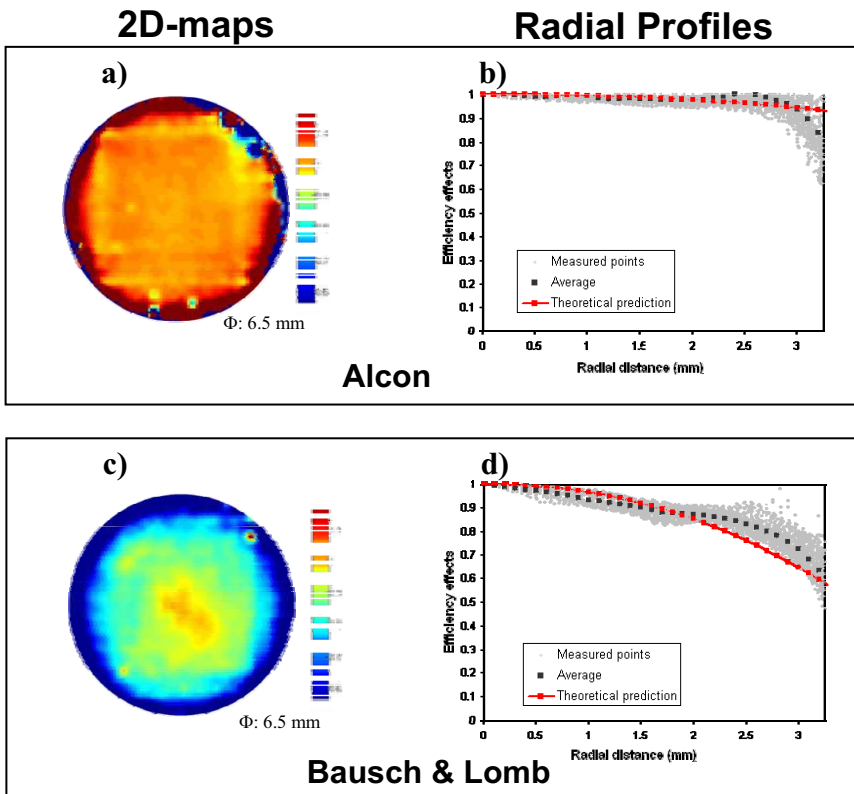
Fig. 5.5. Measured ablation efficiency factor in Filofocon A for the Alcon ((a) and (b)) and for the Bausch & Lomb laser ((c) and (d)). (a) and (c) show the efficiency effects at each point. (b) and (d) are radial profiles of all the measured points (gray). The black squares are the angular averages at each radial position. The red line represents the theoretical ablation efficiency factor for the corresponding laser fluences (400 mJ/cm^2 and 120 mJ/cm^2 for the Alcon and Bausch and Lomb lasers, respectively).

5.3.4. Ablation patterns in cornea

We applied the depth conversion factor and the ablation efficiency factor from Eq. 5.3 to the ablation patterns measured on flat surfaces to predict the ablation pattern on corneal tissue. Figure 5.6 shows predictions of the ablation profiles on flat and spherical corneas (Fig. 5.6(b)), from the ablation profiles measured on flat plastic surfaces (Fig. 5.6(a)). The differences in the ablation profiles as measured on Filofocon A between the Alcon and Bausch and Lomb lasers are clear in Fig. 5.6(a). In Filofocon, the Alcon laser (higher fluence) penetrates deeper in the plastic material and has a narrower ablation area while the Bausch & Lomb pattern on plastic is wider and shallower. The large differences in response between lasers are attenuated when the corresponding conversions to corneal tissue are applied (Fig. 5.6(b)). However, the ablation depth is significantly higher in cornea for the Bausch & Lomb laser, and the laser efficiency effects not negligible for this laser.
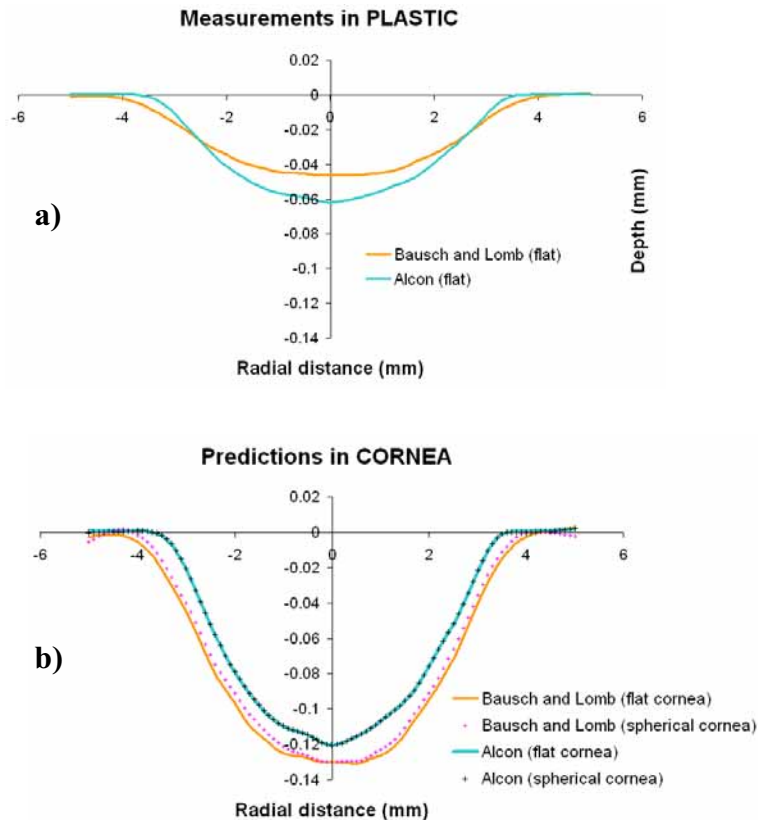
Fig. 5.6. Ablation profiles measured in Filofocon A flat surfaces (a) and predictions in corneal tissue (b) for flat and spherical surfaces.

We also estimated the ablated volume from the predicted 2-dimensional corneal ablation patterns, for the Alcon and the Bausch & Lomb lasers, considering the experimentally measured ablation efficiency factor. Table 5.2 shows the ablation depth measured in Filofocon A, the nominal depth in cornea provided by the laser

software, the corresponding depth conversion factor between cornea and Filofocon A, and the estimated ablated volume for the entire ablated area and within the optical zone.

It is interesting to note that the Zyoptix Tissue Saving algorithm of the Bausch & Lomb laser penetrates deeper in cornea and removes more material than the Standard optimized algorithm of the Alcon laser. Although the optical zone is the same in both lasers (6.5 mm) the ablated area is very different due to different design of the transition zones. Only 0.5% of the ablated volume is outside the optical zone with the Alcon laser (which has minimum transition zones), as opposed to 6.5% with the Bausch & Lomb laser. These ablated volumes were calculated considering the existing efficiency effects. If the efficiency effects were not considered (i.e. application on flat surfaces of the measured ablation profile, multiplied by the plastic-corneal tissue conversion factor) the ablated volume would be 5% larger for the Bausch & Lomb laser and 1% larger for the Alcon laser (within the optical zone in both cases).

5.3.5. Correction factors for efficiency effects in cornea

Figure 5.7 shows the correction factors for efficiency effects ($1/K$) predicted at each point of the human cornea for the Alcon (A) and the Bausch & Lomb (B) lasers. Figure 5.7(c) shows the radial average for both lasers, and the theoretical predictions. The efficiency effects are important for the Bausch & Lomb laser, as already seen in plastic, but not for the Alcon laser. Therefore, the correction factor increases from one (at the ablation center) to higher values toward the periphery for the Bausch & Lomb laser, but remains almost flat for the Alcon laser. The radial average of the correction factor is well predicted by theory.

Table 5.2. Ablation depths, depth conversion factors, and ablated volumes in cornea, for a -9 D correction.

	Alcon	Bausch & Lomb
Depth – Filofocon (µm)	62	47.8
Nominal Depth –Cornea (µm)	120.5	135
Conversion factor	1.94	2.82
Ablated corneal volume (µm^3)	$2.09 \cdot 10^9$	$2.76 \cdot 10^9$
Ablated volume within optical zone (µm^3)	$2.08 \cdot 10^9$	$2.58 \cdot 10^9$

5.3.6. Optical outcomes in cornea

Figure 5.8 shows the asphericities obtained by fitting the ablated spheres of Filofocon A to conics, for the Bausch & Lomb (crosses) and the Alcon laser (diamonds). The figure also shows the asphericities found in a previous study (Dorronsoro et al., 2006a) with a previous generation laser (Chiron Technolas 217c with PlanoScan). As the artificial eyes used in that study were made of PMMA, a conversion from PMMA to Filofocon A (considering the theoretical ablation efficiency factors for both materials) was applied to the measured ablation pattern. The post-operative asphericities with the new generation lasers are clearly below those obtained with previous generation lasers. However, the measured post-operative asphericity is still significantly different from zero (and positive).
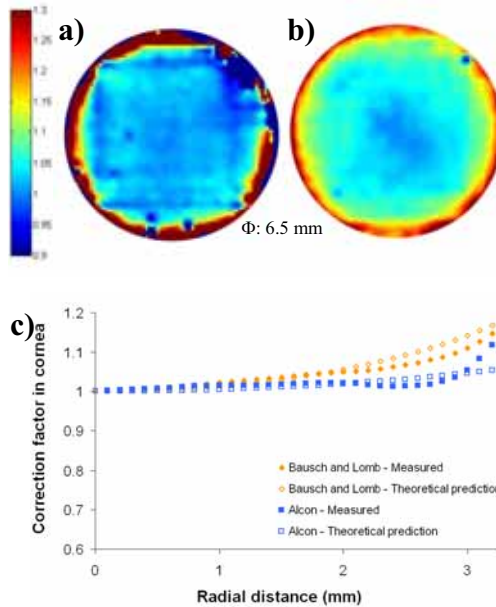
Fig. 5.7. Correction factor for effciency effects in cornea estimated from the experimental measurements in Filofocon A. a) Alcon. b) Bausch & Lomb. c) Radial plots.

The average asphericity in post-operative Filofocon A for a -9 D correction was 0.23 for the Alcon laser, and 0.19 for the Bausch & Lomb laser. When the ablation pattern was transferred to the cornea (considering the corresponding efficiency effects) we obtained a post-operative asphericity of 0.40 for the Alcon laser and 0.71 for the Bausch and Lomb. The corresponding spherical aberration in cornea (Barbero et al., 2002b) was 0.47 μm for the Alcon laser, and 0.61 μm for the Bausch & Lomb laser. . The spherical aberration of an ideal spherical cornea of 7.8 mm is 0.49 microns.
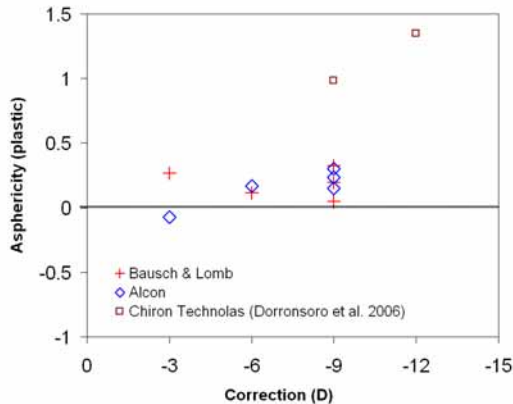
Fig. 5.8. Post-operative asphericities from Filofocon A ablated spheres for the Alcon (diamonds) and Bausch & Lomb lasers (crosses). The asphericities found in a previous study (Dorronsoro et al., 2006a) with a previous generation laser (Chiron Technolas 217c with PlanoScan) are also shown (squares).

5.4. DISCUSSION

This work further develops the use of plastic model corneas, introduced in Chapter 3, to obtain precise quantitative evaluation of the ablation patterns provided by refractive surgery laser systems (Dorronsoro et al., 2006a). The depth patterns are measured on plastic, which can provide an accurate calibration of the laser system. Furthermore, the combination of precise profilometric measurements on plastic surfaces, and knowledge of the ablation and optical properties of the plastic material provides estimations of the ablation pattern on cornea, considering all physical effects, and excluding biomechanical factors. In the study of the ablation properties of Filofocon A (Dorronsoro et al., 2008b) we showed (Chapter 4) that a depth pattern measured on this material can be transformed into a laser spot distribution (considering the fluence of the laser), which can be used to predict depth patterns in cornea, provided that the number of pulses is sufficiently high -as is it the case within the optical zone (see discussion of Chapter 4 for details)-.

The fact that the ablation response of Filofocon A is well predicted by the Beer-Lambert law, for the range fluences and number of pulses used in refractive surgery (Dorronsoro et al., 2008b) allows an accurate characterization of the ablation pattern on plastic. On the other hand, the estimations of the ablation pattern on cornea are accurate within the limitations of the blow-off model in corneal tissue (Beer-Lambert Law) and the accuracy of the optical and ablation parameters. The estimation of the ablation profile on cornea from the measurement of the ablation profile on plastic could be further sophisticated using more complex ablation models (Arba-Mosquera and de Ortueta, 2008, Kwon et al., 2008), or parameters for the cornea, as dynamic coefficients (Fisher and Hahn, 2007).

The geometrical efficiency effects depend on the geometry of the surface on which the corrected ablation pattern is going to be applied. Therefore, strictly speaking, the estimated correction factor to be applied on a spherical surface would be different to that estimated for a conic surface. We performed simulations to quantify the error induced by considering a correction factor calculated for spherical corneas on conic corneas. We found, for a cornea of asphericity -0.4 (upper bound of asphericity in normal corneas) a mean underestimation of 0.21% in the energy applied to the cornea, and a maximum deviation (in the periphery of a 6.5-mm optical zone) of -1.01%. These values are of negligible clinical relevance. In the case of a retreatment of a highly aspherical post-surgical cornea (asphericity = 1), the correction factor for spherical surfaces overestimates the energy applied to the conic cornea (mean 0.63%, maximum 3.31% in the periphery of the ablation).

Equation 5.1 considers all the possible efficiency effects of the laser in plastic (K_P), and an accurate characterizations of the lasers, as the geometry of the plastic surfaces used (and therefore R_P) are well known. The maximum accuracy of the correction factors in cornea (K_C) can obtained when the geometry of individual corneas are taken into account (and not only a generic corneal geometry) in the reflection coefficient R_C used in the conversion from plastic to cornea.

Previous studies (including Chapter 3) were limited by the use of videokeratoscopy to assess the elevation maps of pre- and post-operative spherical surfaces from which the ablation patterns are computed. The use of high resolution non-contact optical profilometry (Section 2.1.1.2) allows mapping both flat and spherical surfaces with the same instrument and with high accuracy (less than 1 micron), without the need of the slight polishing of post-ablated surfaces, required to

achieve proper reflection in videokeratoscopy. This procedure allows accurate point-by-point assessment of the ablation efficiency factor of the laser, using the ablation pattern measured in pairs of flat and spherical surfaces ablated consecutively under similar conditions. The 2-D correction factor for efficiency effects can be applied to any ablation algorithm programmed on a given laser platform.

Our previous study evaluated standard ablation profiles on PMMA. The current study uses the recently proposed Filofocon A material, which we showed in Chapter 4 to have more suitable ablation properties (Dorronsoro et al., 2008b). We used this new model to evaluate the ablation patterns produced by three state-of-the-art refractive surgery laser platforms. We performed a detailed comparison between two of the lasers (Alcon and Bausch & Lomb, with very different nominal fluences). We found marked differences across lasers in the ablation pattern measured in plastic (Fig. 5.4), ablation efficiency factors (Fig. 5.5), predicted post-operative corneal shape, (Fig. 5.6), correction factor in cornea (Fig. 5.7), post-operative asphericities (Fig. 5.8), ablated volume and spherical aberration in plastic and cornea.

5.4.1. Toward an optimized ablation pattern

A comparison of the optical outcomes (both in plastic and cornea) following myopic ablation using new generation and older laser platforms suggest that current ablation patterns have been conveniently optimized to reduce the induction of spherical aberration in the new generation lasers, although there is still room for improvement (Fig 5.8, in Filofocon A). Our predictions suggest that the optimized algorithms are still inducing some change in the asphericity of the cornea (0.40 for the Alcon laser and 0.71 for the Bausch & Lomb, for -9 D correction), although much less than the one reported (1.44 for -9 D) with a previous generation laser and the previous plastic model of Chapter 3 (Dorronsoro et al., 2006a). We can also compare the relative impact of laser efficiency effects and ablation pattern design in the post-operative asphericity. When ablation efficiency effects are cancelled (simulating post-operative corneas by subtraction of the ablation pattern obtained from ablated flat surfaces) we found similar post-operative asphericities with both lasers (~0.35). This suggests that the increase in asphericity for the Alcon laser arises primarily from the ablation pattern while for the Bausch & Lomb laser the efficiency effects account for most of the increase in asphericity.

5.4.2. Ablations on Filofocon A: a method for laser calibration

One especially interesting feature of Filofocon A as a model for refractive surgery is its relatively high sensitivity to fluence changes, compared to PMMA and corneas, due to the combination of its high threshold fluence (90 mJ/cm^2) and high refractive index at 193 nm (1.62), which increases reflection. As a result, the efficiency effects and the associated induced asphericity are more apparent in Filofocon A than in corneas or PMMA, making them easier to measure. On the other hand, the laser penetrates much deeper in cornea than in Filofocon A, and as a result the effects associated to the shape of the ablation pattern are more important in cornea than in Filofocon.

The procedure described in this study can be used to check the calibration state and the performance of individual units of refractive surgery laser systems. The entire ablation pattern in the cornea can be estimated from these measurements. We observed important deviations from rotational symmetry in one of the lasers (Fig. 5.3, Wavelight laser). The asymmetries appeared both on flat and spherical surfaces (and

also with both Q parameters tested) and the location of the irregularity changed across repeated ablations. Validation tests on these patters (Section 2.1.1.2 and Fig. 2.7) proved that the irregularities were a consequence of the ablation process and not of the measurement. Decentration and alignment effects were also discarded as a possible cause for the observed asymmetries, as they should not affect the ablation pattern on flat surfaces. Shielding effects by ablation plume or debris ejected during the ablation (Noack et al., 1997) were the most likely cause for the asymmetry, which may have been produced by insufficient air suction, perhaps as a consequence of the filter wheel position (Fig. 5.2). Figure 5.8 shows a photograph of a flat artificial cornea during the ablation. Smoke and debris are clearly visible. A retrospective analysis of corneal topographies in patients operated with this laser unit did not show important asymmetries, confirming this hypothesis. It is important to note that the procedure of estimating the ablation patterns in cornea is based on the assumption that the ablation pattern in flat surfaces of plastic is created by the superposition of a set of equal spots. If the fluence varies (due to shielding, obscuration, etc), the methodology can detect these changes, but the effects in cornea cannot be correctly quantified. In most cases the assumption of superposition holds, and therefore the model can be used to assess the ablation profile programmed on the laser.

Fig. 5.8. Photograph of a flat artificial eye during the ablation with a clinical laser. Smoke and debris ejected from the ablation zone after repeated pulses could be shielding the following pulses. The exposure time was 1/3 seconds.

5.5. CONCLUSIONS

Plastic (Filofocon A) artificial model eyes have proven useful to assess the outcomes of different refractive surgery laser platforms and algorithms, for a precise calibration of the lasers and to calculate experimental correction factors of efficiency effects.

Different state-of-the-art optimized laser platforms, programmed to produce the same myopic corrections in eyes, showed very different ablation profiles on plastic corneas (30% differences in ablation depths for a -9 D myopic correction) which translated in 34% differences in corneal tissue volume differences.

The ablation efficiency factor varied also substantially across lasers, as estimated from the ratios of the ablation profile on flat and spherical plastic surfaces. For a laser fluence of 120 mJ/cm^2 the efficiency loss (for Filofocon A) was 6.5% at 2.5 mm from the corneal apex, while at 400 mJ/cm^2 this effect was practically negligible.

Both the ablation algorithm design and the strategy of compensation for the ablation efficiency factors contributed to the optical outcomes. The estimated post-operative corneal asphericity is half with the new generation laser algorithms than with non-optimized algorithms (for -9 D correction), but still not negligible. Plastic artificial eye models allow a systematic evaluation of the ablation profile and of the correction factor for efficiency effects, which is essential to further improve ablation algorithms to avoid increase of corneal asphericity (and spherical aberration), which still occurs from purely physical factors.

5.6. OUTLOOK

Chapters 3, 4 and 5 presented the development of an experimental model based on artificial eyes for the study of refractive surgery. Different partial experimental studies and enhancements were performed (material, measurement method, alignment procedure) to improve the model and gain precision and functionality. The methodology was applied to the study of a previous generation laser (inducing a high quantity of spherical aberration), and to three new generation lasers (which induce a reduced amount of spherical aberration).

By comparing the outcomes of the surgery in the physical model and in real patients we could establish a baseline for biological effects. We found that much of the increase of spherical aberration previously attributed to biomechanical factor had in fact a physical origin.

The contribution of biomechanical factors to the optical response to refractive surgery still needs to be quantified. Biomechanical effects may contribute to the final post-operative corneal shape, but if relevant, they will primarily affect the posterior corneal surface, as this may bulge by effect of intraocular pressure on a thinner cornea and lamellar disruption when cutting the flat. There are methodological problems for the quantitative study of the back surface of the cornea and the results in the literature are controversial, as measurements are subject to geometrical and optical distortions.

In Chapter 6, a new experimental model for the validation of measurements of the back surface of the cornea will be presented, and applied to a Pentacam Scheimpflug imaging camera. The validated instrument will be used in Chapter 6 for the study of corneal changes after refractive surgery on real patients, with special emphasis on the posterior surface of the cornea.

Chapter

6

Hybrid Porcine/Plastic Model for the study of the back surface of the cornea

This chapter is based on the ARVO 2009 poster presentation by Laura Remón et al. "Validation of Posterior Cornea Quantitative Scheimpflug Imaging Using a Hybrid Porcine/Plastic Model" (Remon et al., 2009). This corneal model can be used for the study of biometric measurements of the cornea. This chapter describes the model itself, and its particular use for the validation of the Pentacam Scheimpflug imaging system in the measurement of the post-corneal surface shape.

The main contribution of Carlos Dorronsoro was the design of the Hybrid Porcine/Plastic Model and its experimental development, and participation in the design of the experiments, technical support during the measurements, and analysis of the data.

Coauthors of the study are Laura Remón, Sabine Kling, Jesús Merayo-Lloves, and Susana Marcos.

6.1. ABSTRACT

Purpose: Quantitative analysis of posterior corneal Scheimpflug images requires proper correction of geometrical and optical distortion from the anterior surfaces. We developed a hybrid porcine/plastic eye model (with the scattering properties and refractive index of corneal tissue and known posterior corneal geometry) for validation of the posterior corneal reconstruction of the Pentacam Scheimpflug imaging system.

Methods: The hybrid porcine/plastic eye models consisted on excised porcine corneas mounted on a 12-mm diameter plastic piston finished on spherical surfaces with known radii of curvature (7.47, 7.93 and 8.75 mm, as validated by non-contact profilometry). Special care was taken to preserve the endothelium integrity. The porcine's posterior cornea conformed to the underlying plastic surface. Scheimpflug images were obtained within 4 hours post-mortem. The posterior corneal surface was evaluated using the fitting routines of the Pentacam software. We used 12 porcine corneas. The retrieved posterior corneal geometry was compared to the plastic surfaces' nominal data. Correlations between anterior and posterior corneal data were performed to assess that the optical distortion correction was successfully applied.

Results: Measurements on the hybrid model eye of known posterior corneal geometry show that the retrieved parameters (radius, astigmatism, asphericity) are more precise for the anterior surface of the cornea than for the posterior surface. The measured posterior corneal radius of curvature is minimally affected by the geometry of the anterior surface, although consistently underestimated (0.26 ± 0.12 mm on average). There was larger variability and underestimation of the posterior surface asphericity ($Q_{post}=-0.33 \pm 0.44$) than of the same spherical surfaces tested anteriorly ($Q_{ant}=-0.02 \pm 0.22$). The anterior porcine corneas varied in anterior radii (from 8.0 to 9.6) and astigmatism (1.9 ± 1.0 D). However, there was no significant correlation between anterior and posterior corneal radii of curvature, asphericity or astigmatism ($p > 0.26$).

Conclusions: This model has allowed testing the accuracy of the posterior corneal geometry estimates from Pentacam. The independence of the retrieved data from the anterior corneal topography suggests proper correction of optical distortion. This model shows more comparable properties to those of living eyes and could be used for calibration of other anterior segment imaging systems. The Pentacam Scheimpflug system can be used reliably to assess changes in the posterior corneal radius of curvature after LASIK.

6.2. INTRODUCTION

Previous chapters of this thesis were dedicated to the study of the physical changes in the anterior surface of the cornea with refractive surgery. The aim of these studies was achieving the necessary control over the changes in corneal shape to perform successful wavefront guided surgery. The optical influence of the posterior cornea is small compared to the anterior cornea. However, monitoring possible changes on the posterior is important to assess the biomechanical integrity of the cornea, in particular in response to surgery. The FDA recommends preserving at least 250 μm of stromal bed to prevent ectasia (bulging of the cornea). Ectasia is a rare complication in LASIK, but the debate whether the posterior corneal surface is affected in LASIK is still open.

This and the next chapter of this thesis will be devoted to the study of the posterior corneal surface. This chapter will introduce a new experimental model to validate a Scheimpflug-based instrument to characterize the posterior corneal shape. Chapter 7 will present study where the validated instrument is applied to study the effect of myopic laser ablations in humans on the posterior corneal surface.

There is a relatively large body of literature addressing on the posterior surface of the cornea after LASIK (Wang et al., 1999, Seitz et al., 2001, Baek et al., 2001, Twa et al., 2005, Grzybowski et al., 2005). However, measurements of the posterior corneal shape after refractive surgery have been largely contested because they may be due to artifacts caused by the optical distortion produced by the anterior corneal surface (Ueda et al., 2005, Donnenfeld, 2001), which changes dramatically after the procedure. Recently, a Scheimpflug imaging – based commercial corneal topographer which nominally corrects for this distortion, Pentacam (Oculus GmbH, Germany) has become available. The principles of Scheimpflug imaging were presented in the Introduction (Section 2.1.3) as well as methods for correction of the optical and geometrical distortion of this particular instrument (Rosales and Marcos, 2009). The first studies on refractive surgery using this device have reported no significant changes in the posterior surface of the cornea after LASIK and PRK (Ciolino and Belin, 2006, Matsuda et al., 2008). Although some studies have reported a high repeatability of the Pentacam instrument in normal (Lackner et al., 2005) and post-Lasik eyes (Jain et al., 2007), a validation of the accuracy of this system to measure the posterior cornea has never been presented.

The goal of this study is the validation of the reconstruction of the posterior cornea provided by the Pentacam Scheimpflug imaging system. For that, we developed a hybrid porcine/plastic eye model: with the scattering properties and refractive index of corneal tissue and known posterior corneal geometry. This model can be used in anterior segment research and validation/calibration of other biometry and imaging instruments, as OCT.

6.3. METHODS

A validation of the accuracy of the measurements of the posterior corneal surface geometry was performed in vitro using a hybrid porcine/plastic eye model. The use of corneal tissue was motivated to achieve similar intracorneal scattering in the images – which appears to be critical to achieve good edge-detection- and a similar index of refraction –which is a parameter in the reconstruction algorithms.

6.3.1. Hybrid porcine-plastic eye model

The hybrid porcine/plastic eye models consisted on excised porcine corneas mounted on a 12-mm diameter plastic piston finished on a spherical surface. Figure 6.1 shows a schematic diagram of the model and mount. A strip of sclera was left around the cornea. The corneal samples were fixed on a custom-designed support, using an annular metalic ring that pressed the scleral strip. The piston (hydrated with hyaluronic acid) was slid inside the supporting piece until the corneal button was fit on the spherical surface. Special care was taken to preserve the endothelium integrity. Due to its scattering properties, Pentacam detects the back surface of the cornea and not the underlying plastic support. This mount was designed to avoid bubbles, folds and creases of the corneal tissue, by achieving a smooth corneal back surface conformed to the plastic surface. The amount of stress produced by the piston affected the anterior corneal surface geometry. The enucleated eyes were obtained in a local slaughterhouse, and the procedures were performed within 4 hours post-mortem.
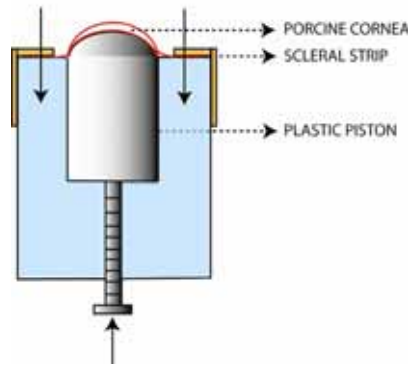
Fig. 6.1. Drawing of the Hybrid Porcine/Plastic model.

Several plastic surfaces (acrylic material) of known radii of curvature (7.47, 7.93 and 8.75 mm) were used as support for the posterior corneas in this validation study. The plastic surfaces were polished in a precision optics lathe. The radii of curvature of the sphere were measured using a microscope non-contact profilometer (Artigas et al., 2004) (Plμ - Sensofar, Barcelona, Spain) that also reported negligible deviations from the spherical shape.

As accurate reconstruction of the posterior corneal surface relies on accurate measurements of the anterior corneal surface and optical and geometrical distortion reconstruction method, a validation of the anterior corneal surface was also performed using high quality optical glass surfaces (optical calipers with nominal radii of 9.65, 8 and 6.15 mm).

6.3.2. Measurements: validation on model eyes

The glass spherical surfaces were measured on the Pentacam system (described on section 2.1.3), acting as anterior corneas. Ten measurements were conducted on each surface. One of the plastic spherical surfaces used in the hybrid porcine/plastic eye model (7.93 mm) was also measured directly (acting as anterior surface).

Unlike other methods previously tested in our laboratory (as artificial corneas of different RGP materials), the posterior surface of the hybrid porcine/plastic cornea provides images very similar to those obtaines in real eyes (Fig. 6.2). The back surface

of the cornea is regular and clearly visible. Therefore, the Pentacam edge detection algorithms work correctly in these images. Besides similar scattering properties, the refraction index in our model cornea is similar to that in the corneas of real eyes, so the geometrical and optical correction algorithms of the Pentacam can be applied.

a)   b)
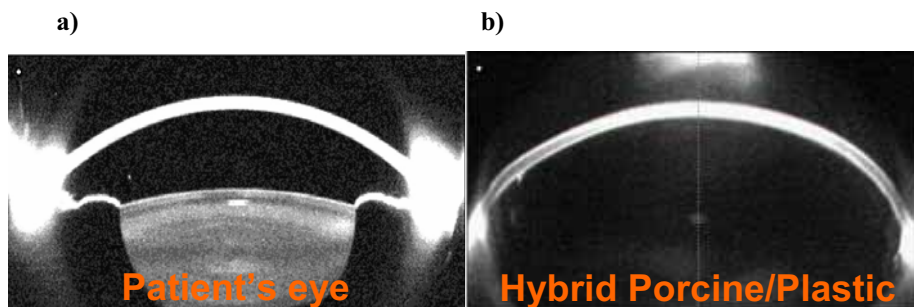
Fig. 6.2. Scheimpflug images of a human eye and a hybrid porcine/plastic model eye.

A total of 12 porcine corneas were used in the validation study (5 porcine corneas were mounted on 7.47-mm and 8.75-mm spherical corneas; and 2 on the 7.93 mm). Each hybrid eye was measured up to 5 times on the Pentacam (with a total of 36 measurements), using identical procedures as in the glass/plastic eyes and patients. The piston pressure was slightly incremented between each two measurements. All the Scheimpflug images (25 per measurement) were carefully supervised to check that the software detected edges of the cornea. Ten measurements (including the whole set of measurements from one porcine cornea) that showed evidences of corneal opacification, edema or bubble formation, either from visual inspection or on the Pentacam, were discarded. Figure 6.3 shows a photograph of the hybrid Porcine/Plastic Model, with an edematized cornea, that produced increased scattering, and prevents Pentacam measurements.

Data of anterior and posterior radius of curvature (from the Best Fitting Sphere or Mean horizontal and vertical radii of curvature), asphericity Q (defined as p-1), and astigmatism were obtained from the Pentacam software.
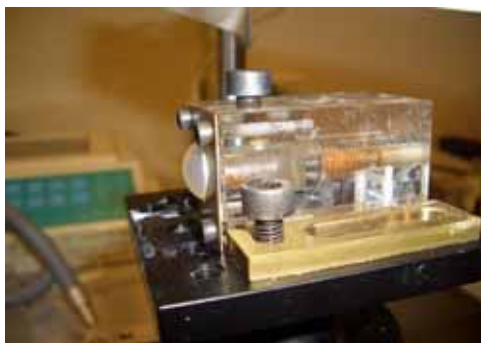
Fig. 6.3. Photograph of the hybrid Porcine/Plastic Model.

Custom fitting routines in Matlab (Chapter 2 - Methods) could not be used in all the hybrid eyes, as the exporting procedure is interrupted by the software when no iris

is detected. Therefore, in this case we used the Pentacam fitting routines. We studied the agreement between the radii of curvature and asphericity obtained by our fitting procedure and those obtained by Pentacam's software (see below).

6.4. RESULTS

6.4.1. Validation of the ANTERIOR surface

Table 6.1 shows the nominal and measured radii of curvature of glass spherical models. Anterior radii of curvature were estimated within an accuracy of 0.04 mm with respect to the nominal values of the reference spheres, being typically slightly underestimated. Asphericity was -0.02 ± 0.22 on average, close to the expected value (zero) for a sphere, although the variability was high. Astigmatism was higher than expected (power 0.32 ± 0.27, on average), but with random angle, indicating that there are not predominant orientations, and that the average surface is a sphere, as expected. The repeated measurements on the 7.93 mm plastic surface provided similar results (although the cylindrical geometry of the piston produced unwanted reflections that prevented from systematic measurements in all samples).

Table 6.1. Validation of Pentacam measurements for ANTERIOR radius.
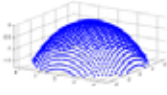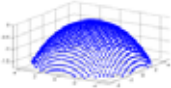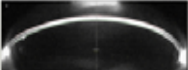
	Non-contact profilometry	Scheimpflug Imaging	
	Nominal R mm	Measured R (anterior surface) mm	Difference mm
Glass Sphere 1	9.65	9.61 ± 0.04	0.04
Glass Sphere 2	8.00	7.97 ± 0.01	0.03
Glass Sphere 3	6.15	6.12 ± 0.02	0.03

Table 6.2. Validation of Pentacam measurements for POSTERIOR radius.

	Non-contact profilometry	Scheimpflug Imaging	
	Nominal R mm	Measured R (posterior surface) mm	Difference mm
Plastic Sphere 1	7.47	7.32 ± 0.1	0.15
Plastic Sphere 2	7.93	7.54 ± 0.05	0.39
Plastic Sphere 3	8.75	8.51 ± 0.08	0.24

6.4.2. Validation of the POSTERIOR surface

Table 6.2 shows the nominal and estimated posterior radii of curvature in the hybrid porcine/plastic eye model. Each data is the average of the different eyes with similar posterior plastic cornea. There is a good correlation between nominal and estimated radius, although there is higher bias (underestimation) than for the anterior cornea (150 to 400 μm). Despite the low accuracy (the absolute values are not recovered exactly), the repeatability is good (below 100 μm), considering that these are individual measurements (non-averaged) of hybrid eyes whose anterior surface varies across measurements.

6.4.3. Correlation between anterior and posterior surfaces

6.4.3.1. Radius

Correlations between anterior and posterior corneal surface were performed to assess that the optical distortion correction was successfully applied. Statistically significant correlations between the posterior (fixed) corneal surface and the anterior (variable, as dependent from the specimen and pressure exerted by the piston) would be indicative of artifacts in the correction. This is particularly critical in the current study, when the same eyes are evaluated before and after a change in the anterior cornea.

Figure 6.4 shows the anterior radius vs. the deviations in posterior radius for all the posterior corneal samples and all the porcine corneas. Our hybrid porcine/plastic model corneas showed a wide range of anterior radii (from 8.0 to 9.6 mm) for the different combinations of anterior porcine corneas and posterior plastic surfaces. A z-test showed no correlation between anterior radius vs. deviations in posterior radius ($p > 0.26$) for all measurements (averaged across identical conditions). Additional z-tests between anterior and posterior corneal radius for each plastic back surface also showed no correlation ($p > 0.6$). These results indicate that the radius of the anterior surface does not affect the radius measured of the posterior surface.
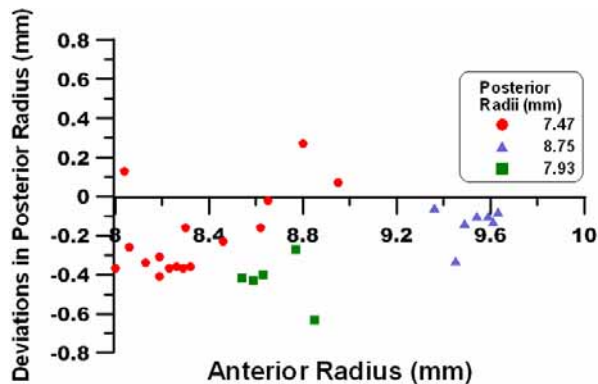
Fig. 6.4. Measurements of Radii

6.4.3.2. Astigmatism

Also, the anterior corneas typically showed significant amount of astigmatism (1.9 ± 1.0 D) with preferential orientations in the vertical and horizontal directions, while the estimated astigmatism for the posterior surface was much lower (0.31 ± 0.15 D), with

no preferential orientation. These retrieved values of astigmatism of the posterior corneal surfaces conformed to spherical plastic surfaces are similar to those found in the calibrations of spherical model eyes (anterior surfaces) in the previous section. There was no correlation between the astigmatism of the anterior and posterior corneal surface (p=0.57 for all eyes).

6.4.3.3. Asphericities

Finally, there was no correlation between the anterior and posterior corneal asphericities (p=0.28 for all the eyes), as shown in Fig. 6.5, where anterior asphericities are plotted vs posterior asphericities (ideally zero). However, the posterior corneal asphericity differed from zero, and was quite variable (-0.33 ± 0.44) for the back surface).
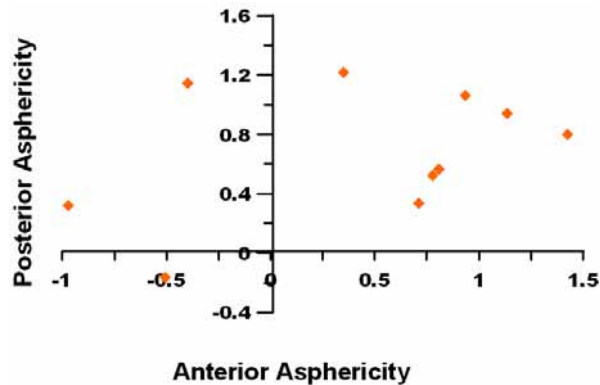
Fig. 6.5. Measurements of Asphericities. Each point is the average across repeated measurements in the same conditions.

6.5. DISCUSSION

In this chapter we have presented a validation of the Pentacam Scheimpflug system to measure the posterior corneal surface geometry. The experiments using a hybrid porcine/plastic eye model indicate that the posterior corneal radius can be obtained with high repeatability and that the reconstructed posterior surface is not affected by changes or asymmetries in the anterior cornea. Posterior corneal radius seems to be slightly underestimated and asphericity overestimated in comparison to the nominal values of the posterior cornea in the model eye used for calibration. While studies on the repeatability of this system had been published before (particularly of the anterior radius of curvature and pachymetry (Lackner et al., 2005, Jain et al., 2007)) this is, to our knowledge, the first time that the accuracy (both for anterior and posterior surface) is studied.

6.6. CONCLUSIONS

We have developed an artificial eye model that shows corneal properties (scattering, refractive index) comparable to those of living eyes and can be used for calibration of anterior segment imaging systems. The accuracy of the posterior corneal geometry data provided by the Pentacam Imaging System was verified using our model. The independence of the retrieved data from the anterior corneal topography indicates

proper correction of optical distorsion in the posterior. These results have implications on the study of posterior cornea, specially in changes after refractive surgery and the assessment of biomechanical properties (Perez-Escudero et al., 2008, Kling et al., 2009) by Scheimpflug Imaging.

6.7. OUTLOOK

The Scheimpflug-based system has proved to be an appropriate technique to measure reliably potential changes on the posterior corneal surface, as we have shown that the posterior corneal shape measurements are not affected by changes on the anterior cornea.

In Chapter 7 we will present a study where the instrument validated here, was used to measure posterior corneal shape changes after standard myopic LASIK surgery, and to evaluate potential longitudinal changes after the procedure.

Chapter

7

Changes in the anterior and posterior corneal elevation maps with refractive surgery

This chapter is based in the article by A. Perez-Escudero, et al. "Minor influence of Myopic Laser In Situ Keratomileusis on the Posterior Corneal Surface," Invest. Ophthalmol. Vis. Sci., 50, 4146-4154 (Perez-Escudero et al., 2009b). It was presented in part at ARVO 2007, Fort Lauderdale, Florida (P.N. 3531), as a poster presentation.

The main contribution of Carlos Dorronsoro was in development of the corneal model and of the data analysis procedures, as well as the interpretation of the results.

Coauthors of the study are Alfonso Pérez-Escudero, Lucie Sawides, Laura Remón, Jesús Merayo-Lloves and Susana Marcos.

Laser beam reshapes the cornea by removing tissue

http://www.fda.gov/cdrh/lasik/
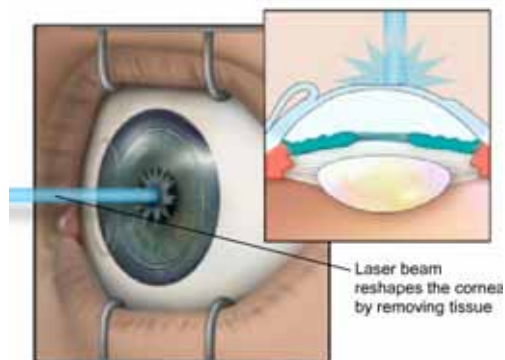
7.1. ABSTRACT

Purpose: To check whether myopic LASIK induces changes on the posterior corneal surface.

Methods: Scheimpflug imaging (Pentacam, Oculus) was used to measure pre- and post-operative posterior corneal topography in 27 eyes (14 subjects) that had undergone standard myopic LASIK surgery (attempted corrections between -1.25 and -8.50 D) and on 18 non-operated eyes (9 subjects). Longitudinal displacement of the posterior corneal apex and changes of the apical radius of curvature and asphericity were computed.

Results: The measurements on patients show that, on average, the only relevant (although clinically unimportant) change in radius of curvature and asphericity occurred the first day after surgery (ΔR = -28 ± 34 μm and ΔQ = -0.06 ± 0.06). No statistically significant change was observed afterwards. The change in radius is more pronounced in the vertical direction than in the horizontal direction. On average, there was no significant displacement of the posterior corneal apex. Individual changes over time do not show a systematic trend across patients, and control subjects experience changes of the same order of magnitude.

Conclusions: There is no evidence of surgically-induced changes in the corneal posterior surface beyond one week after surgery.

7.2. INTRODUCTION

As described in detail in Section 1.7 of the Introduction, there are open clinical questions in refractive surgery which may find an explanation in changes of the posterior surface of the cornea. In this chapter, we will present the use of the methodology developed in Chapter 6 to perform the first validated measurements (to our knowledge) of the effect of LASIK on the back surface of the cornea. As the back surface of the cornea is not directly affected by the procedure, we used these measurements as an indicator of biological changes in the cornea resulting from biomechanical processes and wound healing. The study was conducted longitudinally to investigate potential changes over time.

The change in manifest refraction after LASIK differs from the measured change in corneal power, estimated using the standard keratometric index (Tang et al., 2006). The discrepancies may arise from the change in ratio of the anterior/posterior corneal curvature with LASIK (and therefore the effective keratometric index) (Tang et al., 2006, Jarade et al., 2006), change in the corneal effective index of refraction (due to epithelial hyperplasia) (Spadea et al., 2000), or changes in the posterior corneal curvature with LASIK. Moreover, theoretical calculations of post-operative corneal shape after subtraction of standard ablation profiles differ dramatically from clinical outcomes (Cano et al., 2003, Marcos et al., 2003, Gatinel et al., 2001, Jiménez et al., 2003), as already explained in Section 1.7.2. To a large extent, this effect can be explained by physical laws (Section 1.7.3) (Mrochen and Seiler, 2001, Jimenez et al., 2002). The results of these predictions are very likely affected by the assumption of a mechanically inert cornea (Munnerlyn et al., 1988), but when plastic corneas are ablated (Chapters 3 and 5) (Dorronsoro et al., 2006a), we also find discrepancies with clinical outcomes. Empirical corrections of the ablation algorithms (as those proposed in Chapters 3 and 5) can compensate for laser efficiency losses (Dorronsoro et al., 2006a), and perhaps for systematic deviations found in the average population, but are unable to provide individual adjustments, since the cause of the inter-subject variability in achieved correction is unknown (Dupps and Wilson, 2006). A greater understanding and quantification of the biomechanical processes that take place in the cornea after surgery would help to improve the predictability and stability of achieved corrections.

Some previous experimental studies have reported significant changes in the posterior surface of the cornea after LASIK (Wang et al., 1999, Seitz et al., 2001, Baek et al., 2001, Twa et al., 2005, Grzybowski et al., 2005). However, these results have been largely contested, because they may be due to artifacts caused by the optical distortion produced by the anterior surface of the cornea (Ueda et al., 2005, Donnenfeld, 2001).

In this study we use the Scheimpflug-based Pentacam topographer, validated in Chapter 6, to study the changes in the back corneal surface produced by myopic LASIK in patients, comparing them to physiological changes observed in control subjects.

7.3. METHODS

7.3.1. Subjects

A total of 45 eyes (23 subjects) participated in the study. Fourteen subjects (27 eyes), with ages ranging from 21 to 47 years (mean, std 32 ± 7 years), underwent myopic

LASIK refractive for intended myopic spherical corrections ranging from -1.25 to -8.50 D (mean, std -4 ± 2.0 D). Cylinder ranged from 0 to -2.5 D (-0.84 ± 0.7). Patients were tested before and at various times after the procedure. Nine subjects (18 eyes), with ages ranging from 24 to 43 years (mean, std 32.5 ± 7 years), were not operated and acted as control subjects. The control subjects were measured at the Instituto de Óptica "Daza de Valdés", with the same Pentacam unit as the patients (see section 2.1.3). Experimental protocols were approved by an Institutional Review Board and met the tenets of the Declaration of Helsinki. All patients signed the informed consent.

7.3.2. Surgical procedure

We conducted standard LASIK surgery using a narrow-beam, flying-spot excimer laser (Chiron Technolas 217-C equipped with the PlanoScan program; Bausch & Lomb Surgical). This laser has an emission wavelength of 193 nm, a fixed pulse repetition rate of 50 Hz, and a radiance exposure of 120 mJ/cm^2. The procedure was assisted by an eye tracker. Flaps were performed with suction rings of 8.5-mm (3 eyes) or 9.5-mm (24 eyes) diameter. We used a Hansatome microkeratome (Bausch & Lomb) programmed for 160 μm (22 eyes) or 180 μm (5 eyes) depth. Photoablation was applied to an optical zone of diameter ranging from 5.2 to 7 mm (6.6 ± 0.6 mm). The LASIK procedures were conducted at the Instituto de Oftalmobiología Aplicada, Universidad de Valladolid, Spain.

Pre-operative central pachymetry (measured by Pentacam) ranged from 510 to 643 μm (572 ± 33 μm). Residual bed thickness one day after surgery (computed as central pachymetry one day after surgery minus programmed flap depth) ranged between 271 μm and 421 μm (329 ± 41 μm).

7.3.3. Measurements: patients and control eyes

We collected corneal topographies with the Pentacam system of both eyes of each patient before and several times after surgery. Thirteen eyes were measured at three different time points post-operatively: 1.3±0.5, 10.5±3.2 and 33.4±5.5 days after surgery, which we will refer as "1 day", "1 week" and "1 month" post-operatively. Another eye was measured post-operatively only one day after surgery, 6 eyes were measured only one week after surgery, 2 eyes were measured one week and one month after surgery and 5 eyes were measured only one month after surgery. Average measurement times for the whole group of eyes are 1.3, 10.8 and 33.4 days. In control subjects, we acquired several consecutive topographies of both eyes separated by 1 day and 1 week. These data were used as baseline for normal short and mid-term changes in the posterior corneal shape. The time of the measurement across subjects varied between 9:00 am and 16:00 pm, but for each subject measurements were conducted around the same time of the day (within 3.4±1.4 hours) in all days of measurements. We acquired 3-6 valid topographies per session. One of the control eyes was measured 23 consecutive times to study the instrument repeatability.

7.3.4. Data Analysis

We exported topographic maps of anterior and posterior corneal surfaces from Pentacam (Fig. 7.1 (A)), and used Matlab for the data analysis, in order to have a greater freedom for data manipulation than that permitted by Pentacam's software, and to ensure that the definitions of apical radius of curvature and asphericity complied with known equations.

We computed apical radii and asphericities by fitting the central 6 mm of the corneal elevation maps to bi-elliptical surfaces (ellipsoids). Unless clearly stated otherwise, the data presented in this paper will be referred to a rotationally symmetric ellipsoid.
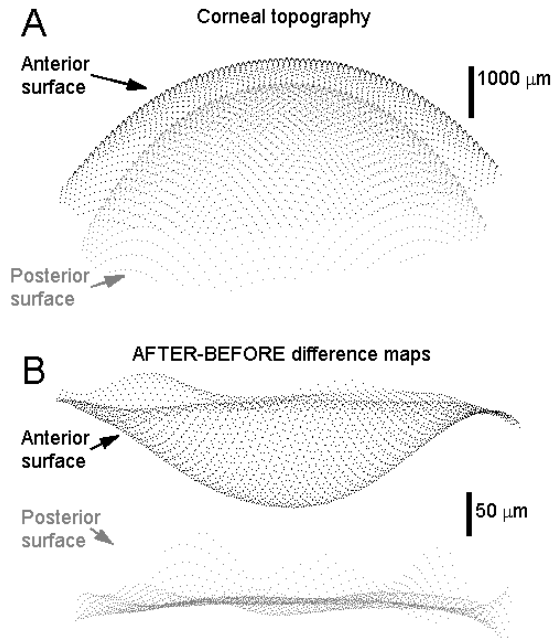
Fig. 7.1. (A) Elevation data exported from Pentacam. Each corneal surface is represented by a cloud of points arranged in x-y on a 100x100 μm square grid. Distance between both corneal surfaces reflects the central pachymetry measured by Pentacam. (B) Difference maps, obtained after alignment as described in the text. Distance between anterior and posterior difference maps is arbitrary, chosen for optimal visualization.

7.3.4.1. Difference maps and corneal elevation

We subtracted pre- and post-operative posterior corneal elevation maps to obtain difference elevation maps (see Fig. 7.1 (B)). Proper alignment of these surfaces is critical to prevent misalignment artifacts from affecting the difference maps. In principle, we should align the topographies both in axis (rotation) and position (translation). We found that the raw topographies are already aligned in axis as we performed the analysis both with and without rotation in the alignment (Navarro et al., 2006), and we did not observe statistically significant differences between the results obtained with either method. In order to align the two measurements in position, we used the fit without rotation to achieve the alignment in the XY plane (where Z is the line of sight). Thus, we translated both topographies so that the center of their best-fit ellipsoids fell in the origin. Then, we translated the post-operative measurement in Z until the differences between both topographies were minimal. For a study of repeatability of Pentacam, we used the whole surface for alignment. For

computation of longitudinal displacement of posterior corneal apex, we used the peripheral ring between 6 and 10 mm diameter for alignment of both topographies. Then, we computed the apex longitudinal displacement as the difference between elevations of the posterior corneal surface's apex after surgery minus elevation of the posterior corneal apex before surgery (a forward bulging corresponds to a positive number). In this paper, we call corneal apex the point where the best-fit ellipsoid's principal axis intersects with the corneal surface.

7.3.4.2. Comparison of Matlab and Pentacam software fitting parameters

We studied whether Matlab and Pentacam provided similar estimates of radius of curvature and asphericity on 18 control eyes (3-5 repeated measurements on each eye). We found a mean difference between methods of 10 μm in the anterior radius of curvature and of -16 μm in the posterior radius of curvature, a mean difference of -0.04 in the asphericity of both surfaces. These values are below the standard deviation of repeated measurements from each method.

7.3.4.3. Significance of changes

The repeatability of the instrument limits the significance of the changes found in the measurements, and the conclusions that can be extracted. We present the average of repeated measurements, and used a Student's t test to assess the significance of the changes across days (at significance level of $p<0.017$ after application of the Bonferroni correction).

7.4 RESULTS

7.4.1. Repeatability of the posterior corneal surface measurements

In order to estimate the repeatability of Pentacam on patients, we measured the eye of one control subject 23 consecutive times. These measurements took less than 30 minutes, so any change should be attributed to short-term dynamic ocular variations and, primarily, measurement errors. We considered the dispersion of these measurements as an estimate of the repeatability of Pentacam in real eyes. We computed the standard deviation of each point of the difference map after aligning the 23 posterior corneal surface's topographies as described in the previous section, (using the whole topography for alignment). These deviations are shown in Fig. 7.2. In the periphery of the topographic map, the standard deviation is as high as 40 μm. By restricting the analysis to the 6-mm diameter central area we ensure that standard deviation is below 10 μm. We also used these 23 measurements to estimate the dispersion of the radii of curvature and asphericities of the anterior and posterior corneal surfaces. The standard deviation for the anterior radius was 10 μm, and 0.03 for the anterior asphericity. We found a higher standard deviation for the posterior radius, $\sigma_R = 25$ μm (being $R = 6.2$ mm the average radius for this eye), and posterior asphericity of $\sigma_Q = 0.06$ (being $Q = 0.11$ the average asphericity for this eye). We obtain the same results with both processing methods (Pencacam processing and our fits to central 6 mm).
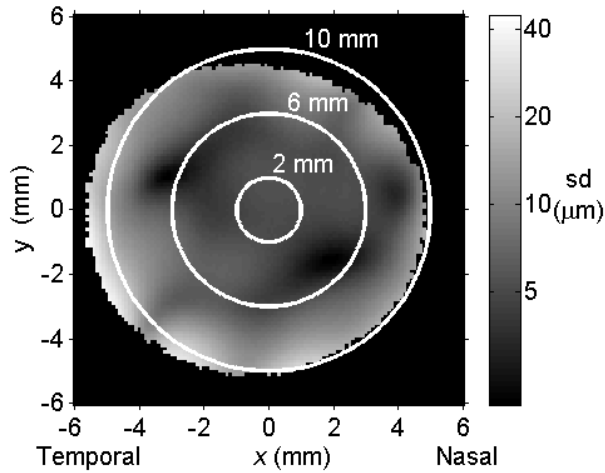
Fig. 7.2: Standard deviation of Pentacam's posterior corneal surface elevation maps (μm). White circles limit central areas with specified diameters. The analysis was done on the 6 mm diameter, where standard deviation is below 10 μm.

7.4.2. Change of the anterior corneal surface with LASIK surgery

Although this study focuses on the posterior corneal surface, we checked that the anterior corneal measurements obtained using Pentacam agree with those previously reported using other methods. We observed a statistically significant increase of both anterior radius and asphericity in all post-operative measurements. The first day after surgery, the change in radius ranged from 268 μm to 1608 μm (mean, std 674 ± 348 μm, $p < 0.0001$), and the change in asphericity (Q) ranged from 0.07 to 1.88 (mean, std 0.55 ± 0.47, $p < 0.0001$). We found high correlations between change in radius and attempted correction ($r = 0.94$, $p < 0.0001$), and between change in asphericity and attempted correction ($r = 0.82$, $p < 0.0001$). These results are consistent with previous reports of changes in the anterior corneal surface after LASIK with the same laser used for the present study.(Cano et al., 2004)

Table 7.1: Average values for all patients. All data are displayed as mean ± standard deviation.

	Anterior corneal surface		Posterior corneal surface	
	Radius (μm)	Asphericity	Radius (μm)	Asphericity
Before surgery	7700 ± 240	-0.10 ± 0.12	6380 ± 220	0.16 ± 0.24
1 day after surg.	8430 ± 430	0.42 ± 0.50	6420 ± 210	0.06 ± 0.28
1 week after surg.	8460 ± 480	0.42 ± 0.53	6400 ± 180	0.19 ± 0.28
1 month after surg.	8520 ± 390	0.59 ± 0.53	6370 ± 220	0.12 ± 0.26

7.4.3. Change of the posterior corneal surface as a function of time

Table 7.1 shows the average radii and asphericities of both corneal surfaces of all patients. We studied the evolution over time of the change in the posterior corneal

175

surface (post-operative minus pre-operative values) for the 13 eyes that were measured at all time points.
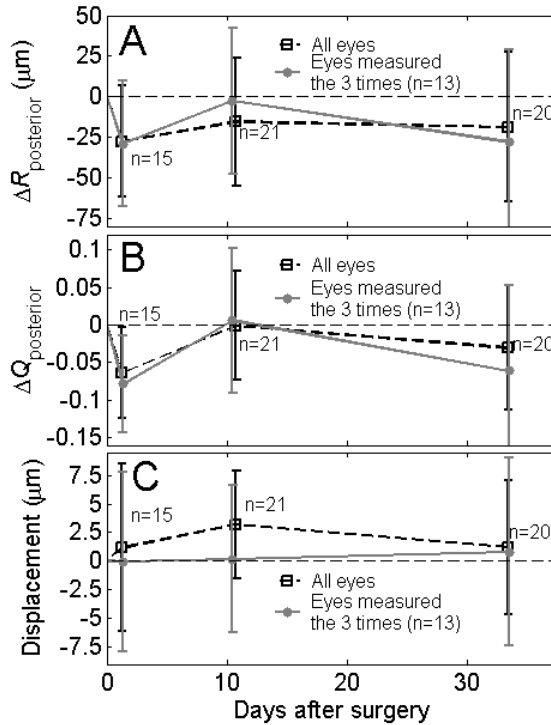
Fig. 7.3: (A) Change in the apical radius of curvature of the posterior corneal surface versus time. Error bars limit the 98.3% confidence interval. Black squares: All eyes (each square comes from averaging a different subset of eyes. The number of eyes in each subset is given by the legends near the squares). Gray dots: Eyes for which all the three measurements are available. Each dot represents an average across 13 eyes. A positive sign is indicative of posterior corneal flattening and negative sign a posterior corneal steepening. (B) Change in the average asphericity of the posterior corneal surface versus time. A positive sign is indicative of changes toward oblateness and a negative sign indicates changes towards prolateness (C) Change in the elevation of the apex of the posterior corneal surface. A positive sign is indicative of posterior forward bulging, and a negative sign indicates backward bulging.

Results are shown for average change of the radius of curvature of the posterior surface of the cornea in Fig. 7.3(A), gray dots, and for average change in asphericity of the posterior corneal surface in Fig. 7.3(B), gray dots. Error bars limit the 98.3% (corresponding to $\alpha = 0.05/3$, according to Bonferroni correction) confidence interval given by Student's t distribution. This population of eyes shows a near-significant decrease radius ($\Delta R = -29$ µm, $p = 0.06$) and a statistically significant decrease of asphericity one day after surgery ($\Delta Q = -0.08$, $p = 0.005$). No statistically significant changes are present one week or one month after surgery. When the entire population of eyes is included (black squares in Fig. 7.3), we observe a near-significant decrease of radius ($\Delta R = -28$ µm, $p = 0.05$) and a statistically significant decrease of asphericity ($\Delta Q = -0.06$, $p = 0.01$) the first day after surgery, and no statistically significant

change 1 week and 1 month after surgery. Figure 7.3(C), shows the measured longitudinal displacements of the apex of the posterior corneal surface. These displacements were less than 35 μm in individual eyes, and on average they were not statistically significant at any time point.
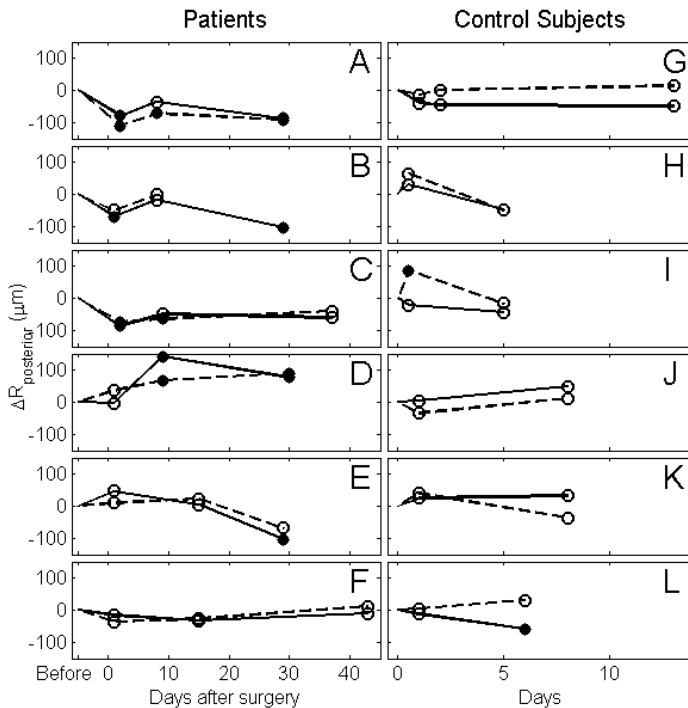
Fig. 7.4: Individual changes in post-operative radii of curvature of the posterior corneal radius relative to the pre-operative value. Each panel shows data for one individual patient. Solid line: Right eye. Dashed line: Left eye. Filled dots indicate statistically significant changes (α = 0.017) (A-F) Patients whose two eyes were measured the three times postoperatively (except for patient B's left eye, with less than three valid topographies 1-month post-operatively). (G-L) Controls whose two eyes were measured the three times.

Figure 7.4 (A-F) shows individual changes in radius of curvature versus time, for the 6 patients whose two eyes which had the the three measurements (1 day, 1 week and 1 month). Each panel shows data on a single subject. Solid lines represent right eyes and dotted lines left eyes. Points marked with a filled dot mean a statistically significant change with respect to the pre-operative measurement, while empty circles mean that the change is not statistically significant (2-sample unpaired Student's t test between the repeated preoperative and postoperative measurements, α=0.05/3). There is no systematic trend followed by all patients, but note that statistically significant changes are frequent. Four eyes show a statistically significant and sustained decrease in posterior radius after surgery (Fig. 7.4 (A,B,E)). On the other hand, another two eyes show the opposite: systematic and sustained increase in radius (Fig. 7.4 (D, F)). Most patients show a non-systematic behavior.

We compared the changes in patients that underwent refractive surgery (Fig. 7.4 (A-F)), with normal control eyes, measured following a similar time-course (Fig. 7.4 (G-L)). In some cases, we observed statistically significant changes in control eyes between measurements separated one day or one week, although no treatment had been applied between the measurements. Very interestingly, left and right eyes of the same subject (in all patients and all but one control subject) follow the same trends with time.

7.4.4. Difference between vertical and horizontal radii and asphericities

The results reported above correspond to radii and asphericities obtained from a fit of the topographies to rotationally symmetric ellipsoids. We have also fitted the topographies to more general non-rotationally symmetric ellipsoids, and analyzed the vertical and horizontal radii and asphericities separately. We did not find statistically significant meridional differences in asphericity (Fig. 7.5 (C, D)). However, the average radius of curvature shows statistically significant meridional differences: while the horizontal radius does not change at any time point (Fig. 7.5 (A)), the vertical radius of curvature suffers a statistically significant change one day after surgery (Fig. 7.5 (B), $\Delta R_y = 47$ µm, $p = 0.004$). This meridional difference is equivalent to a posterior astigmatism of 0.9 D (and an effective astigmatism of 0.037 D), and is responsible for the near-significant change of the average radius of curvature reported before (Fig. 7.3 (A)). This meridional change cannot be attributed to a different variability in the vertical direction for this instrument, as seen from the validation experiments. No meridional differences were found in control subjects.
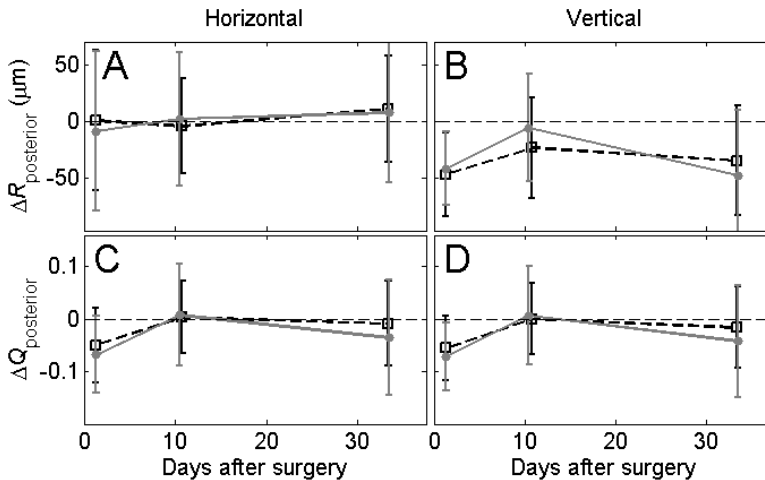
Fig. 7.5: Changes of average horizontal and vertical radii of curvature (A, B) and asphericity (C, D). Gray dots: Patients measured the three times. Black squares: All patients. Error bars indicate the 98.3% confidence interval. Number of eyes per point is the same as in Fig. 7.3.

Figure 7.6 shows histograms of changes between pre-operative and all post-operative measurements for all control eyes (A, B) and all surgical eyes (C, D). Changes in control subjects follow normal distributions (according to Jarque-Bera normality test)

for both meridians (Fig. 7.6 (A, B)). Both distributions have zero mean (Student's *t* test), and although there is more dispersion for the vertical meridian, there is no statistically significant difference between the two standard deviations ($p = 0.06$, Ansari-Bradley test). We conclude that there is no statistically significant difference between horizontal and vertical radius of curvature for control subjects. Changes in patients are not normally distributed (Fig. 7.6 (C, D)), and their standard deviations are slightly greater than the standard deviation of changes in controls for both meridians. We observe no statistically significant shift for the horizontal radius (Fig. 7.6 (C)), but there is a very significant shift of the vertical radius one day after surgery, which disappears afterwards (Fig. 7.6 (D)).
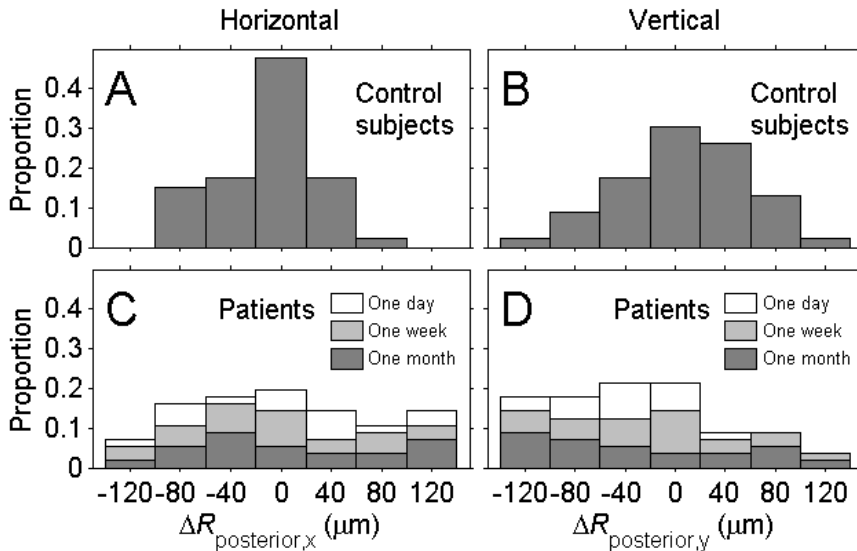
Fig. 7.6: (A) Histogram of changes in horizontal radius of curvature of the posterior corneal surface in all control subjects (all changes at 1 day and 1 week are included in the histogram). (B) The same as (A), for the vertical radius of curvature. (C) Histogram of changes in horizontal radius of curvature of the posterior corneal surface in all patients, between pre-operative measurement and all post-operative ones (1day, 1 week and 1 month). (D) The same as (B), for the vertical radius of curvature.

7.4.5. Correlation of the posterior corneal changes with different parameters

We tested correlations between posterior corneal changes in radius of curvature, asphericity or central elevation with the attempted correction, change of pachymetry, pre-operative central pachymetry, post-operative central pachymetry or post-operative residual bed thickness. We tested all these correlations separately for changes 1 day, 1 week and 1 month after surgery. Of those correlations, only the correlation between attempted correction and posterior corneal apex shift one week after surgery showed a statistically significant correlation ($r = 0.665$, $p = 0.0005$). We only found near-significant correlations (*p*-value ranging from 0.04 to 0.051) between attempted correction and posterior corneal apex shift one day after surgery, and pachymetry, posterior apex shift, and radius of the posterior surface one week after surgery. These correlations disappear if eyes with attempted corrections greater than -6 D are removed from the calculation.

There were no statistically significant correlations one month after surgery.

7.5. DISCUSSION

In this chapter we have presented measurements of changes in the anterior and posterior corneal surface in patients that had undergone myopic LASIK refractive surgery and in control eyes. Our results for anterior surface mean pre-operative radius ($R_{ant} = 7740 \pm 230$ μm) and asphericity ($Q_{ant} = -0.11 \pm 0.13$) in our group of patients agree well with those reported by Dubbelman and collaborators, who used a custom-adapted Scheimpflug imaging system ($R_{ant} = 7870 \pm 270$ μm, $Q_{ant} = -0.18 \pm 0.18$).(Dubbelman et al., 2002) There is also a good agreement between our mean pre-operative posterior corneal radius of curvature ($R_{back} = 6440 \pm 250$ μm) and Dubbelman et al's ($R_{back} = 6400 \pm 280$ μm). However, our mean pre-operative posterior corneal asphericity is significantly higher ($Q_{back} = 0.18 \pm 0.21$ in our study and $Q_{back} = -0.38 \pm 0.27$ in Dubbelman et al.'s, for 6 and 7 mm fitted areas respectively). Differences may arise from differences in the refractive state and age of both populations, as our results from the validation using a hybrid model eye indicate an underestimation, rather than an overestimation of the posterior corneal asphericity.

We have not found evidence of a systematic influence of LASIK on the posterior surface of the cornea on average. We detected a change in the radius of curvature and asphericity of the posterior corneal surface the first day after surgery, but afterwards this change disappeared. The cause of this change is unclear to us. The fact that changes disappear in a timescale of days-weeks suggests the action of biological processes within that timing. Potential factors affecting posterior corneal shape temporarily may include hydration, keratocyte activity, the stress produced by the suction ring of the microkeratome or the medication. Furthermore, we observed a remarkable similarity between both eyes of each subject. This suggests a physiological mechanism acting bilaterally in the same way, as both corneas of the same patient are expected to have similar biomechanical properties and follow similar biological processes. The bilateral similarity also tends to occur in left and right eyes of the control subjects.

We have found that changes in the posterior radius of curvature changes occur primarily in the vertical direction in post-LASIK patients. Possible causes for this effect include the following three: (1) It is possible that surgery affects more strongly the corneal stability in the vertical direction. This might be due to an asymmetrical ablation for correction of astigmatism, but we have not found any statistically significant correlation between astigmatism corrected and radius change. Even with a symmetric ablation corneal stability might be more strongly affected in the vertical direction because of the direction of the flap, which is cut in the vertical direction, leaving a superior hinge. (2) Alternatively, a meridian-independent surgery may cause a greater change in the vertical meridian, if there is a greater mechanical stress of the cornea in that direction. This higher mechanical stress may be caused by the eyelid, which presses on the superior part of the cornea, and has been shown to modify the corneal geometry, having impact on corneal aberrations (Buehren et al., 2003), (3) Interestingly, the intralamellar cohesive strength, studied in human eye bank corneas, has been shown to be lower in the vertical than in the horizontal meridian, suggesting that even a symmetric force applied to the cornea may result in an asymmetric corneal deformation (Smolek, 1993). It is interesting to note that in previous studies (Jain et al., 2007) the vertical posterior radius of curvature was found to be the least repeatable

of the parameters measured by Pentacam, in repeated measurements of post-LASIK subjects.

We have found that control subjects also experience statistically significant changes of the same order of magnitude than those found in patients, although the reported differences between vertical and horizontal meridians are unique to patients (see Fig. 7.6(D), see also Fig. 7.5(B)). These differences between patients and control subjects are indicative of some surgical effect on the posterior corneal surface, although the average magnitude of the changes observed in patients is similar to that of the changes observed in control subjects. This suggests that most of the changes observed in patients are normal, perhaps due to changes in the intraocular pressure. In fact, preliminary results of inflation experiments on porcine eyes show that the radius of curvature of the posterior corneal surface changes about 30 μm per mm Hg (Perez-Escudero et al., 2008). The changes in posterior radius of curvature that we report in the present study (up to 120 μm) are consistent with changes of intraocular pressure of the order of 5 mm Hg, which is the average change in intraocular pressure throughout the day (David et al., 1992). The small changes induced by the surgery are superposed to these physiological changes, and originate the subtle correlations mentioned above.

All changes in the radius of curvature of the posterior corneal surface that we found are smaller than 180 μm (taking into account an interval of confidence of 98.3%). In an average cornea, this change in radius induces a change in the refractive power of the posterior corneal surface below 0.18 D (Barbero, 2006), too small to be clinically relevant. Therefore, the contribution of the posterior corneal surface to shifts from the attempted refraction is minor. Previous studies using Orbscan reported long-term average changes in posterior radius of curvature up to 400 μm (Seitz et al., 2001, Twa et al., 2005), and ectasia measured as forward displacement of the center of the posterior corneal surface up to 40 μm (Wang et al., 1999, Baek et al., 2001), much greater than the changes observed by us (lower than 8 μm on average, including the 98.3% confidence interval, Fig. 7.3 (C)). The discrepancy may be due to improper correction of the distortion due to the anterior corneal surface in Orbscan (Ueda et al., 2005, Donnenfeld, 2001). Our results are consistent with recent data obtained with the same device (Pentacam) (Ciolino and Belin, 2006). Along with the findings of this study, more experimental data on corneal biomechanical properties and more accurate models of corneal biomechanics will help to better understand the corneal shape response to LASIK surgery.

7.6. CONCLUSIONS

In this chapter we have demonstrated that Scheimpflug imaging can reliably assess corneal shape changes following refractive surgery research on real patients, both for the anterior and posterior corneal surfaces.

The anterior corneal measuremens (radius and asphericities) obtained using Pentacam agree with those previously reported using other methods and the same laser.

We found a transitory and clinically irrelevant change in the shape (radius and asphericities) of the posterior cornea the first day after surgery, but we found no evidence of permanent changes as a consequence of LASIK. The changes in the posterior radius of curvature occur primarily in the vertical direction. In equivalent measurements in control eyes, with no treatment between measurements, we observed changes of the same magnitude, but without directional differences.

We found a similar trend in the evolution of the radius of both eyes of each patient. This parallelism between eyes is also found in control eyes, suggesting physiological mechanism acting bilaterally in the same way.

7.7. OUTLOOK

This chapter closes the study of refractive surgery in this thesis. We have developed models for the quantitative evaluation of the anterior and also of the posterior corneal shapes. We have studied the changes in corneal shape induced by corneal refractive surgery both in-vitro (using plastic models) and in vivo. We have compared optical outcomes of standard and optimized laser refractive surgery platforms with new generation algorithms in vivo, studied the impact of those changes on corneal spherical aberration and proposed methods of optimization of current algorithms (compesated

The experience gathered studying ablation algorithms and their effect on optical outcomes is of great use in the the study of contact lenses. Contact lenses modify the refraction of the anterior surface of the eye, as well as the aberration patterns, as an ablation pattern does (by addition, rather than subtraction of material). Like corneal ablation, the fitting of contact lenses is a complex process (Sections 1.9 and 1.10) with many open questions (Section 1.10). As performed for corneal ablation, we will develop an artificial model eye to test contact lenses in vitro (Chapter 8) and will perform measurements on real patients, with rigid (Chapter 9) and soft (Chapter 10) contact lenses. Both studies on LASIK and contact lenses (eye models or patients) share methodology. Furthermore a mutual feedback between both areas is expected, with important implications on the design of ablation algorithms and lenses (i.e. multifocal lenses and presbyopic treatments)

Sir John Herschel and Contact Lenses

Katherine Chalkley has appealed for an exact quotation, from the writings of Sir John F. W. Herschel, of the passage in which he is supposed to have suggested the making of corneal contact lenses (*Science*, 1949, 110, 693). I am glad to supply the information, and to take this opportunity to point out that Herschel probably did not have *corneal* contact lenses in mind.

The passage occurs on p. 398 of Sir John's great article on ''Light,'' occupying pp. 341–586 of Vol. IV of the *Encyclopaedia Metropolitana*, which was published in London in 1845. The article was, however, signed ''Slough, December 12, 1827'' and was apparently published separately as soon as it had been written, for a French translation appeared in 1829–1833 and a German one in 1831. Any discussion of priority in the suggestion of contact lenses *per se*, therefore, should probably credit Herschel with such a suggestion as of 1827.

On his p. 398, Herschel is speaking of possible means of correcting for regular corneal astigmatism, which had been recently discovered by G. B. Airy in his own eyes, and not as yet (in 1827) concisely named.[1] Herschel says:

The strict method, applicable in all such cases, would be to adapt a lens to the eye, of nearly the same refractive power, and having its surface next the eye an exact *intaglio* fac-simile of the irregular cornea, while the external should be exactly spherical of the same general convexity as the cornea itself; for it is clear, that all the distortions of the rays at the posterior surface of such a lens would be exactly counteracted by the equal and opposite distortions at the cornea itself.†

Herschel goes on to describe how Airy solved the problem by means of a spectacle lens in the usual location, but having one spherical and one cylindrical surface—the type of correction used for this common refractive error ever since.

The dagger at the end of the quotation indicates a footnote in which Sir John says:

† Should any very bad cases of irregular cornea be found, it is worthy of consideration, whether at least a temporary distinct vision could not be procured, by applying in contact with the surface of the eye some transparent animal jelly contained in a spherical capsule of glass; or whether an actual mould of the cornea might not be taken, and impressed on some transparent medium. The operation would, of course, be delicate, but certainly less so than that of cutting open a living eye, and taking out its contents.

Certainly, here is a detailed suggestion of a contact lens, and even of the *molded plastic* type which in recent years has become favored. But I do not believe that Sir John literally contemplated what we now call a *corneal* lens, i.e., one edged to the diameter of the cornea, lacking a scleral skirt. Like his father and his aunt, Sir John was an astronomer. His work is not free of errors concerning the eye, and he certainly knew nothing about it from the operative standpoint (else he would not have used the operation of evisceration as an example of ''delicate'' one!). In this instance, his attention was almost entirely upon the cornea, since it is the (only) optical part of the fibrous tunic and hence lay within his department of science. But I would confidently predict backwards and say that if Herschel had tried to make and fit a contact lens, it would have had, from the first or very soon afterward, a scleral portion supporting the ''corneal segment'' out of contact with the sensitive cornea, in the present manner. The technology of the time could not have provided a corneal lens fitted so perfectly as not to stimulate the cornea's abundant pain-endings—and Sir John would have known this as soon as he touched his own cornea.

About ten years ago, I read a 19th century account of the experimental installation of a corneal contact lens, in a rabbit which wore it for several months without ill effects. Unfortunately, I have lost that reference (which might establish a genuine priority).

GORDON L. WALLS

School of Optometry,
University of California, Berkeley

Chapter

8

Optical evaluation of
soft contact lens fitting
using model corneas

This chapter is based on the article by Dorronsoro et al. "Optical evaluation of soft contact lens fitting using model corneas", to be submitted. The work was partially presented at the II Topical Meeting on Physiological Optics, Granada 2004 (Dorronsoro et al., 2004).

The contribution of Carlos Dorronsoro to the study, in collaboration with other coauthors, was the literature search, the design of the experiments, the customization of the measuring instruments and software (in collaboration with L. Llorente), participation in the experimental measurements (led by R.G. Anera), the development of the data analysis routines and the analysis of the data.

Coauthors of the study are Rosario G. Anera, María J. Gonzalez, Lourdes Llorente and Susana Marcos

8.1. ABSTRACT

Purpose: We developed an experimental model to study the optical effects of fitting soft contact-lenses. Knowledge of the coupling between the optics of the eye and of the contact-lens, and how the lens flexes to conform the cornea is essential to understand fitting of multifocal lenses, and why they do not work successfully in many patients.

Methods: Artificial eyes were manufactured on PMMA cylinders. The cornea was a polished spherical surface, and the retina was located in the corneal focal plane. Total and anterior surface aberrations were measured on naked artificial eyes and fitted with positive and negative monofocal and multifocal soft contact lenses. Laser Ray Tracing and videokeratoscopy were adapted to allow measurements in the vertical direction. A special holder was used to provide good centration and hydration of the lens, and uniform tear surface.

Results: The shape of the contact lens on-eye was simulated based on corneal topoghaphy measurements. We found differences between monofocal and multifocal designs in the anterior surface shape. The radii of the lenses were consistent with their nominal power. Multifocal designs tend to produce aspherical surfaces, more complex than simple conics. The analysis in terms of aberrations can be simplified to spherical aberrations. Corneal and total spherical aberration coincide in the artificial eye without lens, validating our aberrometers. The presence of tear does not influence the average result, although it increases the variability. Corneal spherical aberration is reduced less than expected in positive multifocal lenses. Negative multifocal lenses conform to the cornea, not inducing multifocality at all their first surface. Monofocal lenses reduce total spherical aberration. Total spherical aberration is positive in the multifocal designs, which differs from the expectation of the intended optical change.

Conclusions: A new experimental model for the study of soft contact-lenses, based on aberrometry, has been developed which can be used to evaluate the optical factors involved in contact lens fitting without the variability associated to individual eyes. Physical causes are more important than expected to account for the lack of adaptation of patients to multifocal lenses.

8.2. INTRODUCTION

This Chapter, along with Chapters 9 and 10 addresses the fitting of contact lenses, with special interest in the optical factors involved. As described in Section 1.9 and 1.10 of the introduction, the fitting of contact lenses is a complex process, involving shape changes (mainly of the lens, but also of the cornea), tear changes, physiological and neural effects. There are many open questions that are not well understood (Section 1.11). A major issue in contact lens ftting is the high intersubject variability in the adaptation of patients to multifocal designs. The trial and error approach usually undertaken in the contactology practice is high inefficient, causing important disturbances to the patient and costs (Sections 1.9.5 and 1.10.3).

With the aim of simplifying the experimental study of the optical implications of contact lens fitting, and isolating the problem from other factors involved, we developed an in vitro physical model based on fitting lenses on artificial corneas, which will be presented in this chapter.

The model is based on fitting lenses on artificial PMMA corneas, which are more regular, symmetric and stable surfaces than the living cornea, and therefore the optical measurements are subject to less variability. We measured and compared the shape of the front surface before and after the fitting, and also corneal and total aberrations. This chapter will describe this new experimental model and measurements using different lens designs: Monofocal and two designs of multifocal, with different powers and thicknesses. The aim of this work is to evaluate the validity of such a model, and its potential applications. Data on model eyes will be important in the analysis and understanding of the measurements on real eyes fitted with contact lenses (Chapters 9 and 10).

Although several studies in the literature address the measurement of aberrations in eyes wearing contact lenses (see Section 1.10 of the Introduction for a brief review) predictive studies from in vitro measurements or computer simulations are scarce. Conventional off-eye measurements of the contact lens are performed using a wet cell (Jeong et al., 2005, Lopez-Gil et al., 2002, Sabesan et al., 2007). Computer simulations are usually too simplified and do not account fo all the factors that may be relevant in the final optical outcomes (Dietze and Cox, 2004, Martin and Roorda, 2003, De Brabander et al., 2003).

In our method the lens is supported on a solid surface of known shape, as occurs in the eye. As in real fittings, the lens is kept hydrated while in contact with the air. This model considers experimentally the possible conformity of the lens shape to the underlying cornea, and also the tear film. Therefore, it is expected that this model provides more realistic information than direct measurements of the lens alone in inmersion studies.

8.3. METHODS

The eye model consists of a PMMA cylinder finished on a polished spherical surface, similar to that described in Chapter 3 for corneal ablations. Corneal topography measurements allow obtaining anterior surface elevation maps, with and without contact lens. A direct comparison provides a description of the lens flexure and conformity (Fig. 8.1), and to retrieve the shape of the lenses, while fitted.

We have demonstrated in vitro that soft monofocal spherical lenses reduce total spherical aberration.

Multifocal lenses are affected by conformity to the cornea and fitting effects, although the final optical performance depends on the lens power, that determines central thickness.

These results can explain why different progressive contact lenses designs do not induce the intended optical change and fail in a significant number of patients. The tools developed allow an objective test of the contact lenses in vitro and can help to predict the outcomes of different contact lens designs in patients

8.6. OUTLOOK

In this study we have demonstrated that physical causes are more important than expected to study the fitting in multifocal lenses. In fact, physical factors result in large discrepancies from the intended design and optical outcomes in soft contact lenses.

The results were obtained off-eye, in a framework of reduced complexity (in-vitro model). However, contact lenses on-eye are subject to a set of strengths (See Section 1.9 and 1.10) that can affect flexure and conformity. Real eyes have a more irregular base shape, and variable (internal and crystalline lens) aberrations. Lenses on real eyes are also affected by movements and decentrations. Furthermore, the hydration state of a contact lens fitted on a real eye could differ from the simple tear model of the artificial cornea.

In the next chapters we will extend a similar analysis to measurements on real eyes. In Chapter 9 we will study monofocal rigid lenses on-eye. It is expected that conformity to the cornea will have a lower impact in semi-rigid materials than in the soft contact lenses presented here. In Chapter 10 we will present a study of monofocal and multifocal lenses, similar to those of this chapter but in-vivo, on several subjects. As in this chapter, the aspects of conformity and possible influence of internal aberrations (tear lens) will be addressed by aberration measurements in eyes with and without the contact lenses.

Chapter

9

On-eye optical performance of rigid gas permeable contact lenses

This chapter is based on the article by Dorronsoro et al. "On-eye measurement of optical performance of Rigid Gas Permeable contact lenses based on ocular and corneal aberrometry," Optometry and Vision Science. 80, 115-125 (2003). Coauthors of the study are Sergio Barbero, Lourdes Llorente and Susana Marcos.

A preliminary version of this work was presented as a poster presentation at Center for Visual Science's 23rd Symposium, "Engineering the Eye", June 13-15, 2002, University of Rochester, Rochester, New York, USA. This work was presented in June 2003 as an oral presentation at Instituto de Oftalmobiología Aplicada (IOBA), Universidad de Valladolid, Valladolid, Spain, as final research project of the Master in Vision Sciences.

The contribution of Carlos Dorronsoro to the study, in collaboration with other coauthors, was the literature search and analysis of aberrometry in contact lenses, the design of the experiments, the development of the Laser Ray Tracing set-up and software, and the data collection, analysis and processing.

9.1. ABSTRACT

Purpose: Our aim was to obtain a complete description of the interactions of rigid gas permeable (RGP) contact lenses with the optics of normal eyes.

Methods: We measured total and anterior surface aberrations in four subjects, who were all long term RGP contact lens wearers. The anterior surface wave aberration was obtained from videokeratographic elevation maps and ocular wave aberration was measured with a Laser Ray Tracing technique. Measurements were performed with and without their own spherical contact lenses.

Results: With this methodology we evaluated the optical performance with RGP lenses compared to the natural optics. We estimated the contribution of the anterior surface of the contact lens, the internal ocular optics, flexure, and the tear lens aberrations to the optical performance of eyes wearing RGP contact lenses. We found that in 3 of 4 subjects the contact lens significantly improved the natural optics of the eye. For the subject with higher dominance of corneal aberrations, RMS (2nd order and higher) decreased from 1.36 μm to 0.46 μm. 3rd and higher order aberrations decreased from 0.77 μm to 0.39 μm. The internal optics and lens flexure imposed limits on aberration compensation. Spherical RGP contact lenses did not produce spherical aberration due to a compensatory role of the tear lens.

Conclusions: Aberration measurements are useful to understand the fitting of contact lenses, and the interaction with tear, cornea and internal optics of the eye. Aberrometry can help to choose the best standard RGP lens parameters to improve the optics of individual eyes.

9.2. INTRODUCTION

In Chapter 8 we studied in vitro the optical implications of fitting contact lenses. In this Chapter we study the optical factors involved in the fitting of contact lenses on eye, in particular Monofocal Rigid Gas Permeable Contact Lenses, with an expected lower degree of conformity than the soft contact lens if the previous chapter. There are now sources of biological variability, for example movements of the lens on-eye, but the results can be directly applicable to real patients.

It is well accepted in the contactology practice that RGP contact lenses produce superior visual quality than soft contact lenses, although to our knowledge this has not been experimentally demonstrated from an optical point of view. In this study we will address the potential of RGP lenses to reduce ocular aberrations (not only defocus and astigmatism, but also high order aberrations). In this chapter we present measurements in four young healthy subjects, long term RGP CL wearers. Again, we will use the combination of total and anterior surface aberrations measurements, but now applied to these subjects with their natural optics and with their RGP lenses. The combination of these four types of measurements allows a complete description of the interactions of the CL with the subject's natural optics, and to study the optical implications of the RGP CL fitting.

In this chapter we show: 1) The capability of RGP CLs to greatly reduce ocular aberrations beyond defocus, particularly in optically degraded eyes. 2) Flexure effects of the RGP CL's on anterior surface and total aberrations. 3) The contribution of the tear-lens to the ocular aberrations.

9.3. METHODS

9.3.1. Subjects

Four volunteers (two males and two females) participated in the study. RGP CLs were not fit for this particular study, but rather the subjects were selected because they were long term and satisfied RGP CL wearers. Subjects wore their own CLs, which all were RGP with anterior spherical surfaces. Ages ranged from 18 to 33, and spherical refractions from –4.5 to –8 D. Individual autorefractometer refractions, ages, axial lengths, anterior chamber depths and corneal curvatures are reported in Table 9.1. Parameters of each CL provided by the manufacturers are also included Table 9.1. Apart from their ametropia, all eyes were normal, and BCVA was 1.00 or better. Only one eye was tested per subject, right eye for S1, S2 and S4, and left eye for S3. RGP lens stabilization and repositioning after blinking was checked by pupil video monitoring (with respect to the pupil center). While there was not inter-eye differences in the rest of the subjects, in subject S3 centration was significantly better for the left than for the right eye, and therefore the left eye was chosen for measurements. Table 9.1 reports the coordinates of the center of the CL (in its stable position) relative to the pupil center.

All subjects had an eye examination before participating in the experiment. All subjects were informed about the nature of the study and signed an informed consent form, following the tenets of the Declaration of Helsinki. All the protocols and consent forms have been approved by Institutional Review Boards.

9.3.2. General experimental procedure

All measurements were conducted in the same experimental session, which lasted about an hour. Initial routine measurements included slit lamp examination, autorrefraction (Automatic Refractor Model 597, Humphrey-Zeiss), and axial length and anterior chamber depth by optical biometry (IOLmaster, Humphrey-Zeiss). These measurements, as well as videokeratography (Atlas Mastervue Corneal Topography System Model 990, Humphrey-Zeiss) were obtained without the CL. A second videokeratography was obtained with the subject wearing his/her CL. Videokeratographic images were taken when the CL had reached a stable position after blinking. Images distorted by tear fluid irregularities (more frequent when the eye was wearing the CL) were rejected. Pupils were dilated by means of one drop of tropicamide 1% prior to Laser Ray Tracing measurements of ocular aberrations. The first set of measurements was taken without the CL, and the last set of measurements with the CL on.

Table 9.1. Subjects and contact lenses.

	Subject			
	S1	S2	S3	S4
Eye	OD	OD	OS	OD
Age (yr)	27	33	18	24
Retraction (D)	−8.00 −2.00 × 8	−4.50 −1.25 × 92	−8.00 −0.75 × 168	−6.75 −0.50 × 159
Axial length (mm)	25.25	26.14	26.78	27.02
Anterior chamber depth (mm)	3.75	3.83	3.67	4.38
Corneal radius (mm)	7.62	8.21	8.19	8.02
Corneal asphericity	0.15	0.1	0.18	0.12
Contact lens type	Permiflex	Permiflex Aire	Conflex Air 100 UV	Boston E.S.
Manufacturer	Eurolent	Eurolent	Zeiss	Bausch & Lomb
Front optical zone radius—videokeratoscope (mm)	8.41	9.22	9.62	9.05
Back optical zone radius (mm)	7.70	8.25	7.90	7.95
Front surface asphericity—nominal	0	0	0	0
Back surface asphericity—nominal	0	0	−0.16	0
Front optical zone diameter (mm)	—	—	8.5	8.5
Back optical zone diameter (mm)	8.5	8.1	—	8.4
Back vertex power (D)	−3.50	−3.25	−7.00	−5.00
Central thickness (mm)	0.18	0.18	0.15	0.18
Material	PMMA + CAB	Silicone Fluorcarbonate	Fluor silicone metacrilate	Enflufocon A
n	1.469	1.467	1.467	1.443
Lens center (x, y) (mm)[a]	(1.1, 0)	(−1.66, 1.27)	(−1.91, −0.25)	(1.37, 0.47)

[a] Relative to pupil center. Positive horizontal coordinates stand for nasal in right eyes and temporal in left eyes. Negative horizontal coordinates stand for temporal in right eyes and nasal in left eyes. Positive vertical coordinates stand for superior, and negative stand for inferior.

9.3.3. Anterior surface aberration measurements

Anterior surface aberrations were estimated from elevation maps, obtained with the videokeratographer (described in Section 2.1.2) and custom algorithms. Without the CL, these maps represent the corneal elevation. With the CL on, they represent the elevation of the anterior surface of the CL. The experimental procedure has been described in detail in earlier studies (Marcos et al., 2001a, Barbero et al., 2002c, Barbero et al., 2002b). A detailed description can be found in Chapter 2, Section 2.3.1.

9.3.4. Total aberration Measurements

Total aberrations were measured (with and without the RGP CL) using a Laser Ray Tracing technique (LRT). A detailed description of this method can be found in Chapter 2.

Typical pupil diameters for LRT measurements in previous studies were 6.5 mm (with a sample step of 1 mm). In this study we reduced maximum pupil size (6 mm for subject S1, 5.5 mm for subjects S3 and S4, and 5 mm for subject S2). We found that for larger pupil diameters several images (corresponding to the most eccentric entry pupils) were affected by diffraction at the edge of the CL. Sampling step was varied, so that in all cases the pupil was sampled by 37 rays. For comparison purposes, all data were recomputed for 5-mm pupils.

The largest contribution to the displacement of retinal aerial images in measurements without CLs was caused by spherical errors. For the pupil diameters used, all the aerial images fitted within the CCD chip, except for one subject (S3), for whom spherical errors moved the aerial image outside the CCD. For this subject, we compensated for the refractive error with a trial lens (-7D), in measurements performed without the CL. For one subject (S4), we conducted measurements with and without trial lens, to assess any possible contribution of the trial lens correction (see below).

9.3.5. Control and trial experiments

The pupil monitoring channel of the LRT system was especially useful with RGP contact lenses. The fitting of these lenses is usually "open", namely, with a posterior radius flatter than the cornea, and therefore these lenses have a lot of movement, especially after blinking or after eye movements. Besides, the normal fitting position of the lens is off-centered. Similarly to videokeratographic images capture with CLs some training was required to optimize image capture with CLs in LRT, and to ensure that measurements were taken with the lens in its stable position. Initial measurements were performed in one subject wearing RGP CL (S1), using green light (543 nm). The pupil was illuminated by IR (780 nm) light using a ring optical fiber illuminator. A filter (543 nm) was placed in front of the CCD camera that captured the aerial images to eliminate spurious light from the pupil illumination. A frame grabber captured the video signal from the pupil monitoring camera, while the test beam scanned the pupil and the second camera captured the aerial images. Pupil images also show the position of the CL, and the 1st Purkinje images of the sampling beam (actually the reflection comes from the CL, rather than from the anterior corneal surface) as it moves across the pupil. Figure 9.1 shows a schematic description.
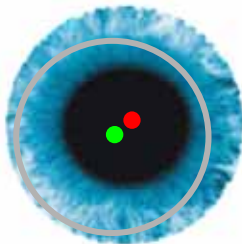
Fig. 9.1. Squematic description of the lens tracking functionality.

With this configuration, we were able to assess the exact entry pupil location for each captured aerial image. In all cases, aerial images showing a diffraction pattern and elongated in a direction perpendicular to the CL edge, corresponded to rays that hit the edge of the optical zone of the CL. We also were able to assess CL motion dynamics in all subjects by pupil monitoring. All of the CLs moved downwards significantly when the subject raised his/her upper lid more than normal. After some feedback, the subject was able to keep a good CL stability.

We performed measurements in S1 in both visible (543 nm) and IR (786 nm) light. Except for exceptional runs for which the CL was clearly displaced (as assessed by the pupil video image during the measurements in green), results in both wavelengths were within the measurement variability (average standard deviation across Zernike coefficients less than 0.1 µm). For the sake of subject's comfort, only IR light was used for the rest of the subjects. Dynamics of the CL was assessed with the described system prior to the measurement, and when stability was achieved, pupil illumination was turned off during aerial image capture in IR light.

Effect of trial lenses: Trial lenses, or in general any correction system (i.e. Badal optometer) that changes ray convergence to optimize retinal focus, may have an effect on the measured spherical aberration. We measured one subject (S4) with his uncorrected eye and with a trial lens (-5 D) in front of the eye. The converging effect of the lens introduces a scaling in the sampling pattern, which was corrected by the software controlling the scanner. We could not find significant differences in the aberrations measured with and without the trial lens.

9.3.6. Data handling and selection

Special care was taken in the processing of data from eyes wearing CLs, since they were subject to problems not present in the natural eyes (lens movement or partial pupil covering by the eyelid). We rejected aerial images with CL edge effects patterns. The presence of more than three diffraction-like patterns of adjacent rays was a cause to reject the whole series, as we suspected the lens or the subject had moved. More than four images rejected for any reason caused the rejection of the whole series, which was not used in further processing. This happened in 17 out of a total 45 number of series. In very exceptional cases (3 out of 28) we found that the wave aberration corresponding to an apparently normal series of images, was very different from the rest of consecutive runs. These abnormal patterns were rarely or never repeated, and we interpreted that they corresponded to unstable positions of the CL or CL shift during the measurement. These abnormal modes usually had also an abnormally high amount of coma and/or astigmatism. All of the aberration estimates presented here were calculated at least from the mean of three series.

9.4 RESULTS

Figure 9.2 shows wave aberration maps for all four subjects. For each subject we show the four measurements performed: total and anterior surface aberrations, with and without CL, respectively. Anterior surface aberrations stand for aberrations of the anterior corneal surface for the eye without CL, and aberrations of the anterior surface of the lens when the eye is wearing the CL. Defocus has been removed in all cases. For each subject, the four upper maps include all aberrations except tilt and defocus, and in the four lower maps astigmatism has also been removed.
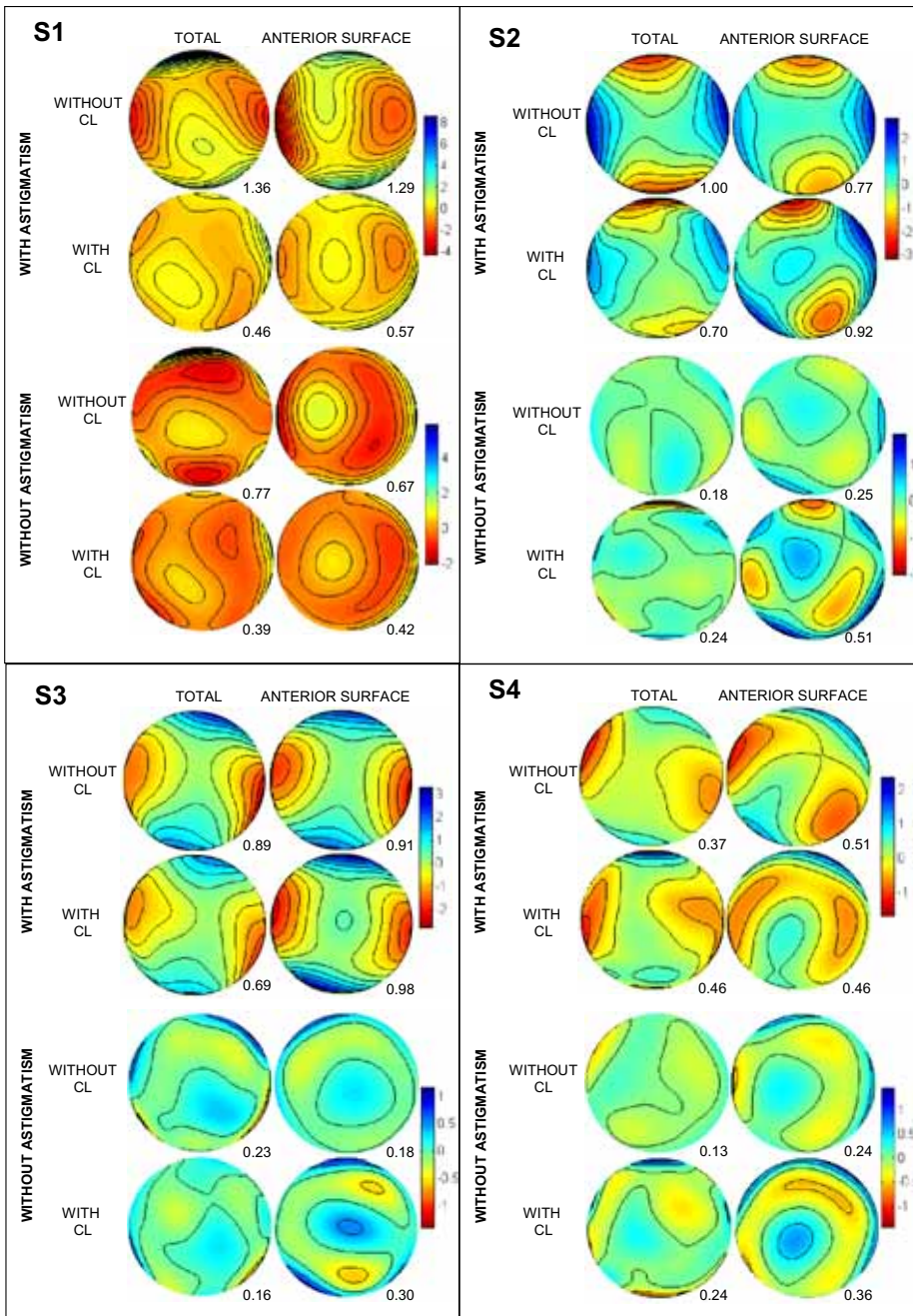
Fig. 9.2 Wave aberration maps for all subjects. For each subject we show the four wavefronts measured: total (left panel) and anterior surface (right panel), with and without rigid gas permeable contact lens (RGP CL). Anterior surface aberrations stand for aberrations of the anterior corneal surface for the natural eye, and aberrations of the anterior surface of the CL when the eye is wearing the CL. For each subject, the four upper maps include all aberrations except tilt and defocus, and in the

four lower maps astigmatism has also been removed. Contours have been plotted at 1 μm interval. Pupil diameter is 5 mm in all cases. The RMS (in microns) is indicated for each wavefront.

To show the effect of CL wear, we have used the same gray scale for anterior surface and total aberration maps for the same subject. Contours have been plotted at 1 μm intervals. Pupil size is 5-mm in all cases. In many cases, and most obviously for S1, the number of contour lines is lower with the CL, indicating a correction of the natural aberrations by the CL. Not only astigmatism decreases (see upper maps), but also higher order aberrations. We found an increase of aberrations with CL only for S4, whose natural aberrations were very low. While the amount of aberrrations decreases in most cases, the aberration pattern with CL follows a pattern similar to the natural wave aberration. This is indicative of some degree of conformity. There is a strong similarity between total and anterior surface wave aberration maps in all subjects and conditions.

Figure 9.3 compares Zernike coefficients for two representative subjects (S1 and S3). S1 (Figs. 9.3(a) and 9.3(b)) is the subject with the highest amount of aberrations without CLs, and highest degree of compensation with RGP CLs. S3 (Figs. 9.3(c) and 9.3(d)) has high astigmatism but low high order aberrations. The ordering and notation of the Zernike coefficients follows the recommendations of the Optical Society of America Standard Committee (Thibos et al., 2000).
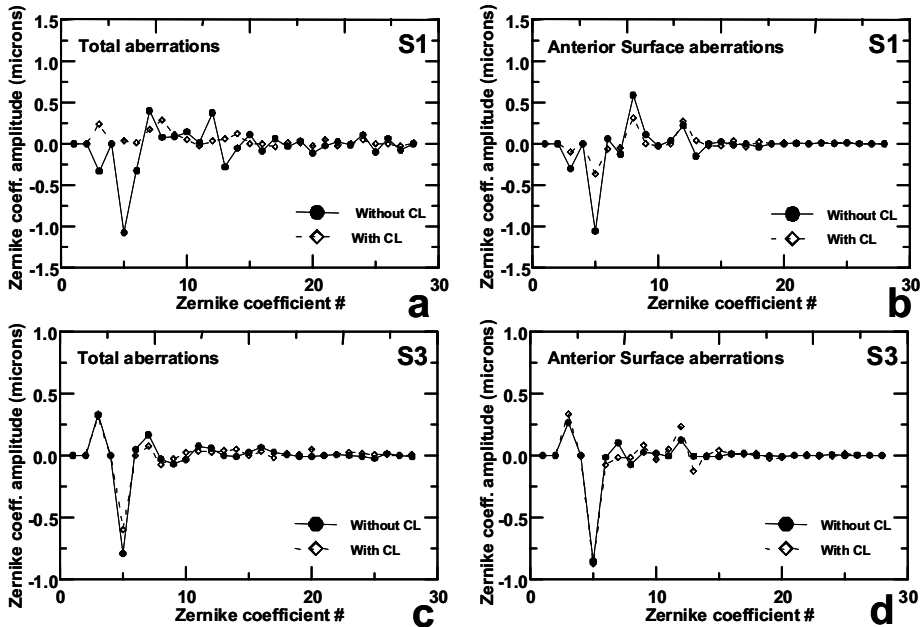
Fig. 9.3. Zernike coefficients for subjects S1 and S3. (a) Total aberrations with and without CL for S1; (b) Anterior surface aberrations with and without CL for S1;(c) Total aberrations with and without CL for S3; (d) Anterior surface aberrations with and without CL for S3.

For subject S1, total astigmatism (terms 3 and 5) is well corrected, but there is also a large reduction of 3rd and higher order aberrations –see for example coefficient 12 (Z_4^0) and 13 (Z_4^{-2}) in Fig. 9.3(a)–. All the most significant anterior surface aberration

coefficients are also largely reduced, with the exception of spherical aberration (Z_4^0): astigmatism, terms 3 (Z_2^2) and 5 (Z_2^{-2}) and comatic term 8 (Z_2^{-1}) in Fig. 9.3(b). There is a good correspondence between total and anterior surface aberrations (Figs. 9.3(a) and 9.3(b)).

S3 shows an aberration pattern dominated by astigmatism (almost as high as S1), practically all corneal in origin, as indicated by the great correspondence of total and corneal aberrations (Figs. 9.3(c) and 9.3(d)). Spherical aberration is the predominant high order aberration of the cornea, but not of the whole eye. In this subject we found only a small correction of aberrations by the RGP CL.

Figure 9.4 summarizes the effect of RGP CLs on total aberrations (RMS) for different orders of the Zernike polynomial expansion, for all subjects. Figure 9.4(a) shows RMS for all terms, excluding tilt and defocus. The CL significantly corrects part of the ocular aberrations in three of our four subjects. RMS decrements range from 0.9 m in S1 to 0.2 μm in S3. For subject S4 there is a slight increase in RMS (0.09 μm). This value is of the order of the RMS variability (0.11 μm for this subject), and therefore it is not statistically significant. This subject has a low amount of aberrations, and internal optics RMS (0.37 μm) is comparable to corneal RMS (0.51 μm). Anterior surface aberrations decrease however (RMS 0.51 to 0.46), with CL wear.
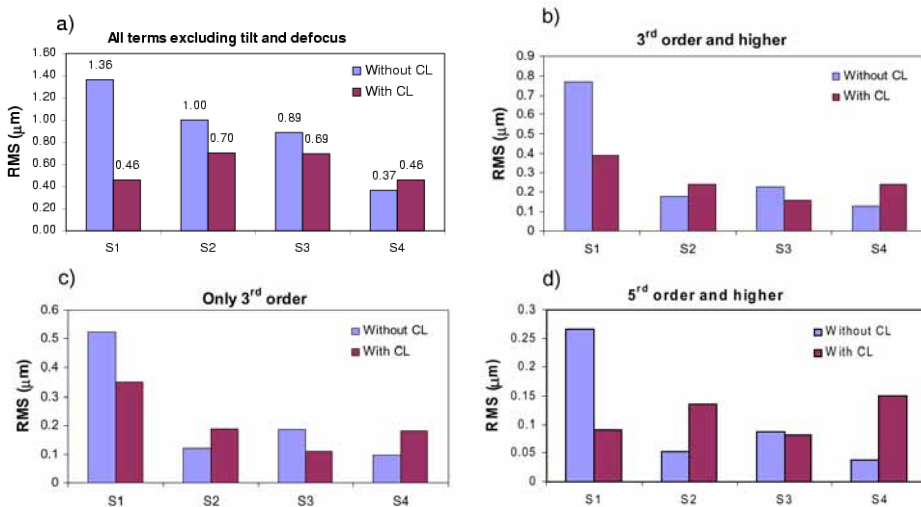
Fig. 9.4. Effect of RGP CLs on total RMS for all subjects. (a): RMS for all terms, excluding tilt and defocus; (b) RMS for 3rd and higher order.terms (c): RMS for 3rd order terms; (d) RMS for 5th and higher order terms.

Figure 9.4 (b) shows RMS for all terms of 3rd and higher order. These terms account for all aberrations that cannot be corrected with conventional ophthalmic lenses.

Figure 9.4(c) shows RMS for Zernike coefficients of 3rd order only, i.e. coma-like aberrations. Figure 9.4(d) shows 5th and higher order aberrations. Subject S1's natural optics shows high amount of aberrations in all orders, and there is a reduction of aberrations in all orders with RGP CL wear.

All other subjects have a low amount of aberrations without CL, other than astigmatism, and the use of CLs does not change them significantly. The effect of RGP wear on 5th and higher order terms (Fig. 9.4(d)) shows different trends across subjects: a decrease for S1, no difference for S3, and an increase for S2 and S4. Increase in the 5th and higher order terms is curiously found in the same subjects who experienced an increase in 3rd order terms and more systematic decentrations of the RGP lens. A possible increase of 3rd and higher order terms due to decentrations had been predicted (Atchison, 1995, Ho et al., 2002) although this effect has proved more relevant for aspheric lenses.

Figure 9.5 shows total and anterior surface 4th order spherical aberration coefficient (Z^0_4) for the different subjects, with and without CL. As expected, despite intersubject differences in the amount of spherical aberration in the natural corneas, we obtained the same amount of spherical aberration for all lenses (increased with respect to natural values because the lenses were spherical). However, the total spherical aberration with CL is close to zero for all subjects.
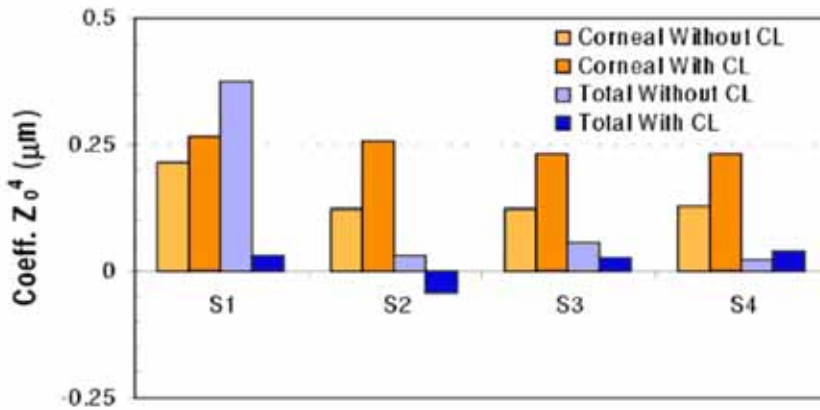
Fig. 9.5. Total and anterior surface 4th order spherical aberration coefficient (Z^0_4) for the four subjects, with and without CL.

9.5. DISCUSSION

9.5.1. Aberration correction

The principle of correction of corneal irregularities (and hence corneal aberrations) by RGP CLs has been explained by several authors (Griffiths et al., 1998, Atchison, 1995). The CL substitutes the anterior surface of the cornea with a polished regular surface. The main refraction is now produced at the anterior surface of the CL. Tear between lens and cornea fills in corneal irregularities. The power of the anterior surface of the cornea decreases to 11 %, as refraction indexes are almost the same (n_{tear} = 1.336, n_{cornea}=1.376). Therefore, the CL correction acts on corneal aberrations. We have found that RGP CLs are able to correct to some extent ocular aberrations. For the most aberrated eye, we found a decrease of RMS (excluding tilt and defocus) by a factor of 3 (or RMS decrement of 0.9 μm). The improvement is not only due to astigmatism corrections. Non conventional aberrations were also significantly reduced: 3rd and higher order RMS decreased by a factor of 2 (a decrement of 0.38

μm). Interestingly, total spherical aberration was close to zero, despite the spherical surfaces of the CL.

These results are comparable to the best case reported by Hong et al. (Hong et al., 2001) (RMS decreasing from 0.5 to 0.14 μm), who compared the impact of RGP CLs, soft CL and spectacles on the ocular aberrations. This degree of compensation is close to that achieved by some custom correction methods, which aim at correcting not only corneal but the whole optical system aberrations. Navarro et al. (Navarro et al., 2000) reported an increase by a factor of 5 (RMS decrease from 1.25 to 0.25, for 6.5-mm pupils) using static correction by custom phase-plates. Preliminary results with custom CLs show a decrease in RMS from 0.83 to 0.35, for 5 mm pupils (N.Lopez-Gil et al., 2002). In addition, the first outcomes of custom refractive surgery show variable results (Mrochen et al., 2000, MacRae et al., 2000). A decrease of the RMS from 1.5 to 0.2 μm for 6.8-mm pupils have been reported using dynamic corrections with adaptive optics (Hofer et al., 2001, Fernandez et al., 2001). These findings may have some implications in myopia management and control. Several clinical trials (Perrigin et al., 1990, Khoo et al., 1999) have found that children wearing RGP CL had a slower myopia progression than other age- and refraction-matched groups wearing glasses or soft CLs. The differences could not be explained by corneal flattening in RGP CL wearers. Degraded vision with occluding diffusers (and conceivably with an increased amount of aberrations) has been linked to myopia development both in animal models and humans. A better optical quality with RGP CLs may be one of the causes for this apparent slow in myopia progression.

The major limitation of aberration correction with standard RGP CLs is that it is restricted to anterior corneal surfaces aberrations, while the previous methods aim at canceling all aberrations. We have found that the amount of aberration corrected depends on the subject initial aberrations, and in particular, whether the ocular aberration pattern was dominated by corneal aberration, or rather the internal aberrations played a significant role.

Measuring anterior surface and total aberration allows, by subtraction, to account for the contribution of internal aberrations to the ocular optics. Previous studies have applied these comparisons to study the interaction of the aberrations of the different ocular components as a function of age (Artal et al., 2002), refractive error (Marcos et al., 2001b) or in refractive surgery (Marcos et al., 2001a). It appears that in young, normal eyes, there is an important degree of balance between corneal and internal aberrations. The measure of anterior surface and total aberrations in patients with and without RGP CLs allowed us for the first time to evaluate the interactions of the ocular components (including the internal optics) with RGP CLs and understand the performance of this type of lenses individually.

From our subjects (see Figs. 9.2 to 9.5), S1 had the greatest amount of corneal aberrations (RMS=1.29 μm, including astigmatism) and the ocular aberration pattern was dominated by corneal aberrations. This is the most favorable case to achieve a good aberration correction with CLs and explains the excellent outcomes for this subject. Subjects S2 and S3 have low internal aberrations (RMS= 0.42 μm, 0.3 μm, respectively) but only moderate corneal aberrations (RMS=0.77 μm and 0.91 μm), and therefore the correction is not so remarkable. Subject S4 had very low corneal aberration (RMS= 0.51 μm), which are partially compensated by internal aberrations (RMS=0.37 μm), producing very low total aberrations (RMS=0.36 μm). In this case,

aberration correction was not achieved despite the fact that anterior surface aberrations decreased by the RGP lens (from 0.51 μm to 0.46 μm).

Our study demonstrates that internal optics limit the aberration correction by the use of RGP CLs. However, in those subjects with predominant corneal aberrations, corrections can be of the same order as those achieved by custom devices. This is particularly relevant in those cases where increased aberrations limit visual performance, such as pathological or surgical corneas. All previous studies of aberration compensation made use of customized optical elements, subjects with increased aberrations by corneal pathology, or specially manufactured CLs, while we have studied normal subjects wearing their own standard spherical RPG CLs.

It may be argued that the subjects in our study may not be considered normal, since it is well known that long term RGP lens wear can alter corneal shape and induce corneal warpage and distortion (Novo et al., 1995). If that was the case, the potential benefits of RGP CLs to improve the optical quality may be overestimated. We compared 3rd and higher order corneal aberrations in our four subjects with a population of other 38 normal young (31 ± 7 years) myopes (-4 ± 2.2 D), measured using the same procedures. For this control group, 3rd and higher order corneal RMS was 0.57 ± 0.2 μm. This value was close to the RMS (0.67 μm) for the most aberrated subject S1 in our study, which had been wearing RGP CLs for more than 10 years. Corneal aberrations in the other three subjects were lower than 0.25 μm as seen in Fig. 9.1. Therefore, the results found in the study are not necessarily unique to this particular set of subjects, and most subjects from the control group could potentially benefit from a reduction of aberrations by RGP CLs.

9.5.2. Flexure

When placed on the eye, the anterior surface of RGP CLs is not perfectly regular but it is also affected by corneal shape. Depending on some factors (lens thickness, flexibility,…) lenses flex to some degree to conform the corneal shape (Corzine and Klein, 1997). Previous studies have used videokeratographic elevation maps to estimate the degree of irregularity introduced by flexure (Collins et al., 2001). To our knowledge, no previous study had estimated real optical aberrations from those maps. The impact of flexure on visual performance is not clear. In our study, the four complementary measurements (with and without lens, anterior surface and total aberration) provide information to assess the impact of flexure not only on anterior surface but also on total aberrations.

Wave aberration maps with and without CLs in Fig. 9.2 show some similarities. This is particularly evident for astigmatism. Less contour lines are indicative of lower amount of astigmatism, but the angle is generally preserved. To study the degree of conformity between the fitted lens and the underlying cornea, in terms of aberrations, we have correlated corneal Zernike coefficients with and without CL on (shown in Fig. 9.6, x-axis showing coefficients without the lens, and y-axis with the lens). Since 5th and higher order aberrations are close to zero, only coefficients up to the 4th order are included. Slopes for each subject's best linear fit and regression coefficients (R) are also shown in Fig. 9.6. A slope between 0 and 1 is indicative of some degree of compensation by the CL: the lower the slope, the larger the compensation. A regression coefficient close to unity indicates that both anterior surface wavefronts, with and without lens, show similar shape, i.e. that the lens conforms to the corneal shape. Spherical aberration has not been included in the computation, as no correlation

was found. This issue will be discussed in detail in the next subsection. We have checked that the inclusion of the spherical term did not change substantially the correlation values. Subject S1 shows the highest correction (Slope=0.37) and high conformity (R=0.94). Subject S2 shows moderate correction and conformity (Slope=0.92, R=0.76). Subject S3 shows no correction and very high conformity (Slope=1.02, R=0.97) indicating that the lens flexure prevents correction. Subject S4 has good corneal correction and low conformity (Slope=0.53, R=0.65).
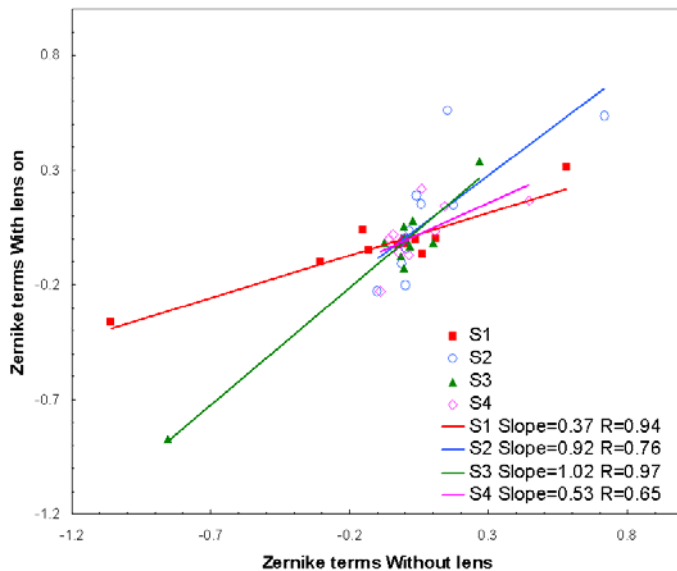
Fig. 9.6. Correlation between anterior surface Zernike coefficients with and without CL on. Only coefficients up to the 4th order are included. Spherical aberration was not included. Slopes for each subject's best linear fit and regression coefficients (R) are also shown.

This analysis agrees well with results shown in Fig. 9.4 (a), except for subject S4, for whom there is good corneal correction, but an increase in total RMS. This can be explained by the contribution of internal aberrations. Flexure analysis relates solely to anterior surface aberrations, and for this subject internal aberrations did partially compensate for corneal aberrations.

While Fig. 9.6 analyses all Zernike coefficients together, the effect of lens flexure can be studied in each term individually. Optimization of aberration compensation may be achieved by using individual total and corneal aberration data and a careful custom control of lens flexure.

Astigmatism is mostly of corneal origin in all subjects but S4. For S1 there is an important decrease in astigmatism (-1.39 D) by RGP CL wear. For S2 and S3 there is only a slight decrease in total astigmatism, as the lens follows the corneal astigmatism almost completely. It is interesting to describe the effects of lens flexure and the different ocular components contribution to astigmatism for subject S4. For S4, internal and corneal astigmatism have values of -0.71 D and -0.47 D but at angles of 142º and 29º. This indicates that corneal and crystalline lens astigmatism have nearly opposite directions (deviation from complete opposition is 23º), so that they are

partially compensating each other to produce a final astigmatism of -0.54 at 162º as measured by LRT (or –0.50 at 159º as measured with the autorefractometer). The RGP lens corrects part of the corneal astigmatism, but introduces a slight rotation of 19º (see Fig. 9.2). The deviation from opposition is now 42º, making the compensation less effective. The final astigmatism slightly increases up to -0.61 D. This detailed study can be performed on other higher order aberration terms other than astigmatism.

This individual analysis of the effects of lens flexure and the contribution of corneal and internal aberrations in each particular eye suggests that a control of the lens flexure can optimize aberration compensation, depending on the particularities of each eye. In eyes dominated by corneal aberrations (such as S1), high rigidity is advisable. However, for eyes where corneal and internal aberrations are well balanced (among our subjects, S4 is the closest case) a high conformity to the corneal shape would produce best results.

All previous analysis has been done for aberrations other than spherical aberration. We did not find that spherical aberration was affected by flexure (Fig. 9.5). Several studies report (Corzine and Klein, 1997) that lens flexure affects the amount of measured regular and irregular astigmatism in astigmatic corneas wearing RGP lens, and this effect depends mostly on lens thickness and to a lesser extent lens material. However, no evidence of flexure has ever been found on spherical corneas suggesting that RGP lenses do not conform to symmetric corneal shapes (Corzine and Klein, 1997).

9.5.3. Tear lens aberrations

The spherical aberration of the natural cornea is positive in all eyes with values varying across subjects (Fig. 9.5). The spherical aberration of the anterior surface of the CL shows larger amounts of positive spherical aberration, consistent with spherical lenses, and very similar across subjects. The total spherical aberration is higher than the corneal aberration in one subject (S1), indicating that the crystalline lens adds up to the spherical aberration of the cornea. In the rest of the subjects, we found the previously reported trend that internal negative spherical aberration partially balances the positive corneal spherical aberration, resulting in a low total spherical aberration (Artal and Guirao, 1998). Despite the positive spherical aberration contribution of the RGP CL, as estimated from videokeratographic measurements, we found very low values of total spherical aberration with the RGP CL. Our results suggest that there is a compensation of the positive spherical aberration induced by the CL by the tear lens (i.e. the tear film meniscus between the back surface of the CL and the anterior corneal surface). In the natural eye, the internal aberrations (total minus corneal aberrations) account for the internal ocular optics. In the eye wearing the CL, internal aberrations include the mentioned internal optics and the tear lens. The difference of the internal aberrations from measurements with the CL and the internal aberrations in natural conditions represents the tear lens aberrations.

Although this is an indirect and somewhat noisy estimate (0.13 μm standard deviation on average, for the spherical aberration coefficient), since it is computed after a double subtraction, we found a common trend in all the tear lens aberration maps from our four subjects. The spherical aberration is typically the largest high order coefficient, and it is always negative (S1:-0.39 μm; S2:-0.21 μm; S3:-0.14 μm; S4:-0.09 μm), which explains the described compensation of the lens positive anterior spherical aberrations.
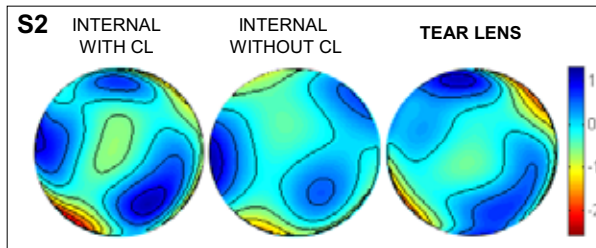
Fig. 9.7. Tear lens wave aberration map for S2 (right panel), estimated as the difference of internal aberrations with CL (left panel) and without CL (central panel).

A potential compensation by the tear lens of other aberrations, such as astigmatism, has been suggested before (Phillips and Speedwell, 1997). As an example, Fig. 9.7 shows the tear lens wave aberration map for S2 (right panel), estimated as the difference of internal aberrations with CL (left panels) and without CL (central panels). Negative spherical aberration dominates the wave aberration tear lens aberration pattern.

We performed a computer simulation to assess potential sources for this additional negative spherical aberration. Using ray tracing, we computed the spherical aberration due only to the tear lens (Ho et al., 2002). We assumed different asphericities for the posterior CL surface (which acted as the anterior surface of the tear lens). We used the actual subjects' anterior corneal surfaces as the posterior surface of the tear lens. We calculated that for spherical posterior lens surfaces, the tear lens spherical aberration was negative in all cases, following the trend found experimentally. However, the estimated amount (-0.016±0.002 on average) was much lower. The spherical aberration of the tear lens depends on the asphericity of the posterior lens surface. We found that an increase in the asphericity, shifted the spherical aberration of the tear lens toward more negative values (for example the mean spherical aberration for asphericity 0.6 was –0.063±0.004). Nominal asphericities of the posterior surface of the lens are zero (spherical surfaces) for all subjects except for subject S3 (see Table 9.1). However, it is well known that nominal specifications of RGP lenses can vary from actual values, particularly for the posterior surface (Defazio and Lowther, 1979). Deviations from ideal spheres may not be unlikely and a potential cause for the increased (in this case beneficial) negative spherical aberration.

9.6. CONCLUSIONS

In this study we have shown the application in real eyes, of combined measurements of aberrometry and corneal topography in RPG CL fitting. By using this methodology, we have been able to evaluate the contribution of the anterior surface of the RGP CL, the internal ocular optics, the flexure and the tear lens aberrations on the optical performance of eyes wearing RGP CL. This information provides an accurate analysis of CL fitting in individual eyes, and allows, for example, to track individual aberration terms through the different optical elements involved (contact lens, tear lens, cornea, internal optics).

We have shown that RGP CLs can improve significantly the natural optics of the subject, provided that corneal aberrations are predominant, and the lens flexure is well

controlled. Our study concludes that the lens flexure (or conformity) has a great impact on the degree of corneal aberration compensation. As there is previous evidence that internal aberrations usually compensate to some extent the aberrations of the cornea (Artal and Guirao, 1998), we conclude that a custom control on lens flexure can improve the cornea/internal optics aberration ratio and result in an improvement of the subject's visual performance.

Finally, we have shown that spherical RGP CLs do not induce higher final spherical aberration on the measured eyes. While the anterior lens surface shows higher spherical aberration than the natural cornea, we found negligible values of total spherical aberration in all our four subjects wearing their RGP CLs. Our results suggest that this compensation is produced by the tear lens, but this could be confirmed on measurements over a larger population, and a strict verification of the parameters of the lens used.

9.7. OUTLOOK

We used in real eyes the methodology developed in Chapter 9 for model eyes, and we have confirmed the importance of combined total and corneal measurements to understand contact lens fitting, and to assess critical factors such as the flexure on-eye.

We have learned that the internal optics are important when evaluating the fitting of contact lenses on real eyes, and that the tear lens (in between the contact lens and the cornea) affects the optical outcomes in semirigid lenses.

With the procedures developed, we can now accomplish the study of more sophisticated contact lens designs on individual eyes. In next Chapter we will use the methodology on real eyes fitted with soft lenses (monofocal and multifocal, as in Chapter 8). In addition, we will conduct measurements of visual outcomes thru-focus, to get an insight of the impact of the optical factors (beyond the contact lens design) on visual performance.

Chapter

10

Optical and visual performance of soft monofocal and multifocal contact lenses

This chapter is based on the paper by Dorronsoro, C., et al. "Optical and Visual Quality With Multifocal Contact Lenses", to be submitted. It was partially presented, as poster presentation, at ARVO 2007 (Fort Lauderdale, FL, USA) (Dorronsoro et al., 2007) and at the VIII Reunión Nacional de Óptica, Alicante, Spain (2006) (Dorronsoro et al., 2006b).

The contribution of Carlos Dorronsoro to the study, in collaboration with other coauthors, was the literature search and analysis of multifocal contact lenses, the design of the experiments, the development and adaptation of the Laser Ray Tracing set-up and software, and the data collection, analysis and processing.

Coauthors of the study are Maria J. Gonzalez, Lourdes Llorente and Susana Marcos.

www.fda.gov/MedicalDevices

10.1. ABSTRACT

Purpose: Multifocal contact lenses (CLs) are a common alternative to correction of presbyopia. Their failure to produce adequate visual quality or significantly expanded depth-of-field (DOF) in some patients is often attributed to lack of neural adaptation. We hypothesize that much of the effect is optical, and relies on coupling effects of the CL and the underlying ocular optics. We investigated this question by measuring total aberrations, and through-focus visual function in eyes wearing multifocal soft CLs.

Methods: We measured total aberrations (using a laser ray tracing system with a circularly symmetric sampling pattern) and visual acuity (Snellen E, 4 alternative forced choice paradigm) on 4 healthy cyclopeged eyes from 4 subjects (28±5 years). Each eye was measured without CL, with multifocal CL (Essilor Rythmic multifocal) of +3.5D (multiCL+) and -3.5D (multiCL-), and with a reference monofocal CL (monoCL-, Proclear Cooper Vision) of -3.5D. All CLs had the same base radius (8.60 mm) and similar material. Thru-focus modulation transfer functions and simulations of retinal images of acuity charts were obtained from the wave aberrations, and Strehl ratio was used as a metric. Visual acuity was measured through focus at steps between 1 and 0.5 D (30 trials per focus and stimulus duration of 0.5 s). All comparisons were performed for 4-mm pupil diameters.

Results: 1) We found high correlations between aberrations of the naked eye and aberrations of the eye with any of the CLs (R^2=0.88 for multiCL+, 0.90 for multiCL-, and 0.91 for the monoCL-, on average), indicating conformity of the CL to the cornea. 2) Negative spherical aberration was induced with 11 out of 12 CLs (mono or multifocal) (-0.10±0.02 for multiCL+, -0.04±0.09 for multiCL-, -0.09±0.04 for monoCL). 3) Only multiCL+ increased DOF (in 2 cases), at the expense of optical quality losses, as shown both from optical quality and visual acuity measurements. 4) Simulated through focus image quality correlates well with through focus visual acuity, indicating that optical aberrations are a major cause for the intersubject variability in visual function, and for the limits in the performance of the CLs.

Conclusions: 1) Ocular aberrations play a major role in the visual outcomes with soft multifocal CLs. 2) Negative multifocal CLs behave essentially as monofocal CLs, while the positive (thicker) multifocal CLs seem to expand DOF some, confirming previous results of this thesis on an in vitro model. 3) Understanding the coupling of the ocular optics to the CL is essential to improve current designs, prior to attribute their failure or success to neural effects.

Annex

A

Correlation between radius and asphericity in surfaces fitted by conics

This chapter is based on the article by Pérez-Escudero et al. "Correlation between radius and asphericity in surfaces fitted by conics", submitted to the Journal of the Optical Society of america A (Perez-Escudero et al., 2009a).

The contribution of Carlos Dorronsoro, in collaboration with other coauthors, was the initial idea of the study and the preliminary simulations showing its viability, the literature search, the design of the experiments, the experimental work, the analysis of the data and the design of the simulations.

Coauthors of the study are Alfonso Pérez-Escudero and Susana Marcos.

A.1. ABSTRACT

The optical surfaces of the eye are often described in terms of their radius and asphericity. We found that the variation in measured radius and asphericity due to experimental noise is strongly correlated. We show this correlation in experimental corneal elevation data from videokeratoscopy (Atlas, Zeiss) and Scheimpflug topography (Pentacam, Oculus), in non-contact profilometry data of artificial lenses, and in simulations. The effect is a characteristic of conic curves, and not restricted to any experimental device or fitting procedure. A separate analysis of radius and asphericity may estimate incorrectly the statistical significance of the changes of the ocular surfaces. We propose a MANOVA-based statistical analysis that increases sensitivity by a factor of 4.

A.2. INTRODUCTION

As already described in Section 2.2.1, ocular surfaces are typically described by surfaces whose profiles are conic sections. The radius and asphericity of these conic sections have been widely used to characterize the geometry of the cornea and the crystalline lens. For example, they have been used for assessment of the optical biometry of different populations, differences in corneal geometry between myopes and hyperopes ((Llorente et al., 2004b) and references therein), assessment of diurnal changes in corneal topography (Kiely et al., 1982), changes of anterior and posterior corneal geometry with aging (Sicam et al., 2006), evaluation of the geometrical changes induced by corneal refractive surgery (Marcos et al., 2003, Perez-Escudero et al., 2009b) or design of custom-guided ablation algorithms aiming at controlling anterior corneal asphericity (Manns et al., 2002a). They have also been used to describe the geometry of the crystalline lens in vitro (Manns et al., 2004) and in vivo as a function of age (Jones et al., 2007), and in vivo as a function of accommodation (Jones et al., 2007, Dubbelman et al., 2005, Dubbelman and Heijde, 2001). In this thesis we have used the description in terms of radius and asphericities in Chapters 3, 5, 6, 7 and 8 to describe the shape of the postoperative corneal surfaces or the contact lens on-eye.

Contact and intraocular lenses have evolved to aspheric designs, allowing the manipulation of the spherical aberration that they induce. In contact lenses, aspheric monofocal designs may provide a better optical quality (Dietze and Cox, 2004), and also may modify the depth of focus in multifocal designs (Dorronsoro et al., 2007). In intraocular lenses, aspheric designs are used to mimic the compensatory effect of the young crystalline lens (Tabernero et al., 2006, Marcos et al., 2005a).

Ocular surface geometry can be assessed by corneal topography (Schwiegerling et al., 1995), Scheimpflug imaging (Dubbelman et al., 2002) or OCT in vivo (Radhakrishnan et al., 2001, Kaluzy et al., 2006). Shadow photography is used for crystalline lenses in vitro (Rosen et al., 2006). Profilometry is often used for plastic samples and artificial eyes (Dorronsoro et al., 2009).

Typically, both radius of curvarture and asphericity are treated independently. Many studies in the literature assess ocular biometry in different populations, changes induced by a treatment, or changes with aging of accommodation, by a separate comparison of R and Q across conditions. In this study we describe the strong correlation between the values of R and Q that are obtained from repeated measurements of the same surface. We found this correlation both in measurements of the corneal surface and of plastic lenses, regardless the instrument used to measure the elevation. We also found the correlation in numerically simulated noisy surfaces. We concluded that the correlation is a feature inherent to the fitting of noisy profiles to conics. This finding has important implications on the analysis of measurements of radius and asphericities of surfaces.

A.3. MATERIALS AND METHODS

We studied the correlation between radius and asphericity of corneal and intraocular lens surfaces fitted by conics. The analysis was performed on repeated measurements from three different instruments: Scheimpflug imaging topography, videokeratoscopy and non-contact profilometry. We also performed computer simulations to explore the origin of the correlations.

A.3.1. Scheimpflug imaging topography

We collected repeated measurements of the anterior and posterior corneal surface of three healthy eyes of three subjects with a Pentacam® (Oculus, Wetzlar, Germany) Scheimpflug-imaging topographer. This method provides quantitative elevation maps of both surfaces, sampled in a uniform square grid of side 100 μm (see Fig. A.1, left) (Perez-Escudero et al., 2009b). The instrument's software corrects the geometrical distortion of both corneal surfaces (due to the tilt of optical surfaces which is a characteristic of Scheimpflug cameras), and the optical distortion of the posterior surface, (due to its imaging through the anterior corneal surface (Dubbelman and Heijde, 2001)). We collected 33 measurements of the right eye of Subject 1 (age 26), 23 measurements of the right eye of Subject 2 (age 25), and 35 measurements of the right eye of Subject 3 (age 37). All the measurements on each eye were taken consecutively in one single session, which took 45 minutes or less.

In addition to these data, we used data from a previous study (Perez-Escudero et al., 2009b), of 27 eyes of 14 patients before and after LASIK surgery, and 18 eyes of 9 control subjects. Each subject was measured in three or four experimental sessions on different days (over the first month post-surgery in patients , and over one week for controls), and the measurements were repeated between 3 and 6 times per experimental session.

A.3.2. Corneal videokeratoscopy

We used an Atlas® 990 (Carl Zeiss Meditec AG, Jena, Germany) topographer based on Placido disks to collect repeated measurements of the anterior corneal surface of eyes. We obtained 55 repeated measurements on Subject 1 and 20 measurements on Subject 2. The subjects and eyes are the same that participated in the Scheimpflug corneal topography measurements described above. Each session took less than two hours. The videokeratoscope provides a 3D elevation map sampled in concentric circles around the corneal apex (see Fig. A.1, center).

A.3.3. Lens profilometry

In-vivo corneal measurements are subject to variability in the sample, and also to uncertainty in centration and alignment. We also used a microscopy-based non-contact optical profilometer (Plμ 2300, Sensofar, Barcelona, Spain) (Artigas et al., 2004) to obtain repeated profilometric measurements of an aspheric intraocular lens. The instrument was programmed to take 36 2-D profiles at identical exact conditions (within less than 140 minutes), using the confocal mode of the instrument, as described in Ref. (Dorronsoro et al., 2009). Each profile extends about 5.5 mm, consisting of 1658 data points equispaced in the horizontal direction. Accuracy in the vertical direction is within 0.1 μm.

A.3.4. Simulations

We generated an ideal rotationally symmetric ellipsoid of radius R = 8 mm and asphericity Q = 0.3. We used the same sampling as the one used by Pentacam (grid of 100 μm squares). We added gaussian noise along the z direction at each point, with 10-μm standard deviation. The procedure was repeated 1000 times.

A.3.5. Fits and data analysis

All elevation maps were exported from the instruments and analyzed in Matlab (The Mathworks, Natick, MA, USA). For the corneal surfaces and simulations, we fitted the central 6 mm (diameter) of the elevation maps to quadrics (Navarro et al., 2006), whose general equation is

$$\frac{x^2}{\alpha} + \frac{y^2}{\beta} + \frac{z^2}{\gamma} = 1$$ (A.1)

Rotationally symmetric quadrics have the restriction $\alpha = \beta$. When fitting corneal surfaces, we found that in all cases the best fit corresponded to an ellipsoid, i.e. α, β and γ are positive. Radii and asphericities of the two main meridians are calculated as $R_x = \alpha / \sqrt{\gamma}$, $R_y = \beta / \sqrt{\gamma}$, $Q_x = \alpha / \gamma - 1$ and $Q_y = \beta / \gamma - 1$. In all cases, we allowed free translation in space of the fitting surface, but no rotation.

The profiles of the intraocular lens were fitted by conics (See Section 2.2.1 and Eq. 2.1). In this case we allowed both free translation and rotation of the fitting curve, because we found that the profiles were tilted.
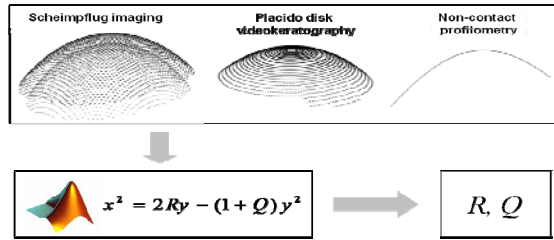
Fig. A.1. Scheme of the experimental methodology. Experimental data are obtained from real eyes with a Scheimpflug-imaging topographer (left) and a Placido-disk topographer (center), and from a intraocular lens with an optical profilometer (right). The data are exported to a computer, and fitted by ellipsoids or ellipses, described a given radius and asphericity.

A.4. RESULTS

A.4.1. Experimental measurements

Figure A.2 shows the correlation plot (radius vs. asphericity) for the data measured with Pentacam for the three subjects. Figure A.2(a) shows the data for the anterior cornea, and Fig. A.2(b) for the posterior cornea. For the six datasets, radii and asphericities are strongly and significantly correlated, except the posterior surface of Subject 2 ($p=0.07$, black dots; nonetheless, when the data were fitted to non-rotationally-symmetric ellipsoids, there was a significant correlation in the vertical meridian, $p=0.02$). Table A.1 shows the correlation coefficients (r) and p-values (p) for these measurements. These data correspond to fits to rotationally-symmetric ellipsoids, and the results hold (some of them with improved correlations) for non-rotationally symmetric ellipsoids.
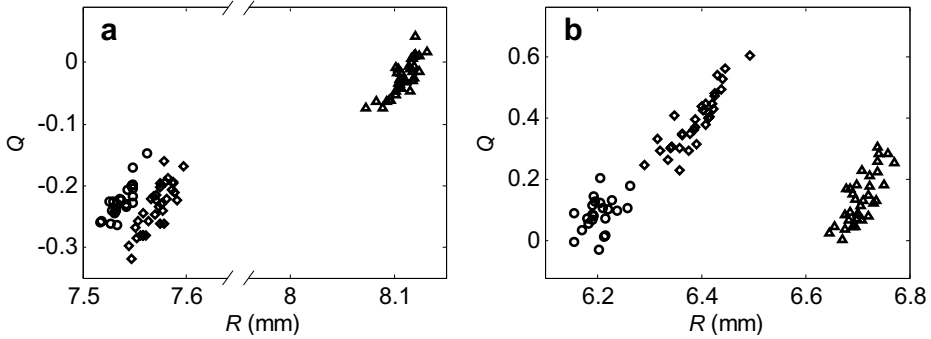
Fig. A.2. Correlation between fitted radius and asphericity for Pentacam data of corneal anterior (a) and posterior (b) surface. Diamonds: Subject 1. Circles: Subject 2. Triangles Subject 3.

In order to find the degree of correlation in a broader set of conditions, we analyzed a dataset of repeated Pentacam measurements on patients before and after LASIK, at different time points, taken by three different operators in a clinical environment, and measurements of non-operated control subjects taken in a laboratory environment,. This dataset consists of measurements from different subjects obtained on different days (3-6 measurements per day). In order to analyze the dispersion in these consecutive measurements, the average value of radius and asphericity for each subject and session was subtracted from all the measurements of the session. Figure A.3(a) shows the correlation between the dispersion in R and Q of the anterior corneal surface, for all patients pre- and post-LASIK, and for all controls. Figure A.3(b) shows the results for the posterior surface on the same eyes. The correlations are very strong ($r=0.93$ and $p<10^{-15}$ for the anterior surface, $r=0.77$ and $p<10^{-15}$ for the posterior), especially considering the heterogeneity of this set of measurements.
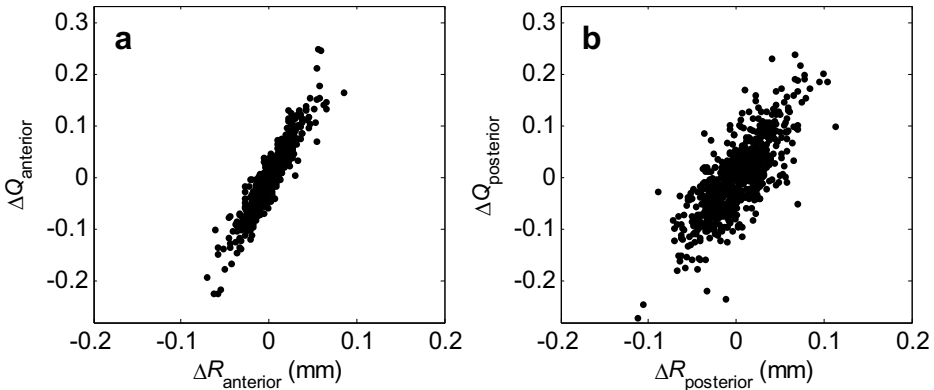
Fig. A.3. Dispersion in radius and asphericity from measurements obtained on different subjects (pre- and post-LASIK patients and controls) on different days (within one month, 3-6 consecutive measurements per session). (a) Anterior surface of the cornea. (b) Posterior surface of the cornea.

Figure A.4 shows the correlation between R and Q from fits to Placido videokeratoscopy data. (a) Subject 1. (b) Subject 2. As data are affected by the shadows and occlusions by the eyelashes and eyelids in the upper quarter of the

topography, data in the horizontal meridian are more reliable than those of the vertical meridian, and only the radii and asphericities for the horizontal meridian are depicted.
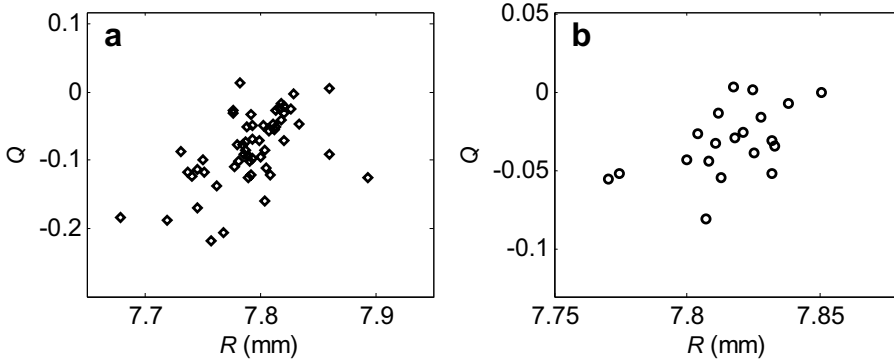
Fig. A.4. Correlation between fitted radius and asphericity, for Placido disk videokeratoscopy data of the anterior corneal surface of (a) Subject 1 and (b) Subject 2. Data are fitted to non-rotationally symmetric ellipsoids. The plotted data are for the horizontal meridian.

The correlation in the horizontal direction is stronger than the corresponding correlations for the vertical direction or for rotationally symmetric fits (not shown), but all correlations are highly significant (Table A.1). In general, the videokeratoscopy data show a lower correlation than the Scheimpflug-imaging data.

Table A.1. Correlations between fitted radii and asphericities in the experimental data: Correlation coefficient (r), p-value of the correlation (p) and number of measurements (n). "Multiple" refers to data from a group of LASIK patients and non-operated controls.

			Subject 1	Subject 2	Subject 3	Multiple	IOL
Scheimpflug imaging	Anterior surface	r	0.82	0.83	0.76	0.93	-
		p	$5 \cdot 10^{-9}$	$8 \cdot 10^{-7}$	10^{-7}	$< 10^{-15}$	-
		n	33	23	35	717	-
	Posterior surface	r	0.88	0.38	0.76	0.77	-
		p	10^{-11}	0.07	10^{-7}	$<10^{-15}$	-
		n	33	23	35	717	-
Placido disk videokera-toscopy	Symmetrical	r	0.39	0.45	-	-	-
		p	0.003	0.047	-	-	-
		n	55	20	-	-	-
	Horizontal meridian	r	0.54	0.53	-	-	-
		p	$2 \cdot 10^{-5}$	0.016	-	-	-
		n	55	20	-	-	-
	Vertical meridian	r	0.28	0.48	-	-	-
		p	0.04	0.03	-	-	-
		n	55	20	-	-	-
Profilometer		r	-	-	-	-	0.83
		p	-	-	-	-	$4 \cdot 10^{-10}$
		n	-	-	-	-	36

Figure A.5 shows the correlation between radius and asphericity of repeated measurements of the profile of an aspheric intraocular lens, obtained with the Plμ non-contact optical profilometer. The correlation is also very high, $r=0.83$, $p=4·10^{-10}$.
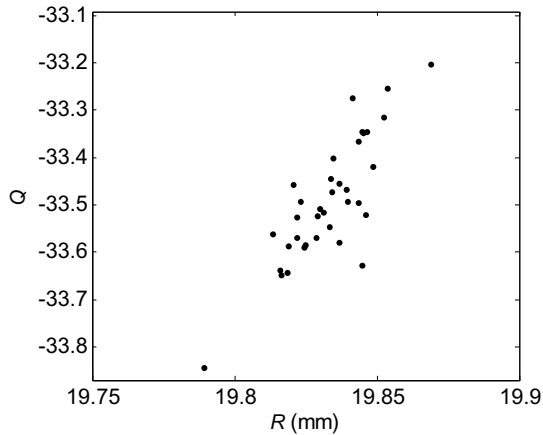
Fig. A.5. Correlation between fitted radii and asphericities for the profilometer data. Note that in this case, corresponding to a strongly aspherical intraocular lens (with a very different geometry from that of normal eyes) the slope is much higher. Therefore, this graph has been plotted with a different aspect ratio than Figs. A.2-A.4.

A.4.2. Simulations

We built a synthetic dataset corresponding to a perfect ellipsoid with $R=8$ mm and $Q=0.3$. When no noise is added to the data, the fitting algorithm provides exactly the correct ellipsoid parameters. The noise added to the synthetic ellipsoids causes dispersion in the fitted parameters, Fig. A.6, and the correlation arises ($r=0.95$, $p<10^{-15}$). Figure A.6 also shows the histograms along the R and Q directions. Interestingly, the histograms are slightly displaced, and therefore the rectangle representing the 95% confidence intervals is shifted in both axes (radius and asphericity) with respect to the nominal values.

A.5. DISCUSSION

A.5.1. The origin of the correlation

Possible causes for the correlation may be (1) noise artifacts, (2) features of the sampling of the experimental data, (3) an artifact in the fitting algorithm or (4) some intrinsic property of ellipsoids. The presence of the correlation in data from different instruments and in simulations rules out possibilities (1) and (2). We checked that the correlation is still present when the fits are performed by the instruments' built-in software (data not shown), so possibility (3) is also unlikely. Therefore, we explored the possibility that the correlation comes from an intrinsic property of ellipsoids. We found in simulations that radius and asphericities of very similar ellipsoids are correlated. We obtained this result from the following calculation: We built synthetic ellipsoids with radii ranging from 7.7 mm to 8.3 mm and asphericities ranging from -0.2 to 0.7 (no noise was added). Fig. A.7 shows the mean squared error between each of these ellipsoids and the one with $R=8$ mm and $Q=0.3$, (aligning them so that the

mean squared error was minimum, and for a region of 6 mm of diameter around the apex). The region with lowest difference is tilted in the R-Q plane.
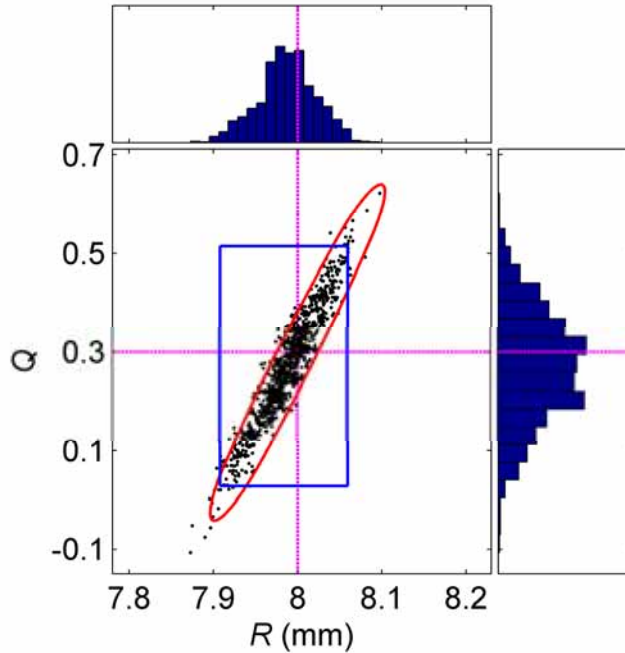
Fig. A.6. Results of the simulations for an ideal rotationally symmetric ellipsoid with R=8 mm and Q= 0.3, and added gaussian noise of 10 μm standard deviation. The central box shows the fitted parameters of 1000 fits, and the histograms show the dispersion in radius (top) and asphericity (right). The dashed lines indicate the nominal values. The elliptical contour limits the region where the mean squared error with respect to the nominal ellipsoid is lower than 0.5 μm (see Fig. A.7). The rectangular contour limits the region of 95% confidence intervals in R and Q.

Then, we compared the results of this calculation with the results of the experimental fits. We plotted one of the isocontours of Fig. A.7 on the results from the simulation, and found a perfect agreement (elliptic contour in Fig. A.6). We conclude that the experimental noise produces a dispersion of the fitted parameters, which result in ellipsoids statistically more similar to the nominal one. As these preferential parameters are located along a diagonal in the R-Q space, the fitted data are correlated. We repeated the same calculation of mean squared error using ellipses instead of ellipsoids, with similar results, indicating that the largest part of the effect is intrinsic to the geometry of ellipses, and not due to factors of the 3D geometry.
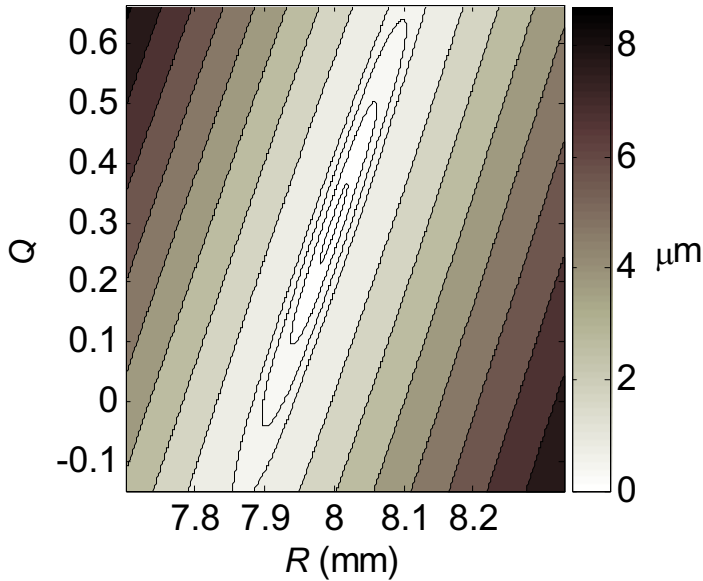
Fig. A.7. Mean squared error between an ellipsoid with R=8 mm and Q=0.3 and ellipsoids with the radii and asphericities specified in the axes. Contours have been plotted for mean squared errors at 0.2-μm steps between 0.1 and 0.7 μm and at 1-μm steps between 1 and 8 μm.

A.5.2. Consequences in the statistical analysis

In most scientific literature, the confidence intervals for radius and asphericity are calculated separately, to assess the significance of changes. The separate confidence intervals for radius and asphericity limit a region in the Q-R plane shown by the blue rectangle in Fig. A.6 (95% confidence). However, the true 95% confidence region (region inside which the 95% of the randomly generated points fall) is actually very different from the rectangle, as it is close to the elliptical contour of Fig. A.6 (the exact region is not drawn for clarity). Considering the confidence intervals estimated by considering R and Q separately (blue rectangle) instead of the true region (ellipse) can lead to false positives and false negatives. Points within the rectangle but outside the ellipse will be erroneously identified as significantly different, while points outside the ellipse but within the rectangle will be erroneously identified as not significantly different. In order to overcome this problem in practice, when only a few samples are available (and therefore the full statistics of the data and the degree of correlation cannot be quantified) one must use a multivariate statistical test, which takes into account the possible correlation between the two variables. One adequate test is the multivariate analysis of variance (MANOVA). Briefly, this method finds the direction of maximum separation between the two datasets, and performs a one-dimensional test along that direction, correcting the p-value for the extra degree of freedom introduced by the search of the direction of best discrimination.

Fig. A.8 compares the different sensitivity when using separated Student's t-tests for R and Q and when using MANOVA. We simulated an experiment to test the probability of detecting significant differences between corneal surfaces. We

simulated corneal topography measurements of pairs of corneal surfaces. One cornea had R=8 mm and Q=0.3 in all cases, while in the other R took values between 8 and 8.1 mm (Fig. A.8(a)), or Q took values between 0.3 and 0.5 (Fig. A.8(b)). To simulate realistic corneal topography measurements, Gaussian noise (with a standard deviation of 10 μm) was added to the ellipsoid. Each simulated experimental session consisted on five measurements per cornea. Each pair of series of 5 measurements each was compared, to estimate whether the two corneal surfaces were statistically different. Each experimental session was repeated 1000 times to obtain accurate probability estimates. Two statistical methods were tested: separate t-tests on R and Q (with and without the Bonferroni correction) and the MANOVA test proposed in this study. Figure A.8 shows the probability that the two corneas are identified as significantly different, according to the three statistical methods. The probability was computed for 20 increments of radius in Fig. A.8(a) and 14 increments of asphericity in Fig. A.8(b). We found that MANOVA is capable of detecting changes in R and Q about 4 times smaller than the separate tests. Both the Student's t-test and MANOVA share most assumptions about the data, including that of normally distributed data. However, MANOVA takes into account the possible correlation between the variables, which we have demonstrated to occur between R and Q of repeated measurements on the same surface.
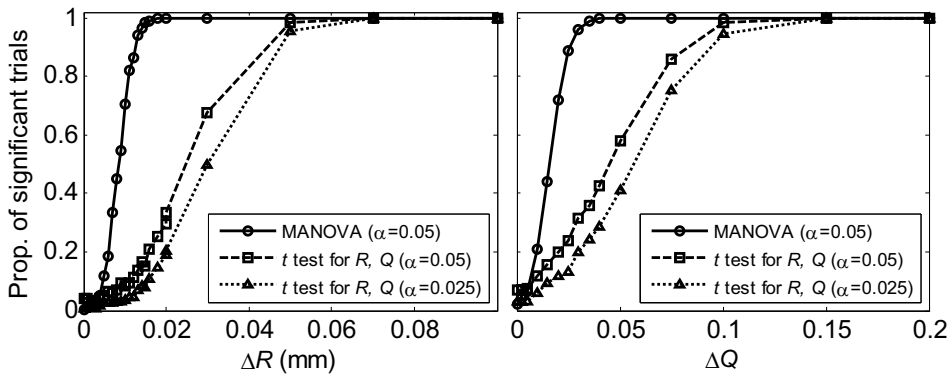
Fig. A.8. Proportion of simulated experiments where a significant difference was detected between a reference ellipsoid with R=8 mm and Q=0.3 and a test ellipsoid with (a) R=8+ΔR mm and Q=0.3 or (b) R=8 mm and Q=0.3+ΔQ. Each experiment compares 5 fits to the reference ellipsoid and 5 fits to the test one, simulating two sets of five repeated noisy mesurements (10 μm standard deviation at each point of the ellipsoid). For each amount of change of R or Q, we simulated 1000 experiments, and the proportion of detected significant differences is plotted. Circles: Proportion of trials where MANOVA identified a significant change. Squares: Proportion of trials where the Student's t test identified a significant change, either in radius or in asphericity. Triangles: Same as squares but applying the Bonferroni correction. This correction is needed because when we perform two simultaneous statistical tests on the same data, the probability of false positives increases about two times, so we must divide the significance threshold by two.

MANOVA does not use previous knowledge about the correlation between the two variables, and therefore it is the method of choice in order to check the significance of measurements, when the instrument is not characterized. However, if the correlation specific to a given instrument is well known from a careful

characterization, other statistical methods that make use of this previous knowledge can be implemented, increasing further the sensitivity of the tests.

A.5.3. Implications of the results

The presence of strong correlations between radius and asphericities describing a surface has important implications in the detection of changes in conic surfaces. Certain combination of changes in the asphericity and radius along the correlation line can be interpreted as a change in the surface that does not really exist, while changes in radius and asphericities of the same magnitude but in the perpendicular direction can describe certainly significant changes in the surface. This is particularly important in physiological optics where conic surfaces are used to describe the surfaces of the ocular component. Studies of the geometry of crystalline lens reveal correlations between radius and asphericity (Manns et al., 2004) which may be overinterpreted as a particular feature of the lens, in association with development, growth or aging. However, our results indicate that this is actually a consequence of the fit. Similarly, the impact of corneal treatments on corneal geometry and optical quality is usually assessed in terms of changes in radius of curvature and asphericity (Marcos et al., 2003, Perez-Escudero et al., 2009b). Current efforts in refractive surgery aim at not inducing changes in corneal asphericity to prevent the induction of spherical aberration. Statistical analysis of the significancy of these changes should take into account the existing correlations between radius and asphericity in the statistical analysis of possible induced changes in asphericity.

A.6. CONCLUSIONS

There is an important degree of correlation between radius and asphericitiy, observed in repeated measurements with different instruments (Scheimpflug imaging topographer, Placido disk videokeatoscope, non-contact optical profilometer). This strong correlation holds across different measurement conditions: anterior surface and posterior surface of the cornea, and intraocular lens. Simulations show that this correlation effect is produced even by subtle measurement noise or surface variability (as with the profilometer, Fig. A.5). Measurement noise and surface variability will always be present experimentally, and we therefore can conclude that when fitting surface measurements to conics or conic-based surfaces the retrieved R and Q parameters will be usually correlated. It is clear from the examples and also from the simulations, that when reporting the results of conic fittings, as those routinely used in ocular biometry, radius and asphericity cannot be treated separately: a correct description of the surface needs both parameters. We have proposed to use the statistical test MANOVA to study corneal changes. This test increases the sensitivity of the analysis, detecting changes about 4 times smaller than the separate analysis in R and Q.

Conclusions

This thesis addresses physical aspects related to two procedures applied to the cornea to change its refractive state and consequently, to change the optical properties of the eye: corneal laser refractive surgery and contact lenses for the correction of myopia and the correction of presbyopia. In particular, this thesis has focused on better understanding corneal laser ablation mechanisms (and the changes induced on the cornea) and contact lens fitting of contact lenses. We have studied the changes induced in the geometry of the optical surfaces, and also the optical outcomes in terms of optical aberrations. We have demonstrated the use of in-vitro models for the isolated study of the effects of the ablation, the measurement of the back surface of the cornea, or the fitting of contact lenses, both for validation of the measurement techniques and as tools to predict (and correct) the outcomes without the biological variability present in real eyes. Measurements on real patients have allowed us to assess the influence of biomechanical processes, and of the individual ocular properties in the optical/visual outcomes of refractive surgery (for myopia correction) and contact lenses (for myopia and presbyopia correction).

ACHIEVED GOALS AND SPECIFIC CONCLUSIONS

1 We have developed different instrument implementations, measurement procedures and processing algorithms for the accurate study of the geometry of optical surfaces. These techniques include Placido disk corneal topography, Scheimpflug imaging and profilometry. The technology has proved useful to measure both artificial and real eyes, to measure the changes induced by different procedures (refractive surgery and corneal lens fitting), and to obtain anterior and posterior surface shape differences across conditions, as well as the optical consequences of these changes.

2 We have developed a compact and versatile Laser Ray Tracing aberrometer, to measure the optical aberrations of the eye with high dynamic range and configurable parameters (for example the number of samples in the wavefront or their spatial distribution). It has proved capable of achieving the demanding requirements of the measurement of multifocal contact lenses with high aberrations. The system has been validated (against corneal wavefront measurements on artificial eyes). The system has also been applied in other studies of the Visual Optics and Biophotonics Laboratory (Llorente et al., 2004a) (Llorente et al., 2007).

3 We have reported the optical and ablation properties of two polymer materials (PMMA and Filofocon A) for their use in refractive surgery research. The absence of ablation artifacts (central islands), a lower number of incubation pulses, a lower pulse-number dependence of the ablation threshold, and a good correspondence between the effective absoption coefficient of the ablation and the absorption coefficient estimated from spectroscopic measurements make Filofocon A a more appropriate material than PMMA for experimental models in refractive surgery and for calibration of clinical lasers. The accurate description of the physical properties obtained in a laboratory laser is essential to analyze the outputs from clinical lasers and for correct estimations in corneal tissue.

4 We have developed (and later evolved) an experimental model eye for the study of the physical effects involved in refractive surgery that allowed us to measure experimentally the ablation patterns of four different clinical platforms. The outputs of three state of the art algorithms were compared with one of previous generation. We concluded that the new algorithms have been optimized to reduce the induction of spherical aberration in non-biological materials, although the induced spherical aberration is still not negligible (up to 0.7 microns). We have shown that physical effects can explain most of the increase in asphericity found clinically (70 % in a non-optimized laser). However, and particularly for high corrections, there is still some room for biomechanical effects.

5 We have developed a procedure to experimentally measure the laser efficiency effects on curved surfaces (laser efficiency losses from the center to the periphery of the ablated surface) and also to estimate the effect in cornea. We found important differences across laser platforms, depending on their fluence (6.5% for 120 mJ/cm^2 at 2.5 mm from the corneal apex and almost negligible for 400 mJ/cm^2). We obtained correction factors for these effects, to be applied in the clinical units.

6 A hybrid porcine plastic model for the calibration of anterior segment imaging systems was developed. This artificial eye shows corneal properties (scattering, refractive index) comparable to those of living eyes, but without biological variability. The model was used to validate a Pentacam Sheimpflug imaging system, nominally corrected of geometrical and optical distortion. We proved that this instrument can reliably measure potential changes in the posterior corneal surface after refractive surgery.

7 We found that myopic LASIK refractive surgery (from -1.25 to -8.5 D) did not induce systematic long-term changes in the posterior corneal surface shape. Differences were only significant one-day after surgery, and the changes were more relevant in the vertical than in the horizontal meridian. The amount of individual changes in the posterior cornea (radius of curvature) in post-LASIK patients is similar to that found in normal eyes. Left and right eyes show similar changes, suggesting physiological mechanisms acting bilaterally in the same way.

8 We developed another in-vitro model based on artificial plastic eyes, aimed at studying the fitting of soft contact lenses. The model allowed eliminating the biological variability associated with real eyes (movements and decentrations of the lens, ocular aberrations) while simulating a more realistic situation than a standard inmersion measurement. Using this in vitro model we found that soft monofocal spherical lenses reduce total spherical aberration. Multifocal lenses are affected by conformity to the cornea and fitting effects that cancel out the multifocal properties of the design, although the final optical performance depends on the lens power that determines the central thickness.

9 We used aberration measurements on real eyes fitted with semirigid (RGP) contact lenses and found this tool useful to understand the fitting process and the optical coupling between the optics of the lens and the optics of the eye. We demonstrated that RGP contact lenses can significantly improve the natural optics of the eye. The internal optics and the lens flexure can impose limits on this compensation. We found a marked correlation between the corneal and ocular aberrations of the same eye measured with and without semirigid (RGP) contact lenses. We were able to measure the aberrations of the tear lens in RGP contact lenses, and reported a compensatory effect on the total spherical aberration. This methodology provides an accurate analysis of CL fitting in individual eyes, and can help to choose the best lens parameters to improve the optics of individual eyes.

10

In eyes fitted with soft contact lenses we found that ocular aberrations play a major role in the optical and visual outcomes. The correlations between the aberrations of the naked eye and those of the same eyes with soft lenses are higher than in the case of RGP lenses indicating a higher degree of conformity to the cornea. Negative spherical aberration was induced in most cases, both with monofocal and multifocal contact lenses. However, the natural aberrations of the eye have a larger impact on the final optical performance, and in fact we have found that conformity to the cornea makes the negative multifocal lenses that we tested behave essentially as monofocal lenses. We found some positive contact lenses (with the same designs) expand the depth of focus, confirming previous results of the in-vitro model. The larger thickness (less conformity) of the positive lens can explain why these lenses may preserve their multifocal design more than negative lenses of similar central addition. Understanding the coupling of the ocular optics to the contact lens is essential to improve current designs.

11

Through focus experiments of visual acuity confirm the lack of induced multifocality of most of the multifocal designs tested in this study. In general, the trends of through-focus optical (Strehl) and visual acuity measurements are in good agreement. Retinal simulations based on physical (objective) measurements can explain subtle variations in the through-focus visual performance. The lack of multifocality of most designs, as well as the expanded depth-of-focus found in some subjects and conditions can be explained on optical basis, without invoking neural effects or lack of visual adaptation of individual subjects to certain multifocal contact lenses.

12

Ocular and ophthalmic surfaces are often described by conics. The radius and asphericities of conic fits are correlated. We found this correlation in experimental corneal elevation data from videokeratoscopy (Atlas, Zeiss) and Scheimpflug topography (Pentacam, Oculus), in non-contact profilometry data of artificial lenses, and in simulations. The effect is a characteristic of conic curves fitted to experimental data, and not restricted to any measurement device or fitting procedure. When reporting the results of conic fittings, as those routinely used in ocular biometry, radius and asphericity cannot be treated separately: a correct description of the surface needs both parameters. We propose to use the statistical test MANOVA to study corneal changes. This test increases the sensitivity of the analysis, detecting changes about 4 times smaller than the separate analysis in R and Q.

LIST OF METHODOLOGICAL OUTPUTS

1. Physical model eyes for refractive laser ablation evaluation.
2. Physical model for the study of biomechanical processes, through the validation of instruments measuring the anterior and posterior cornea.
3. Physical model eye for contact lens fitting.
4. Laser Ray Tracing instrument (optomechanics, electronics, control and data processing software) for optical aberration measurements.
5. Measurement procedures and new analysis software for surface characterization based on corneal topography, Scheimpflug imaging and contact and non-contact profilometry.
6. Advanced software tools for comparing surfaces and detecting changes.
7. Analysis tools for contact lens and ablation pattern measurements (in real and model eyes).
8. Ablation properties of model eye materials (PMMA and filofocon A)
9. Empirical correction factor for correction of corneal ablation algorithms.
10. Visual psychophysics paradigms for visual performance evaluation.
11. Protocols for customization of contact lens prescription.
12. Proposal for a statistical method (MANOVA) to improve sensitivity of detection of changes in surfaces, or differences between surfaces.

IMPLICATIONS OF THIS RESEARCH

1. The results reported in this thesis are of direct application in laser refractive surgery. The induction of spherical aberration is still a problem in today's LASIK surgery. We have demonstrated that most of the increase in asphericty can be explained by purely physical factors, and that biomechanical effects have a secondary impact on the shape of the cornea in normal situations. We have obtained experimentally laser efficiency correction factors, which along with the use of physical models and the measurement protocols and optical and ablations parameters obtained in this thesis, can be directly applied in the evaluation of current algorithms and design of the next generation of ablation profiles.

2. The results reported in this thesis demonstrate the great value of aberrometry (corneal and ocular) in the contactology practice. Similar protocols based on those followed in this thesis can be established to help identifying the most suitable lens to each individual patient.

3. The results reported in this thesis on multifocal contact lenses have important implications for the design of multifocal corrections in general, not only in the context of contact lenses, but also in refractive surgery or intraocular lenses. Providing the eye with an efficient multifocal range is a complex problem. We have provided evidence that the aberrations of individual eyes determine (and very often compromise) the final depth of focus of a multifocal correction. Optical factors must be considered prior to effects related to neural adaptation in the design of multifocal lenses.

4. Surface metrology and ocular biometry techniques can benefit directly from the developments of this thesis on physical models. These artificial eyes can become useful tools for validation and calibration of laboratory and commercial systems as profilometers, corneal topographers, or Scheimpflug or OCT imaging techniques. In addition, they can be implemented in systems for the in vitro assessment of contact lens and calibration of laser ablation systems.

FUTURE RESEARCH LINES

The results can establish the basis for future research line directions:

1. In this thesis we have provided the optical and ablation properties of plastic materials for refractive surgery models and extrapolated the results to the cornea. This work opens the path for studies of optical and ablation properties of corneal tissue, including accurate measurement of the physics of the ablation in non-normal surfaces and ejection dynamics. These will provide a better control on the clinical ablative procedures, a needed step in the search for reliable wavefront optimized corrections.

2. Testing of current wavefront guided clinical procedures in vivo and in vitro with the methology developed will lead to improved laser ablation algorithms, and to the design of new wavefront guided strategies.

3. The knowledge gathered on ablation of polymer curved surfaces opens the possibility for the fabrication of contact lenses of complicated designs (i.e. free-form, multifocal) by means of laser ablation.

4. The use of the hybrid porcine plastic corneal models, and of newly validated and calibrated instruments (providing information on both the anterior and posterior corneal surface) opens the possibility for quantitative studies of processes where biomechanical effects are expected to play a role: post-refractive ectasia, assessment of keratoconus, corneal deformations after long term contact lens wearing (corneal warpage) or during Ortho-K treatments with inverse geometry contact lenses, or collagen cross-linking, among others.

5. Application of high resolution anterior segment optical coherence tomography in the study of contact lens fitting will be essential to evaluate the discrepancies between the nominal design and the one measured on eye found in multifocal contact lenses, and the influence of the tear film on the anterior and posterior surface of the contact lens. The instrument should be corrected from fan and optical distortion, and validated for quantitative imaging.

6. The parallel measurements of optical quality and visual performance on the same subjects (in a wide range of conditions and for different subjects) reported in this thesis to evaluate through focus performance, and the associated methodology provide the basis to develop more sophisticated methods of prediction of the visual outcomes, and contribute to the understanding of the limits to spatial vision. These studies will be undertaken with the aid of adaptive-optics, which allow the manipulation of the optical aberrations (correction and simulation of multiple corrections, in particular multifocal designs).

5. Multifocality entails a reduction of optical quality. Provided that effective multifocality is achieved with new designs (in terms of optical quality through focus or visual depth of focus), there is still a need for screening methods to detect those patients that cannot adapt to simultaneous vision. New optical methods are needed to provide patients with simulations of the visual experience of simultaneous vision.

LIST OF PUBLICATIONS AND PATENTS

List of Publications and Patents by the author of this thesis in the field of visual optics:

BARBERO, S., DORRONSORO, C. & MARCOS, S. (2007) Analytical design of intraocular lenses. IN OEPM (Ed.), PCT Patent Application PCT/ES2008/070086.

DORRONSORO, C., BARBERO, S., LLORENTE, L. & MARCOS, S. (2003) On-eye measurement of optical performance of Rigid Gas Permeable contact lenses based on ocular and corneal aberrometry. *Optometry and Vision Science.,* 80**,** 115-125.

DORRONSORO, C., CANO, D., MERAYO, J. & MARCOS, S. (2006) Experiments on PMMA models to predict the impact of corneal refractive surgery on corneal shape. *Optics Express,* 14**,** 6142-6156.

DORRONSORO, C. & MARCOS, S. (2007) Experiments on PMMA models to predict the impact of corneal refractive surgery on corneal shape: reply. *Optics Express,* 15**,** 7245-7246.

DORRONSORO, C. & MARCOS, S. (2009) Instrument for the simulation of multifocal opthtalmic corrections. Spain, OEPM Patent Application P200930055.

DORRONSORO, C., REMON, L., MERAYO-LLOVES, J. & MARCOS, S. (2009) Experimental evaluation of optimized ablation patterns for laser refractive surgery. *Optics Express,* 17**,** 15292-15307.

DORRONSORO, C., SIEGEL, J., REMON, L. & MARCOS, S. (2008) Suitability of Filofocon A and PMMA for experimental models in excimer laser ablation refractive surgery. *Optics Express,* 16**,** 20955-20967.

GAMBRA, E., SAWIDES, L., DORRONSORO, C. & MARCOS, S. (2009) Accommodative lag and fluctuations when optical aberrations are manipulated. *Journal of Vision,* 9**,** 1-15.

LLORENTE, L., BARBERO, S., CANO, D., DORRONSORO, C. & MARCOS, S. (2004) Myopic versus hyperopic eyes: axial length, corneal shape and optical aberrations. *Journal of Vision,* 4**,** 288.

LLORENTE, L., MARCOS, S., DORRONSORO, C. & BURNS, S. (2007) The effect of sampling on real ocular aberration measurements. *Journal of the Optical Society of America A.,* 24**,** 2783-2796

MARCOS, S., DORRONSORO, C. & CANO, D. (2005) Spherical aberration prevention method in e.g. laser refractive surgery system. Patent WO 2005/122873 A1.

MARCOS, S., SAWIDES, L., GAMBRA, E. & DORRONSORO, C. (2008) Influence of adaptive-optics ocular aberration correction on visual acuity at different luminances and contrast polarities. *Journal of Vision,* 8**,** 12.

MARIN, G., HERNANDEZ, M., DE GRACIA, P., MARCOS, S. & DORRONSORO, C. (2008) A method for providing a spectacle opthalmic lens by calculating or selecting a design. EPO Patent Application EP08306010.3.

NAVARRO, R., MORENO, E. & DORRONSORO, C. (1998) Monochromatic aberrations and point-spread functions of the human eye across the visual field. *Journal of the Optical Society of America A,* 15**,** 2522-2529.

PEREZ-ESCUDERO, A., DORRONSORO, C., SAWIDES, L., REMON, L., MERAYO-LLOVES, J. & MARCOS, S. (2009) Minor Influence of Myopic Laser In Situ Keratomileusis on the Posterior Corneal Surface. *Investigative Ophthalmology & Visual Science,* 50**,** 4146-4154.

SAWIDES, L., GAMBRA, E., PASCUAL, D., DORRONSORO, C. & MARCOS, S. (2009) Visual performance with real-life tasks under Adaptive-Optics ocular aberration correction. *Journal of Vision, Submitted.*

References

AIZAWA, D., SHIMIZU, K., KOMATSU, M., ITO, M., SUZUKI, M., OHNO, K. & UOZATO, H. (2003) Clinical outcomes of wavefront-guided laser in situ keratomileusis: 6-month follow-up. *Journal of Cataract and Refractive Surgery,* 29**,** 1507-1513.

ALIO, J. L. & MONTES-MICO, R. (2006) Wavefront-guided versus standard LASIK enhancement for residual refractive errors. *Ophthalmology,* 113**,** 191-197.

ANERA, R. G., JIMENEZ, J. R., JIMENEZ DEL BARCO, L. & HITA, E. (2003) Changes in corneal asphericity after laser refractive surgery, including reflection losses and nonnormal incidence upon the anterior cornea. *Optics Letters,* 28**,** 417-419.

ANSI (1993) ANSI Z136.1 American National Standard for the safe use of lasers. American National Standard Institute.

ANSI (2007) ANSI Z80.11 Laser Systems for Corneal Reshaping. American National Standard Institute.

APPLEGATE, R. A., DONNELLY, W. J., MARSACK, J. D., KOENIG, D. E. & PESUDOVS, K. (2007) Three-dimensional relationship between high-order root-mean-square wavefront error, pupil diameter, and aging. *Journal of the Optical Society of America a-Optics Image Science and Vision,* 24**,** 578-587.

APPLEGATE, R. A., HILMANTE, L. G., HOWLAND, H. C., TU, E. Y., STARCK, T. & ZAYAC, E. J. (2000) Corneal first surface optical aberrations and visual performance. *Journal of Refractive Surgery,* 16**,** 507-514.

APPLEGATE, R. A., HILMANTEL, G. & HOWLAND, H. C. (1996) Corneal aberrations increase with the magnitude of radial keratotomy refractive correction. *Optometry and Vision Science,* 73**,** 585-9.

ARTAL, P., BERRIO, E., GUIRAO, A. & PIERS, P. (2002) Contribution of the cornea and internal surfaces to the change of ocular aberrations with age. *J. Opt. Soc. Am. A,* 19**,** 137-143.

ARTAL, P. & GUIRAO, A. (1998) Contributions of the cornea and the lens to the aberrations of the human eye. *Optics Letters,* 23**,** 1713-1715.

ARTAL, P., GUIRAO, A., BERRIO, E. & WILLIAMS, D. R. (2001) Compensation of corneal aberrations by the internal optics in the human eye. *Journal of Vision.,* 1**,** 1-8. http://journalofvision.org/1/1/1, DOI 10.1167/1.1.1.

ARTAL, P., MARCOS, S., NAVARRO, R., MIRANDA, I. & FERRO, M. (1995) Through-focus image quality of eyes implanted with monofocal and multifocal intraocular lenses. *Optical Engineering,* 34**,** 772-779.

ARTIGAS, R., LAGUARTA, F. & CADEVALL, C. (2004) Dual-technology optical sensor head for 3D surface shape measurements on the micro- and nanoscales. IN WOLFGANG, O. & MITSUO, T. (Eds.) Strasbourg, France, SPIE.

ATCHISON, D. (1995) Aberrations associated with rigid contact lenses. *J Opt Soc Am A,* 12**,** 2267-73.

ATCHISON, D. A., CHARMAN, W. N. & WOODS, R. L. (1997) Subjective depth-of-focus of the human eye. *Optometry and Vision Science,* 74**,** 511-520.

ATCHISON, D. A., MARKWELL, E. L., KASTHURIRANGAN, S., POPE, J. M., SMITH, G. & SWANN, P. G. (2008) Age-related changes in optical and biometric characteristics of emmetropic eyes. *Journal of Vision,* 8.

ATCHISON, D. A. & SMITH, G. (2000) *Optics of the Human Eye,* Oxford, Butterworth-Heinemann.

AWWAD, S. T., SANCHEZ, P., SANCHEZ, A., MCCULLEY, J. P. & CAVANAGH, H. D. (2008) A preliminary in vivo assessment of higher-order aberrations induced by a silicone hydrogel monofocal contact lens. *Eye & Contact Lens-Science and Clinical Practice,* 34**,** 2-5.

BAEK, T., LEE, K., KAGAYA, F., TOMIDOKORO, A., AMANO, S. & OSHIKA, T. (2001) Factors affecting the forward shift of posterior corneal surface after laser in situ keratomileusis. *Ophthalmology,* 108**,** 317-320.

BARBERO, S. (2004) Optical quality of the cornea and the cristalline lens: Implementation of objective techniques and clinical applications. PhD thesis, University of Valladolid.

BARBERO, S. (2006) Refractive power of a multilayer rotationally symmetric model of the human cornea and tear film. *Journal of the Optical Society of America a-Optics Image Science and Vision,* 23**,** 1578-1585.

BARBERO S & MARCOS, S. (2008) Analysis of the optical field at the human retina from wavefront aberration data. *Journal of the Optical Society of America A*.

BARBERO, S., MARCOS, S. & LLORENTE, L. (2002a) Optical changes in corneal and internal optics with cararact surgery. *2002 Annual Meeting Abstract and Program Planner accessed at www.arvo.org. Association for Research in Vision and Ophthalmology. Abstract 388,* 73.

BARBERO, S., MARCOS, S., MERAYO-LLOVES, J. & MORENO-BARRIUSO, E. (2002b) Validation of the estimation of corneal aberrations from videokeratography in keratoconus. *Journal of Refractive Surgery,* 18**,** 263-270.

BARBERO, S., MARCOS, S. & MERAYO-LLOVES, J. M. (2002c) Total and corneal aberrations in an unilateral aphakic subject. *Journal of Cataract and Refractive Surgery.,* 28**,** 1594-1600.

BARRAQUER, J. I. (1967) Keratomileusis. *Int Surg,* 48**,** 103-17.

BERNS, M. W., CHAO, L., GIEBEL, A. W., LIAW, L. H., ANDREWS, J. & VERSTEEG, B. (1999) Human corneal ablation threshold using the 193-nm ArF excimer laser. *Investigative Ophthalmology & Visual Science,* 40**,** 826-830.

BORN, M. & WOLF, E. (1993) *Principles of Optics,* Oxford, U.K., Pergamon Press.

BRAINARD, D. H. (1997) The Psychophysics Toolbox. *Spatial Vision,* 10**,** 433-436.

BRAREN, B. & SEEGER, D. (1986) LOW-TEMPERATURE UV LASER ETCHING OF PMMA - ON THE MECHANISM OF ABLATIVE

PHOTODECOMPOSITION (APD). *Journal of Polymer Science Part C-Polymer Letters,* 24**,** 371-376.

BUEHREN, T., COLLINS, M. J. & CARNEY, L. (2003) Corneal aberrations and reading. *Optometry and Vision Science,* 80**,** 159-166.

BURNS, S. A., MARCOS, S., ELSNSER, A. E. & BARÁ, S. (2002) Contrast improvement for confocal retinal imaging using phase correcting plates. *Optics Letters,* 27**,** 400-402.

CALVER, R., COX, M. & ELLIOTT, D. (1999) Effect of aging on the monochromatic aberrations of the human eye. *J Opt Soc Am A,* 16**,** 2069-2078.

CAMPBELL, C. (1997) Reconstruction of the corneal shape with the MasterVue corneal topography system. *Optometry and Vision Science,* 74**,** 899-905.

CAMPBELL, C. (2005) A test eye for wavefront eye refractors. *Journal of Refractive Surgery,* 21**,** 127-140.

CAMPBELL, C. (2007) Personal communication.

CANO, D., BARBERO, B. & MARCOS, S. (2004) Comparison of real and computer-simulated outcomes of LASIK refractive surgery. *Journal of the Optical Society of America A,* 21**,** 926-936.

CANO, D., BARBERO, S. & MARCOS, S. (2003) Computer simulations of corneal shape and corneal aberrations after laser correction: do they match real outcomes? *ARVO E-abstract 2090.*

CASTEJON-MOCHON, F. J., LOPEZ-GIL, N., BENITO, A. & ARTAL, P. (2002) Ocular wave-front aberration statistics in a normal young population. *Vision Research,* 42**,** 1611-1617.

CASTER, A. I., HOFF, J. L. & RUIZ, R. (2004) Conventional vs wavefront-guided LASIK using the LADARVision4000 excimer laser. *Annual Meeting of the American-Society-of-Cataract-and-Refractive-Surgery.* San Diego, CA, Slack Inc.

CIOLINO, J. B. & BELIN, M. W. (2006) Changes in the posterior cornea after laser in situ keratomileusis and photorefractive keratectomy. *J Cataract Refract Surg,* 32**,** 1426-1431.

COLLINS, M., FRANKLIN, R., CARNEY, L., BERGIEL, C., LAGOS, P. & CHEBIB, D. (2001) Flexure of Thin Rigid Contact Lenses. *Contact Lens and Anterior Eye,* 24**,** 59-64.

COLLINS, M. J., WILDSOET, C. F. & ATCHISON, D. A. (1995) Monochromatic Aberrations and Myopia. *Vision Research,* 35**,** 1157-1163.

CORZINE, J. & KLEIN, S. (1997) Factors determining rigid contact lens flexure. *Optom Vis Sci,* 74**,** 639-45.

COSTELA, A., FIGUERA, J. M., FLORIDO, F., GARCIAMORENO, I., COLLAR, E. P. & SASTRE, R. (1995) Ablation of Poly(Methyl Methacrylate) and Poly(2-Hydroxyethyl Methacrylate) by 308-nm, 222-nm and 193-nm excimer-laser radiation. *Applied Physics a-Materials Science & Processing,* 60**,** 261-270.

CUBALCHINI, R. (1979) Modal wave-front estimation from phase derivate measurements. *Journal of the Optical Society of America A,* 69**,** 972-977.

CHARMAN, W. N. (1991) Wavefront Aberrations of the Eye: A Review. *Optometry and Vision Science,* 68**,** 574-583.

CHARMAN, W. N. (2005) Wavefront technology: past, present and future. *Cont Lens Anterior Eye,* 28**,** 75-92.

CHARMAN, W. N. (2008) The eye in focus: accommodation and presbyopia. *Clinical and Experimental Optometry,* 91**,** 207-225.

CHARMAN, W. N. & JENNINGS, J. A. M. (1976) Objective measurements of the longitudinal chromatic aberration of the human eye. *Vision Research,* 16**,** 999-1005.

CHAYET, A. S., ASSIL, K. K., MONTES, M., ESPINOSA-LAGANA, M., CASTELLANOS, A. & TSIOULIAS, G. (1996) Regression and its mechanisms after laser in situ keratomileusis in moderate and high myopia. *Opthalmology,* 105**,** 1194-1199.

CHENG, X., BRADLEY, A. & THIBOS, L. N. (2004) Predicting subjective judgment of best focus with objective image quality metrics. *Journal of Vision,* 4**,** 310-321.

CHERNYAK, D. A. & CAMPBELL, C. E. (2003) System for the design, manufacture, and testing of custom lenses with known amounts of high-order aberrations. *Journal of the Optical Society of America a-Optics Image Science and Vision,* 20**,** 2016-2021.

DAVID, R., ZANGWILL, L., BRISCOE, D., DAGAN, M., YAGEV, R. & YASSUR, Y. (1992) Diurnal intraocular pressure variations: an analysis of 690 diurnal curves. *British Journal of Ophthalmology,* 76**,** 280-283.

DE BRABANDER, J., CHATEAU, N., MARIN, G., LOPEZ-GIL, N., VAN DER WORP, E. & BENITO, A. (2003) Simulated optical performance of custom wavefront soft contact lenses for keratoconus. *Optometry and Vision Science,* 80**,** 637-643.

DE CASTRO, A., ROSALES, P. & MARCOS, S. (2007) Tilt and decentration of intraocular lenses in vivo from Purkinje and Scheimpflug imaging - Validation study. *Journal of Cataract and Refractive Surgery,* 33**,** 418-429.

DEFAZIO, A. & LOWTHER, G. (1979) Inspection of back surface aspheric contact lenses. *Am J Optom Physiol Opt,* 56**,** 471-479.

DIERICK, H. & MISSOTTEN, L. (1996) Corneal ablation profiles for correction of hyperopia with the excimer laser. *J Refract Surg.,* 12**,** 767-73.

DIETZE, H. H. & COX, M. J. (2004) Correcting ocular spherical aberration with soft contact lenses. *Journal of the Optical Society of America a-Optics Image Science and Vision,* 21**,** 473-485.

DONDERS, F. C. (1864) *On the anomalies of accommodation and refraction of the eye: With a preliminary essay on physiological dioptrics,* London, New Sydenham Society.

DONNENFELD, E. D. (2001) Discussion by Eric D. Donnenfeld, MD. *Ophthalmology,* 108**,** 673-673.

DORRONSORO, C., ALONSO-FERNÁNDEZ, B. & MARCOS, S. (2008a) Ablation-Induced Changes in Corneal Shape and Aberrations in a Plastic Cornea Refractive Surgery Model *IOVS 2009: ARVO E-Abstract: 2445.*

DORRONSORO, C., ANERA, R. G., GONZALEZ, M. J., LLORENTE, L. & MARCOS, S. (2004) Development of an experimental model on artificial corneas for the study of adaptation and optical quality of contact lenses. *II EOS Topical Meeting on Physiological Optics* Granada, Spain.

DORRONSORO, C., BARBERO, S., LLORENTE, L. & MARCOS, S. (2003a) On-eye measurement of optical performance of Rigid Gas Permeable contact lenses based on ocular and corneal aberrometry. *Optometry and Vision Science.,* 80**,** 115-125.

DORRONSORO, C., CANO, D., BARBERO, S., MERAYO, J., LLORENTE, L. & MARCOS, S. (2003b) Understanding the standard algorithm for corneal refractive surgery using laser ablation of PMMA surfaces. *ARVO E-abstract 2535*.

DORRONSORO, C., CANO, D., MERAYO, J. & MARCOS, S. (2006a) Experiments on PMMA models to predict the impact of corneal refractive surgery on corneal shape. *Optics Express,* 14**,** 6142-6156.

DORRONSORO, C., GARCÍA DE LA CERA, E., LLORENTE, L., BARBERO, S. & MARCOS, S. (2003c) Implementación de dos aberrómetros para aplicaciones biomédicas. *VII Reunión Nacional de Óptica.* Santander.

DORRONSORO, C., GONZALEZ, M. J., LLORENTE, L. & MARCOS, S. (2006b) Medida de la profundidad de foco con lentes de contacto. *VIII Reunión Nacional de Óptica.* Alicante, Spain.

DORRONSORO, C., GONZÁLEZ, M. J., LLORENTE, L. & MARCOS, S. (2007) Optical and Visual quality with multifocal contact lenses. *Investigative Opthalmology and Visual Science, (Suppl.).47 Fort Lauderdale, Florida, USA*.

DORRONSORO, C. & MARCOS, S. (2007) Experiments on PMMA models to predict the impact of corneal refractive surgery on corneal shape: reply. *Optics Express,* 15**,** 7245-7246.

DORRONSORO, C., MERAYO-LLOVES, J. & MARCOS, S. (2006c) An Experimental Correction Factor of Radial Laser Efficiency Losses in Corneal Refractive Surgery. *IOVS 2009: ARVO E-Abstract: 3611.*

DORRONSORO, C., REMON, L., MERAYO-LLOVES, J. & MARCOS, S. (2009) Experimental evaluation of optimized ablation patterns for laser refractive surgery. *Optics Express,* 17**,** 15292-15307.

DORRONSORO, C., SIEGEL, J., REMON, L. & MARCOS, S. (2008b) Suitability of Filofocon A and PMMA for experimental models in excimer laser ablation refractive surgery. *Optics Express,* 16**,** 20955-20967.

DRUM, B. (2003) Evaluating the Safety and Effectiveness of "Aberration-Free" Ophthalmic Refractive Surgery. *9th Annual FDA Science Forum.* Washington, DC.

DRUM, B. (2005) Radial efficiency function in refractive surgery: Ablation losses caused by corneal curvature. *11th annual FDA Science Forum.* Washington, DC.

DRUM, B. (2007) The Evolution of the Optical Zone in Corneal Refractive Surgery. *Wavefront Congress.* Santa Fe, New Mexico.

DUBBELMAN, M. & HEIJDE, V. (2001) The shape of the aging human lens: curvature, equivalent refractive index and the lens paradox. *Vision research,* 41**,** 1867-1877.

DUBBELMAN, M., SICAM, V. A. D. P. & VAN DER HEIJDE, R. G. L. (2007) The contribution of the posterior surface to the coma aberration of the human cornea, http://journalofvision.org/7/7/10/, doi:10.1167/7.7.10. *Journal of Vision,* 7**,** 1-8.

DUBBELMAN, M., SICARN, V. & VAN DER HEIJDE, G. L. (2006) The shape of the anterior and posterior surface of the aging human cornea. *Vision Research,* 46**,** 993-1001.

DUBBELMAN, M., VAN DER HEIJDE, G. L. & WEEBER, H. A. (2005) Change in shape of the aging human crystalline lens with accommodation. *Vision Research,* 45**,** 117-132.

DUBBELMAN, M., WEEBER, H., VAN DER HEIJDE, R. & VOLKER-DIEBEN, H. (2002) Radius and asphericity of the posterior corneal surface determined by corrected Scheimpflug photography. *Acta Ophthalmol Scand,* 80**,** 379-383.

DUPPS, W. J. & WILSON, S. E. (2006) Biomechanics and wound healing in the cornea. *Experimental Eye Research,* 83**,** 709-720.

EFRON, S., EFRON, N. & MORGAN, P. B. (2008) Optical and visual performance of aspheric soft contact lenses. *Optometry and Vision Science,* 85**,** 201-210.

EL HAGE, S. G. & BERNY, F. (1973) Contribution of the crystalline lens to the spherical aberratin of the eye. *Journal of the Optical Society of America A,* 63**,** 205-211.

ELLIN, A. (2008) Lasik Surgery: When the Fine Print Applies to You. *The New York Times.* New York.

FDA (2008) OPTHALMIC DEVICES PANEL 110TH MEETING. Food and Drug Administration.

FELTHAM, M. H. & STAPLETON, F. (2002) The effect of water content on the 193 nm excimer laser ablation. *Clinical and Experimental Ophthalmology,* 30**,** 99-103.

FERNANDEZ, E. J., IGLESIAS, I. & ARTAL , P. (2001) Closed-loop adaptive optics in the human eye. *Optics Letters,* 26**,** 746-748.

FINDL, O. & LEYDOLT, C. (2007) Meta-analysis of accommodating intraocular lenses. *Journal of Cataract and Refractive Surgery,* 33**,** 522-527.

FISHER, B. T. & HAHN, D. W. (2004) Determination of Excimer laser ablation rates of corneal tissue using wax impressions of ablation craters and white-light interferometry. *Ophthalmic Surgery Lasers & Imaging,* 35**,** 41-51.

FISHER, B. T. & HAHN, D. W. (2007) Development and numerical solution of a mechanistic model for corneal tissue ablation with the 193 nm argon fluoride excimer laser. *Journal of the Optical Society of America a-Optics Image Science and Vision,* 24**,** 265-277.

FYODOROV, S. N. & DURNEV, V. V. (1979) OPERATION OF DOSAGED DISSECTION OF CORNEAL CIRCULAR LIGAMENT IN CASES OF MYOPIA OF MILD DEGREE. *Annals of Ophthalmology,* 11**,** 1885-1889.

GAMBRA, E., SAWIDES, L., DORRONSORO, C. & MARCOS, S. (2009) Accommodative lag and fluctuations when optical aberrations are manipulated. *Journal of Vision,* 9**,** 1-15.

GARCÍA DE LA CERA, E. (2008) Optical Quality and Role of the Ocular Aberrations in animal models of myopia. PhD Thesis, Universidad de Valladolid.

GATINEL, D., HOANG-XUAN, T. & AZAR, D. (2001) Determination of corneal asphericity after myopia surgery with the excimer laser: a mathematical model. *Invest Ophthalmol Vis Sci,* 42**,** 1736-1742.

GEMOULES, G. & MORRIS, K. M. (2007) Rigid gas-permeable contact lenses and severe higher-order aberrations in postsurgical corneas. *Eye Contact Lens,* 33**,** 304-7.

GISPETS, J., ARJONA, M. & PUJOL, J. (2002) Image quality in wearers of a centre distance concentric design bifocal contact lens. *Ophthalmic and Physiological Optics,* 22**,** 221-233.

GLASSER, A. & CAMPBELL, M. (1998) Presbyopia and the optical changes in the human crystalline lens with age. *Vision Research,* 38**,** 209-229.

GLASSER, A. & CAMPBELL, M. (1999) Biometric, optical and physical changes in the isolated human crystalline lens with age in relation to presbyopia. *Vision Research,* 39**,** 1991-2015.

GOODS, S. H., WATSON, R. M. & YI, M. (2003) Thermal Expansion and Hydration Behavior of PMMA Molding Materials for LIGA Applications. Albuquerque, New Mexico, Sandia National Laboratories.

GRIFFITHS, M., ZAHNER, K., COLLINS, M. & CARNEY, L. (1998) Masking of irregular corneal topography with contact lenses. *CLAO J,* 24**,** 76-81.

GRULKOWSKI, I., GORA, M., SZKULMOWSKI, M., GORCZYNSKA, I., SZLAG, D., MARCOS, S., KOWALCZYK, A. & WOJTKOWSKI, M. (2009) Anterior segment imaging with Spectral OCT system using a high-speed CMOS camera. *Optics Express,* 17**,** 4842-4858.

GRZYBOWSKI, D. M., ROBERTS, C. J., MAHMOUD, A. M. & CHANG, J. S. (2005) Model for nonectatic increase in posterior corneal elevation after ablative procedures. *J Cataract Refract Surg,* 31**,** 72-81.

GUIRAO, A. & ARTAL, P. (2000) Corneal wave aberration from videokeratography: accuracy and limitations of the procedure. *Journal of the Optical Society of America a-Optics Image Science and Vision,* 17**,** 955-965.

GUIRAO, A., WILLIAMS, D. R. & COX, I. G. (2001) Effect of rotation and translation on the expected benefit of an ideal method to correct the eye's higher-order aberrations. *Journal of the Optical Society of America a-Optics Image Science and Vision,* 18**,** 1003-1015.

HE, J. C., BURNS, S. A. & MARCOS, S. (2000) Monochromatic aberrations in the accommodated human eye. *Vision Research,* 40**,** 41-48.

HE, J. C., MARCOS, S., WEBB, R. H. & BURNS, S. A. (1998) Measurement of the wave-front aberration of the eye by a fast psychophysical procedure. *Journal of the Optical Society of America A,* 15**,** 2449-2456.

HO, A., MANNS, F., PHAM, T. & FARRAR, S. (2002) The Effect of RGP Lens Decentration on Aberration: the Influence of the Tear Lens. *2002 Annual Meeting Abstract and Program Planner accessed at www.arvo.org. Association for Research in Vision and Ophthalmology. Abstract 3105.*

HOFER, H., CHEN, L., YOON, G., SINGER, B., YAMAUCHI, Y. & WILLIAMS, D. (2001) Improvement in retinal image quality with dynamic correction of the eye's aberrations. *Opt. Express. http://www.opticsexpress.org/oearchive/source/31887.htm,* 8**,** 631-643.

HONG, X., HIMEBAUGH, N. & THIBOS, L. (2001) On-eye evaluation of optical performance of rigid and soft contact lenses. *Optom Vis Sci,* 78**,** 872-80.

HOWLAND, B. (1968) Use of Crossed Cylinder Lens in Photographic Lens Evaluation. *Applied Optics,* 7**,** 1587-1599.

HOWLAND, B. & HOWLAND, H. C. (1976) Subjective Measurement of High-Order Aberrations of the Eye. *Science,* 193**,** 580-582.

HOWLAND, H. C. (2000) The history and methods of ophthalmic wavefront sensing. *1st International Congress of Wavefront Sensing and Aberration-free Refractive Correction.* Santa Fe, New Mexico, Slack Inc.

HUANG, D. & ARIF, M. (2002) Spot size and quality of scanning laser correction of higher-order wavefront aberrations. *J Cataract Refract Surg,* 28**,** 407-416.

JAIN, R., DILRAJ, G. & GREWAL, S. P. S. (2007) Repeatability of corneal parameters with Pentacam after laser in situ keratomileusis. *Indian J Ophthalmol,* 55**,** 341-7.

JARADE, E., ABI NADER, F. & TABBARA, K. (2006) Intraocular lens power calculation following LASIK: determination of the new effective index of refraction. . *J Refract Surg,* 22**,** 75-80.

JEONG, T. M., MENON, M. & YOON, G. Y. (2005) Measurement of wave-front aberration in soft contact lenses by use of a Shack-Hartmann wave-front sensor. *Applied Optics,* 44**,** 4523-4527.

JIANG, H. J., WANG, D., YANG, L. N., XIE, P. Y. & HE, J. C. (2006) A comparison of wavefront aberrations in eyes wearing different types of soft contact lenses. *Optometry and Vision Science,* 83**,** 769-774.

JIMÉNEZ, J., ANERA, R. & JIMÉNEZ DEL BARCO, L. (2003) Equation for corneal asphericity after corneal refractive surgery. *J Refract Surg.***,** 65-69.

JIMENEZ, J. R., ANERA, R. G., JIMÉNEZ DEL BARCO, L. & HITA, E. (2002) Effect on laser-ablation algorithms of reflection losses and nonnormal incidence on the anterior cornea. *Appl. Phys. Lett.,* 81**,** 1521-1523.

JIMENEZ, J. R., RODRIGUEZ-MARIN, F., ANERA, R. G. & DEL BARCO, L. J. (2006) Deviations of Lambert-Beer's law affect corneal refractive parameters after refractive surgery. *Optics Express,* 14**,** 5411-5417.

JIMENEZ, J. R., RODRIGUEZ-MARIN, F., ANERA, R. G. & DEL BARCO, L. J. (2007) Experiment on PMMA models to predict the impact of corneal refractive surgery on corneal shape: Comment. *Optics Express,* 15**,** 7243-7244.

JONES, C. E., ATCHISON, D. A. & POPE, J. M. (2007) Changes in lens dimensions and refractive index with age and accommodation. *Optometry and Vision Science,* 84**,** 990-995.

KALUZY, B. J., KALUZNY, J. J., SZKULMOWSKA, A., GORCZYNSKA, I., SZKULMOWSKI, M., BAJRASZEWSKI, T., WOJTKOWSKI, M. & TARGOWSKI, P. (2006) Spectral optical coherence tomography - A novel technique for cornea imaging. *Cornea,* 25**,** 960-965.

KELLY, J. E., MIHASHI, T. & HOWLAND, H. C. (2004) Compensation of corneal horizontal/vertical astigmatism, lateral coma, and spherical aberration by internal optics of the eye. *Journal of Vision,* 4**,** 262-271.

KHOO, C., CHONG, J. & RAJAN, U. (1999) A 3-year study on the effect of RGP contact lenses on myopic children. *Singapore Med J,* 40**,** 230-237.

KIELY, P. M., CARNEY, L. G. & SMITH, G. (1982) DIURNAL-VARIATIONS OF CORNEAL TOPOGRAPHY AND THICKNESS. *American Journal of Optometry and Physiological Optics,* 59**,** 976-982.

KIM, A. & CHUCK, R. S. (2008) Wavefront-guided customized corneal ablation. *Current Opinion in Ophthalmology,* 19**,** 314-320.

KLING, S., REMON, L., PEREZ-ESCUDERO, A., MERAYO-LLOVES, J. & MARCOS, S. (2009) Biomechanical Response of Normal and Cross-linked Porcine Corneas. *IOVS 2009: ARVO E-Abstract: 5477.*

KOHNEN, T., KUHNE, C. & BUHREN, J. (2007) The future role of wavefront-guided excimer ablation. *Graefes Archive for Clinical and Experimental Ophthalmology,* 245**,** 189-194.

KOPF, M., YI, F., ISKANDER, D. R., COLLINS, M. J., SHAW, A. J. & STRAKER, B. (2008) Tear Film Surface Quality with Soft Contact Lenses Using Dynamic Videokeratoscopy. *Journal of Optometry,* 1**,** 14-21

KUPER, S. & STUKE, M. (1987) FEMTOSECOND UV EXCIMER LASER ABLATION. *Applied Physics B-Photophysics and Laser Chemistry,* 44**,** 199-204.

KWON, Y. & BOTT, S. (2008) Postsurgery corneal asphericity and spherical aberration due to ablation efficiency reduction and corneal remodelling in refractive surgeries. *Eye*.

LACKNER, B., SCHMIDINGER, G., PIEH, S., FUNOVICS, M. A. & SKORPIK, C. (2005) Repeatability and reproducibility of central corneal thickness measurement with Pentacam, Orbscan, and ultrasound. *Optometry and Vision Science,* 82**,** 892-899.

LE GRAND, Y. & EL HAGE, S. G. (1980) *Physiological Optics (Vol. 1),* Berlin-Heidelberg, Springer Verlag.

LIANG, J., GRIMM, B., GOELZ, S. & BILLE, J. F. (1994) Objective measurement of wave aberrations of the human eye with the use of a Hartmann-Shack wave-front sensor. *Journal of the Optical Society of America A,* 11**,** 1949-1957.

LINDSKOOG PETTERSSON, A., JARKO, C., ALVIN, A., UNSBO, P. & BRAUTASET, R. (2008) Spherical aberration in contact lens wear. *Cont Lens Anterior Eye,* 31**,** 189-93.

LOPEZ-GIL, N., CASTEJON-MOCHON, J. F., BENITO, A., MARIN, J. M., LO-A-FOE, G., MARIN, G., FERMIGIER, B., RENARD, D., JOYEUX, D., CHATEAU, N. & ARTAL, P. (2002) Aberration generation by contact lenses with aspheric and asymmetric surfaces. *3rd International Confress of Wavefront Sensing and Aberration-free Refractive Correction.* Interlaken, Switzerland, Slack Inc.

LU, F., MAO, X. J., QU, J., XU, D. & HE, J. C. (2003) Monochromatic wavefront aberrations in the human eye with contact lenses. *Optometry and Vision Science,* 80**,** 135-141.

LLORENTE, L. (2009) Optical aberrations in ametropic eyes and their change with corneal refractive surgery. PhD Thesis, City University London.

LLORENTE, L., BARBERO, B., MERAYO, J. & MARCOS, S. (2004a) Changes in corneal and total aberrations induced by LASIK surgery for hyperopia. *Journal of Refractive Surgery,* 20**,** 203-216.

LLORENTE, L., BARBERO, S., CANO, D., DORRONSORO, C. & MARCOS, S. (2004b) Myopic versus hyperopic eyes: axial length, corneal shape and optical aberrations. http://journalofvision.org/4/4/5/. *Journal of Vision,* 4**,** 288.

LLORENTE, L., DIAZ-SANTANA, L., LARA-SAUCEDO, D. & MARCOS, S. (2003) Aberrations of the human eye in visible and near infrared illumination. *Optometry and Vision Science,* 80**,** 26-35.

LLORENTE, L., MARCOS, S., BARBERO, S., NAVARRO, R. & MORENO-BARRIUSO, E. (2001) Ocular aberrations in infrared and visible light using a laser ray tracing technique. *Investigative Opthalmology and Visual Science,* (Suppl.) 42**,** 87.

LLORENTE, L., MARCOS, S., DORRONSORO, C. & BURNS, S. (2007) The effect of sampling on real ocular aberration measurements. *Journal of the Optical Society of America A.,* 24**,** 2783-2796

MACRAE, S. M., SCHWIEGERLING, J. & SNYDER, R. (2000) Customized corneal ablation and super vision. *Journal of Refractive Surgery,* 16**,** 230-235.

MAEDA, N. (2009) Clinical applications of wavefront aberrometry - a review. *Clinical and Experimental Ophthalmology,* 37**,** 118-129.

MAEDA, P. Y. (2003) Zernike Polynomials and Their Use in Describing the Wavefront Aberrations of the Human Eye. *Applied Vision and Imaging Systems.* Stanford University.

MALACARA, D. (1992) *Optical Shop Testing,* New York, John Wiley & Sons, Inc.

MANNS, F., FERNANDEZ, V., ZIPPER, S., SANDADI, S., HAMAOUI, M., HO, A. & PAREL, J. M. (2004) Radius of curvature and asphericity of the anterior and posterior surface of human cadaver crystalline lenses. *Experimental Eye Research,* 78**,** 39-51.

MANNS, F., HO, A., PAREL, J. M. & CULBERTSON, W. (2002a) Ablation profiles for wavefront-guided correction of myopia and primary spherical aberration. *Journal of Cataract and Refractive Surgery,* 28**,** 766-774.

MANNS, F., MILNE, P. & PAREL, J. M. (2002b) Ultraviolet corneal photoablation. *3rd International Confress of Wavefront Sensing and Aberration-free Refractive Correction.* Interlaken, Switzerland, Slack Inc.

MANZANERA, S., PRIETO, P. M., CANOVAS, C., WEEBER, H., PIERS, P. & ARTAL, P. (2009) Predicting Visual Estimates of Depth of Focus From Optical Data. *ARVO Abstract.* Invest. Ophthalmol. Vis. Sci., 50, E-Abstract 1157.

MARCOS, S. (2001) Aberrations and Visual Performance following standard laser vision correction. *J. Refract. Surgery,* 17**,** 596-601.

MARCOS, S. (2002) Are changes in ocular aberrations with age a significant problem for refractive surgery? *Journal of Refractive Surgery,* 18**,** 572-578.

MARCOS, S., BARBERO, B., LLORENTE, L. & MERAYO-LLOVES, J. (2001a) Optical response to LASIK for myopia from total and corneal aberration measurements. *Investigative Ophthalmology and Visual Science,* 42**,** 3349-3356.

MARCOS, S., BARBERO, S. & JIMÉNEZ-ALFARO, I. (2005a) Optical quality and depth-of-field of eyes implanted with spherical and aspheric intraocular lenses. *Journal of Refractive Surgery,* 21**,** 223-235.

MARCOS, S., BARBERO, S. & LLORENTE, L. (2001b) Why high myopic eyes tend to be more aberrated? *Optical Society of America Technical Digest.* Long Beach, CA.

MARCOS, S. & BURNS, S. A. (2000) On the symmetry between eyes of wavefront aberration and cone directionality. *Vision Research,* 40**,** 2437-2447.

MARCOS, S., BURNS, S. A., MORENO-BARRIUSO, E. & NAVARRO, R. (1999) A new approach to the study of ocular chromatic aberrations. *Vision Research,* 39**,** 4309-4323.

MARCOS, S., CANO, D. & BARBERO, S. (2003) Increase of corneal asphericity after standard myopic LASIK surgery is not inherent to the Munnerlyn algorithm. *Journal of Refractive Surgery,* 19**,** 592-596.

MARCOS, S., DÍAZ-SANTANA, L., LLORENTE, L. & DAINTY, C. (2002) Ocular aberrations with ray tracing and Shack-Hartmann wavefront sensors: does polarization play a role? *Journal of the Optical Society of America A.,* 19**,** 1063-1072.

MARCOS, S., DORRONSORO, C. & CANO, D. (2005b) Spherical aberration prevention method in e.g. laser refractive surgery system. Patent WO 2005/122873 A1.

MARCOS, S., MORENO-BARRIUSO, E., LLORENTE, L., NAVARRO, R. & BARBERO, S. (2000) Do myopic eyes suffer from larger amount of aberrations? IN THORN, F., TROILO, D. & GWIAZDA, J. (Eds.) *Myopia 200. Proceedings of the 8th International Conference on Myopia.* Boston, International Conference on Myopia 2000 Press.

MARCOS, S., SAWIDES, L., GAMBRA, E. & DORRONSORO, C. (2008) Influence of adaptive-optics ocular aberration correction on visual acuity at different luminances and contrast polarities. *Journal of Vision,* 8**,** 12.

MARKETSCOPE (2008) 2008 Comprehensive Report on the Global Refractive Surgery Market. *Market Reports.* MarketScope, LLC.

MARTIN, J. A. & ROORDA, A. (2003) Predicting and assessing visual performance with multizone bifocal contact lenses. *Optometry and Vision Science,* 80**,** 812-819.

MATSUDA, J., HIEDA, O. & KINOSHITA, S. (2008) Comparison of central corneal thickness measurements by Orbscan II and Pentacam after corneal refractive surgery. *Japanese Journal of Ophthalmology,* 52**,** 245-249.

MCDONALD, M. B., KAUFMAN, H. E., FRANTZ, J. M., SHOFNER, S., SALMERON, B. & KLYCE, S. D. (1989) EXCIMER LASER ABLATION IN A HUMAN-EYE. *Archives of Ophthalmology,* 107**,** 641-642.

MCLELLAN, J., MARCOS, S. & BURNS, S. (2001) Age-related changes in monochromatic wave aberrations in the human eye. *Investigative Ophthalmology and Visual Science***,** 1390-1395.

MILLER, D. T., WILLIAMS, D. R., MORRIS, G. M. & LIANG, J. (1996) Images of the cone photoreceptors in the living human eye. *Vision Research,* 36**,** 1067-1079.

MILLODOT, M. & SIVAK, J. (1979) Contribution of the cornea and lens to the spherical aberration of the eye. *Vision Research,* 19**,** 685-687.

MOLEBNY, V. V., PALLIKARIS, I. G., NAOUMIDIS, L. P., CHYZH, I. H., MOLEBNY, S. V. & SOKURENKO, V. M. (1997) Retina Ray-Tracing technique for eye-refraction mapping. *Proceedings of the SPIE,* 2971**,** 175-183.

MORENO-BARRIUSO, E. (2000) Laser Ray Tracing in the human eye: measurement and correction of the aberrations by means of phase plates. PhD thesis, University of Cantabria.

MORENO-BARRIUSO, E., MARCOS, S., NAVARRO, R. & BURNS, S. A. (2001a) Comparing Laser Ray Tracing, Spatially Resolved Refractometer and Hartmann-Shack sensor to measure the ocular wavefront aberration. *Optometry and Vision Science,* 78**,** 152 - 156.

MORENO-BARRIUSO, E., MERAYO-LLOVES, J., MARCOS, S., NAVARRO, R., LLORENTE, L. & BARBERO, S. (2001b) Ocular aberrations before and after myopic corneal refractive surgery: LASIK-induced changes measured with Laser Ray Tracing. *Investigative Ophthalmology and Visual Science,* 42**,** 1396-1403.

MORENO-BARRIUSO, E. & NAVARRO, R. (2000) Laser Ray Tracing versus Hartmann-Shack Sensor for Measuring Optical Aberrations in the Human Eye. *Journal of the Optical Society of America A,* 17**,** 974-985.

MORGAN, P. B., WOODS, C. A., TRANOUDIS, I. G., EFRON, N., KNAJIAN, R., GRUPCHEVA, C. N., JONES, D., TAN, K.-O., PESINOVA, A., RAVN, O., SANTODOMINGO, J., VODNYANSZKY, E., MONTANI, G., ITOI, M., BENDORIENE, J., VAN DER WORP, E., HELLAND, M., PHILLIPS, G., GONZÁLEZ-MÉIJOME, J., RADU, S., BELOUSOV, V., SILIH, M. S., HSIAO, J. C. & NICHOLS, J. J. (2009) International contact lens prescribing in 2008. *Contact Lens Spectrum,* 24.

MROCHEN, M., KAEMMERER, M. & SEILER, T. (2000) Wavefront-guided Laser in situ Keratomileusis: Early results in three eyes. *Journal of Refractive Surgery,* 16**,** 116-121.

MROCHEN, M. & SEILER, T. (2001) Influence of corneal curvature on calculation of ablation patterns used in photorefractive laser surgery. *Journal of Refractive Surgery,* 17**,** S584-S587.

MUNNERLYN, C., KOONS, S. & MARSHALL, J. (1988) Photorefractive keratectomy: a technique for laser refractive surgery. *J Cataract Refract Surg,* 14**,** 46-52.

MUNNERLYN, C. R., ARNOLDUSSEN, M. E., MUNNERLYN, A. L. & LOGAN, B. A. (2006) Theory concerning the ablation of corneal tissue with large-area, 193-nm excimer laser beams. *Journal of Biomedical Optics,* 11**,** 8.

MUNSON, K., HONG, X. & THIBOS, L. (2001) Use of a Shack-Hartmann aberrometer to assess the optical outcome of corneal transplantation in a keratoconic eye. *Optom Vis Sci.,* 78**,** 866-871.

N.LOPEZ-GIL, A.BENITO, CASTEJÓN-MOCHÓN, J. F., MARÍN, J. M., G.LO-A-FOE, G.MARIN, B.FERMIGIER, D.JOYEUX, N.CHATEAU & P.ARTAL (2002) Aberration Correction using Customized Soft Contact Lenses with Aspheric and Asymmetric Surfaces [abstract]. *Annual Meeting Abstract and Program Planner accessed at www.arvo.org. Association for Research in Vision and Ophthalmology. Abstract 973.,* 73.

NAVARRO, R., GONZALEZ, L. & HERNANDEZ, J. L. (2006) Optics of the average normal cornea from general and canonical representations of its surface topography. *Journal of the Optical Society of America a-Optics Image Science and Vision,* 23**,** 219-232.

NAVARRO, R. & LOSADA, M. A. (1997) Aberrations and relative efficiency of light pencils in the living human eye. *Optometry and Vision Science,* 74**,** 540-547.

NAVARRO, R. & MORENO-BARRIUSO, E. (1999) Laser ray-tracing method for optical testing. *Optics Letters,* 24**,** 1-3.

NAVARRO, R., MORENO-BARRIUSO, E., BARÁ, S. & MANCEBO, T. (2000) Phase-plates for wave-aberration compensation in the human eye. *Optics Letters,* 25**,** 236 - 238.

NETTO, M. V., DUPPS, W. & WILSON, S. E. (2006) Wavefront-guided ablation: Evidence for efficacy compared to traditional ablation. *American Journal of Ophthalmology,* 141**,** 360-368.

NISHI, Y., MIRESKANDARI, K., KHAW, P. & FINDL, O. (2009) Lens refilling to restore accommodation. *Journal of Cataract and Refractive Surgery,* 35**,** 374-382.

NOACK, J., TONNIES, R., HOHLA, K., BIRNGRUBER, R. & VOGEL, A. (1997) Influence of ablation plume dynamics on the formation of central islands in excimer laser photorefractive keratectomy. *Ophthalmology,* 104**,** 823-830.

NOVO, A., PAVLOPOULOS, G. & FELDMAN, S. (1995) Corneal topographic changes after refitting polymethylmethacrylate contact lens wearers into rigid gas permeable materials. *CLAO J,* 21**,** 47-51.

OSHIKA, T., KLYCE, S. D., APPLEGATE, R. A. & HOWLAND, H. C. (1999) Changes in corneal wavefront aberrations with aging. *Investigative Ophthalmology and Visual Science,* 40**,** 1351-5.

PADMANABHAN, P., MROCHEN, M., BASUTHKAR, S., VISWANATHAN, D. & JOSEPH, R. (2008) Wavefront-guided versus wavefront-optimized laser in situ keratomileusis: Contralateral comparative study. *Journal of Cataract and Refractive Surgery,* 34**,** 389-397.

PALLIKARIS, I., PAPATZANAKI, M., STATHI, E., FRENSCHOCK, O. & GEORGIADIS, A. (1990) Laser in situ keratomileusis. *Lasers Surg Med,* 10**,** 463-468.

PAREL, J. M., GELENDER, H., TREFERS, W. F. & NORTON, E. W. D. (1986) PHACO-ERSATZ - CATARACT-SURGERY DESIGNED TO PRESERVE ACCOMMODATION. *Graefes Archive for Clinical and Experimental Ophthalmology,* 224**,** 165-173.

PELLI, D. G. (1997) The VideoToolbox software for visual psychophysics: Transforming numbers into movies. *Spatial Vision,* 10**,** 437-442.

PENNEY, C. M., WEBB, R. H., TIEMANN, J. J. & THOMPSON, K. P. (1993) Spatially resolved objective autorefractometer. United States, General Electric Company.

PEREZ-ESCUDERO, A., DORRONSORO, C. & MARCOS, S. (2009a) Correlation between radius and asphericity in surfaces fitted by conics. *Journal of the optical Society of America A, submitted.*

PEREZ-ESCUDERO, A., DORRONSORO, C., SAWIDES, L., REMON, L., MERAYO-LLOVES, J. & MARCOS, S. (2009b) Minor Influence of Myopic Laser In Situ Keratomileusis on the Posterior Corneal Surface. *Investigative Ophthalmology & Visual Science,* 50**,** 4146-4154.

PEREZ-ESCUDERO, A., REQUEJO-ISIDRO, J. & MARCOS, S. (2008) Corneal Deformation in an Inflation Porcine Corneal Model Measured with Scheimpflug Imaging. *IOVS 2008: ARVO E-Abstract: 664.*

PERRIGIN, J., PERRIGIN, D., QUINTERO, S. & GROSVENOR, T. (1990) Silicone-acrylate contact lenses for myopia control: 3-year results. *Optom Vis Sci.,* 67**,** 764-769.

PETTIT, G. & EDIGER, M. (1996) Corneal-tissue absorption coefficients for 193- and 213-nm ultraviolet radiation. *Appl. Opt.,* 35**,** 3386-3391.

PETTIT, G. H., CAMPIN, J. A. & LIEDEL, K. K. (2005) Practical issues of wavefront-guided refractive surgery. *Frontiers in Optics.* Tucson, Arizona, OSA Technical Digest Series (Optical Society of America).

PETTIT, G. H., EDIGER, M. N. & WEIBLINGER, R. P. (1991) Excimer laser corneal ablation - absence of a significant incubation effect. *Lasers in Surgery and Medicine,* 11**,** 411-418.

PHILLIPS, A. & SPEEDWELL, L. (1997) *Contact Lenses,* Oxford, Butterworth-Heinemann.

PLAINIS, S. & PALLIKARIS, I. G. (2006) Ocular monochromatic aberration statistics in a large emmetropic population. *3rd European Meeting in Physiological Optics.* London, ENGLAND, Taylor & Francis Ltd.

PORTER, J., GUIRAO , A., COX , I. & WILLIAMS, D. (2001) Monochromatic aberrations of the human eye in a large population. *J Opt Soc Am A,* 18**,** 1793-803.

PUJOL, J., GISPETS, J. & ARJONA, M. (2003) Optical performance in eyes wearing two multifocal contact lens designs. *Ophthalmic and Physiological Optics,* 23**,** 347-360.

RADHAKRISHNAN, S., ROLLINS, A., ROTH, J., YAZDANFAR, S., WESTPHAL, V., BARDENSTEIN, D. & IZATT, J. (2001) Real-time optical coherence tomography of the anterior segment at 1310 nm. *Arch Ophthalmol.,* 119**,** 1179-1185.

REMON, L., DORRONSORO, C., KLING, S., MERAYO-LLOVES, J. & MARCOS, S. (2009) Validation of Posterior Cornea Quantitative Scheimpflug Imaging Using a Hybrid Porcine/Plastic Model. *IOVS 2009: ARVO E-Abstract: 5105.*

RIOS, S., ACOSTA, E. & BARA, S. (1997) Hartmann sensing with Albrecht grids. *Optics Communications,* 133**,** 443-453.

ROBERTS, B., ATHAPPILLY, G., TINIO, B., NAIKOO, H. & ASBELL, P. (2006) Higher order aberrations induced by soft contact lenses in normal eyes with myopia. *Eye Contact Lens,* 32**,** 138-42.

ROBERTS, C. (2000) The cornea is not a piece of plastic. *Journal of Refractive surgery,* 16**,** 407-413.

ROBERTS, C. (2002) Biomechanics of the cornea and wavefront-guided laser refractive surgery. *3rd International Confress of Wavefront Sensing and Aberration-free Refractive Correction.* Interlaken, Switzerland, Slack Inc.

ROBERTS, C. & DUPPS, W. (2001) Corneal biomechanics and their role in corneal ablative procedures. IN MCRAE, S., KRUEGER, R. & APPLEGATE, R. (Eds.) *Customized corneal ablation: The quest for super vision.* Stack publising.

ROSALES, E. (2008) Purkinje and Scheimpflug imaging for the evaluation of crystalline and intraocular lenses in vivo. PhD thesis, University of Valladolid.

ROSALES, P., DUBBELMAN, M., MARCOS, S. & VAN DER HEIJDE, R. (2006) Crystalline lens radii of curvature from Purkinje and Scheimpflug imaging. http://journalofvision.org/6/10/5/. *Journal of Vision,* 6**,** 1057-1067.

ROSALES, P. & MARCOS, S. (2006) Phakometry and lens tilt and decentration using a custom-developed Purkinje imaging apparatus: validation and measurements. *Journal of the Optical Society of America a-Optics Image Science and Vision,* 23**,** 509-520.

ROSALES, P. & MARCOS, S. (2009) Pentacam Scheimpflug Quantitative Imaging of the Crystalline Lens and Intralocular Lens. *Journal of Refractive Surgery,* 25**,** 421-428.

ROSEN, A. M., DENHARN, D. B., FERNANDEZ, V., BORIA, D., HO, A., MATINS, F., PAREL, J. M. & AUGUSTEYN, R. C. (2006) In vitro dimensions and curvatures of human lenses. *Vision Research,* 46**,** 1002-1009.

SABESAN, R., JEONG, T. M., CARVALHO, L., COX, I. G., WILLIAMS, D. R. & YOON, G. (2007) Vision improvement by correcting higher-order aberrations with customized soft contact lenses in keratoconic eyes. *Optics Letters,* 32**,** 1000-1002.

SABESAN, R. & YOON, G. (2009) Visual performance after correcting higher order aberrations in keratoconic eyes. *Journal of Vision,* 9**,** 10.

SAKIMOTO, T., ROSENBLATT, M. I. & AZAR, D. T. (2006) Laser eye surgery for refractive errors. *Lancet,* 367**,** 1432-1447.

SALMON, T. O. & DE POL, C. V. (2006) Normal-eye Zernike coefficients and root-mean-square wavefront errors. *Annual Meeting of the American-Academy-of-Optometry.* San Diego, CA, Elsevier Science Inc.

SAWIDES, L., GAMBRA, E., PASCUAL, D., DORRONSORO, C. & MARCOS, S. (2009) Visual performance with real-life tasks under Adaptive-Optics ocular aberration correction. *Journal of Vision, Submitted.*

SCHULTZE, R. (1998) Accuracy of corneal elevation with four corneal topography systems. *J Refract Surg,* 14**,** 100-104.

SCHWIEGERLING, J., GREIVENKAMP, J. & MILLER, J. (1995) Representation of videokeratoscopic height data with Zernike polynomials. *Journal of the Optical Society of America A,* 12**,** 2105-2113.

SCHWIEGERLING, J. & GREIVENKAMP, J. E. (1997) Using corneal height maps and polynomial decomposition to determine corneal aberrations. *Optometry and Vision Science,* 74**,** 906-16.

SCHWIEGERLING, J., SNYDER, R. & MACRAE, S. (2001) Optical aberrations and ablation pattern design. IN MCRAE, S., KRUEGER, R. & APPLEGATE, R. (Eds.) *Customized corneal ablation: The quest for super vision.*

SEILER, T., KAEMMERER, M., MIERDEL, P. & KRINKE, H.-E. (2000) Ocular optical aberrations after photorefractive keratectomy for myopia and myopic astigmatism. *Archive of Ophthalmology,* 118**,** 17-21.

SEILER, T. & WOLLENSAK, J. (1986) INVIVO EXPERIMENTS WITH THE EXCIMER LASER - TECHNICAL PARAMETERS AND HEALING-PROCESSES. *Ophthalmologica,* 192**,** 65-70.

SEITZ, B., TORRES, F., LANGENBUCHER, A., BEHRENS, A. & SUAREZ, E. (2001) Posterior corneal curvature changes after myopic laser in situ keratomileusis. *Ophthalmology,* 108**,** 666-673.

SHACK, R. V. & PLATT, B. C. (1971) PRODUCTION AND USE OF A LENTICULAR HARTMANN SCREEN. *Journal of the Optical Society of America,* 61**,** 656-&.

SICAM, V., DUBBELMAN, M. & VAN DER HEIJDE, R. G. L. (2006) Spherical aberration of the anterior and posterior surface of the human cornea. *Journal of the Optical Society of America a-Optics Image Science and Vision,* 23**,** 544-549.

SMIRNOV, M. S. (1961) Measurement of the wave aberration of the human eye. *Biofizika,* 6**,** 687-703.

SMITH, G. & ATCHISON, D. A. (1997) *The Eye and Visual Optical Instruments*, Cambridge University Press.

SMITH, G., COX, M., CALVER, R. & GARNER, L. (2001) The spherical aberration of the crystalline lens of the human eye. *Vision Research,* 15**,** 235-243.

SMOLEK, M. K. (1993) Interlamellar cohesive strength in the vertical meridian of human eye bank corneas. *Investigative Ophthalmology & Visual Science,* 34**,** 2962-2969.

SPADEA, L., FASCIANI, R., NECOZIONE, S. & BALESTRAZZI, E. (2000) Role of the corneal epithelium in refractive changes following laser in situ keratomileusis for high myopia. *J Refract Surg.,* 16**,** 133-139.

SRINIVASAN, R. (1986) Ablation of polymers and biological tissue by ultraviolet lasers. *Science,* 234**,** 559-565.

SRINIVASAN, R. & BRAREN, B. (1984) Ablative photodecomposition of polymer-films by pulsed far-ultraviolet (193 nm) laser-radiation - dependence of etch depth on experimental conditions. *Journal of Polymer Science Part a-Polymer Chemistry,* 22**,** 2601-2609.

SRINIVASAN, R., BRAREN, B., SEEGER, D. E. & DREYFUS, R. W. (1986) PHOTOCHEMICAL CLEAVAGE OF A POLYMERIC SOLID - DETAILS OF THE ULTRAVIOLET-LASER ABLATION OF POLY(METHYL METHACRYLATE) AT 193-NM AND 248-NM. *Macromolecules,* 19**,** 916-921.

TABERNERO, J., PIERS, P., BENITO, A., REDONDO, M. & ARTAL, P. (2006) Predicting the optical performance of eyes implanted with IOLs to correct spherical aberration. *Investigative Ophthalmology & Visual Science,* 47**,** 4651-4658.

TANG, M., LI, Y., AVILA, M. & HUANG, D. (2006) Measuring total corneal power before and after laser in situ keratomileusis with high-speed optical coherence tomography. *Journal of Cataract and Refractive Surgery,* 32**,** 1843-1850.

THIBOS, L., HONG, X., BRADLEY, A. & CHENG, X. (2002) Statistical variation of aberration structure and image quality in a normal population of healthy eyes. *J Opt Soc Am A,* 19**,** 2329-2348.

THIBOS, L. N., APPLEGATE, R. A., SCHWIEGERLING, J. T., WEBB, R. H. & MEMBERS, V. S. T. (2000) Standards for reporting the optical aberrations of eyes. *Vision Science and its Applications, OSA Trends in Optics & Photonics,* 35**,** 110-130.

TOMLINSON, A., HEMENGER, R. P. & GARRIOTT, R. (1993) Method for Estimating the Spheric Aberration of the Human Crystalline Lens in Vivo. *Investigative Ophthalmology and Visual Science,* 34**,** 621-629.

TORRENTS, A., GISPETS, J. & PUJOL, J. (1997) Double-pass measurements of retinal image quality in monofocal contact lens wearers. *Ophthalmic and Physiological Optics,* 17**,** 357-366.

TSCHERNING, M. (1894) Die monochromatishen Aberrationen des menschlichen auges. *Z. Psychol. Physiol. Sinn.,* 6**,** 456-471.

TUCKER, J. & CHARMAN, W. N. (1975) The depth of focus of the human eye for Snellen letters. *American Journal of Optometry and Physiological Optics,* 52**,** 3-21.

TWA, M. D., ROBERTS, C., MAHMOUD, A. M. & CHANG, J. S. (2005) Response of the posterior in situ keratomileusis for corneal surface to laser myopia. *Journal of Cataract and Refractive Surgery,* 31**,** 61-71.

UEDA, T., NAWA, Y., MASUDA, K., ISHIBASHI, H., HARA, Y. & UOZATO, H. (2005) Posterior corneal surface changes after hyperopic laser in situ keratomileusis. *Journal of Cataract and Refractive Surgery,* 31**,** 2084-2087.

VON HELMHOLTZ, H. (1909) *Helmholtz's Treatise on Physiological Optics,* New York, Optical Society of America.

WALSH, G., CHARMAN, W. N. & HOWLAND, H. C. (1984) Objective technique for the determination of monochromatic aberrations of the human eye. *Journal of the Optical Society of America A,* 1**,** 987-992.

WALLS, G. L. (1950) HERSCHEL,JOHN AND CONTACT LENSES. *Science,* 111**,** 501-501.

WANG, L., DAI, E., KOCH, D. D. & NATHOO, A. (2003) Optical aberrations of the human anterior cornea. *Journal of Cataract and Refractive Surgery,* 29**,** 1514-1521.

WANG, Z., CHEN, J. Q. & YANG, B. (1999) Posterior corneal surface topographic changes after laser in situ keratomileusis are related to residual corneal bed thickness. *Ophthalmology,* 106**,** 406-409.

WATSON, A. B. & RAMIREZ, C. (2000) A standard observer for spatial vision. *Investigative Ophthalmology & Visual Science,* 41**,** 3794B892.

WEBB, R. H., PENNEY, C. M. & THOMPSON, K. P. (1992) Measurement of ocular wavefront distortion with a spatially resolved refractometer. *Applied Optics,* 31**,** 3678-3686.

WEEBER, H. A. & VAN DER HEIJDE, R. G. L. (2007) On the relationship between lens stiffness and accommodative amplitude. *Experimental Eye Research,* 85**,** 602-607.

Resúmenes

3 Predicción experimental de la elevación corneal tras cirugía refractiva utilizando un modelo de cornea en PMMA

Propósito: Medir la contribución de los cambios de la eficiencia de ablación del laser a lo largo de la cornea en la asfericidad corneal postoperativa, usando un modelo experiemental de cornea en PMMA (poli-metil-metacrilato).

Métodos: Superficies planas y esféricas (radio de curvatura 8 mm) de PMMA fueron ablacionadas con un sistema laser estándar de cirugía refractiva para correcciones corneales miópicas de 3, 6, 9 y 12 D. Las superficies ablacionadas fueron medidas con profilometría (planos) y topografía corneal (esferas). El perfil de ablación programado en el sistema laser fue obtenido a partir de las superficies planas ablacionadas, multiplicadas por un factor de tasa de ablación PMMA-cornea. El ratio de los perfiles en superficies planas frente a los de superficies esféricas se usó para estimar experimentalmente el factor de alblación experimental, debido a cambios en la eficiencia laser del centro a la periferia de la superficie esférica. El factor de eficiencia de ablación para PMMA se usó para obtener estimaciones experimentales del factor de eficiencia de ablación en cornea, aplicando la ley de Beer-Lambert y umbrales de ablación conocidos para PMMA y tejido corneal.

Results: La profundidad de ablación nominal en cornea fue 2.35 la profundidad de ablación en PMMA. Las superficies esféricas ablacionadas en PMMA muestran un aumento significativo de asfericidad (0.89 ± 0.73). El cambio en asfericidad corneal en

pacientes reales fue comparado con predicciones a partir de estimaciones experimentales del perfil de ablación, teniendo en cuenta o no el factor de eficiencia de ablacion experimental (y el factor de eficiencia teórico). Encontramos que los patrones de ablación corneal reales (a partir de medida en superficies planas) no producen un cambio significativo de asfericidad (0.03 ± 0.49) mientras que los cambios en la eficiencia de ablación son responsables de una parte significativa (1.39 ± 0.92) del aumento de asfericidad encontrado clínicamente (1.97 ± 2.00), usando el mismo sistema laser. La contribución de la biomecánica al incremento de la asfericidad corneal en cirugía refractiva miópica puede se puede estimar por comparación con las predicciones obtenidas en medidas sobre PMMA y con los resultados clínicos.

Conclusiones: Hemos obtenido un factor de eficiencia de ablación experimental, basado en en modelo corneal en PMMA, que permite explicar la contribución de los cambios de eficiencia del laser a lo largo de la cornea al cambio de asfericidad corneal tras la ablación. Este protocolo es útil para obtener un factor corrector para cualquier algoritmo de ablación o sistema laser, y para estimar la contribución de la biomecánica al incremento de asfericidad corneal en cirugía refractiva miópica.

4

Evaluación de las propiedades de ablación de un nuevo material (Filofocon A) para modelos corneales

Propósito: Se han propuesto recientemente modelos corneales experimentales en plástico (en PMMA, y más recientemente Filofocon A, un material de lentes de contacto) para superar algunas de las limitaciones de las aproximaciones experimentales que buscan mejorar la precisión de las predicciones del remodelado corneal por ablación laser. Estos modelos también se han propuesto para la evaluación precisa de patrones de ablación corneal laser. El objetivo de este capítulo es estudiar las propiedades ópticas y de ablación del Filofocon A y del PMMA usando un montaje experimental con laser de excímero.

Métodos: Se midió la relación entre número de pulsos y profundidad de ablación para Filofocon A y PMMA, para el rango de fluencias típico de plataformas laser de cirugía refractiva. Se obtuvieron los efectos de incubación, umbrales de ablación y coeficientes de absorción.

Resultados: Ambos materiales siguen una ley de Beer-Lambert en el rango de fluencias usado en cirugía refractiva, y el número de pulsos de incubación fue menor de 4 (PMMA) y 2 (Filofocon A) por encima de los 140 mJ/cm^2. Encontramos que por encima de los 40 pulsos para Filofocon A y 70 pulsos para PMMA, el umbral de ablación y el coeficiente de absorción efectivo pueden considerarse constantes (F_{th} = 90 mJ/cm^2 y α_{eff} = 36000 cm^{-1}, para Filofocon A, y F_{th} = 67 mJ/cm^2 y α_{eff} = 52000 cm^{-1} para PMMA, respectivamente).

Conclusiones: La ausencia de artificios de ablación (islas centrales), un número más bajo de pulsos de incubación, una menor dependencia del umbral de ablación frente al número de pulsos, y una buena correspondencia entre el efectivo α_{eff} y el coeficiente de absorción α estimado de medidas espectroscópicas hacen del Filofocon A un material más apropiado que el PMMA para modelos

experimentales de cirugía refractiva y para calibración de láseres clínicos.

5 Evaluación de perfiles de ablación, resultados post-operativos y efectos de eficiencia de ablación de diferentes plataformas laser optimizadas

Propósito: Estudios previos analíticos, computacionales y experimentales sugieren que el incremento de asfericidad que se encuentra tras cirugía refractiva miópica (y como consecuencia, la aberración esférica inducida) se debe en buena parte a las pérdidas de eficiciencia del laser desde el apex corneal a la periferia. Estos efectos se pueden medir experimentalmente para calcular un factor corrector para cada laser. Este capítulo investiga las pérdidas de eficiencia del laser desde el apex a la periferia, relacionadas con la geometría, para tres plataformas laser estado del arte, dotadas de algoritmos optimizados, y su efecto en modelos corneales de plástico.

Métodos: Se usó un nuevo modelo experimental basado en ojos artificiales de plástico (Filofocon A) para estudiar los perfiles de ablación y los resultados de tres láseres cínicos de excímero para cirugía refractiva dotados de punto volante (flying spot) de haz estrecho y algoritmos optimizados (Ladarvision 4000, Alcon; Technolas 217 Z100, Bausch&Lomb; Allegretto wave Eye-Q, Wavelight). La línea de mirada del ojo artificial se alineó con la referencia de fijación del laser, usando una retina artificial (chip CMOS) y una mesa de inclinación. Unas pupilas artificiales dentro del ojo permitieron un centrado similar al de los ojos de los pacientes. Los patrones de ablación 3-D producidos por las correcciónes miópicas del laser (-9, -6 y -3 D) en superficies planas y esféricas de Filofocon A se midieron usando profilometría óptica de alta resolución.

Resultados: Encontramos diferencias significativas entre láseres en la forma y la profundidad de las ablaciones. La comparación entre los patrones de ablación en superficies planas y esféricas da lugar a una medida de las pérdidas de eficiencia del centro a la periferia en

cada punto de las corneas de plástico esféricas. Este efecto también cambió entre láseres, dependiendo de su fluencia (120-400 mJ/cm^2). Se obtuvieron estimaciones de la forma postoperativa de la cornea a partir de medidas sobre Filofocon A y factores de corrección entre plástico y cornea. La forma postoperativa corneal predicha, el volumen ablacionado, la asfericidad y la aberración esférica varían según el laser, así como la contribución relativa al incremento de asfericidad de los diseños de los patrones de ablación y las pérdidas de eficiencia del laser.

Conclusiones: Aunque los resultados muestran que los algoritmos han sido optimizados para reducir la inducción de aberración esférica, aún podrían beneficiarse de la aplicación de factores de corrección para efectos de eficiencia derivados de una aproximación sistemática usando modelos experimentales en plástico. Estos modelos han probado ser útiles (1) para evaluar los resultados de diferentes laseres o algoritmos de ablacion, (2) para calibraciones precisas y homologación de los láseres, y (3) para calcular factores de corrección experimentales para efectos de eficiencia.

6 Modelo híbrido porcino-plástico para el estudio de la superficie posterior de la cornea

Propósito: El análisis cuantitiativo de las imágenes de Scheimpflug de la cornea posterior exige una adecuada corrección de la distorsión geométrica y de la distorsión óptica producida en las superficies anteriores. Desarrollamos un modelo de ojo híbrido porcino-plástico (con las propiedades de scattering y el índice de refracción del tejido corneal y con geometría corneal posterior conocida) para la validación de la reconstrucción de la cornea posterior proporcionado por Pentacam, un sistema de imagen Scheimpflug.

Métodos: Los modelos de ojo híbridos porcino-plástico consisten en corneas porcinas montadas en un pistones de 12 mm de diámetro acabados en superficies esféricas con radio de curvatura conocido (7.47, 7.93 y 8.75 mm, según validación en un profilómetro de no contacto). Se prestó especial cuidado en preservar la integridad del endotelio corneal. La cornea posterio porcina se conformó a la superficie soporte de plástico. Las imágenes de Scheimpflug se tomaron en las primeras 4 horas post-mortem. La superficie corneal posterior se evaluó usando rutinas de ajuste del software de la Pentacam. Se usaron 12 corneas porcinas. La geometría posterior obtenida se comparó con los datos nominales de las superficies plásticas de soporte. Se realizaron correlaciones entre los datos de la cornea anterior y posterior para evaluar que la corrección de la distorsión óptica fue correctamente aplicada.

Resultados: Las medidas sobre modelos de ojo híbridos de la geometría corneal posterior muestran que los parámetros recuperados (radio, astigmatismo, asfericidad) son más precisos para la cara anterior de la cornea que para la cara posterior. La medida del radio de curvatura posterior está mínimamente afectado por la geometría de la superficie anterior, aunque consistentemente subestimado (0.26±0.12 mm de media). Se obtuvo mayor variabilidad y subestimación en la asfericidad de la superficie corneal posterior (Qpost=-0.33±0.44) que en las superficies de

plástico medidas anteriormente (Qant=-0.02±0.22). Las superficies porcinas tenían un gran rango de variación en radio (de 8.0 a 9.6 mm) y astigmatismo (1.9 ±1.0 D). Sin embargo no se encontró correlación significativa entre el radio de curvatura anterior y posterior, asfericidad o astigmatismo (p>0.26).

Conclusiones: Este modelo ha permitido probar la precisión de la geometría posterior estimada por Pentacam. La independencia de los datos recuperados con respecto a la topografía corneal anterior sugiere una adecuada corrección de la distorsión óptica. Este modelo muestra propiedades más comparables a la de los ojos vicvos y podría ser usado para calibración de otros sistemas de imagen del segmento anterior. El sistema Pentacam de imagen de Scheimpflug es fiable para evaluar cambios en el radio corneal posterior tras LASIK.

7 Cambios en los mapas de elevación corneal anterior y posterior tras cirugía refractiva

Propósito: Comprobar si el LASIK miópico introduce cambios en la superficie corneal posterior.

Métodos: Se usó la técnica de imagen de Scheimpflug (Pentacam, Oculus) para medir la topografía corneal posterior antes y despúes de cirugía LASIK miópica estándar (correcciones entre -1.25 y -8.50 D) en 27 ojos (14 pacientes) y en en 18 ojos no operados (9 sujetos). Se calcularon los desplazamientos longitudinales del apex de la cornea posterior y los cambios en el radio de curvatura y la asfericidad.

Resultados: Las medidas en pacientes muestran que, en promedio, el único cambio relevante (aunque clínicamente insignificante) en radio de curvatura y asfericidad se produce el primer día tras la cirugía (ΔR = -28 ± 34 μm y ΔQ = -0.06 ± 0.06). Después no se observan cambios estadísticamente significativos. El cambio en el radio es más pronunciado en la dirección vertical que en la horizontal. En promedio, no hubo desplazamiento significativo del apex de la cornea posterior. Los cambios individuales a lo largo del tiempo no muestran una tendencia sistemática entre pacientes, y los sujetos de control experimentan cambios del mismo orden de magnitud.

Conclusiones: No se encuentra evidencia de cambios inducidos por la cirugía en la superficie corneal posterior más allá de una semana tras cirugía.

8 Evaluación óptica del ajuste de lentes de contacto blandas usando corneas modelo

Propósito: Desarrollamos un modelo experimental para estudiar los efectos ópticos de la adaptación de lentes de contacto. El conocimiento del acoplamiento entre la óptica del ojo y la de la lente de contacto, y cómo la lente se flexiona para conformarse a la cornea es esencial para comprender la adaptación de lentes multifocales, y por qué no funcionan con éxito en muchos pacientes.

Métodos: Se fabricaron ojos artificiales a partir de cilindros de PMMA. La cornea es una superficie esférica pulida, y la retina se situó en el plano focal corneal. Se midieron las aberraciones totales totales y de la superficie anterior en los ojos artificiales desnudos y en los ojos adaptados con lentes de contacto blandas, positicas y negativas, monofocales y multifocales. Los sistemas de trazados de rayos laser y topografía corneal se adaptaron para permitir medidas en la dirección vertical. Se usó una sujección especial para proporcionar un buen centrado, una correcta hidratación de la lente, y una superficie de lágrima uniforme.

Resultados: Usando las medidas de topografía corneal, se simuló la forma de la lente de contacto en el ojo. Encontramos diferencias en la forma de la cara anterior entre diseños monofocales y multifocales. El radio de las lentes es consistente con su potencia nominal. Los diseños multifocales tienden a producir superficies asféricas más complejas que simples cónicas. El análisis en términos de aberraciones se pueden simplificar a aberraciones esféricas. La aberración esférica corneal coincide con la total en el ojo artificial sin lente, lo que valida nuestros aberómetros. La presencia de lágrima no influencia el resultado promedio, aunque incrementa la variabilidad. La aberración esférica corneal se reduce menos de lo esperado en lentes multifocales positivas. Las lentes multifocales negativas se conforman a la cornea, sin inducir ninguna multifocalidad en su superficie anterior. Las lentes monofocales reducen la aberración esférica total. La aberración esférica total es positiva en los diseños multifocales, lo que discrepa con el cambio óptico esperado.

Conclusiones: Se ha desarrollado un nuevo modelo experimental, basado en aberrometría, que puede usarse para evaluar los factores ópticos involucrados en la adaptación de lentes de contacto si la variabilidad asociada a ojos individuales. Las causas físicas son más importantes de lo esperado para explicar la falta de adaptación de los pacientes a lentes multifocales.

9 Prestaciones ópticas en el ojo de las lentes rígidas permeables al gas

Propósito: Evaluar el impacto de la adaptación de lentes rígidas permeables al gas (RGP) sobre las aberraciones y explorar las posibilidades de la aberrometría como una nueva herramienta para la adaptación de lentes de contacto.

Métodos: Se realizaron cuatro medidas distintas de aberraciones a cuatro sujetos, usuarios habituales de lentes de contacto RGP. Se midieron las aberraciones totales y corneales, con y sin lente. Las aberraciones corneales se obtuvieron a partir de datos de elevación de topógrafo corneal y algoritmos a medida y las aberraciones totales con una técnica de trazado de rayos laser.

Resultados: Comparando ojos desnudos con ojos con lente de contacto, se encontró un descenso significativo en las aberraciones totales en 3 de los 4 sujetos. Para el sujeto con mayores aberraciones corneales, la raíz cuadrática media (RMS) de las aberraciones de segundo y mayor orden cayó de 1.36 a 0.46 μm, y las aberraciones no convencionales de 0.77 a 0.39 μm (RMS). Por comparación entre las aberraciones de la superficie anterior de la lente con la superficie corneal anterior a ojo desnudo, se evaluaron los efectos de la flexión de la lente en las prestaciones ópticas de la lente. Se concluye que los ojos en los que dominan las aberraciones corneales se benefician de flexiones bajas mientras que los ojos con gran compensación de las aberraciones corneales por las aberraciones internas se benefician de flexiones grandes. Comparando las cuatro medidas en ojos individuales se estimó la contribución de la lente de lágrima a la aberración de onda. Se encontró que la lente de lágrima tiende a compensar la aberración esférica positiva inducida por la lente de contacto, para dar una aberración esférica total cercana a cero en todos los ojos estudiados.

Conclusiones: El análisis de aberraciones es una herramienta útil para comprender la adaptación de lentes de contacto, y la interacción con las superficies internas del ojo. La aberrometría puede ayudar a elegir los mejores parámetros estándar de las lentes RGP. Las lentes

RGP pueden reducir en gran medida la cantidad de aberraciones, particularmente en ojos con grandes aberraciones corneales. El control de la flexión y un conocimiento de la óptica interna pueden ayudar a mejorar las prestaciones ópticas de las lentes de contacto.

10

Calidad óptica y calidad visual con lentes de contacto blandas monofocales y multifocales

Propósito: Las lentes de contacto (LC) multifocales son una alternativa común para la corrección de la presbicia. Su fracaso en algunos pacientes en producir una calidad visual adecuada o una expansión significativa en la profundidad de campo se atribuye a menudo a falta de adaptación neuronal. Nuestra hipótesis es que gran parte del efecto es óptico, y reside en efectos de acoplamiento entre la LC y la óptica del ojo subyacente. Esta cuestión fue investigada por medio de la medida de las aberraciones totales y la función visual en ojos con y sin LC blandas multifocales.

Métodos: Se midieron las aberraciones totales (usando un sistema de trazado de rayos con un patrón de muestreo circularmente simétrico) y la agudeza visual (E de Snellen, paradigma de elección forzada entre 4 alternativas) en 4 ojos sanos (bajo ciclopegia) de 4 sujetos (edad 28±5). Cada ojo se midió sin LC, con LC multifocal (Essilor Rythmic multifocal) de +3.5D (multiCL+) y -3.5D (multiCL-), y con una LC monofocal de referencia (monoCL-, Proclear Cooper Vision) de -3.5D. Todas las LC tienen el mismo radio base (8.60 mm) y materiales similares. A partir de las aberraciones de onda, se obtuvieron funciones de transferencia de modulación y simulaciones de la imágenes retinianas de cartas de agudeza visual, y se usó la razón de Strehl como métrica. Se midió la agudeza visual a través de foco en pasos entre 1 y 0.5 D (30 presentaciones por posición de foco, con una duración del estímulo de 0.5 s). Todas las comparaciones se realizaron para pupilas de 4 mm de diámetro.

Resultados: 1) Encontramos una alta correlación entre las aberraciones del ojo desnudo y las aberraciones del ojo con cada una de las lentes de contacto (R^2=0.88 para multiCL+, 0.90 para multiCL-, y 0.91 para la monoCL-, en promedio), indicando conformidad de las LC a la cornea. 2) Se indujo aberración esférica negativa con 11 de las 12 LC (mono o multifocal) (-0.10±0.02 para

multiCL+, -0.04±0.09 para multiCL-, -0.09±0.04 para monoCL). 3) Sólo multiCL+ aumentó la profundidad de foco (en dos casos), a costa de pérdidas de calidad óptica, como se muestra tanto en las medidas de calidad óptica como en las de agudeza visual. 4) La calidad de imagen a través de foco simulada se correlaciona con la agudeza visual a través de foco, indicando que las aberraciones ópticas son una causa importante en la variabilidad de función visual entre sujetos, y para los límites en prestaciones de las LC.

Conclusión: 1) Las aberraciones oculares juegan un importante papel en los resultados visuales con LC blandas multifocales. 2) Las LC multifocales negativas se comportan esencialmente como LC monofocales, mientras que las LC multifocales positivas (más gruesas) parecen extender algo la profundidad de foco, confirmando resultados previos de esta tesis en un modelo in vitro. 3) Comprender el acoplamiento entre la óptica ocular y las LC es esencial para mejorar los diseños actuales, antes de atribuir su éxito o fracaso a efectos neuronales.

A Correlación entre radio y asfericidad en superficies ajustadas a cónicas

Las superficies ópticas del ojo a menudo se describe en términos de us radio y asfericidad. Encontramos que las variaciones en los radios y en las asfericidad medidas, están fuertemente correlacionadas. En este anexo mostramos esta correlación en datos experimentales de elevación corneal procedentes de videokeratometría (Atlas, Zeiss) and topografía Scheimpflug (Pentacam, Oculus), en profilometría de no contacto de lentes artificiales, y en simulaciones. El efecto es una característica de curvas cónicas ajustadas a datos experimentales, y no restringidas a ningún dispositivo experimental o procedimiento de ajuste. Un análisis separado del radio o la asfericidad podría dar lugar a una estimación incorrecta de la significación estadística de los cambios en las superficies oculares. Proponemos un análisis estadístico basado en MANOVA que incrementa la sensibilidad en un factor 4.

Conclusiones

LOGROS ALCANZADOS Y CONCLUSIONES ESPECÍFICAS

1 Hemos desarrollado diferentes implementaciones de instrumentos, procedimientos de medida y algoritmos de procesado para el estudio con precisión de la geometría de superficies ópticas. Estas técnicas incluyen topografía corneal por disco de Plácido, imagen de Scheimpflug y profilometría. La tecnología ha demostrado ser útil para medir tanto ojos artificiales como reales, para medir los cambios inducidos por distintos procedimientos (cirugía refractiva y ajuste de lentes de contacto), y para obtener diferencias en la forma de la superficie anterior y posterior entre condiciones, así como las consecuencias estos cambios.

2 Hemos desarrollado un aberrómetro compacto y versátil por Trazado de Rayos Laser, para medir las aberraciones ópticas del ojo con amplio rango dinámico y parámetros configurables (por ejemplo el número de muestras en el frente de onda o su distribución espacial). Ha mostrado ser capaz de alcanzar los exigentes requisitos de la medida de lentes de contacto multifocales con altas aberraciones. El sistema ha sido validado (frente a medidas de frente de onda corneal en ojos artificiales). El sistema también ha sido aplicado en otros estudios del Laboratorio de Óptica Visual y Biofotónica (Llorente et al., 2004a) (Llorente et al., 2007).

3 Hemos descrito las propiedades ópticas y propiedades de ablación de dos materiales poliméricos (PMMA y Filofocon A) para su uso en investigación en cirugía refractiva. La ausencia de artificios de ablación (islas centrales), un menor número de pulsos de incubación, una menor dependencia del umbral de ablación con el número de pulsos, y una buena correspondencia entre el coeficiente de absorción efectivo y el coeficiente de absorción estimado de medidas espectroscópicas, hacen del Filofocon A un material más apropiado que el PMMA para modelos experimentales en cirugía refractiva y para calibración de laseres

clínicos. La descripción detallada de las propiedades físicas obtenidas con un laser de laboratorio es esencial para interpretar los resultados de los láseres clínicos y para realizar estimaciones correctas en tejido corneal.

4 Hemos desarrollado (y posteriormente evolucionado) un modelo experimental para el estudio de los efectos físicos involucrados en la cirugía refractiva que nos ha permitido medir experimentalmente los patrones de ablación de cuatro plataformas clínicas diferentes. Los resultados de tres algoritmos estado del arte se compararon con otro de una generación previa. Concluimos que los nuevos algoritmos han sido optimizados para reducir la inducción de aberración esférica en materiales no biológicos, aunque la aberración esférica inducida aún no es despreciable (hasta 0.7 micras). Hemos mostrado que los efectos físicos pueden explicar la mayor parte del incremento en asfericidad que se encuentra en la práctica clínica (el 70 % en un láser no optimizado). Sin embargo, y particularmente para altas aberraciones, aún hay espacio para efectos biomecánicos.

5 Hemos desarrollado un procedimiento para medir experimentalmente los efectos de eficiencia del laser en superficies curvas (pérdidas de eficiencia del centro a la periferia de la superficie ablacionada) y también para estimar los efectos en cornea. Hemos encontrado importantes diferencias entre plataformas laser, dependiendo de su fluencia (6.5% para 120 mJ/cm^2 a 2.5 mm del apex corneal y prácticamente despreciable para 400 mJ/cm^2). Hemos encontrado factores de corrección para estos efectos, para ser aplicados en las unidades clínicas.

6 Se ha desarrollado un modelo híbrido plástico-porcino para la calibración de sistemas de imagen del segmento anterior. Este ojo artificial muestra propiedades corneales (scattering, índice de refracción) comparables a la de los ojos vivos, pero sin variabilidad biológica. El modelo se ha usado para validar el sistema Pentacam de imagen de Sheimpflug, nominalmente corregido para distorsión óptica y geométrica. Hemos probado que este instrumento puede medir de forma fiable los cambios en la superficie corneal posterior que se produzcan durante la cirugía refractiva.

7 Hemos encontrado que la cirugía refractiva LASIK miópica (de -1.25 a -8.5 D) no induce cambios sistemáticos a largo plazo en la forma de la superficie corneal porterior. Las diferencias sólo fueron significativas un día tras la cirugía, y los cambios fueron más relevantes en el meridiano vertical que en el horizontal. La cantidad de cambios individuales en la cornea posterior (radio de curvatura) en pacientes post-LASIK es similar a la que se encuentra en ojos normales. Los ojos derechos e izquierdos muestran cambios similares, lo que sugiere que existen mecanismos fisiológicos actuando de la misma forma bilateralmente.

8 Hemos desarrollado otro modelo in-vitro basado en ojos artificiales de plástico, orientado al estudio de la adaptación de lentes de contacto blandas. El modelo permite eliminar la variabilidad biológica asociada con ojos reales (movimientos y descentramientos de la lente, aberraciones oculares) a la vez que simula una situación más realista que una medida convencional en inmersión. Usando este

modelo in-vitro encontramos que las lentes blandas monofocales esféricas reducen la aberración esférica total. Las lentes multifocales están afectadas por conformidad a la cornea y efectos de adaptación que cancelan las propiedades multifocales del diseño, aunque las prestaciones ópticas finales dependen de la potencia de la lente, que determina su espesor central.

9 Hemos usado medidas de aberraciones en ojos reales adaptadas con lentes de contacto semirrígidas (RGP) y encontramos que esta herramienta es útil para comprender el proceso de adaptación de lentes, y el acoplamiento óptico que se produce entre la óptica de la lente y la óptica del ojo. Demostramos que las lentes de contacto RGP pueden mejorar significativamente la óptica natural del ojo. La óptica interna y la flexión de la lente pueden imponer límites a esta compensación. Encontramos una marcada correlación entre las aberraciones corneales y oculares de cada ojo medidas con y sin lente semirrígida (RGP). Fuimos capaces de medir las aberraciones de la lente de lágrima en lentes de contacto RGP, y describimos un efecto compensatorio en la aberración esférica totla. Esta metodología proporciona un análisis preciso de la adaptación de lentes de contacto en ojos individuales y puede ayudar a elegir los mejores parámetros de la lente para mejorar la óptica de ojos individuales.

10 En ojos adaptados con lentes de contacto blandas encontramos que las aberraciones oculares juegan un papel determinante en los resultados ópticos y visuales. Las correlaciones entre las aberraciones del ojo desnudo y las del mismo ojo con lentes de contacto blandas son mayores que en el caso de las lentes RGP, indicando un mayor grado de conformidad a la cornea. La gran mayoría de las lentes de contacto indujeron aberración esférica negativa, tanto las monofocales como las multifocales. Sin embargo, las aberraciones naturales del ojo tienen un impacto mayor en las prestaciones ópticas finales de las lentes blandas, y de hecho hemos encontrado que la conformidad a la cornea hace que las lentes negativas multifocales que hemos medido se comporten esencialmente como lentes monofocales. Encontramos que algunas de las lentes positivas (con el mismo diseño) expanden la profundidad de foco, lo que confirma hallazgos previos del modelo in-vitro. El mayor espesor (menor conformidad) de las lentes positivas puede explicar por qué estas lentes pueden preservar su diseño multifocal más que las lentes negativas de adición central similar. Para mejorar los diseños actuales, es fundamental comprender el acoplamiento de la óptica ocular a las lentes de contacto.

11 Los experimentos de agudeza visual a través de foco confirman la falta de multifocalidad inducida en la mayoría de los diseños multifocales probados en este estudio. En general, las tendencias de las medidas ópticas (Strehl) y visuales (agudeza visual) a través de foco tienen una buena correspondencia. Las simulaciones retinianas basadas en medidas físicas (objetivas) pueden explicar variaciones sutiles en las respuesta visual a través de foco. La falta de multifocalidad de la mayoría de los diseños, así como la profundidad de foco expandida en algunos de los sujetos y condiciones pueden ser explicados desde un punto de vista óptico, sin necesidad de invocar efectos neuronales o falta de adaptación visual de sujetos individuales a ciertaas lentes de contacto multifocales.

12

Las superficies oculares y oftálmicas se describen a menudo en términos de cónicas. Los radios y asfericidades de cónicas ajustadas están bien correlacionadas. Nosotros hemos encontrado esta correlación en datos de elevación corneal experimentales procedentes de videoqueratoscopía (Atlas, Zeiss) y topografía de Scheimpflug (Pentacam, Oculus), en datos de profilometría de no contacto sobre lentes artificiales, y en simulaciones. El efecto es una característica de cónicas ajustadas a datos experimentales, y no restrigido a ningún sistema de medida o procedimiento de ajuste. Cuando se describen los resultados de ajustes a cónicas, como los que se usan rutinariamente en biometría ocular, el radio y la asfericidad no se pueden tratar separadamente: una descripción correcta de la superficie necesita ambos parámetros. Proponemos el uso del test estadístico MANOVA para estudiar cambios corneales. Este test incrementa la sensibilidad del análisis, detectando cambios unas 4 veces más pequeños que en un análisis separado de R y Q.

LISTA DE RESULTADOS METODOLÓGICOS

1. Modelos físicos de ojo para el análisis de la ablación de cirugía refractiva láser.
2. Modelo físico para el análisis de los procesos biomecánicos, a través de la validación de instrumentación para la medida de la cara anterior y posterior de la cornea.
3. Modelos físicos para la adaptación de lentes de contacto.
4. Sistema de trazado de rayos láser (optomecánica, electrónica, software para el control y procesado de datos) para la medida de aberraciones ópticas.
5. Procedimientos de medida y software para el análisis y caracterización de superficies basado en topografía corneal. Técnicas de imagen y profilometría de contacto y no-contacto.
6. Herramientas de software avanzado para comparación entre superficies y detección de cambios.
7. Herramientas de análisis para lentes de contacto y medidas de patrones de ablación en ojos reales y modelo.
8. Propiedades de ablación de materiales usados en modelos de ojo (PMMA y filofocón A)
9. Factores de corrección empíricos para la corrección de algoritmos de ablación corneal.
10. Paradigmas de psicofísica visual para la evaluación de la calidad visual.
11. Protocolos para la personalización de la prescripción de lentes de contacto.
12. Propuesta de un método estadístico (MANOVA) para mejorar la resolución en la detección de cambios superficiales o de diferencias entre superficies.

IMPLICACIONES DE ESTA INVESTIGACIÓN

1. Los resultados mostrados en esta tesis son de directa aplicación en cirugía refractiva laser. La inducción de aberración esférica aún representa un problema en la cirugía refractiva de hoy en día. Hemos demostrado que la mayor parte del incremento de asfericidad se puede explicar por factores puramente físicos, y que los efectos biomecánicos tienen un impacto secundario en la forma de la cornea, en condiciones normales. Hemos obtenido experimentalmente factores de corrección de la eficiencia del laser, que junto con el uso de modelos físicos y los protocolos de medidas y los parámetros ópticos y de ablación obtenidos en esta tesis, pueden ser directamente aplicados en la evaluación de los algoritmos actuales y en el diseño de la próxima generación de perfiles de ablación.

2. Los resultados descritos en esta tesis demuestran el gran valor de la aberrometría (corneal y ocular) en la práctica de la contactología. Se pueden establecer protocolos similares a los seguidos en esta tesis para ayudar en la identificación de la lente más adecuada para cada paciente individual.

3. Los resultados descritos en esta tesis para lentes de contacto multifocal tienen importantes implicaciones para el diseño de correcciones multifocales en general, no sólo en el contexto de las lentes de contacto, sino también en cirugía refractiva o en lentes intraoculares. Dotar al ojo de un rango eficiente de multifocalidad es un problema complejo. Hemos aportado evidencia de que las aberraciones de ojos individuales determinan (y muy a menudo comprometen) las profundidad de foco final de una corrección multifocal. En el diseño de lentes multifocales, antes de considerar efectos relativos a adaptación neuronal, se deben considerar los efectos ópticos.

4. Las técnicas de metrología de superficies y biometría corneal se pueden beneficiar directamente de los desarrollos de esta tesis en modelos físicos. Estos ojos artificiales pueden llegar a ser herramientas muy útiles para la validación y calibración de sistemas de laboratorio y comerciales como profilómetros, topógrafos corneales, y técnicas de imagen como OCT o imagen de Scheimpflug. Además, pueden ser implementadas en equipos para la evaluación in-vitro de lentes de contacto y calibración de sistemas de ablación laser.

LÍNEAS DE INVESTIGACIÓN FUTURA

Los resultados pueden establecer las bases para las líneas de investigación futura:

1. En esta tesis hemos descrito las propiedades ópticas y de ablación de los materiales plásticos para modelos de cirugía refractiva, y hemos extrapolado para predecir los resultados en cornea. Este trabajo abre el paso para posteriores estudios ópticos y de las propiedades de ablación del tejido corneal, incluyendo medidas precisas de la física de la ablación y la dinámica de expulsión. Estas investigaciones proporcionarán un mejor control de los procedimientos de ablación usados en clínica, un paso necesario en la búsqueda de las correcciones optimizadas basadas en el frente onda.

2. El estudio de los procedimientos clínicos actuales guiados por la información del frente de onda, tanto en vivo como in vitro, con la metodología desarrollada, permitirá mejorar los algoritmos de ablación laser, y diseñar nuevas estrategias basadas en frentes de onda.

3. El conocimiento adquirido sobre ablaciones de materiales plásticos en superficies curvas abre la posibilidad de fabricar lentes de contacto con superficies complejas (i.e. free form, multifocal) por medio de ablaciones láser.

4. El uso de modelos de cornea híbridos porcino-plástico, y de nuevos instrumentos calibrados (proporcionando información sobre la cara anterior y posterior de la cornea) abre la posibilidad de estudios cuantitativos de los procesos en los que los efectos biomecánicos pueden jugar un papel importante: ectasia post-cirugía, evaluación del queratocono, deformaciones corneales tras largos periodos de uso de lentes de contacto (corneal warpage) o durante tratamientos de ortoqueratología con lentes de contacto de geometría inversa y tratamientos de cross-linking del colágeno, entre otros.

5. La aplicación de tomografía de coherencia óptica del segmento anterior de alta resolución en el estudio de la adaptación de lentes de contacto será esencial para evaluar las discrepancias que aparecen en lentes multifocales entre los diseños nominales y los medidos en el ojo, y la influencia de la película de lágrima sobre la superficie anterior y posterior de las lentes de contacto. El instrumento debe ser corregido para distorsión óptica y de barrido, y validada para la obtención de imágenes cuantitativas.

6. Las medidas en paralelo de calidad óptica y capacidades visuales sobre el mismo sujeto (en un amplio rango de condiciones y para diferentes sujetos) mostradas en esta tesis para evaluar las prestaciones a través de foco, y la metodología asociada, proporcionan las bases para desarrollar métodos más sofisticados de predicción de las prestaciones visuales, y

contribuyen a la comprensión de los límites de la visión espacial. Estos estudios serán acometidos con la ayuda de óptica adaptativa, que permite la manipulación de las aberraciones ópticas (corrección de aberraciones del ojo y simulación de lentes, en particular con diseños multifocales).

7. La multifocalidad conlleva una reducción de calidad óptica. Asumiento que los nuevos diseños alcanza multifocalidad efectiva (en términos de calidad óptica a través de foco o profundidad de foco visual), existe aún la necesidad de métodos de exploración para detectar a aquellos pacientes que no pueden adaptarse a visión simultánea. Se necesitan nuevos métodos ópticos para dotar a los pacientes cn herramientas de simulación de la experiencia visual de la visión simultánea.

Agradecimientos

Hace muchos años ya, a la vez que asimilaba que la vida y la muerte se entremezclan en cada uno de nuestros días, y que el afecto es lo que puede darle un poco de sentido a todo esto, decidí que todo lo que yo hiciera de valor en esta vida se lo tendría que agradecer, sin remedio, a los médicos, a las enfermeras, y a la gente de ese mundillo. Y ya desde el primer momento me estaba dando yo cuenta perfectamente de que esto no iba a ser nada nada justo. Que a la sufrida dedicación de algunos a los que les vi las manos y las caras, hay que unir las preocupaciones anteriores de muchos otros: los muchos que buscaron los remedios, los pocos que los encontraron, y los que contribuyeron a mejorarlos. Pero puestos a ser injustos y a elegir un capitán, yo elijo, como siempre, al Doctor Juan Jesús Cruz. No es sólo que le esté agradecido, es que para mí es un referente: resulta que uno se puede enfrentar a las situaciones más graves con naturalidad y sencillez. Y si te lo propones, hasta los peores momentos admiten un pelín de buen humor. Aquello fue un descubrimiento estupendo en aquellos momentos (¡y muy útil de ahí en adelante!).

Ahora, en aquel entonces e incluso en los inocentes tiempos antes de aquel entonces (casi "cuando las cosas no tenían nombre y había que señalarlas con el dedo"), a mis padres y a mis hermanos les he tenido siempre igual de cerca. Me he divertido mucho con ellos y no me han dejado pasarlo mal ni cuando tocaba. Sin embargo, cuando tocaba (y toca) pasarlo bien, sí que lo pasamos bien, ¿eh?

Copio aquí de otras muchas tesis que hablaban de otros muchos padres para decir que son "responsables de todo lo bueno que pueda haber en mí". Por *cierto*, que esto que es tan obvio, al pararme a pensarlo dos veces, me estremece (por lo cierto). Tengo que agradecer a mi madre especialmente, por su ejemplo y por su positiva visión del mundo, que suavemente me ha ido impregnando y me ha empujado a ser feliz. Hablando de ejemplo, estoy convencido de que si no hubiera visto a mi padre disfrutar tanto con el trabajo nunca me hubiera sentido capaz de lanzarme a esto "en mis ratos libres". Esas largas tardes que duraban días y días, jugando con mis hermanos en la alfombra mientras mi padre trabajaba en sus cosas, mi madre iba, venía o se quedaba, y todos escuchábamos música, es uno de mis recuerdos más dulces, uno de esos que me han acompañado en los solitarios y sacrificados días de procesar datos e intentar escribir. Otro: las tardes en el campo, las lianas, las abubillas...

Pero un día el tiempo se puso en marcha, y hasta aquí hemos llegado: Berna e Isa me marcaron el camino en esto de las tesis, y Yeyo al final también me ha adelantado con su proyecto. La verdad (si se me permite decirlo aquí) es que estoy super orgulloso de mi familia. Y aunque no pueda dedicar mucho espacio, esto también va por mis estupendos suegros, cuñados y sobrinos, sin los cuales mi vida sería aburrida

(y muchísimo más difícil). Me da pena que ya no quepamos todos en la alfombra para echar unas canicas…

Ver el mundo a través de los ojos de mis hijos me ha enseñado que la vida, por encima de cualquier cosa, debe ser feliz y sencilla ("Papá está escribiendo un cuento muy largo, pero ya va a acabar"). Ni os veo inocentes ni ingenuos frente a las muchas cosas que os suceden y las que pasan a nuestro alrededor. Veo que aceptáis las cosas con una serenidad y entereza que ya querría yo para mí. Gracias, chicos. Me habéis animado un montón. ¡Prometo ayudaros con vuestras cosas! ¡Y con vuestras tesis!

Tendría que dar las gracias (inexcusablemente) a montones de amigos, más familiares, compañeros y excompañeros de aquí y de allá, maestros e incluso ascendentes, por miles de cosas distintas, pero tengo que llevar esto a encuadernar (y tengo un miedo reptil a los olvidos en las enumeraciones). Pero claro, no me puedo permitir ni pensar en dejar de nombrar a Susana, mi maestra, que siempre ha confiado en mí, que me ha enseñado tantísimo, y que en un momento dado me hizo un hueco en su equipo (que no hace tanto tiempo era más bien pequeño). Ha trabajado muchísimo para que este trabajo salga adelante. Limitándome a lo que es el trabajo científico, quiero mencionar a algunos coautores clave (también buenos amigos), que con gran paciencia y tolerancia han dado enormes empujones a este trabajo, y valiosos consejos: E. Moreno-Barriuso, L. Llorente, D. Cano, R.G. Anera, J. Merayo, A. Pérez-Escudero, L. Remón y J. Siegel. Ya puestos, agradezco también a todos mis profes de física y de óptica. Y a la gente de Leica (especialmente Roman Nachbauer) que me enseñaron lo que es la industria de la óptica. Y a los Beale, de Richmond, que me enseñaron inglés (aunque en el fondo eso ha acabado siendo lo de menos), y probablemente enseñarán inglés (y muchas otras cosas) a mis hijos. Y a Eloy, Chari, Encarnita, Belén, Carlos, Jorge… que hacen que el IO pueda funcionar. También muchas muchas gracias a todos los de VioBio, los de ahora y también a los de antes, que me habéis ayudado muchísimo (Lourdes, Sergios, Dani, Helena, Patricia, Alberto, Lucie, Alfonso, Enrique, Jose, Benja, Damian, Laura, Pablos, Daniel). Y a los del GPL. Y a la gente del CIDA, especialmente a María y a Fernando que me animasteis mucho y me ayudasteis a empezar. Y a las marus y a sus parejas… un poquito de distracción viene muy bien. Y hablando de distracción que no se me olvide: los de la obra… habéis estado siempre muy presentes mientras escribía. Ya está bien. Y a todos los que me retrasasteis mientras intentaba acabar esta tesis, con un café, con unas cañas, con unas vacaciones o incluso con un proyecto o con una nueva empresa: he decidido que os perdono, e incluso os lo agradezco.

Para Uca, amiga y mil cosas más, no he encontrado las palabras. Lo he intentado, pero nada. Algún día me gustaría escribir un libro de verdad, de cuentos por lo menos, y dejaré que se me cuele por los personajes. Páginas y páginas. Mientras tanto, acabo esta tesis como la empecé. Dedicándosela a ella.

A Uca.

316